Die approbierte Originalversion dieser Dissertation ist an der Hauptbibliothek der Technischen Universität Wien aufgestellt (http://www.ub.tuwien.ac.at).

The approved original version of this thesis is available at the main library of the Vienna University of Technology (http://www.ub.tuwien.ac.at/englweb/).

Diese Arbeit wurde begutachtet von:

DISSERTATION

Thermoluminescence Dosemeters as Biologically Relevant Detectors

Correlation of Biochemical Cellular Events with LET-Selective Thermoluminescence Dosimetry

ausgeführt zum Zwecke der Erlangung des akademischen Grades
eines Doktors der technischen Wissenschaften unter der Leitung von

Univ.-Prof. DI Dr.techn. Norbert Vana
E141
Atominstitut der Österreichischen Universitäten

eingereicht an der Technischen Universität Wien
Fakultät für Physik

von

DI Christoph Fürweger
Matrikelnummer: 9626307
3350 Haag, Siedlungsring 11

Wien, im September 2007

Acknowledgements

First and foremost, I want to express my gratitude to Univ.-Prof. DI Dr. Norbert Vana who gave me the opportunity to delve into the challenging topic of radiation protection, dosimetry and radiobiology. His open-minded, interdisciplinary vision of his field of expertise has been an exemplary guideline for developing my personal view of current issues. It is largely attributable to his personal, long-time dedication to a combined physical and radiobiological approach for advancing the knowledge in radiation protection, which allowed for this project to take off in the first place.

Furthermore, I am highly indebted to Ao. Univ.-Prof. Dr. Reinhard Kodym for conveying his immense theoretical and practical knowledge on biologic radiation effects as well as biochemical methodology, which constitute the basis of a great part of this thesis. Frequently, I could not help but be impressed by his talent of generating experimental solutions to diverse problems in an unbelievably fast fashion. It is especially noteworthy that he remained available for fruitful discussions until the end of my work despite his transfer to the University of Texas Southwestern Medical Center in 2005.

It is a particular pleasure to extend my thanks to Univ.Ass. DI Dr. Michael Hajek for his crucial assistance in dosimetry and for proof-reading parts of this work. Apart from that, he has tremendously facilitated my efforts by acting as an experienced guide to the Japanese scientific and general way of life. Thereby, he has often extended his support beyond a purely professional level, which I am much obliged for.

I want to convey a special thanks to Dr. Elfriede Hörth for taking upon her the time-consuming task of introducing me to the "mysteries" of cell culture and a manifold of biochemical techniques. Her continuous interest in my work and invaluable help in conquering various bureaucratic challenges has built up my great appreciation of her as a dear colleague.

I have come to highly value the friendly relationship and productive discussions with the members of the "Radiation Physics, Radiation Protection and Nuclear Engineering" group of the Atomic Institute, DI Peter Hofmann, DI Robert Bergmann and DI Florian Smetana. Furthermore, especially in times of technical need, the skilful and committed support of ADir. Ing. Manfred Fugger could always be relied upon. His straight-forward and efficient

methods of identifying and solving problems of different nature have gravely promoted the progress of this work.

My sincere thanks shall be addressed to the staff members and scientists at the National Institute of Radiological Sciences in Chiba, Dr. Ryuichi Okayasu, Dr. Maki Okada, Dr. Yukio Uchihori, Dr. Hisashi Kitamura, and Dr. Nakahiro Yasuda, as well as to the operating personnel of the Heavy Ion Medical Accelerator facility. It is due to their combined efforts and professional assistance in technical and organizational issues that my irradiation experiments with high-energy charged particles, the core of this thesis, could be successfully performed.

I highly appreciated the friendly and supportive attitude of my colleagues at the Clinic for Radiotherapy, which includes Ao. Univ.-Prof. Dr. Edgar Selzer, the assistant medical technicians of the Radiobiology group, and the members of the Physics department.

Furthermore, I am grateful for the funding of my studies by the Anniversary Funds for the Promotion of Scientific Research and Teaching of the Austrian National Bank (OeNB), and for financial support of my experiments in Japan by the Vienna Technical University.

Throughout my PhD studies, I could always rely on the persistent backup of Gabriele Hinteramskogler. Apart from greatly amending the readability of this work due to her English expertise, her unconditional understanding, her catchingly bright and light-hearted nature and her unbiased attitude have been my personal source of inspiration.

Finally, I want to express my greatest thanks to my parents, Franz and Ilse Fürweger, and my grandmother Hermine Winkler. Without their patience and continuous support of my studies and scientific ventures, the completion of my PhD thesis would not have been possible.

Abstract

Radiation protection relies on the exact determination of absorbed dose and its translation into potential health risks. In recent years, significant progress in the field of radiobiology has led to a refined understanding of the radiation-induced biologic response, which challenges common macroscopic views of radiation effects. Especially for low doses of high-energy charged particle radiation, a microscopic approach is warranted in order to account for the specific patterns of energy deposition on the cellular level, which are known to result in the induction of DNA damage in both directly hit and bystander cells.

Thermoluminescence (TL) dosimetry with LiF:Mg,Ti detectors allows for parallel assessment of absorbed dose and the effective LET in the detector material by evaluation according to the High Temperature Ratio (HTR) method, which abuses the LET-dependent shape of LiF:Mg,Ti glow curves. Since the HTR is affected by the energy deposition characteristics of ionizing radiation, it represents a microdosimetric measure for radiation quality. The similar LET-dependence of the HTR and the quality factor Q as given in the ICRP publication 60 (1) suggests the possibility of LiF:Mg,Ti material to act as a "quasi-biologic" detector that is able to directly assess the biologic damage potential of various radiation types.

Therefore, the presented work is aimed at correlating the cellular response induced by radiation of varying quality with TL measurements. For this purpose, exposures of cultivated human skin fibroblasts and LiF:Mg,Ti detectors to high-energy charged particles have been performed at the Heavy Ion Medical Accelerator, HIMAC, in Chiba, Japan. Special emphasis has been laid on the low dose region, where bystander effects are expected to contribute significantly to overall radiation risks, which may greatly influence future directions of radiation protection in particle fields. Thereby, it is intended to investigate the dependence of the cellular response on physical exposure parameters and to elucidate the time course of biochemical events. Based on these data, the application of the HTR method as a tool for prediction of biologic effects is evaluated.

In more detail, the biological effects assessed include specific biochemical events that are known to play a major role in the early cellular response to DNA double-strand breaks (DSBs), such as the formation of pATM (serine 1981), γH2AX (serine 139) and pDNA-PKcs (threonine 2609) foci. Using immunocytochemical and image analysis techniques,

methods for quantification and characterization of these events have been developed and optimized.

In exposures to equal particle fluences (7.4×10^4 cm^{-2}) of different LET, no radiation-induced cellular response could be detected at two hours after irradiation for particles with an LET of 30 keV/µm H_2O and below. In contrast, the number of all different types of foci has been found to increase with particle LET starting at about 60 up to 300 keV/µm. For ^{56}Fe ions (198 keV/µm), there is indication that the number of affected cells even exceeds the fraction of cells with direct DNA damage due to nuclear particle traversals, thus arguing for a spread of the initial radiation damage signal to bystander cells as early as two hours after exposure.

Furthermore, fibroblasts have been treated with an equal dose of 60 mGy delivered with beams of different LET and particle species in order to assess cellular signalling at three different time points (20', 1h, 2h) after irradiation. Independent of LET, the present sites of DNA damage as marked by foci are most numerous at the earliest recovery time and decline thereafter, which may be attributed to repair activities. However, whereas most radiation-induced foci due to lower-LET particles have already dissolved after two hours, the number of foci in samples exposed to the highest-LET ^{56}Fe ions (198 keV/µm) remains at a high, almost constant level throughout the observation period. This finding suggests a relatively efficient repair of damage due to lower-LET radiation, whereas higher local ionisation densities cause more complex DNA lesions that require substantial and prolonged processing efforts. This conclusion is further supported by a detailed analysis of focus sizes induced by different particle beams, which exhibits a clear increase in size with LET, thus indicating the presences of extensive damage clusters along tracks of high-LET particles.

As further results from the exposures to ^{56}Fe ions, good correspondence between the number of nuclear particle traversals and the initial number of detected foci has been found, which demonstrates that single particles of sufficiently high lineal energy are able to initialize a pronounced cellular response. Moreover, evidence has been accumulated that the decrease in the number of foci due to repair is followed by another period of increasing DSB-induced signalling activity starting about one hour after exposure, which hints at the occurrence of delayed DNA DSBs. This behaviour is most plausibly explained by an onset of non-targeted effects, which further promotes the hypothesis that bystander effects significantly contribute to the early cellular response to high-LET radiation.

Absorbed dose and HTR values obtained from co-exposed LiF:Mg,Ti detectors have been found to fit well into established data. Comparison of HTR with pATM (serine 1981) and pDNA-PKcs (threonine 2609) data as functions of LET shows that the initial radiation-induced signalling response detected at 20' after exposure exhibits a behaviour remarkably similar to HTR(LET). However, due to the LET-dependent time course of DNA damage repair, the observed extent of ATM and DNA-PKcs phosphorylation increasingly deviates from HTR(LET) with time. Nevertheless, the promising correspondence between the initial DNA damage and the HTR strongly argues for the feasibility of a quasi-biologic

dosemeter system based on LiF:Mg,Ti TL detectors and outlines directions of future studies that must be aimed at a detailed modelling of non-targeted effects and their contribution to radiation risk on a larger time scale.

Overall, it has been demonstrated that the microscopic aspect of energy deposition greatly modulates the cellular response to low doses of ionizing radiation. The presented work has illustrated that current challenges in the field of radiation protection may be successfully met with a combined dosimetric and radiobiologic approach, which is suited to eventually provide the means for direct prediction of biologic effects based on physical measurement systems.

Kurzfassung

Die genaue Messung der absorbierten Strahlendosis und deren Übersetzung in ein potentielles Gesundheitsrisiko bilden die Grundlage für den Strahlenschutz. In den letzten Jahren konnte im Bereich der Strahlenbiologie ein detailliertes Wissen über die mikrobiologischen Grundlagen strahleninduzierter Effekte entwickelt werden, das die im Strahlenschutz etablierte makroskopische Betrachtung der Strahlenwirkung um wesentliche Aspekte ergänzt. Dies gilt insbesondere für die Wirkung von niedrigen Dosen hochenergetischer Teilchen, bei denen sich die Energiedeposition im Gewebe weitgehend auf kleine Volumina entlang der Teilchenspuren beschränkt. Auf zellulärer Ebene führt diese Inhomogenität zu spezifischen Schäden der DNA sowohl in getroffenen als auch in umliegenden "Bystander" Zellen.

Die High Temperature Ratio (HTR) Methode zur Auswertung von LiF:Mg,Ti Thermolumineszenz (TL)-Detektoren erlaubt die gleichzeitige Bestimmung der absorbierten Dosis und des effektiven linearen Energietransfers (LET) aus der LET-abhängigen Form der TL Glow-Kurven. Der HTR stellt dabei eine Messgröße dar, die die Ionisationsdichte der Strahlung widerspiegelt, und lässt sich daher als mikrodosimetrisches Maß für die Strahlenqualität interpretieren. Die ähnliche LET-Abhängigkeit des HTR und des Qualitätsfaktors Q gemäß ICRP Publikation 60 (1) weist auf eine mögliche Verwendung von LiF:Mg,Ti als "quasi-biologisches" Detektormaterial hin, was eine direkte Beurteilung des biologischen Schadenspotentials aus der Messung ermöglichen würde.

Die vorliegende Arbeit beschäftigt sich daher mit der Korrelation der zellulären Reaktion auf Strahlung unterschiedlicher Qualität mit TL Messgrößen. Zu diesem Zweck wurden Kulturen von humanen Hautfibroblasten und LiF:Mg,Ti Detektoren mit hochenergetischer Teilchenstrahlung am Heavy Ion Medical Accelerator, HIMAC, in Chiba, Japan, bestrahlt. Besonderes Augenmerk wurde auf den Bereich der niedrigen Strahlendosen gelegt, für den vermutet wird, dass Bystander-Effekte in wesentlichem Maß zum Gesamtrisiko beitragen könnten. Eine mögliche Verstärkung der Strahlenwirkung wäre von zentraler Bedeutung für den Strahlenschutz in Teilchenfeldern und für die Entwicklung von zukünftigen, praxisrelevanten Richtlinien und Grenzwerten. Der gewählte experimentelle Ansatz ermöglicht eine Untersuchung der zellulären Reaktion in Abhängigkeit von physikalischen Bestrahlungsparametern und die

Beobachtung der zeitlichen Abfolge der biochemischen Signalübertragungsereignisse. Auf Basis dieser Daten ist es möglich, den potentiellen Einsatz der HTR Methode für die Abschätzung spezifischer biologischer Strahlenwirkungen zu beurteilen.

Als strahlenbiologische Endpunkte wurden bestimmte biochemische Ereignisse betrachtet, die in der zellulären Antwort auf DNA Doppelstrangbrüche (DSBs) eine zentrale Rolle spielen, wie etwa die Bildung von pATM (Serin 1981), γH2AX (Serin 139) und pDNA-PKcs (Threonin 2609) Foci. Zum Zweck der Quantifizierung und Charakterisierung dieser Ereignisse wurden immuno-cytochemische Färbemethoden optimiert und geeignete Techniken zur Bildanalyse entwickelt.

In Zellbestrahlungen mit einer konstanten Teilchenfluenz von $7{,}3\times10^4/cm^2$ konnte für eine Inkubationszeit von zwei Stunden keine strahleninduzierte zelluläre Reaktion für Teilchen mit einem LET bis zu 30 keV/µm H_2O nachgewiesen werden. Hingegen wurde ein deutlicher Anstieg der Anzahl verschiedener Focitypen mit dem LET für den Bereich von 60 bis 300 keV/µm H_2O beobachtet. In jenen Proben, die einer Bestrahlung mit ^{56}Fe Ionen (198 keV/µm) ausgesetzt waren, gab es Hinweise dafür, dass die Strahlenwirkung eine größere Zahl an Zellen umfasste als durch einen Teilchentreffer im Zellkern direkt beschädigt wurden, was auf eine Ausweitung des primären Strahlenschadens auf Bystander-Zellen hindeutet.

In einer weiteren Bestrahlungsserie wurden Fibroblasten einer konstanten Dosis von etwa 60 mGy ausgesetzt, wobei die Arten geladener Teilchen und die LET-Werte variiert wurden. Durch die Auswahl von drei Beobachtungszeitpunkten (20', 1 h, 2 h) nach Bestrahlung konnte der Zeitverlauf der zellulären Signalübertragungsmechanismen beobachtet werden. Für alle LET-Werte wurde eine Abnahme des vorliegenden DNA-Schadens, der sich in verschiedenen Focitypen manifestiert, mit zunehmender Inkubationszeit registriert, was auf Reparaturaktivitäten der Zelle zurückzuführen ist. Während sich allerdings die Mehrzahl der durch Strahlung von niedrigerem LET induzierten Foci nach zwei Stunden bereits wieder aufgelöst hatte, blieb die Focizahl nach Bestrahlung mit hoch-LET ^{56}Fe Ionen (198 keV/µm) über den gesamten Beobachtungszeitraum auf einem hohen, beinahe konstanten Level. Aus diesem Umstand lässt sich ableiten, dass die zellulären Mechanismen DNA-Schäden durch niedrig-LET Teilchen vergleichsweise effizient beheben können, während eine höhere lokale Ionisationsdichte ein komplexeres Schadensbild hervorruft, das eine entsprechend aufwändigere Bearbeitung verlangt. Für diese Schlussfolgerung spricht weiters, dass in einer detaillierten Analyse der Focigrößen eine Größenzunahme mit steigendem LET ermittelt wurde, die durch das konzentriertere Auftreten von DNA-Schäden entlang der Spuren von hoch-LET Teilchen erklärt werden kann.

Als ein weiteres Ergebnis der Zellexpositionen mit dem ^{56}Fe Strahl konnte eine gute Übereinstimmung zwischen der Zahl an Zellkerntreffern und der beobachteten Foci nachgewiesen werden, was illustriert, dass bereits einzelne Teilchen von entsprechend hoher linealer Energie in der Lage sind, eine ausgeprägte zelluläre Reaktion zu initialisieren. Weiters hat sich gezeigt, dass etwa eine Stunde nach Bestrahlung auf den

frühen Abfall der Foci-Anzahl durch Schadensreparatur ein weiterer Anstieg in der DSB-induzierten Signalübertragung folgt, der auf das verspätete Auftreten von weiteren DNA-Läsionen hindeutet. Dieses Verhalten lässt sich auf plausible Weise durch das Einsetzen von sekundären, „non-targeted" Strahleneffekten erklären, zu denen auch der Bystander-Effekt zählt, was als ein weiterer Hinweis für dessen Beitrag zur frühen zellulären Reaktion auf hoch-LET Strahlung zu werten ist.

Die Messwerte für die absorbierte Dosis und den HTR, die im Rahmen dieser Arbeit aus gleichzeitig bestrahlten LiF:Mg,Ti Detektoren gewonnen wurden, fügen sich nahtlos in bestehende, etablierte Daten ein. Ein Vergleich des HTR mit den Resultaten für pATM (Serin 1981) und pDNA-PKcs (Threonin 2609) als Funktionen des LET zeigt, dass die unmittelbare strahleninduzierte Reaktion 20 Minuten nach Bestrahlung ein bemerkenswert ähnliches Verhalten wie HTR(LET) aufweist. Aufgrund des LET-abhängigen Zeitverlaufs der Schadensreparatur weicht allerdings das beobachtete Ausmaß der ATM und DNA-PKcs Phosphorylierung mit zunehmender Inkubationszeit immer mehr von HTR(LET) ab. Trotzdem liefert die viel versprechende funktionale Übereinstimmung zwischen dem ursprünglichen Schadensausmaß und dem HTR ein wesentliches Argument dafür, dass LiF:Mg,Ti Detektoren eine geeignete Basis für ein quasi-biologisches Dosimetersystem darstellen. Der beobachtete zeitliche Verlauf der zellulären Reaktion gibt die Richtung für notwendige, zukünftige Arbeiten vor, die sich mit einer detaillierten Modellierung von "non-targeted" Strahleneffekten über einen erweiterten Zeitraum und deren Beitrag zu Risikobetrachtungen auseinandersetzen.

Insgesamt konnte experimentell gezeigt werden, dass der mikroskopische Aspekt der Energiedeposition die zelluläre Reaktion auf ionisierende Strahlung in wesentlichem Maß beeinflusst. Die vorliegende Arbeit stellt ein Beispiel dar, wie man gegenwärtigen Herausforderungen im Strahlenschutz erfolgreich mit einem die Fächer der Dosimetrie und Strahlenbiologie umfassenden Ansatz begegnen kann, und weist den Weg zur direkten Vorhersage von biologischen Strahleneffekten mittels physikalischer Messmethoden.

Contents

Acknowledgements ii

Abstract iv

Kurzfassung vii

Contents x

Part I: Introduction 1

1. Scope of the Work 2

2. Dosimetric and Particle Field Quantities 5

2.1. Dosimetric Quantities 5

2.1.1. Absorbed Dose 5

2.1.2. Linear Energy Transfer 6

2.1.3. Relative Biologic Effectiveness 7

2.1.4. Dose Equivalent 7

2.1.5. Equivalent Dose 8

2.1.6. Effective Dose 9

2.1.7. Ambient Dose Equivalent 10

2.2. Particle Field Quantities 11

2.2.1. Particle Flux 11

2.2.2. Particle Fluence 11

2.2.3. Particle Fluence Rate 11

2.3. Microdosimetric Quantities 12

2.3.1. Specific Energy 13

2.3.2. Lineal Energy 14

3. Thermoluminescence 16

3.1. The Phenomenon of Thermoluminescence 16

3.2. Application in Dosimetry 18

4. Radiobiology on the Cellular Level 20
4.1. The Cell 20
4.2. The DNA Molecule – Coiling the Helix 23
4.3. The Cell Cycle 24
4.4. Radiation Induced Cellular Effects 26
4.4.1. Basic Radiation Chemistry 26
4.4.2. DNA Damage 28
4.5. Basic Principles in Radiobiology – an Overview 29

5. The Cellular Response to DNA Double-Strand Breaks 32
5.1. DNA Double-Strand Breaks – Occurrence and Consequences 32
5.2. Ataxia-Telangiectasia Mutated – ATM 33
5.3. DNA-dependent Protein Kinase – DNA-PK 34
5.4. Non-Homologous End Joining (NHEJ) 35
5.5. Homologous Recombination (HR) 38
5.6. Cell Cycle Dependence of DSB Repair Mechanisms 43
5.7. Cell Cycle Checkpoints 45
5.8. The P53-Mediated Response 49
5.9. The Histone H2AX 50

6. Non-Targeted Radiation Effects 52
6.1. The Bystander Response 53
6.2. Genomic Instability 57
6.3. Implications of Non-Targeted Effects and Future Perspectives 58

Part II: Materials and Methods 60

7. Thermoluminescence Dosimetry 61
7.1. Properties of Applied Dosemeter Types 61
7.2. The TL-Dat II Reader 63
7.3. The TLD Software for Glow Curve Analysis 64
7.4. Calibration and Annealing Procedures 65
7.5. The HTR-Method 67

8. Microbiological and Biochemical Methodology 71
8.1. Cell Cultivation and Exposure Preparations 71
8.2. Exposure to High-Energy Charged Particle Beams – the HIMAC Facility 72

8.3. Exposures to low-LET photon radiation....78
8.4. Immunocytochemistry....79
8.4.1. Basic Concept....79
8.4.2. Long-term Fixation of Cell Layers on Chamber Slides....81
8.4.3. Immunofluorescence Staining....82
8.4.4. Immunocytochemical Staining with Signal Amplification....83
8.4.5. Primary and Secondary Antibodies....84
8.5. Sample Transportation....85
8.6. Other Methods....86

9. Quantitative Analysis of Biological Samples....87
9.1. Basic Concepts of Staining Analysis and Quantification....87
9.2. Picture Acquisition....89
9.3. Personal Computer Based Image Processing and Analysis....90
9.4. Determination of the Amount of Phospho-Chk2 (Thr68) per Cell....92
9.5. γH2AX (Ser139) in Hit and Bystander Cells....98
9.6. Evaluation of Foci Sizes for Phospho-ATM (Ser1981) and Phospho-DNA-PKcs (Ser2609)....98
9.7. Colocalization of Foci in Immunofluorescence Dual-Stainings....101

Part III: Results and Discussion....104

10. Exposure Plan....105
10.1. Exposure Series at HIMAC....105
10.2. LET Calculation with SRIM....107
10.3. Dose Distribution on the Cellular Level....108

11. Radiobiological Pre-Experiments....114
11.1. Exposures to Low-LET Radiation – Results from Immunocytochemical Staining....114
11.1.1. pChk2 (thr 68) in HeLa Cells Irradiated with X-Rays....115
11.1.2. ATM Activation after Low-Dose γ-Exposure....117
11.1.3. γH2AX in Human Fibroblasts Exposed to 60 mGy of X-Rays....118
11.2. Western Blotting – pP53 (Ser15)....119

12. TL-Measurements at HIMAC....121
12.1. Determination of absorbed dose....121
12.2. HTR vs. LET results....124

13. Cellular Response to High-LET Charged Particles....126

13.1. Cell Effects Induced by Equal Fluences of Different Particles 126
13.1.1. Formation of pATM (Ser 1981) Foci.....127
13.1.2. Formation of pDNA-PKcs (Thr 2609) Foci 130
13.1.3. Colocalization of γH2AX and pATM 132
13.1.4. Colocalization of γH2AX and pDNA-PKcs.....134
13.1.5. Checkpoint Signalling – pChk2 (Thr 68) 136
13.1.6. P53-Mediated Signalling – pP53 (Ser 15).....138
13.1.7. Double-Strand Breaks in Hit and Bystander Cells.....139
13.2. Time-Dependence of the Cellular Response to Equal Doses of Different Particles 141
13.2.1. Formation and Persistence of pATM (Ser 1981) Foci 142
13.2.2. Formation and Persistence of pDNA-PKcs (Thr 2609) Foci.....145
13.2.3. Colocalization of γH2AX and pATM 149
13.2.4. Colocalization of γH2AX and pDNA-PKcs.....152
13.2.5. Combined γH2AX (Ser 139) Results.....155
13.2.6. The Influence of Particle Species.....157

14. Comparison of TL- and Radiobiological Results 160
14.1. Characteristics of Single Particle Tracks 160
14.2. HTR(LET) and DSB-Induced Signalling Events 164

15. Conclusions and Discussion 169
15.1. A Brief Summary of Individual Results 169
15.2. Where is the Bystander Effect? 171
15.3. Is the HTR Method a Suitable Tool for Prediction of Microbiologic Radiation Effects? 175

References.....180

Appendix A: SRIM Simulations 191

Appendix B: Suppliers of Materials, Chemicals and Devices 195

Part I:
Introduction

The first section of the introductory part outlines the scope of this thesis and is intended to give a detailed view of the general topic. This includes the discussion of motivational aspects by highlighting fundamental characteristics of current recommendations on radiological protection, and is concluded by a brief description of the structure and contents of the presented PhD thesis.

In chapters on quantities and concepts in radiation protection and dosimetry, essential aspects of these scientific fields are introduced. This is followed by a brief description of the phenomenon of thermoluminescence, simple theoretical models and the practical application of this effect in dosimetry.

In the latter sections of part I, special emphasis is laid on the discussion of radiobiologic basics and the current status of research in cellular radiobiology in order to provide a solid theoretical foundation for discussion of experimental results in later parts of this work.

1. Scope of the Work

Radiological protection relies on two fundamental concepts: The precise measuring of dosimetric quantities such as absorbed dose and linear energy transfer (LET), and the translation of these physical quantities into radiation-induced health risks. Thus, different scientific fields, which include metrology, epidemiology, medicine and radiobiology, are required to complement one another in order to rise to the complex challenges posed by human exposure to ionizing radiation.

The International Commission on Radiological Protection (ICRP, 2) is the main source for recommendations on the manifold exposure situations encountered. These guidelines incorporate scientific knowledge from the various fields and are commonly utilized as a foundation for occupational thresholds. In a process of steady improvement, the efforts of the ICRP are comprised of the continual assessment of further insights into effects due to ionizing radiation and their integration into a refined view of the radiation hazard. Recently, a new set of recommendations has been approved (3) and is expected to be published in the near future.

For exposures to low radiation doses, the implications on human health are exceptionally difficult to determine. In epidemiology, stochastic radiation effects such as tumorigenesis cannot be easily attributed to a single cause and, besides, are overlaid by a much larger number of cases that arise without any radiation impact. As a consequence, epidemiologic surveys are not ideally suited to provide conclusive evidence on health effects of very low doses. On the other hand, radiobiological studies on the cellular level have demonstrated that even a few mGy of ionizing radiation are sufficient to cause DNA damage, which supports the hypothesis that even lowest radiation doses may promote the induction of stochastic effects. In a wake of these issues, the current recommendations of the ICRP are based on the so-called linear non-threshold (LNT) approach, which suggests an increased probability of stochastic effects with increasing radiation levels, starting at lowest values above the natural background.

However, this view is challenged by various surprising insights on radiation effects, which mainly originate from the field of radiobiology, where steadily advancing methodology allows for the detection of biochemical events on a microscopic level. Bystander effects, genetic instability and adaptive response argue for a deviation from the LNT assumption

in a seemingly contradicting manner. Especially for high-LET charged particle radiation, which is known to cause specific damage patterns on the cellular level due to a highly inhomogeneous distribution of radiation energy, evidence has been accumulated which severely questions the applicability of macroscopic concepts such as dose for biologic effects at extremely low radiation levels. While being chiefly based on in-vitro experiments until today, further knowledge about the underlying mechanisms, the dependency on radiation parameters and their significance for human exposure may eventually lead to implications on future ICRP recommendations.

In light of these developments, interest in the cellular response to high-LET radiation has increased, which is further augmented by the successful application of high-energy charged particle accelerators in cancer therapy and renewed multinational ambitions for human space exploration, where astronaut crews are exposed to high-LET particles of the space radiation environment. This is accompanied by the need for precise monitoring devices that are suited to measure dosimetric quantities in complex fields of interest.

Based on the expertise in thermoluminescence dosimetry that has been built up in the department for "Radiation Physics, Radiation Protection & Nuclear Engineering" of the Atomic Institute of the Austrian Universities, this PhD thesis is aimed at linking dosimetric quantities such as absorbed dose and effective LET to biochemical events on the cellular level, which are already initialized in response to a few high-LET particle hits per 100 cells. For this purpose, several exposures of thermoluminescence detectors and cultivated human cells to high-energy charged particles have been performed at the Heavy Ion Medical Accelerator (HIMAC) of the National Institute of Radiological Sciences, Chiba, Japan. Special emphasis is laid on the crucial low dose area, where events in bystander cells are presumed to contribute to the overall damage response in a significant manner, thereby amplifying the stochastic damage potential in these exposure situations.

The generated dosimetric and radiobiologic data is used to explore the qualification of TL-measurements to act as a tool for prediction of relevant cellular effects. By directly bridging the gap between measured physical quantities and the biologic response, the "detour" via radiation quality factors for the determination of the biologically effective dose is omitted. The inherent advantage of this approach lies in its complete exclusion of intrinsic discrepancies between the macroscopic concept of quality factors and microscopic events in tissue. In future studies based on this PhD thesis, the correlation of radiobiologic and dosimetric results may eventually culminate in the possibility to directly translate TL data into biologic consequences, thus further strengthening the role of LiF:Mg,Ti materials as "quasi-biologic" detectors.

This work is composed of three major parts, which are divided into several chapters, each of which are comprised of a brief introduction announcing its contents and a varying number of subsections. The introductory part I is intended to provide an overview of the concepts of thermoluminescence dosimetry as well as the microbiologic processes that govern the cellular response to radiation exposure. Consecutively, quantities used in

dosimetry and for description of particle fields are introduced in chapter 2, which is followed by a general explanation of the TL-phenomenon and its utilization for dosimetric purposes in chapter 3. In the next chapter 4, fundamental micro- and radiobiologic processes are elucidated in order to provide a solid basis for the subsequent description of the cellular events in the response to DNA double strand breaks in chapter 5, which includes a detailed analysis of current scientific knowledge on the specific biochemical events that have been experimentally assessed in the frame of this thesis. Due to their complex characteristics and their significance for the interpretation of results, a separate chapter 6 has been dedicated to the so-called "non-targeted" biologic effects, which include the bystander response and genetic instability.

Part II provides a detailed description of the methods applied in experimental practise. Chapter 7 outlines the procedures involved in preparation and read-out of TL-detectors, which includes a description of the analysis techniques that allow for determination of dose and effective LET from LiF:Mg,Ti glow curves. In the following chapter 8, the handling of cell samples is covered, which ranges from cultivation over the selected exposure geometries to the conservation of cell layers for storage and transportation, and is concluded by a listing of the employed biochemical methods for the assessment of cellular signalling events via immunological staining techniques. The complex analysis procedures, which have been developed or adapted for the quantification of stained cell layers, are introduced in chapter 9 for different staining characteristics, which are specific to the applied biochemical technique and the assessed biologic event of interest.

Part III is dedicated to the presentation and interpretation of experimental results. A detailed description of the parameters for all exposures to high-energy charged particles is given in chapter 10, which is based on Monte-Carlo simulation of the experimental setup and is concluded by a statistical assessment of the exposure situation on the cell layer level. Results from radiobiologic pre-experiments with low-LET photon radiation performed for optimization of biochemical techniques and development of quantification procedures are presented in chapter 11. This is followed by a presentation of results for dose and effective LET measured with TL-detectors in chapter 12, and radiobiologic data in chapter 13, which focuses on the investigation of various cellular events in response to different high-energy charged particle beams. Chapter 14 is devoted to the comparison of dosimetric and radiobiologic results and illustrates similarities and differences between measured TL quantities and the cellular response to radiation. In chapter 15, a brief summary of individual results is given. On this basis, final conclusions on the contribution of non-targeted effects to the observed radiobiologic response are drawn and the applicability of LiF:Mg,Ti TL-detectors as a tool for prediction of cellular effects induced by low doses of high-LET radiation is critically discussed.

2. Dosimetric and Particle Field Quantities

Chapter 2 provides a brief overview of the field quantities and dosimetric concepts commonly applied in radiation protection and radiobiology. In the first of three sections, dosimetric quantities are introduced based on the definitions provided by the International Commission on Radiological Protection (ICRP) and the International Commission on Radiation Units and Measurement (ICRU). In the second part, quantities are defined which describe the properties of a particle radiation field as a function of place and time. The third section is devoted to the concept of microdosimetry, which deals with energy deposition in volumes of cell size or below.

2.1. Dosimetric Quantities

As a basic principle, radiation protection is concerned with protecting life from harmful effects associated with the exposure to radiation. For this purpose, detrimental radiation-induced biologic effects need to be determined and quantified in order to provide a basis for recommendations on legal limits for exposed personnel and the general public as well as for the assessment of risks associated with specific exposure cases. However, measurement of these biologic effects is a difficult task and is by no means suited for routine monitoring in operational radiation protection or for public purposes. Therefore, physical quantities, which are measured more easily in comparison, are assessed and used as a measure for the relevant biologic consequences.

2.1.1. Absorbed Dose

The fundamental quantity in radiation protection is the absorbed dose, which is a measure for the energy imparted to matter by radiation. The energy ε imparted to the volume of mass m can be written as

$$\varepsilon = R_{in} - R_{out} + \sum Q, \tag{2.1}$$

where R_{in} is the radiation energy incident on the volume, R_{out} is the radiation energy exiting the volume, both excluding rest energy of the corresponding incident and outgoing radiation particles, and all Q added up corresponds to the sum of all changes in the rest energy of the matter and particle radiation involved in interaction processes inside the volume.

The absorbed dose D is defined as

$$D = \frac{d\bar{\varepsilon}}{dm} , \tag{2.2}$$

where $d\bar{\varepsilon}$ is the mean energy imparted on matter of mass dm. The SI unit for absorbed dose is Joule per kilogram $[J \cdot kg^{-1}]$ and is given the special name Gray [Gy].

In radiation protection, it is common to consider an organ or tissue T of mass m_T as a relevant target volume for radiation exposure. The corresponding organ- or tissue-dose D_T is thus given by

$$D_T = \frac{\varepsilon_T}{m_T} \tag{2.3}$$

with ε_T as the total energy imparted on the organ or tissue volume. For the purpose of absorbed dose measurements, the condition of secondary particle equilibrium for the sensor volume is to be taken into account.

2.1.2. Linear Energy Transfer

The linear energy transfer (LET) is a measure of the energy transferred to a medium, which is lost by a traversing charged particle on a given distance. More precisely, the so-called “unrestricted” linear energy transfer L is defined as the mean energy dE transferred to the medium by a particle traversing the distance dl. “Unrestricted”, in this case, means that secondary particles of all energies and ranges are to be accounted for.

$$L = \frac{dE}{dl} \tag{2.4}$$

Common units for the LET are [J/m], [keV/µm], or [MeV/(mg/cm²)] when referring to target density.

The LET in water is a quantity of crucial importance for radiation protection, as it is directly linked to the biologic damage potential of a particle, the so-called relative biologic effectiveness (RBE).

2.1.3. Relative Biologic Effectiveness

Radiation of different quality (i.e. different LET-values and particle species) causes significantly different damage patterns on the tissue- and cell level, which result in varying threats to the exposed organism in the short and long term as well as to its offspring, potentially. To account for these differences, another quantity, the so-called relative biologic effectiveness (RBE) has been introduced. For a given, quantifiable radiobiologic effect or "endpoint" of interest, it is defined as the quotient

$$\mathrm{RBE}_{\mathrm{endpoint}} = \frac{\mathrm{D}_{\mathrm{ref}}}{\mathrm{D}_{\mathrm{T}}} \tag{2.5}$$

where D_T is the test dose of a specific radiation type of interest, and D_{ref} is the dose of a reference radiation (usually Co-60 gamma or 250 keV X-ray) needed to induce the same effect. RBE values are by no means constant for a given radiation type, but vary greatly for different effects observed, with applied doses as well as the biologic target and its specific condition. Nevertheless, the collection of RBE data for a broad range of exposure parameters provides the means for an overall estimation of the biologic damage potential of different types of radiation.

2.1.4. Dose Equivalent

On the sole basis of the vast number of RBE values, routine radiation protection issues cannot be handled. Therefore, simplified concepts had to be developed to allow for determination of the biologically relevant radiation dose from measured "physical" quantities.

The "dose equivalent" has been introduced by the ICRP, including a comparably simple classification of radiation quality based on radiation type and LET. The dose equivalent H is therefore given by the absorbed dose D multiplied with the dimensionless "quality factor" Q:

$$\mathrm{H} = \mathrm{Q}(\mathrm{LET}) \cdot \mathrm{D} \tag{2.6}$$

Therefore, the SI unit for dose equivalent is the same as for absorbed dose, [J/kg], but is given the special name Sievert [Sv] instead. Essentially, for determination of the factor Q, the ICRP has evaluated a multitude of published RBE values according to their significance for radiation induced short and long term health risks as well as genetic damage, and "summarized" with one value for a given radiation type. The currently valid Q-values for charged particles as recommended in the ICRP Publication 60 (1) are given in table 2.1 and visualized in figure 2.1.

Q (LET)	LET
1	< 10 keV/μm
$0.32 \cdot LET - 2.2$	10 keV/μm to 100 keV/μm
$300/\sqrt{LET}$	> 100 keV/μm

Table 2.1: The quality factor Q (LET) for charged particles.

However, quality factors according to ICRP60 still need to be considered an – though highly educated – estimation, which may change in the future, when further radiobiological studies are available and taken into account. Especially for exposure to low doses of high-LET particles, recent radiobiological findings suggest a possibly higher damage potential than anticipated, thereby challenging established concepts in radiation protection.

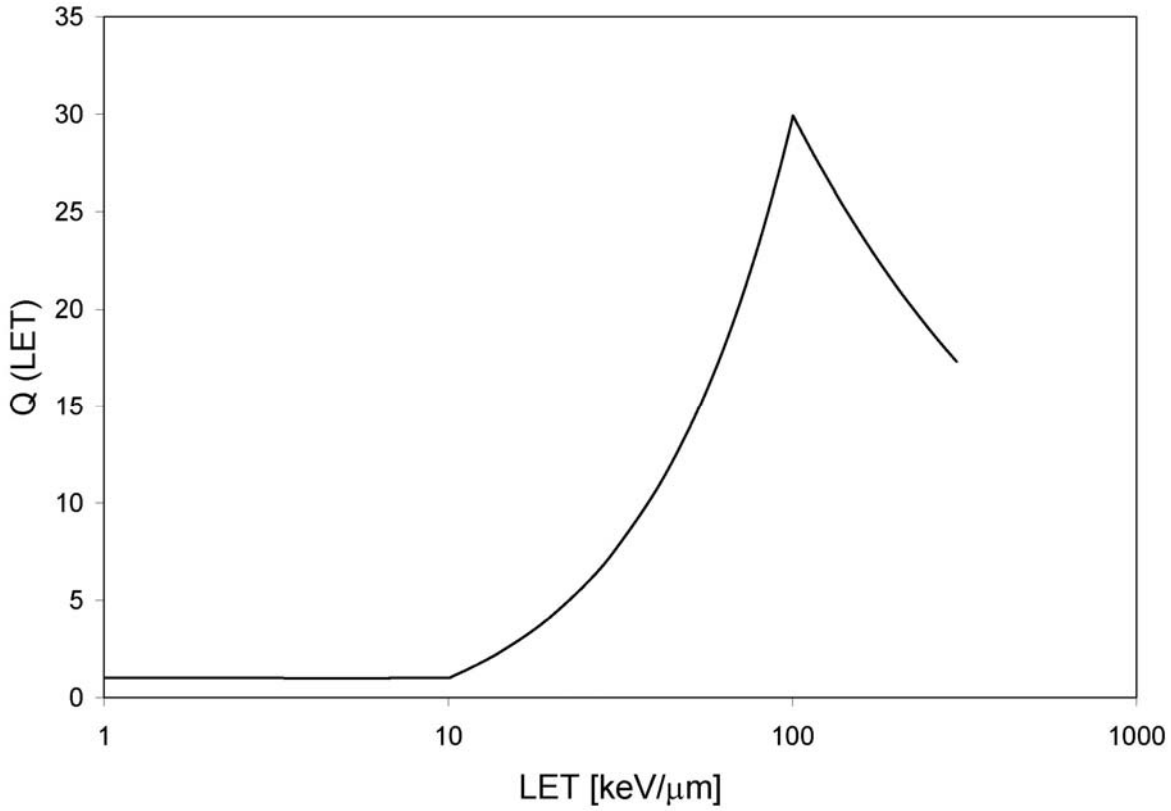

Figure 2.1. The quality factor Q(LET) for charged particles as recommended in the ICRP Publication 60 (1).

2.1.5. Equivalent Dose

Considerable uncertainties in the Q(LET) relationship, which are mainly due to a lack of precision and conformance in radiobiological data, led to the implementation of dimensionless radiation weighting factors w_R by the ICRP as an even more simplified concept instead of the LET-dependent quality factor, which inherently implied a greater

precision than was justified. Thus, the so-called equivalent dose $H_{T,R}$ for an organ or tissue T exposed to radiation R is given by

$$H_{T,R} = w_R \cdot D_{T,R} \tag{2.7}$$

where $D_{T,R}$ is the absorbed dose averaged over the tissue or organ, as given in (1). Identical to dose equivalent, the SI unit for $H_{T,R}$ is [J/kg] and is also called Sievert [Sv]. In radiation fields consisting of various radiation types with different weighting factors, the total equivalent dose is calculated by summation over all contributing components:

$$H_{T,R} = \sum_R w_R \cdot D_{T,R} \tag{2.8}$$

Table 2.2 shows the radiation weighting factors as given by ICRP60 (1).

Type and energy range		Radiation weighting factor, w_R
Photons, all energies		1
Electrons and muons, all energies		1
Neutrons, energy	< 10 keV	5
	10 keV to 100 keV	10
	100 keV to 2 MeV	20
	> 2 MeV	10
Protons, other than recoil protons, energy > 2 MeV		5
Alpha particles, fission fragments, heavy nuclei		20

Table 2.2: Radiation weighting factors, w_R

2.1.6. Effective Dose

Within an organism, different types of cells were found to exhibit diverse responses to ionizing radiation, thus showing varying degrees of radioresistance. Therefore, the relationship between radiation induced stochastic effects and equivalent dose varies for different organs and tissue. The effective dose E is introduced in order to account for these variations. It is obtained by summation over all organ and tissue equivalent doses H_T, each multiplied with its corresponding tissue weighting factor w_T:

$$E = \sum_T w_T \cdot H_T = \sum_T w_T \sum_R w_R \cdot D_{T,R} \tag{2.9}$$

The values for the tissue weighting factors w_T recommended by the ICRP (1) are given in table 2.3. Even though the effective dose is not directly measurable, it is used for all current dose limits, since it is considered to be an indicator for the overall radiation risk of an exposed individual.

Tissue or organ	Tissue weighting factor, w_T
Gonads	0.20
Bone marrow (red)	0.12
Colon	0.12
Lung	0.12
Stomach	0.12
Bladder	0.05
Breast	0.05
Liver	0.05
Oesophagus	0.05
Thyroid	0.05
Skin	0.01
Bone surface	0.01
Remainder	0.05

Table 2.3: Tissue weighting factor w_T

2.1.7. Ambient Dose Equivalent

In order to provide a single dose equivalent quantity for use in routine radiation protection, the "ambient dose equivalent" has been introduced, which allows a simple characterization of the potential irradiation of a human-being in a given radiation field. The ambient dose equivalent $H^*(d)$ at a point in a radiation field is the dose equivalent which would be exerted by the field at that location in a depth d along the radius of a phantom reference sphere, the so-called ICRU sphere. For this purpose, the field needs to be considered as aligned, opposing the depth d, and expanded throughout the sphere, thus requiring its fluence to be unidirectional. The ICRU sphere is intended to mimic the characteristics of the human body, has a diameter of 30 cm and is composed of tissue equivalent plastic material with a corresponding mass composition of 76.2% oxygen, 11.1% carbon, 10.1% hydrogen and 2.6% nitrogen at a density of 1 g/cm³.

The SI unit for ambient dose equivalent is [J/kg] and is called Sievert [Sv]. Different types of reference depths are recommended depending on the penetration depth of the radiation. Thus, 10 mm for strongly penetrating and 3 mm (eye) as well as 0.07 mm (skin) for weakly penetrating radiation are to be employed.

2.2. Particle Field Quantities

2.2.1. Particle Flux

For a complete description of a radiation field, the type, direction, energy and the number of particles need to be known. The particle flux is defined as

$$\dot{N}(t) = \frac{dN}{dt} \tag{2.10}$$

where dN is the number of particles in the time interval dt. In this definition, dN needs to be interpreted as the differential of an expectation value, which is due to the intrinsic statistical nature of a radiation field. The SI unit for the flux is [s^{-1}].

2.2.2. Particle Fluence

Per definition, the particle fluence Φ corresponds to the quotient

$$\Phi(r) = \frac{dN}{dA_{\perp}}, \tag{2.11}$$

where dN is the number of particles impinging on a sphere with a small cross-sectional area of $dA_{\perp}$. As indicated by its symbol, the area $dA_{\perp}$ is to be arranged perpendicular to the direction of the incident particles. The SI unit for the particle fluence is [m^{-2}]. For practical purposes, [cm^{-2}] is used frequently.

2.2.3. Particle Fluence Rate

The particle fluence rate φ (t,r) is given by the quotient of the incremental particle fluence dΦ by the infinitesimal time interval dt:

$$\varphi(t,r) = \frac{d\Phi(r)}{dA_{\perp}} = \frac{d^2N}{dt \cdot dA_{\perp}} \tag{2.12}$$

Thus, the fluence rate corresponds to the number of particles incident on a given area per unit time at the time point of interest. The SI unit is [$m^{-2} \cdot s^{-1}$]. In analogy to fluence, [$cm^{-2} \cdot s^{-1}$] is also commonly used.

2.3. Microdosimetric Quantities

In radiobiology, it is often necessary to study radiation induced effects at cellular or even subcellular levels. Therefore, there is considerable interest in the microscopic nature of the energy deposition due to radiation exposure. Among the crucial biologic volumes of interest are the cell and the nucleus, which both correspond to diameters of several micrometers, other cellular organelles and even single macromolecules such as the DNA.

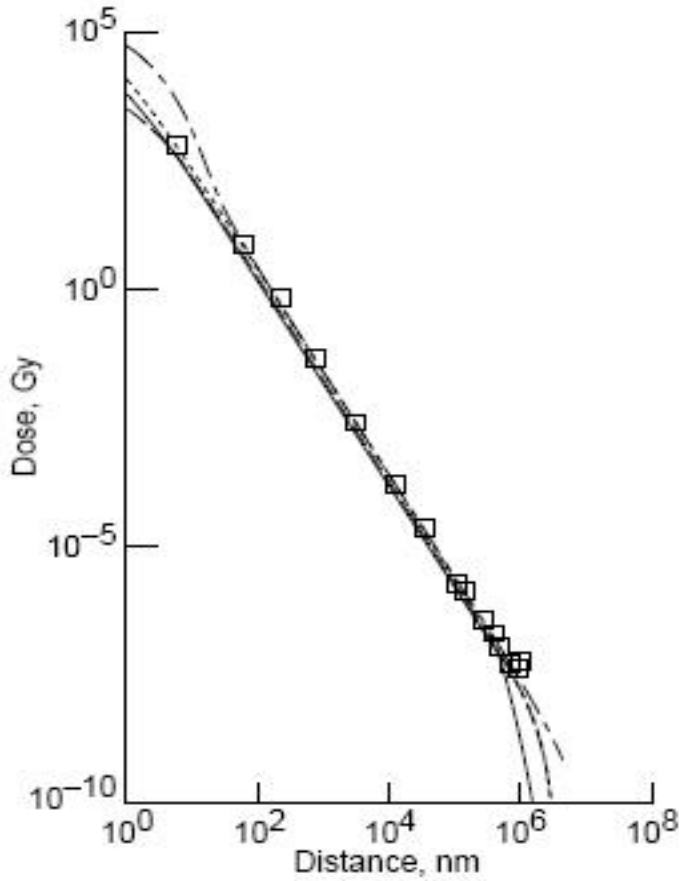

Figure 2.2. High-energy charged particles deposit energy in small volumes along their tracks, as is indicated by the radial dose distribution of 377 MeV/amu ^{20}Ne ions in water (adopted from 152) as an illustrative example. Squares correspond to measured data, the dotted and continuous lines resemble different model calculations.

Obviously, macroscopic units such as absorbed dose are not sufficient to deal with this challenging situation. Especially for low doses of high energy charged particle radiation, where the energy is deposited highly localized along particle tracks (see figure 2.2) while causing only a very small number of ionization events several micrometers off the track, the concept of absorbed dose is seriously misleading when considering cellular effects.

Furthermore, the microscopic distribution of ionization events is of "vital" importance with regard to the specific shape and structure of crucial macromolecules such as the

DNA, which is often the key to understanding specific damage patterns as induced by different types of radiation. Therefore, the macroscopic point of view needs to be refined and extended with microdosimetric quantities, which are able to describe the deposition of radiation energy in the micro- and nanometer dimension.

2.3.1. Specific Energy

Per se, microdosimetric parameters are of a stochastic nature, which is due to the stochastic process of energy deposition by radiation. According to the ICRU definition, a stochastic quantity is a quantity which is subject to random fluctuations. Thus, only the expectation value of a stochastic, microdosimetric quantity, which is a non-stochastic quantity, can be directly compared to macroscopic dosimetric quantities.

The stochastic microdosimetric equivalent to absorbed dose is the specific energy z. Following the ICRU definition, the specific energy is given by

$$z = \frac{\varepsilon}{m}, \tag{2.13}$$

where ε is the energy deposited by ionizing radiation in the matter of mass m. The imparted energy ε, a stochastic quantity, consists of a multitude of energy deposits ε_i, and is thus given by

$$\varepsilon = \sum_i \varepsilon_i \ . \tag{2.14}$$

ε_i corresponds to the energy deposited to the volume of the matter in a single interaction event. The unit for ε is the Joule [J]. The unit for z is [J/kg] and is given the special name Gray [Gy].

Due to ε being a stochastic quantity, this also applies to z, which can therefore be described by a probability function. Thus, the probability that the specific energy is less than or equal to z shall be given by the distribution function F(z). The derivative of F(z) is the probability density f(z) as is written in equation (2.15).

$$f(z) = \frac{dF(z)}{dz} \ \text{with} \ \int_0^\infty f(z)dz = 1 \tag{2.15}$$

The non-stochastic expectation value $\bar{z}$, which is called the mean specific energy, is determined by integration over all specific energies z, and therefore corresponds to the total energy E deposited in the matter of mass m, which is equal to the macroscopic quantity of absorbed dose D:

$$\bar{z} = \int_0^\infty z \cdot f(z) dz = \frac{E}{m} = D \tag{2.16}$$

For specific microdosimetric or radiobiological questions, each single energy deposition also needs to be seen as distributed and described by a probability function $f_j(z_j)dz_j$ (with the index j indicating different deposition events), similarly to f(z)dz for the specific energy (see equation (2.15)). With $\overline{z_j}$ as the expectation value of the specific energy for the deposition event j,

$$\overline{z_j} = \int_0^\infty z_j \cdot f_j(z_j) dz_j \ , \tag{2.17}$$

the number of energy depositions n can be written as

$$n = \frac{\bar{z}}{\overline{z_j}} \ . \tag{2.18}$$

2.3.2. Lineal Energy

In analogy to the macroscopic quantity of linear energy transfer (LET, see equation (2.4)), the microdosimetric lineal energy y is defined as the quotient

$$y = \frac{\varepsilon}{\bar{l}} \ . \tag{2.19}$$

Thereby, ε is the energy imparted to the matter (see equation (2.14)), and $\bar{l}$ is the mean chord length in the volume of the matter. For a sphere with diameter d, the mean chord length $\bar{l}$ amounts to

$$\bar{l} = \frac{2}{3} \cdot d \tag{2.20}$$

As the microscopic analogue to LET, the lineal energy is of a stochastic nature and is usually given in [keV/μm]. Following the same procedure as for the specific energy, the lineal energy can be described by a distribution function F(y), its value being the probability for the lineal energy to be lower than or equal to y. Again the derivative of F(y) is the (unified) probability density f(y):

$$f(y) = \frac{dF(y)}{dy} \quad \text{with} \int_o^\infty f(y) dy = 1 \tag{2.21}$$

The expectation value of y,

$$\overline{y_F} = \int_0^\infty y \cdot f(y) dy \ , \tag{2.22}$$

is a non-stochastic quantity and is called the frequency mean lineal energy $\overline{y_F}$. For particles with a range much higher compared to the diameter d of the matter sphere, the frequency mean lineal energy is equal to the macroscopic quantity of the linear energy transfer.

From the viewpoint of cellular and subcellular radiobiology, the concepts of specific and lineal energy are highly suited tools for the description of an exposure situation in a biological target volume of interest, such as a cell layer, a single cell or a particle track through tissue. However, in experimental practise it is often the case that only the macroscopic exposure parameters are known to the researcher due to inherent limitations in measurement, geometrical uncertainties or biological issues. In these cases, microdosimetric concepts are frequently used for a qualitative, theoretical interpretation of experimental results rather than for a quantitative description of the local exposure.

3. Thermoluminescence

In this chapter, the concept of thermoluminescence dosimetry shall be outlined. This will be done by describing the effect of thermoluminescence on a phenomenological basis as well as discussing a simple model approach that is suited for explaining commonly known thermoluminescence effects. The practical application of thermoluminescence as a method for measurement of dosimetric quantities will be briefly introduced. A more detailed discussion of methodology in thermoluminescence dosimetry can be found in chapter 7.5, where the sophisticated High Temperature Ratio-Method is described, which is routinely applied in the working group "Radiology, Radiation Protection and Nuclear Measurement" at the Atomic Institute of the Austrian Universities.

3.1. The Phenomenon of Thermoluminescence

Thermoluminescence (TL) is a long known effect that has already been described in 1663 by British chemist Robert Boyle, who was able to observe a weak emission of light by a diamond warmed up by the human body heat. Since then, it has been found that TL is a phenomenon whereby crystalline solids absorb and store energy from different sources, which may then be released through the emission of light upon heating. Furthermore, only insulator or semiconductor materials may exhibit thermoluminescence, which is due to their intrinsic physical properties (4). It is imperative to distinguish the thermally stimulated emission of light due to TL from photons emitted by an incandescent object at high temperatures, which adhere to Planck's law of black-body radiation.

In 1945, a theoretical and mathematical description of the mechanism underlying the TL phenomenon was published by Randall and Wilkins (5). Because the basic statements of this first-order-kinetics model have ever since been widely accepted as a simplified yet correct description of thermoluminescence, it shall be described in the following:

Since TL effects are limited to crystalline solids, the presented model is based on the energy band description of electron energies. In insulator and semiconductor materials, at temperatures close to absolute zero all electrons are located in the so-called valence band. The valence band is separated from the conduction band by a gap with energy E_g, the so-

called forbidden zone, which does not contain any allowed electron energy levels in perfect crystals as given by the Schrödinger equation for electrons in a periodically altering potential, corresponding to the crystalline structure. Electrons can be temporarily elevated from the valence to the conduction band as a result of energy absorption, leaving behind an electron "hole" located in the valence band.

Defects in crystalline structure or compositional impurities cause local deviations from the strict periodicity of the potential function, leading to allowed states within the forbidden zone. The simplest model description of the TL phenomenon, the so-called one trap – one recombination centre (OTOR) model, which is described in detail in (6), only relies on two different energy states in the forbidden zone: One, which is assumed to be empty in the equilibrium state and acts as a potential electron trap, and another one that is occupied in the equilibrium state and thus represents a potential trap for an electron hole. It needs to be stressed, however, that while this model is able to describe the basic TL-phenomenon, it fails to explain the complex light emission characteristics of real TL materials (see also chapters 3.2 and 7).

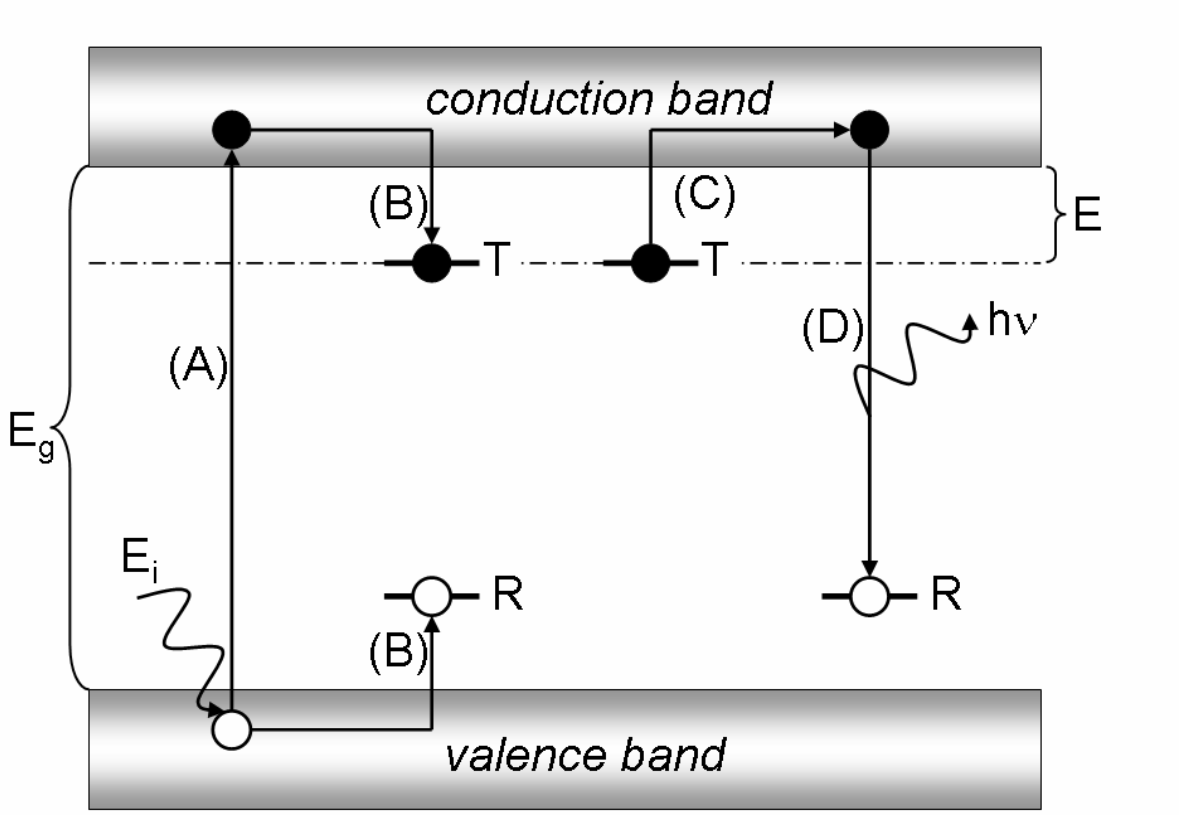

Figure 3.1. Simplified depiction of the TL process in the "one trap – one centre" energy band model. T refers to an electron trap, R to a hole trap or recombination centre. Upon energy absorption, electron-hole pairs are formed (A) and caught in their corresponding traps (B). By heating, trapped electrons are elevated into the conduction band (C) and may recombine with trapped holes, which is accompanied by light emission (D).

In a crystal with the described allowed energy levels, the TL process may proceed as follows (see figure 3.1 for a schematic representation of events): Before exposure to ionizing radiation, the crystal is thought to be in its equilibrium state, and therefore, the valence band and the potential hole trap or "recombination centre" R, are occupied, while the electron trap T and the conduction band are empty. When radiation with energy E_i greater than E_g is absorbed, electrons may traverse from the valence to the conduction band, which results in the occurrence of an electron hole or defect electron in the valence band, thus together representing a so-called electron-hole pair that consists of a free charge carrier in both bands (step A). The elevated electron may either recombine with a hole, which results in the emission of the excess energy via fluorescent light, or be trapped. Thereby, electrons occupy energy levels of electron traps T, and holes settle at levels of recombination centres R (step B). With the energy E as the depth or activation energy of the electron traps, this state is metastable at sufficiently low temperatures ($E>>k_BT$). With rising temperature, the probability increases for a trapped electron to return to the conduction band (step C). Thus, when an irradiated thermoluminescent material is heated, more and more electrons absorb enough thermal energy to be released from their traps. From the valence band, they may either be trapped again, or recombine with a trapped hole. The latter is coupled with the emission of light (step D), which is then termed thermoluminescence. Therefore, by this process, a continuous recombination of electrons and holes is achieved with increasing temperature, thus progressively emptying the traps.

3.2. Application in Dosimetry

The light emitted by thermoluminescent materials that have been exposed to ionizing radiation may be utilized for determination of dosimetric quantities. For this purpose, the usual proceeding is to record the intensity of the emitted light as a function of temperature, which is continually raised in a defined way using an external heating source. The resulting intensity vs. temperature diagram is commonly referred to as "glow curve". For typical TL materials, the glow curve features several peaks, which cannot be derived from the one trap – one centre model introduced in chapter 3.1 that would essentially account for the appearance of only one peak. Complex glow curves can only be explained by more sophisticated models that include several energy levels for electron traps and recombination centres and further on allow for the release of trapped holes due to thermal energy and additional recombination processes (7).

In principle, the emitted TL intensity is proportional to the dose absorbed by the material. Therefore, specific parts of the glow curve may be used to derive the absorbed dose. Usually, the height of and/or the integrated area under one or more peaks are calibrated to absorbed dose in a specific type of radiation field. Obviously, refined methods need to be applied for background correction and subtraction of the contribution of the black body radiation to the glow curve. Furthermore, for individual materials, specific properties such as signal fading, saturation effects and the dependence of TL efficiency on field parameters

(e.g. LET, particle species) must be accounted for. Thus, the maximization of accuracy in TL dosimetry is a complex process that relies heavily on accurate calibration procedures, carefully applied and precise handling techniques and sophisticated mathematical analysis of glow curve structure.

The High Temperature Ratio-Method, which is utilized in this thesis and allows for the determination of the effective LET in addition to absorbed dose, is discussed in section 7.5. For a detailed description of TL materials used in the performed measurements, see part II, “materials and methods”, section 7.1.

4. Radiobiology on the Cellular Level

For routine radiation protection purposes, it is usually sufficient to consider an individual or specific tissue and organs (as are specified in section 2.1.6) as target volumes of interest, which is suitable for the estimation of radiation health risks. However, all "macroscopic" radiation induced effects such as cancer originate from events at a molecular level. Thus, as a first step in a cascade of events, which can finally lead to a serious impact on the health of an individual, radiation damage is incidentally caused in the basic unit of life, the cell. Therefore, in order to understand the origin of the detrimental effects of ionizing radiation, it is necessary to refer to events at the single-cell-level. Cells are structured complexes with diameters of a few micrometers, which efficiently perform a multitude of tasks.

In the first few subsections, a brief overview of fundamental cellular functions and anatomy shall be given, including a detailed description of the DNA molecule and cell cycle progression. Following this introduction of microbiologic basics, elementary concepts of radiobiology will be developed based on the interaction of radiation with cellular matter. Finally, general aspects of the cellular response to radiation damage and implications on experimental practise as well as the interpretation of radiobiological results will be outlined.

4.1. The Cell

A cell consists of a multitude of chemical substances termed protoplasm. The cell is the smallest unit of protoplasm which is able to exist independently. The human body contains a huge number of different types of cells, which greatly vary in size, shape and function. They may be spherical, rectangular or of irregular shape and usually feature a characteristic structure that is necessary to excel in performing a specialized task. A specific type of tissue consists of a large number of similar cells. The combination of one or several types of tissue is necessary to form an organ.

From the chemical viewpoint, protoplasm consists of organic and inorganic compounds dissolved or suspended in water. Water represents by far the greatest fraction of the

protoplasmic matter (70 to 80 percent, depending on cell type). Inorganic compounds are mainly mineral salts; the organic compounds can be subdivided in proteins, lipids, carbohydrates and nucleic acids.

However different the various types of human cells may be, they show many similarities in structural composition. Firstly, all cells are surrounded by a cell membrane which forms the outer boundary of a cell, thus separating one cell from another as well as its exterior surroundings. Inside the cell membrane, the cell's nucleus and other organelles can be found embedded in the cytoplasm. For the sake of completeness it shall be mentioned that there are a few types of human cells that do not contain a nucleus, the most famous being the erythrocyte (the mature red blood cell).

The different parts of a cell and their basic functions shall be presented briefly in the following (see figure 4.1 for a schematic of the cellular structure). For an in-depth description of cellular structure, function and metabolism, the author recommends the study of specialized literature such as by G. Alberts et al (8) or G. Fuchs et al (9, in German). A simple yet highly illustrative and interactive depiction of cellular structure and processes can also be found online (10).

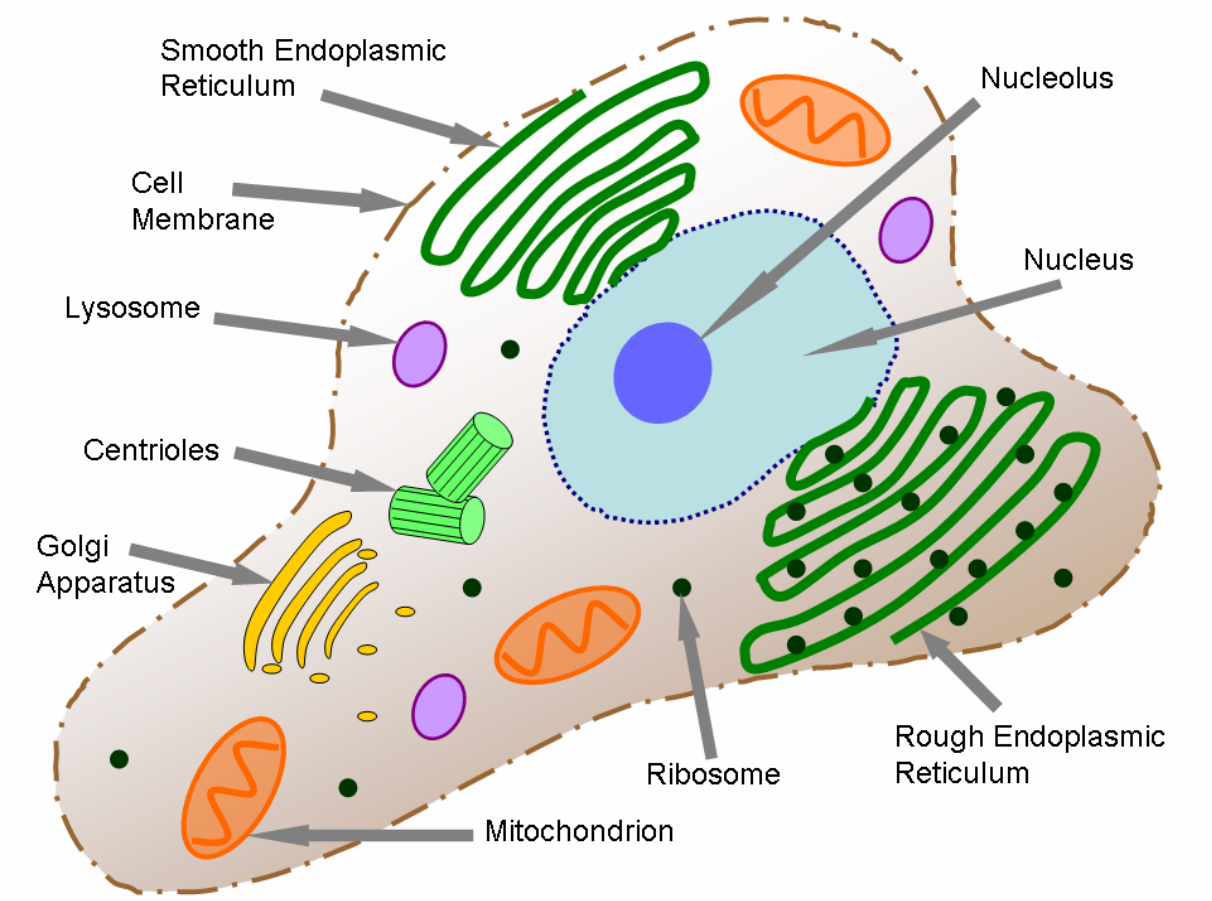

Figure 4.1. Schematic of a cell and its organelles.

Separating a cell from its exterior, the **cell membrane** consists of a double-layer of phospholipids, which prevents uncontrolled flow of water in and out of the cell. Complex mechanisms regulate the transport of substances through the membrane. Special membrane-bound proteins act as sensors to the chemical environment, allowing for the cell to react to its surroundings.

The **cytoplasm** is a watery solution containing the various cellular organelles such as the nucleus, the smooth and rough endoplasmic reticulum, the centrosome, ribosomes, mitochondria and the Golgi apparatus. The cytoskeleton, a network of protein filaments, spans across the cytoplasm. It maintains the shape of the cell and governs the intracellular movement of the organelles.

Mitochondria are the power generating centers of a cell. They are enclosed by a double-membrane and provide ATP through cell respiration, the oxidation of carbohydrates. The number of mitochondria in a particular cell type is dependent on its need for ATP – muscle cells require a lot of energy for muscle contraction, thus feature a large number of mitochondria.

The **centrosome** is a spherical organelle containing two so-called centrioles, cylindrical organelles, which are attached orthogonally to each other. During the process of cell division, the centrioles detach from one another and form a complex spindle apparatus, which is used for distribution of the duplicated chromosomes to the two daughter cells.

The **endoplasmic reticulum** represents a tubular network extending from the nuclear to the cell membrane. Two types can be distinguished due to their appearance in electron microscopy, the so-called rough and the smooth endoplasmic reticulum. The rough endoplasmic reticulum has numerous ribosomes (see below) attached to its surface whereas the smooth endoplasmic reticulum is free of ribosomes. Both play essential roles in protein folding and transportation as well as in cellular metabolism.

Ribosomes are centres of protein synthesis. They assemble amino acids to polypeptide chains according to the genetic information which is provided by so-called messenger RNA (mRNA). The mRNA is a processed (spliced) RNA copy of the DNA, which is used to transfer information stored in encoding DNA sequences to the sites of protein synthesis. Ribosomes can be found throughout the cell, either floating around freely in the cytoplasm or being bound to the rough endoplasmic reticulum.

Lysosomes are single-membraned organelles containing digestive enzymes. Their use is to digest worn-out organelles as well as foreign material such as bacteria. They also feature heavily in the process of programmed cell death, the so-called apoptosis, where the digestive enzymes are released for self-digestion of the cell.

The primary function of the **Golgi apparatus** is to package macromolecules into small vesicles for transportation and secretion purposes. It consists of several membrane-like layers. Furthermore, lysosomes are built in the Golgi apparatus.

Finally, the **nucleus**, which may be considered the most essential cellular organelle, is enclosed by a double-layered membrane and contains most of the genetic material of a cell, the deoxyribonucleid acid (DNA), which is assembled in multiple, long threads called chromatin. Furthermore, the nucleus contains one or more nucleoli. A nucleolus is a spherical, subnuclear body which governs the production and assembly of ribosomal RNA. Moreover, the nucleus plays an essential role in the process of cell reproduction (the so-called mitosis, see chapter 4.3), when a cell divides and forms two new ones. Only during cell division, the chromatin contracts and becomes visible in rod-like, well defined structures, the so-called chromosomes. Their number in a human cell amounts to a total of 46 single chromosomes or 22 homologous pairs plus the gender-defining chromosomes x and y. As has already been mentioned, mRNA, which is necessary for protein synthesis in the ribosomes, is assembled in the nucleus with the DNA as template.

Since the DNA molecule is generally regarded as the most important target for radiation, its structure shall be explored in more detail in the following section.

4.2. The DNA Molecule – Coiling the Helix

Basically, a DNA molecule is formed by two strands of nucleotides, each consisting of a phosphate group, a deoxyribose (a pentose, i.e. a sugar containing five carbon atoms) and one of four possible organic, nitrogenous bases. The two strands are assembled in a ladder-like structure, with the ladder sides being formed by an alternation of phosphate and deoxyribose, and its rungs consisting of pairs of organic bases which are cross-linked via Hydrogen bridge bonds. The four bases are adenine, guanine, cytosine and thymine. Due to their specific chemical structure, only adenine and thymine (two hydrogen bridges) as well as guanine and cytosine (three hydrogen bridges) can be linked. The genetic information is encoded in the sequence of organic basis along the DNA molecule. Three consecutive bases represent an informational unit, a so-called codon or base triplet, which translates into one amino acid. Thus, a long sequence of codons is necessary in order to fully describe a protein consisting of several hundred amino acids. Obviously, there exist 64 ($= 4^3$) different base combinations for a codon. However, since only a total number of twenty types of amino acids are utilized in protein synthesis, several amino acids are represented by a few different codons.

A directional reference can be attributed to each DNA single-strand that is determined by its chemical configuration, which is directly related to the “read-out” direction of the genetic information encoded in the base sequence. Thus, one end of a DNA strand is termed the 3’, the other the 5’ end, as is given by the orientation of deoxyribose molecule (and its third and fifth carbon atom) in the strand’s backbone. All read-out operations as necessary for DNA or protein synthesis are performed heading along the DNA template in its 3’-to-5’ direction, thus generating a 5’ to 3’ copy. In the DNA double strand, the two opposing strands are arranged in anti-parallel direction.

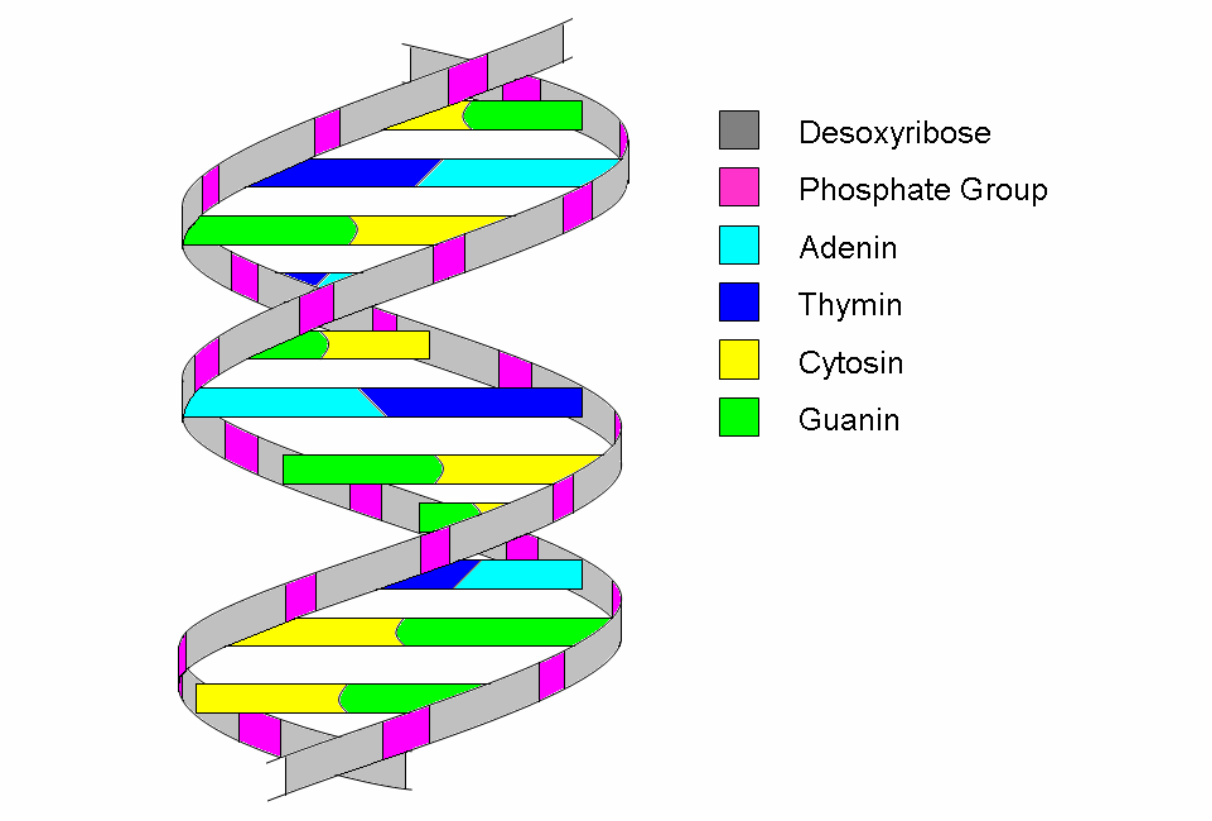

Figure 4.2. The DNA double helix.

The double-stranded DNA is coiled to form a so-called double helix (see figure 4.2). The coiled DNA molecule is again wrapped around spherical proteins, the histones. Thereby, 147 base pairs of DNA are wound around a core consisting of 8 histones (two copies of each histone type H2A, H2B, H3 and H4) to form a so-called nucleosome (95)). Nucleosome linkage is achieved by histone H1 in mitosis, which leads to a further condensation of the DNA molecule. In human cells, several isoforms of the histone proteins can be found, with the most prominent being the H2AX subtype of H2A (see chapter 5.9). The nucleosome chain is further twisted to form an even more compact, supercoiled 3D-structure which supports the integrity of the DNA molecule.

4.3. The Cell Cycle

The cellular course of events from one cell division to the next is termed the cell cycle. The process of cell division is necessary for growth of an organism, replacement of older cells and adaptation to specific circumstances, hazards and environmental surroundings. Not all cells are constantly going through all phases of the cell cycle and are steadily proceeding from one division to the next, but instead "rest" in order to exclusively perform their specific functional tasks or halt their progression through the cell cycle for a sustained period of DNA damage repair (see section 5.7).

From the viewpoint of radiation protection, cell cycle progression is important due to a varying radiation sensitivity of the cells in different phases of the cell cycle (11, 12), which is partly due to varying mechanisms of DNA damage repair in different cell cycle phases and will be discussed later (see section 5.6). Moreover, in an adult human-being, certain cell types such as the cells from the nervous system hardly ever undergo division. Thus, nervous cells damaged or killed by ionizing radiation cannot be replaced easily which needs to be taken into account when referring to doses delivered to specific organs.

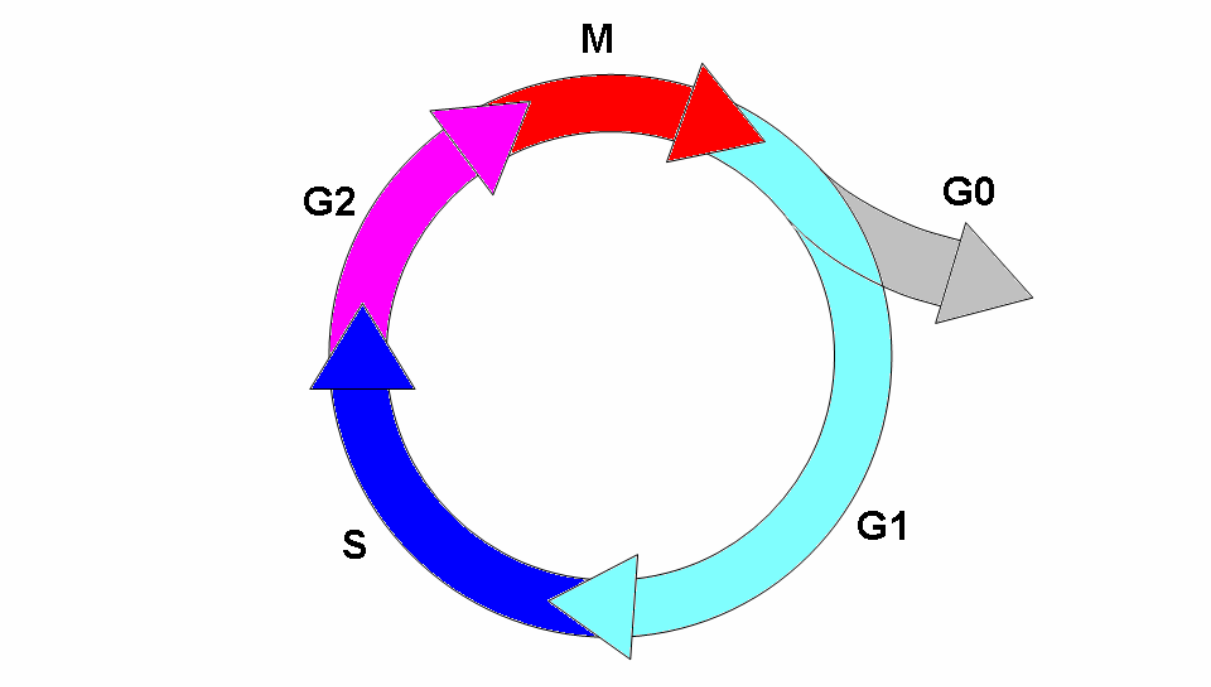

Figure 4.3. The eukaryotic cell cycle.

The different phases of the cell cycle are illustrated in figure 4.3. In the M ("mitosis") phase, the cell divides into two daughter cells. The time between two M phases, the G1, S and G2 phases combined, is termed **interphase**. During the **G1** ("gap 1") phase, metabolic activity is high in order to prepare the cell for DNA-replication, which takes place in the **S** (DNA-"synthesis") phase. The duplication of the DNA is needed in order to provide an exact and complete copy of the genetic information of the parent cell for both daughter cells. In the **G2** ("gap 2") phase, cellular growth continues for preparation of mitosis.

Mitosis is a rather complex process and is therefore subdivided into four phases, including prophase, metaphase, anaphase and telophase. In **prophase**, the duplicated chromosomes condense, so that they can eventually be distributed equally to both compartments that will be transformed into two autonomous cells. After condensation, each (duplicated) chromosome consists of two identical DNA strands termed chromatids, which are connected by the so-called centromere and can be seen as X-shaped objects with light microscopy. The nuclear membrane starts to dissolve. The centrioles detach from one another and migrate towards opposite ends of the cell and start formation of spindle fibres. In **metaphase**, the nuclear membrane has completely disappeared. The condensed chromosomes move to the "equatorial" plane of the cell (when thinking of the centrioles

as located at the cellular "poles"). Spindle fibres from each centriole attach to every centromere. In **anaphase**, the centromeres separate. Matching chromatids are pulled to opposite poles of the cell and now represent new, complete chromosomes. In **telophase**, the distribution of chromosomes has been finalized and the condensed DNA uncoils again to form chromatin. Nuclear membranes are assembled for both sets of DNA. Cell division is completed by separation of the cytoplasm and formation of new cell membranes, enveloping each daughter cell.

The progression through the cell cycle is mediated by numerous regulatory proteins such as the cyclin dependent kinases (cdks) and the cyclin proteins (13), which are also involved in the damage induced activation of cell cycle checkpoints (see section 5.7). Furthermore, in G1 phase, cells may cease further cell cycle progression by enter a state of quiescence, the so-called G0 phase. Thus, cell division may either be deliberately postponed for a limited period of time due to scarce supply of nutrients or limited need for new cells, or be cancelled completely, which is common for certain cell types such as mature nervous cells. Furthermore, cells that have accumulated extensive DNA-damage due to age or hazardous environmental conditions may also halt cell cycle progression permanently in order to minimize the risk of oncogenic transformation due to genetic defects passed on to their daughter cells. Therefore, the duration between two cell divisions varies greatly, depending on cell type, from minutes to years.

4.4. Radiation Induced Cellular Effects

The following section describes basic radiobiology, roughly following S. Forshier (14) and J. Kiefer (15), supplemented with additional information were necessary.

4.4.1. Basic Radiation Chemistry

As a basic principle, the interaction of ionizing radiation with matter leads to excitation or ionisation of the target molecules and atoms. These events may be homogenously distributed over the whole target volume, or highly localized, as is the case for high energy charged particle radiation. In the interaction processes, chemical bonds may be broken due to transferred energy, and radicals may be formed, which are chemically unstable and highly reactive because of unpaired electrons in the outer shell. Their reactive nature eventually leads to chemical reactions which involve other molecules that have not directly interacted with radiation, and are thus termed indirect effects.

For cellular exposure to radiation, the specific chemical composition and the structure of a cell need to be considered. Firstly, essential macromolecules (e.g. DNA and RNA molecules, functional proteins) may be altered due to direct, radiation induced ionization events, which may either have a negligible effect, impair their functionality or even render them useless and beyond repair. However, since protoplasm consists of water for

the most part, the greatest fraction of radiation energy is absorbed by the H_2O molecule. This leads to various specific ionization events and the separation of water into different molecular products, which is termed the radiolysis of water. Since the products of this process are starting points for many indirect radiation effects, they shall be explored in more detail.

Absorption of radiation energy by the water molecule either leads to ionization or excitation, which may cause splitting of the H_2O molecule into an Hydrogen atom and a hydroxyl radical $OH^{\bullet}$:

$$H_2O + E_{rad} \rightarrow H_2O^+ + e^- \quad \text{ionization} \tag{4.1}$$

$$H_2O + E_{rad} \rightarrow H^{\bullet} + OH^{\bullet} \quad \text{splitting} \tag{4.2}$$

All four primary reaction products are radicals due to unpaired electrons in their hull as indicated. In both cases (equations (4.1) and (4.2)), the two reaction products may either recombine, or react with other targets, leading to the production of secondary products of the initial radiolysis. Again, a likely reaction partner of the primary products is the water molecule, which gives the following reactions:

$$H_2O^+ + H_2O \rightarrow H_3O^+ + OH^{\bullet} \tag{4.3}$$

$$2e^- + H_2O \rightarrow H_2 + 2OH^- \tag{4.4}$$

Other likely partners in secondary reactions include the hydronium-ion (H3O+),

$$e^- + H_3O^+ \rightarrow H^{\bullet} + H_2O\ , \tag{4.5}$$

and molecular oxygen:

$$e^- + O_2 \rightarrow O_2^- \tag{4.6}$$

$$H^{\bullet} + O_2 \rightarrow HO_2^{\bullet} \leftrightarrow O_2^- + H^+ \tag{4.7}$$

Depending on the local concentration of the primary radicals generated by the radiolysis of water (and thus, on the locally deposited radiation energy) as well as on the local presence of molecular oxygen, the probability for the production of the more stable, cytotoxic hydrogen peroxide molecule, H_2O_2, increases. Hydrogen peroxide may be formed via several different reactions, including most of the so far mentioned primary and secondary reaction products:

$$OH^{\bullet} + OH^{\bullet} \rightarrow H_2O_2 \quad (4.8)$$

$$HO_2^{\bullet} + HO_2^{\bullet} \rightarrow H_2O_2 + O_2 \quad (4.9)$$

$$O_2^{-} + O_2^{-} + 2H^{+} \rightarrow H_2O_2 + O_2 \quad (4.10)$$

Overall, a great part of the indirect effects of radiation are due to the formation of hydrogen peroxide, which may travel longer intracellular distances, reaching crucial macromolecules such as DNA. The DNA-damaging potential of H_2O_2 is well established (e.g. 16, 17) and is mainly reflected in the occurrence of DNA single strand breaks and base damage, which may eventually lead to cell death or carcinogenesis. However, since both direct and indirect radiation effects cause similar damage, they cannot be distinguished directly.

4.4.2. DNA Damage

The DNA molecule is generally considered the most important target for radiation due to several reasons. Firstly, it is extremely large and is therefore a likely target for direct ionization as well as chemical alteration by radicals generated through secondary reactions. Furthermore, a DNA molecule contains the genetic code used for generating numerous proteins, which means that even the smallest changes may, theoretically, lead to serious repercussions on cellular functionality. And finally, radiation induced mutations are passed on to daughter cells, which may eventually cause oncogenic transformation several cell divisions later, thus generating a serious threat to the health of the whole organism.

There are various types of DNA damage, which differ greatly as to their consequences. DNA damage can be limited to a single base that may be chemically altered, lost, substituted incorrectly, or the hydrogen bonds between two corresponding bases may be disrupted. Lesions of this type are very common and likely to appear due to radicals generated endogenously or by radiation, or due to errors in DNA replication. Eukaryotes have therefore developed efficient cellular mechanisms, the so-called base excision repair (BER), nucleotide excision repair (NER) and mismatch repair (MMR), that allow for detection and correct replacement of altered bases (18). Nevertheless, if left uncorrected or repaired wrongly, these lesions may transform into a permanent change in the genetic code at the corresponding site, which is termed a point mutation and may be transferred to daughter cells.

Furthermore, breaks in one or both of the two sugar backbones of the DNA double helix may occur, which are termed DNA single or double strand breaks, respectively. The generation of single and double strand breaks cannot be treated independently, since the occurrence of a single strand break in the vicinity of an already present and not yet repaired break in the opposing strands automatically leads to a double strand break. Correct repair of a single strand break can be achieved comparably easily, as long as the

opposing is still intact, thus providing the correct base template for reconstruction of the damaged strand. The consequences of DNA double strand breaks and the involved repair mechanisms are of special interest for this thesis and will therefore be discussed in greater detail in chapter 5.

4.5. Basic Principles in Radiobiology – an Overview

This chapter is intended to point out a few fundamental concepts that govern the course of radiobiological events after exposure to radiation. Some already discussed biological effects shall be briefly summarized and connected to further thoughts and to an outlook on the following chapters that will analyze some specific biochemical pathways in the cellular response to radiation. Thereby, a clear and simplified picture of the complex radiobiological concepts involved shall be drawn to provide a guideline for the reader through the upcoming, more detailed discussion of intracellular mechanisms as well as to allow for a measured approach to the evaluation of experimental results presented in later chapters.

As has already been explained, radiation-induced damage is due to direct ionization and excitation as well as secondary chemical reactions due to radicals, thus altering molecules in the protoplasm. Cellular damage caused by direct or indirect effects is similar and cannot be distinguished in a simple and straight-forward way, but only through conclusions drawn from comparison of different biological systems that may be supplemented by special chemicals or genetically manipulated, or from different exposure situations.

Furthermore, radiation induced effects must always be regarded as superimposed by more or less similar events that occur endogenously in the normal cellular metabolism or due to stress. They may also be caused by cytotoxic, mutagenic chemicals or an inhospitable physical environmental situation such as high and low temperature, pressure, or microgravity as encountered in space. It is therefore imperative not to consider radiation-induced biologic events as isolated but to also regard the likely interaction with other factors, which may very well lead to attenuation or amplification of particular effects.

As a consequence, it is of great importance to select suitable control groups or reference samples in order to elucidate a specific epidemiologic or therapeutic effect as well as a particular cellular mechanism of interest as induced by exposure to radiation. Thus, for exposure of cultivated cells, control samples are usually kept under conditions as similar as possible in comparison to exposed cells, except for the radiation field.

Generally, unintended changes to protoplasm molecules occur frequently due to the various causes given above. However, by far the greatest fraction of these “damaging” events does not pose a sustained threat to the cell. The reasons for this fact are manifold: Firstly, a large number of changes in specific molecules such as proteins may have little or

even negligible impact on its functionality in the cellular metabolism. Furthermore, in case of loss of functionality, most components of the protoplasm are highly redundant or may be replaced fast and easily. There are a few exceptions, however, with the most prominent being the DNA, which is, basically, only available in two copies per cell. Nevertheless, a vast number of lesions in DNA can be efficiently and correctly repaired via various optimized repair mechanisms that even include cell cycle regulation for optimal effectiveness. Failure of perfect or – at least – sufficiently correct repair occurs rarely and is most often limited to specific types of DNA damage, which may be a result of highly hazardous circumstances. Even in extreme cases, where the overall cellular damage is overwhelming and cannot be dealt with by applying the repair mechanisms at the cell's disposal, the cell can react by induction of its own demise and undergoing apoptosis, thereby limiting the damage to the organism and avoiding further spread of detrimental genetic information to daughter cells. Overall, a cell is very capable of dealing with a multitude of threats due to radicals or direct energy deposition by radiation. Only on very few occasions, all cellular "safety" procedures for preserving the correct genomic information fail, thus giving rise to permanent base mutations or extensive chromosomal damage, which play crucial roles in the process of oncogenic transformation. Correspondingly, long term radiation-induced health risks emerge from these specific failure cases, which are therefore of special importance for radiation protection.

On the protein level, cellular processes such as cell cycle regulation or DNA damage repair are mediated by the overall or local concentration of one or more activated and mechanism-specific proteins. In principle, in order to regulate the local activity of a particular protein, a cell applies several different kinds of measures: Firstly, the total amount of a certain protein may be changed, which is achieved either by synthesis or degradation of the protein of interest, resulting in an overall concentration increase or decrease. Additionally, a manifold of proteins is usually present in an inactive form, and are only activated when the need arises, which is done through situation-specific chemical modification. Finally, various proteins may be recruited or relocated to different parts of the cell, thereby mediating their function. Obviously, a combination of the mentioned mechanisms may be applied as well. As for DNA damage induced by ionizing radiation, for a variety of processes, the concentration of a particular, activated protein increases with the amount of the damage (up to a certain extent), e.g. leading to a continuous increase in repair activity. However, other mechanisms such as the induction of a cell cycle halt or apoptosis can only be regulated in an all-or-nothing manner, and are thus irreversibly initialized after surpassing a threshold-like activity level of specific proteins.

Furthermore, it is absolutely vital to keep in mind that the cellular response to ionizing radiation depends on a multitude of parameters, which may set severe limitations on drawing generally valid conclusions from the observation of a single or a few radiobiological endpoints that are meant to be of relevance for radiation protection or risk assessment. At the very least – assuming a "standardized" chemical and physical environment –, biologic results will depend on dose, LET, cell type and cell density (which implies a specific distribution of the cells with regard to cell cycle phases). In

many cases, variations due to dose rate, exposure time and geometry, as well as due to specific exposure conditions may be expected. Lastly, each and every radiation induced biological effect is to be interpreted as a function of time: The occurrence of direct damage is quickly followed by indirect primary effects, leading to a cascade of intracellular events, starting seconds after irradiation and persisting for several days or even weeks. Specific damage such as genomic mutation can have no significant short term effect at all, but may contribute to oncogenic transformation of a cell decades after the initial radiation exposure.

And finally, methodology may also have an impact on results and especially on quantification of specific cellular parameters, which is largely due to highly varying sensitivities of different methods applied. Thus, comparison of results obtained with different experimental procedures must be performed very carefully in order to avoid misinterpretation.

5. The Cellular Response to DNA Double-Strand Breaks

Radiobiologic effects are manifold and include a great variety of different biologic endpoints and radiation-induced events. As an inevitable consequence, every radiobiologic study must be focused on a limited selection of biologic parameters, events or functional factors of interest. Within the frame of this thesis, radiation-induced DNA double-strand breaks and the corresponding cellular response, covering repair activity and cell cycle regulation, have been investigated. Therefore, in the following sections, the current knowledge of several aspects of double-strand breaks, connected cellular mechanisms and some of their key players will be presented, as are of importance for the scope of this thesis.

5.1. DNA Double-Strand Breaks – Occurrence and Consequences

Generally, DNA double-strand breaks (DSBs) are considered to be one of the most dangerous types of DNA damage, and are encountered when breaks in the sugar backbones of complementary DNA strands occur in close proximity, so that the cohering forces due to base-pairing and the three-dimensional chromatin structure are not sufficient to maintain the overall structural integrity of the DNA double helix (33). This results in the liberation of free DNA ends, which may separate and drift away from one another, thus making repair extremely difficult. They are induced by ionizing radiation (IR), chemicals, or arise endogenously due to oxidative damage or during DNA replication, and are even created deliberately in a process called V(D)J recombination when generating B- and T-lymphocytes (34). The repair of DSBs is essential for maintaining viability and full functionality of a cell – unrepaired DSBs likely lead to indefinite cell cycle arrest, apoptosis or mitotic cell death resulting from the loss of genomic material (35). Errors in the reconstruction of the DNA molecule, which are promoted by the fact that the generated free DNA ends often also suffer from additional base damage, may result in unintended changes in the genomic information, thus increasing the probability of the initiation of oncogenesis (36). Furthermore, the formation of various types of chromosomal aberrations is directly connected to failure of correct DSB repair (19, 20). Chromosome aberrations include translocation (inversion of a chromosomal section or transfer to another location in the chromatin), terminal or intra-chromosomal deletion (irreversible loss of a terminal or inner part of a chromosome),

dicentric chromosomes and acentric fragments (chromosomes with two or no centromeres instead of one) as well as ring-shaped chromosomes. Since chromosome aberrations are commonly associated with cancer induction (50) and hereditary diseases, efficient repair of DSBs is essential for the health of the organism.

Because of the great need to restore and maintain genomic integrity even despite the presence of DNA DSBs, higher eukaryotes have developed complex mechanisms suited for this task. Since the distribution and 3D-structure of the DNA varies significantly with cell cycle progression, the repair mechanisms are adapted to specific configurations and their induction is highly dependent on the particular cell cycle phase. In mammals, the repair of DSBs generally includes two separable primary DSB repair pathways, the so-called non-homologous end-joining and homologous recombination, which will be explained in sections 5.4 and 5.5.

Several proteins feature in cellular mechanisms activated by radiation induced DNA DSBs. ATM and DNA-PK may probably be considered the most prominent players in this response and are involved in the regulation of various, cooperating and intertwined processes. Since many of the experimental results that will be presented in later chapters refer to the activity of these two proteins, they shall be introduced in more detail.

5.2. Ataxia-Telangiectasia Mutated – ATM

Ataxia-telangiectasia (A-T) is a rare human disease with an estimated incidence rate of 1 in 40000 to 1 in 300000 births. A-T is a genetic instability syndrome characterized by progressive cerebellar degeneration, immunodeficiency, high sensitivity to ionizing radiation and cancer predisposition, which lead to a patient's death at an age of 20 to 30 years.

A-T is caused by a mutation in the ATM (ataxia-telangiectasia mutated) gene, as has been discovered by Savitsky et al in 1995 (21), where ATM is either lost or inactivated. In the following years, extensive research lead to the finding that the ATM protein is one of the key players in the regulation of the cellular response to ionizing radiation and other genotoxic hazards. ATM regulates the induction of various cellular events that lead to DNA damage repair, plays a major role in the activation of cell cycle checkpoints that result in an arrest in the G1/S, S or G2/M phase, and is involved in the mediation of apoptotic pathways. Its multitude of functions, which are crucial for maintaining genomic integrity of single cells or "cleansing" an organism from cells beyond repair, has been the subject of many recent reviews (22, 23, 24, 25, 26), and shall be elucidated in the following chapters (see 5.5, 5.7 to 5.9), to provide a theoretical basis for the extensive analysis of ATM activity presented in part III of this thesis.

Protein kinases are enzymes which transfer a phosphate group ($H_2PO_4^-$) from adenosine triphosphate (ATP) to the free hydroxyl group of an aminoacid residue of a substrate

protein. The covalently linked phosphate group significantly changes the charge distribution in the protein usually affecting its function. As a member of the family of the phosphatidylinositol 3-kinaselike serine/threonine protein kinases (PIKKs), ATM adds phosphate groups to serine and threonine amino acids of other proteins. Other members of this kinase family include DNA dependent protein kinase catalytic subunit (DNA-PKcs, see chapter 5.3), ATM- and Rad3-related (ATR), mammalian target of rapamycin (mTOR) and ATX/hSMG-1. For a multitude of proteins, the process of phosphorylation and dephosphorylation of specific amino acids is used to transform the protein from an inactive to its activated form, or, to put it in simple terms, to "switch" the protein on or off.

In more detail, ATM is a polypeptide consisting of 3056 amino acids. Like the other PIKKs, ATM contains the PI3K domain which includes the catalytic site (i.e. the site responsible for its kinase activity) of the PIKK family members. The PI3K domain is highly conserved in organisms as diverse as mammals and yeast, and the human ATM protein shows significant similarities with proteins of other species involved in DNA damage repair and cell cycle control (27). ATM phosphorylates its target proteins on so-called SQ and TQ sites, i.e. a serine or threonine amino acid followed by glutamine.

5.3. DNA-dependent Protein Kinase – DNA-PK

The DNA-PK protein complex plays a central role in one of the mechanisms applied by higher eukaryotes for repair of DNA damage. It consists of an exceptionally large (approx. 470 kDa) catalytic subunit DNA-PKcs and the Ku component (28), which is a heterodimer of two proteins with an approximate size of 70 and 80 kDa, which are therefore called Ku70 and Ku80 (29). Like ATM, DNA-PKcs contains the PI3K catalytic domain, and is therefore another member of the PIKK family. This implies the characteristic properties of PIKKs, the ability of DNA-PKcs to phosphorylate its substrate proteins on SQ and TQ sites.

The different subunits of the DNA-PK complex can be attributed to different functions, which have been the subject of many recent reviews (30, 31, 32). As with ATM, genetic defects in the functional domains of DNA-PKcs or the Ku-proteins result in a phenotype suffering from immunodeficiency, extreme radiosensitivity and premature aging, suggesting a role in a DNA-repair pathway. It is now known that the highly conserved Ku proteins are exceptionally prone to binding free DNA ends as are encountered at DNA double strand breaks, whereas the catalytic subunit governs the activation of several substrate proteins, which are involved in the ligation of the broken DNA strands. Furthermore – to a much lesser extent than ATM – DNA-PKcs participates in regulation of cell cycle progression and apoptotic pathways and, for some specific target proteins, even plays a somewhat "redundant" or supporting role of ATM. Thus, both ATM and the DNA-PK complex are key players in the immediate and prolonged cellular response to DSBs, which shall be elucidated in the following chapters.

5.4. Non-Homologous End Joining (NHEJ)

The NHEJ mechanism rejoins the free DNA ends without using the information in the intact homologous sequence of the corresponding sister chromatid. Since the DNA ends often suffer from additional damage or need to be refined before rejoining, which may require the deletion of nucleotides, NHEJ is prone to introducing errors at the DNA junctions, thus altering the corresponding base sequence and changing the DNA code (41). However, this is largely dependent on the precise structure of the DNA termini at the DSB: "Blunt" ended DSBs (i.e. with a hydroxyl (OH)-group on the 3' and a phosphate on the 5' end that can be directly reconnected) or with complementary overhangs are easily repaired, whereas for more complex breaks a much lower probability for accurate repair is observed (47).

Several proteins are known to be required for non-homologous end joining. Among them, there are the Ku70/Ku80 heterodimer and DNA-PKcs, which form the DNA-PK complex, and the XRCC4/Ligase IV as another heterodimer (49). Some others such as WRN and Artemis are supposed to be involved in processing of DNA ends (31), whereas BRCA1 seems a likely candidate for limiting the loss of genetic information due to excessive end processing before rejoining (40).

However, as a simplified approach only the essential players, DNA-PK and XRCC4/LigIV, shall be considered in the following modelling of NHEJ. For illustrative purposes, figure 5.1 shows a basic depiction of the NHEJ mechanism, indicating the function of the involved key proteins, as is based on current scientific opinion. As a first step, the Ku70 and Ku80 proteins bind to both terminal regions of the broken DNA double strand, thereby preventing the DNA ends from further degradation. This is followed by recruitment of the DNA-PK catalytic subunit to the DSB site, thereby assembling the DNA-PK complex. In this process, the kinase activity of DNA-PKcs is stimulated, which allows for regulation and initiation of a variety of downstream events. After processing of DNA ends as is mediated by DNA-PK activity, the XRCC4/LigIV complex joins the other DSB-bound proteins and reconnects the two parts of the DNA molecule. Finally, after completion of the repair task, all NHEJ proteins depart from the formerly damaged site, leaving behind a fully operational DNA double strand.

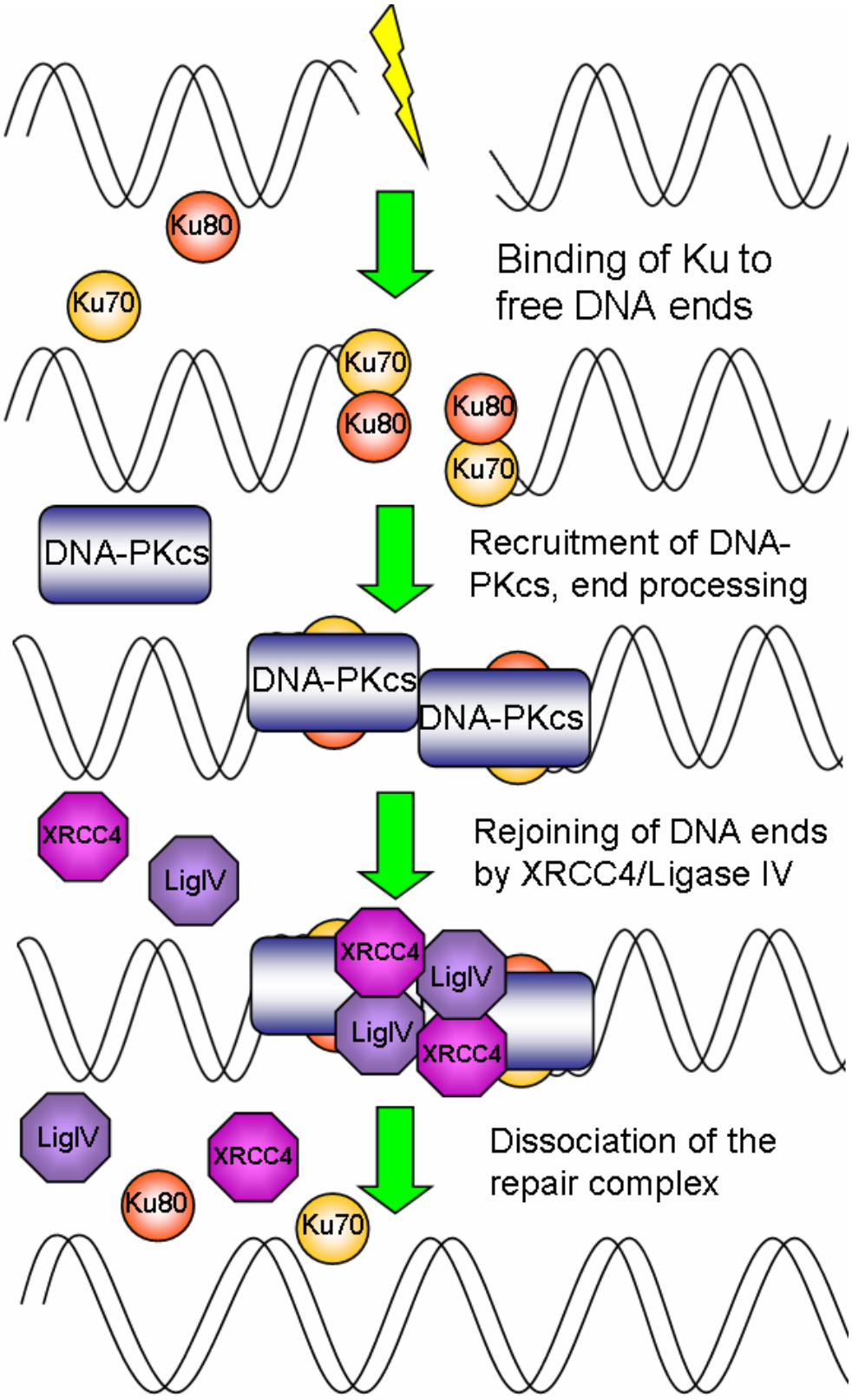

Figure 5.1. Non-homologous DNA end joining in eukaryotes. This schematic is roughly based on depictions of NHEJ as presented in (39), (60) and (31).

Still, the overall understanding of NHEJ is far from complete, although there are several hints as to the exact function of key players in this mechanism. For example, even if it is

yet not unambiguously proven, there is indication that the Ku-proteins are the actual primary "detectors" of a DSB in the NHEJ-pathway, which is suggested by their high activity of binding free DNA ends (39). Furthermore, it seems plausible that it is the DNA-bound Ku70/80 heterodimer that recruits DNA-PKcs to sites of DSBs, thereby stimulating its kinase activity (38, 51), although the corresponding mechanism is not yet fully understood. Moreover, it is well established that activated DNA-PK bound to DNA ends phosphorylates a number of substrate proteins that feature in NHEJ, such as XRCC4 (56) and Artemis (57), advertising a diverse regulatory function of DNA-PK. This may include directing the processing of DNA ends as well as further recruitment and activation of other factors involved in NHEJ, as well as mediating the actual reconnecting of the DNA ends. Completion of this rejoining process is achieved by XRCC4 and Ligase IV (31, 39), which form a functional complex for performing this task.

Furthermore, the kinase activity of the DNA-PK complex leads to phosphorylation of its subcomponents, DNA-PKcs and the Ku-proteins (53). It has been demonstrated that the autophosphorylation process of DNA-PKcs (i.e. due to its own kinase activity, a phosphate group is added to DNA-PKcs) at threonine 2609, can already be detected within minutes after the formation of DSBs (38) as induced by radiation exposure. DNA-PKcs phosphorylated at threonine 2609 can be found predominantly located at sites of DSBs, forming discrete foci very rapidly after exposure (31, own results, see sections 13.1.4 and 13.2.4). Additionally, it has been confirmed that DNA-PKcs autophosphorylation is dependent on the Ku-proteins in vivo, and that cells with DNA-PKcs mutated at threonine 2609 exhibit a higher sensitivity to ionizing radiation and are less proficient in rejoining DSBs (38, 51). Other phosphorylation sites of DNA-PKcs (threonine 2638 and threonine 2647) are known to be of importance in the cellular response to ionizing radiation as well, as is indicated by increased radiation sensitivity in case of mutation (52). Autophosphorylation of DNA-PKcs at threonine 2609 is believed to have negative regulatory function in NHEJ because it leads to the dissociation of the DNA complex in vitro (58), thus suggesting a flexible mechanism for regulation of DNA-PK kinase activity and relocation in order to make room for other factors, as may be necessary for the various steps in the course of NHEJ. This, however, is not unequivocally accepted (31), since it can be demonstrated that DNA-PKcs phosphorylated at threonine 2609 is retained at sites of DSBs for an extended period of several hours (38 and own results, see section 13.2.4), somewhat arguing against the phosphorylation-induced disruption of the DNA-bound DNA-PK complex in vivo.

Finally, there is also convincing evidence that further, yet unknown factors are needed in the NHEJ mechanism (55). Additionally, it needs to be regarded that the activity of the key players in NHEJ is not necessarily limited to the repair process itself, but may influence other cellular mechanisms as well. With this in mind, it is hardly surprising that DNA-PK has been demonstrated to be also involved in the induction of the P53-mediated apoptotic response (54) and other cellular processes (see also section 5.8).

The NHEJ mechanism can be initialized throughout the cell cycle, but is also supported by homologous recombination, which even performs the majority of all DSB repair tasks in

specific cell cycle phases. This situation is dealt with in more detail in section 5.6 after the following in-depth description of the homologous recombination mechanism.

5.5. Homologous Recombination (HR)

The exchange of DNA sequences between homologous DNA molecules is termed homologous recombination (HR). This mechanism plays an essential role in different cellular processes such as during DNA replication (59) and the repair of DNA DSBs. Since this thesis is mainly concerned with radiation induced cellular consequences, the following discussion of HR will focus on its role in the cellular response to DSBs, as DSB induction is to be considered the most imminent threat to cellular health.

The main difference between DSB repair via NHEJ and HR is the fact that for HR, the presence of the homologous DNA strand containing the corresponding undamaged DNA sequence is needed in the vicinity of the broken DNA double strand, whereas for NHEJ it is not. In HR, the correct homologous base sequence is used as a template for replacing the damaged part of DNA with a copy of the homologous DNA molecule. As a consequence, assuming an error-free template, DNA repair via HR is much less likely to introduce errors into the genetic code in comparison to NHEJ, which cannot correctly reconstruct lost genetic information at the free DNA ends for intrinsic reasons.

However, due to the necessity of the local presence of a suitable DNA template, HR is essentially limited to phases in the cell cycle, where a corresponding “information donor” is easily accessible. This is mainly the case after DNA replication and during mitosis (37), where duplicated DNA sequences are available in sister chromatids that are still attached to each other at the centromeres (see section 4.3). The contribution of both HR and NHEJ in different phases of the cell cycle will be covered more extensively in section 5.6.

The biochemical course of events in the eukaryotic HR process is highly complex and not yet fully understood in every detail. Most of the present knowledge about HR in mammalian cells has been gathered by comparison with HR in bacteria and yeast and by searching for analogies, which is an efficient approach due to the highly conserved nature of the HR pathway throughout different organisms (62, 73). In a simplistic description of events (following 61, 48, 74 and 22, see figure 5.2), DSB repair via HR may be divided into three stages: Firstly, the DNA ends need to be processed for preparation of a connection to the template DNA molecule (pre-synapsis phase). Thereafter, a joint molecule between the damaged and the homologous template strand is formed via establishment of so-called Holliday junctions, allowing for reconstruction of the lost base sequence (synapsis phase). Finally, the two DNA molecules are separated and completed individually (post-synapsis phase).

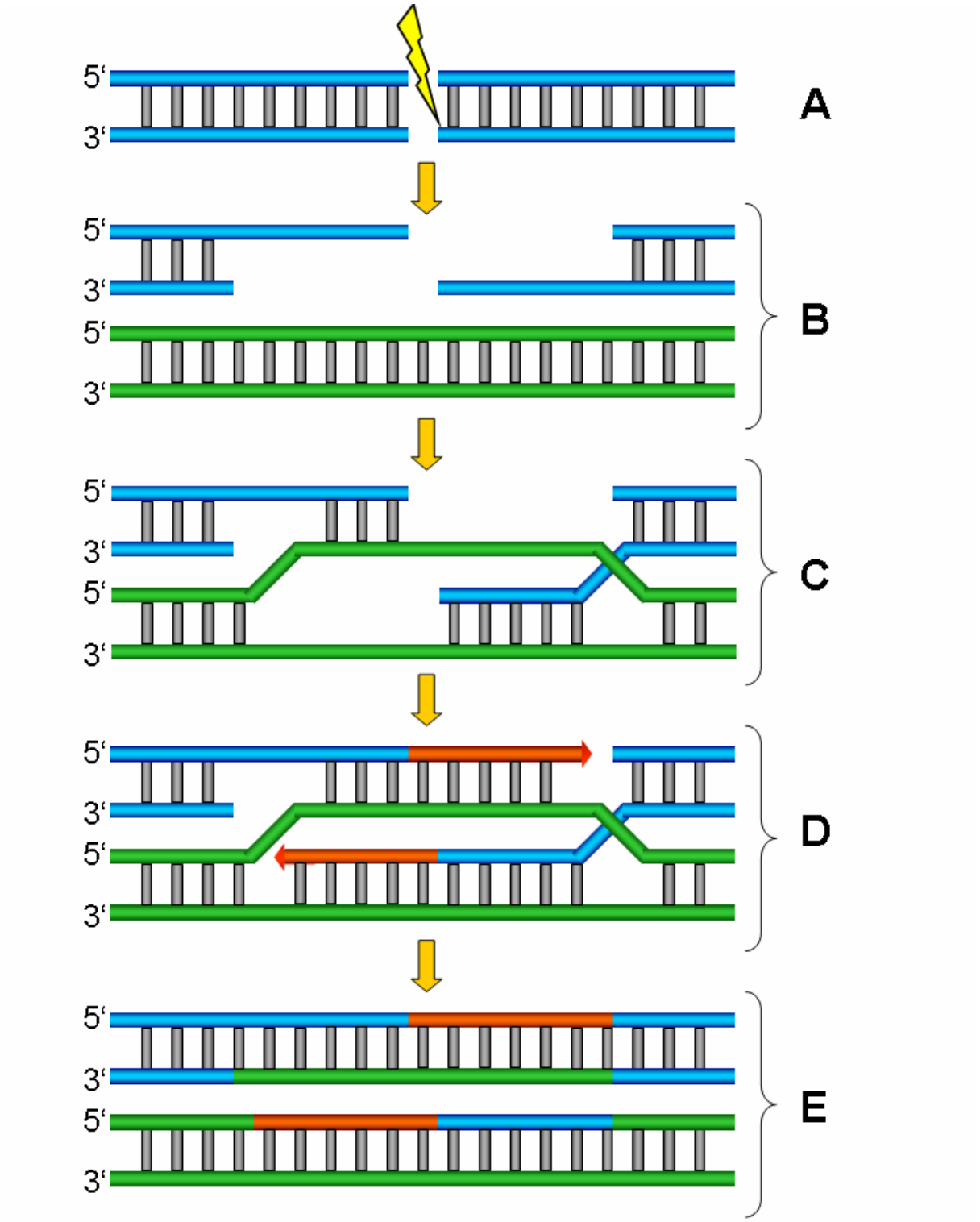

Figure 5.2. Phases in DSB repair via homologous recombination: After DSB incidence (blue, A), the free DNA ends are processed and the homologous sequence (green) is recruited (B). After single strand exchange (C), missing nucleotides are added via DNA synthesis (red, D). Finally, double strands are separated and completed (E).

A large number of factors are known to be involved in the HR mechanism of higher eukaryotic cells. In the following description of biochemical events necessary for or

directly linked to HR, a selection of the most essential players will be considered and discussed to provide a well-founded background for interpretation of the experimental results presented in later chapters. The HR mechanism has been the subject of many recent reviews and other publications, where a more detailed analysis of current knowledge about HR can be found (41, 43, 44, 61, 63, 74).

In analogy to NHEJ, as a first step, the DSB needs to be identified by the cellular repair machinery. Presumably, this is performed by the Rad52 protein, which has been shown to be highly prone to binding free DNA ends (64). It has been suggested that the DNA-binding of Rad52 – leading to DSB repair via HR – competes with the corresponding process involving Ku70/80, which initializes the NHEJ pathway (41, 60). Another early event in the HR mechanism is the binding of a protein complex consisting of Mre11, Rad51 and Nbs1, thus being termed MRN-complex (or occasionally, Mre11-complex), which may take place within minutes after the occurrence of a DSB and performs a variety of tasks (44). ATM is another factor that is recruited to DSBs very early in the signal transduction cascade, where it is retained for a prolonged period of up to several hours (65). It needs to be stressed that ATM activity is not limited to DSB repair by HR, but is linked to DSB incidence in general (26). Nevertheless, a few of the many functions of ATM shall be discussed in this section due to the diverse interaction of ATM with several players of HR such as the MRN complex, which, while featuring heavily in HR, is involved in NHEJ only to a minor degree (46), even though similar ATM-mediated responses to DNA damage may be observed for NHEJ as well.

Both the MRN proteins and ATM take part in a complex series of mutual chemical modification processes (26). The causality and the exact course of events is not yet fully understood, however, there is indication that the binding of Mre11 to free DNA ends is independent of ATM (66), and that ATM is not activated by DSBs in cells with mutated Mre11 that prohibits formation of the MRN complex (67), which leads to the conclusion that the initial binding of the MRN complex to free DNA ends is to be considered an upstream event to ATM recruitment and activation.

In the absence of DNA DSBs, ATM is present in its kinase-inactive dimeric (or higher order) form. At sites of DSBs, the inactive forms are split up into ATM monomers, which is accompanied by autophosphorylation of ATM at serine 1981 (68), thereby activating the kinase function of ATM. This process of ATM activation works at an amazingly fast pace, with more than 50% of cellular ATM being phosphorylated in a duration of several minutes to half an hour, as induced by the presence of only a few DSBs caused by irradiation doses of 0.5 Gy gamma (68). Phosphorylated ATM (pATM) stays predominantly located at sites of DSBs – with a smaller amount of activated ATM being free to move around in the nucleus – (68, own results), where it regulates a number of cellular pathways by ATM-induced phosphorylation of a manifold of substrate proteins (26).

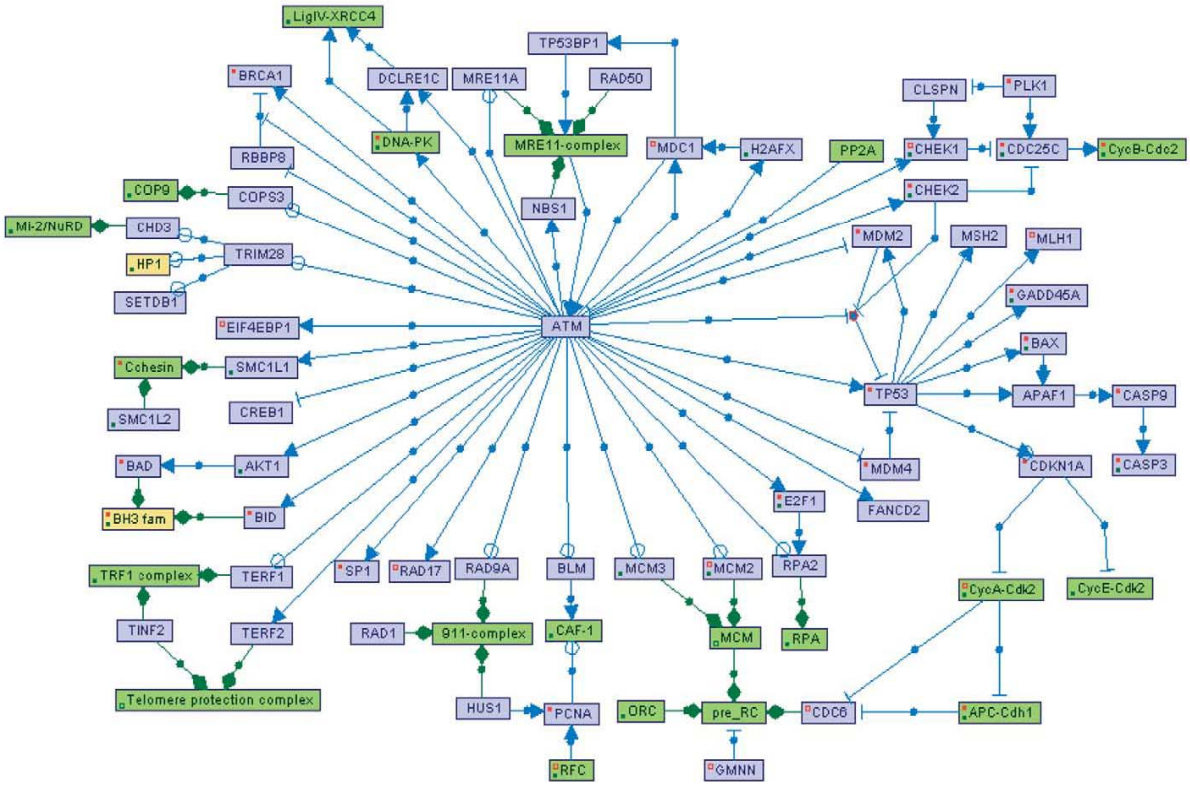

Figure 5.3. The current view of the ATM regulatory network as presented in a review by Y. Shiloh (63), commented as follows: "This map contains all information published on ATM as of 15 April 2006, and data presented at the recent International Workshop on Ataxia-Telangiectasia, ATM and the DNA-damage Response (Belgirate, Italy, 2005)." Blue lines with arrowheads indicate activation, T-ends stand for inhibitory regulation, open circles point at a lack of knowledge as to the effect of the signal transduction event. Green lines symbolize "containment" relations, e.g. Mre11, Rad50 and Nbs1 are contained in the MRN complex (here: MRE11-complex). Blue background represents single proteins, yellow marks protein families, and complexes are highlighted green.

In the framework of this thesis, further discussion of ATM-mediated cellular signal shall be simplified greatly, since the overall number of known interactions involving ATM is overwhelming (see figure 5.3). A few of these ATM-mediated events will be discussed later on in sections 5.5 and 5.7 to 5.9. As for DSB repair, pATM is known to phosphorylate Nbs1 at serine 343 (69), suggesting an interwoven functional relationship between ATM and the MRN complex. Other factors such as MDC1 and 53BP1, which are also known to participate in the cellular response to DNA DSBs, suffer from a dilemma similar to MRN as well: On the one hand, they are phosphorylated and activated in an ATM-dependent manner as well, whereas, on the other hand, they are also indispensable for ATM activation, thus placing them both up- and downstream of ATM (70, 63). This evidence strengthens the suggestion that the ATM-mediated response to DNA damage is to be viewed as a cyclic process that is possibly intended to amplify the initial damage signal (43, 63).

There is still considerable controversy as to how ATM can be activated so swiftly in response to DSBs and as to what exactly is the key feature of a DSB that is recognised so efficiently by the upstream proteins. Since DSBs lead to changes in the 3D structure of chromatin, it has thus been hypothesized that it is these structural changes that may be easily detected and that induce further biochemical events (68).

Whereas a rather large amount of knowledge has been gathered on the sensory events that initialize DSB repair via HR, less is known about the exact course of events that leads to formation and resolution of the synapsis between homologous strands as well as the reconstruction of the DNA strand in human cells. It is commonly accepted, that the single strand binding protein RPA plays a major role in this mechanism (71), supported by S. cerevisiae homologs Rad51, Rad52 and Rad54, as well as XRCC2 and XRCC3 (61, 37). For most of the mentioned factors, it has been demonstrated that mutations which render them inactive are either lethal or lead to increased radiosensitivity (72, 75). Furthermore, in analogy to the process of DNA replication, the DNA polymerase and its accessory proteins (a helicase, DNA ligase) govern the rebuilding of the "donated" single strand that has been translocated from the homologous template to the damaged DNA molecule. Additionally, the DNA polymerase adds missing nucleotides to the double strand that is subject to repair by copying the donated strand (61).

There are some proteins that appear to be involved in both mechanisms of DSB repair, NHEJ and HR. Apart from ATM as a transducer of the DSB signal in general, the most prominent among them may be the histone H2AX, which will be discussed in more detail in section 5.9, since a large part of the experimental results that will be presented later deal with the phosphorylated version of H2AX. Brca1 is another such factor that is assumed to perform a variety of tasks, including recruitment of other factors as well as transduction of cell cycle-regulating and apoptosis signals (40). Furthermore, proteins of the MRN complex, even though not required, can participate in certain steps of NHEJ such as DNA end processing and protection from degradation as well as transduction of the damage signal (39).

Finally, while various factors involved in DSB repair have been found localized at sites of DSBs, it is yet to be fully determined whether these repair mechanisms rely exclusively on recruitment of these factors to each DSB, or whether the HR machinery also gets concentrated to a few locations, with the free ends of broken DNA being relocated to these "repair centres". For HR, there is evidence for the latter option (101), nevertheless, the issue of DSB repair kinetics is still far from being completely solved.

Obviously, as has been elaborated in this section, the general role and importance of HR in DSB repair has been established very well so far, however, there are still many uncertainties as to the precise mechanism and specific steps that are being performed, especially in human cells. This is mostly due to the complex interaction processes between key players and the nature of the cellular response to DSBs, which appears to include not only straightforward, one-way signal cascades, but needs to be seen as complicated biochemical network.

5.6. Cell Cycle Dependence of DSB Repair Mechanisms

As has been discussed in the previous sections, two different mechanisms are at the disposal of eukaryotic cells for maintaining genomic integrity even despite the occurrence of DNA DSBs, namely HR and NHEJ. There are intrinsic differences between these two processes, which are essentially "competing" for each single DSB as to which mechanism is initialized at the corresponding site. Basically, DSB repair via NHEJ works under all circumstances, but is more error-prone, whereas HR, while being considered a high-fidelity process, requires the presence of a homologous DNA template and, therefore, cannot be applied in every case.

Quantitative data concerning the contribution of the HR and NHEJ mechanisms to overall DSB repair is scarce and difficult to generate. Rothkamm et al (37) have performed extensive studies on DSB repair in wild-type Chinese hamster ovary (CHO) cells as well as cells defective either in the NHEJ or the HR pathway. X-ray doses of 500 mGy and above were chosen and DSB incidence and persistence over several hours after exposure have been observed. For the greater part of their experiments, the formation of γH2AX foci was examined, which are widely accepted as a marker of DSBs and have also been studied in the frame of this thesis (see also chapter 5.9). Since the work done by Rothkamm et al supposedly represents the most in-depth and comprehensive analysis of the cell cycle dependence of HR and NHEJ until today, the following discussion is based exclusively on their results.

Firstly, cells defective in HR (with defunct XRCC2) still show DSB repair activity independent of the position in cell cycle. It thus can be concluded that NHEJ, which does not depend on a functional XRCC2 protein, is applied throughout all cell cycle phases. Furthermore, wild-type and HR-defective cells that have both been synchronized in G1 and exposed to very high doses of X-rays exhibited similarly effective DSB-repair, whereas equally treated cells defective in NHEJ (with defunct DNA-PKcs) showed seriously inhibited DSB repair. Identical results have been gained by observation of γH2AX focus formation and resolution after a lower dose of 1 Gy. Thus, NHEJ has been demonstrated to be the dominant mechanism in the G1 phase.

Additionally, dose-dependent cell survivability has been assessed. In asynchronous cultures, HR- and NHEJ-defective cells both show increased radiosensitivity compared to fully functional wild-type cells. For G1 cells, NHEJ defective cells are much more radiosensitive than cells with a defunct DSB-repair via HR, whereas for G2/S phase cells, the situation is reversed (although much less pronounced, with the radiosensitivity being only slightly different).

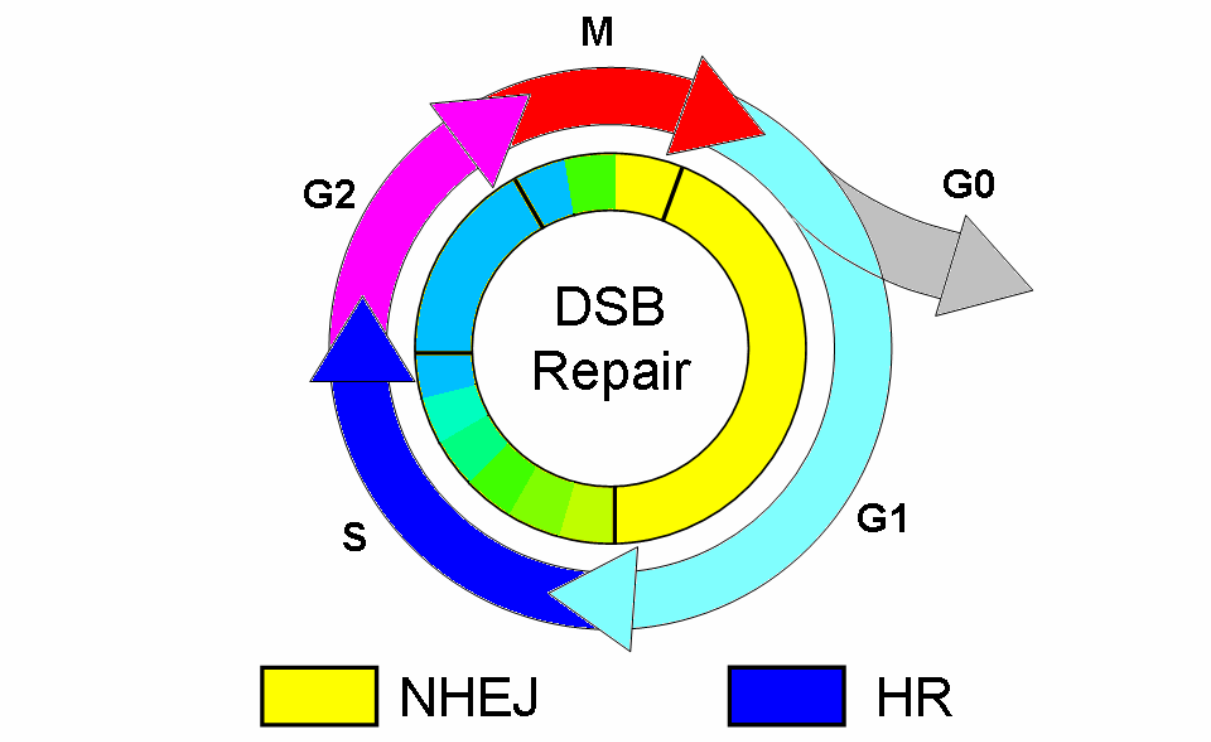

Figure 5.4. Schematic depiction of the relative contribution of HR and NHEJ to DSB-repair in different cell cycle phases after exposure to ionizing radiation (based on a picture in Rothkamm et al, 37). The various colour shades of the inner circle from yellow (NHEJ) to dark blue (HR) indicate the different relative contribution of both mechanisms to overall DSB repair.

These findings, together with conclusions from even more experiments intended to further clarify the contribution of HR and NHEJ in different cell cycle phases, which shall not be discussed in detail here, lead to the development of a model, as is visualized in figure 5.4. The model is based on the following principles, which incorporate all gathered data:

- NHEJ contributes to DSB repair throughout the cell cycle.
- NHEJ dominates DSB repair in G1/G0 phase as well as in the early S-phase.
- HR contribution is minimal throughout G1/G0 and S-phase, but increases with ongoing DNA replication throughout S phase.
- The maximal activity of the HR repair mechanism is reached in the last part of S phase, and kept up during G2 phase.
- During mitosis, HR repair is set back to its minimum level.

This model agrees very well with the intrinsic prerequisite of HR, the local presence of homologous genetic information as a template, which can be accessed most easily in late S and G2 phases, where a duplicated DNA double strand is available.

5.7. Cell Cycle Checkpoints

It has long been known that exposure to radiation or other genotoxic hazards lead to an elongation of the cell cycle and delay of mitosis (80), as can be seen by observing the mean duration between two cell divisions. In recent years, extensive knowledge has been accumulated as to the nature of this phenomenon. In addition to a variety of DNA repair mechanisms, the eukaryotic cell responds to DNA damage by arresting or delaying cell cycle progression in order to provide sufficient time for DNA repair or – in case of extensive damage beyond repair – to permanently close down cell proliferation and enter a state of senescence (76). Cell cycle delay or halt can be triggered in different cell cycle phases at so-called cell cycle checkpoints, which are initialized by checkpoint specific signal cascades. The basic underlying mechanisms shall be introduced briefly in the following.

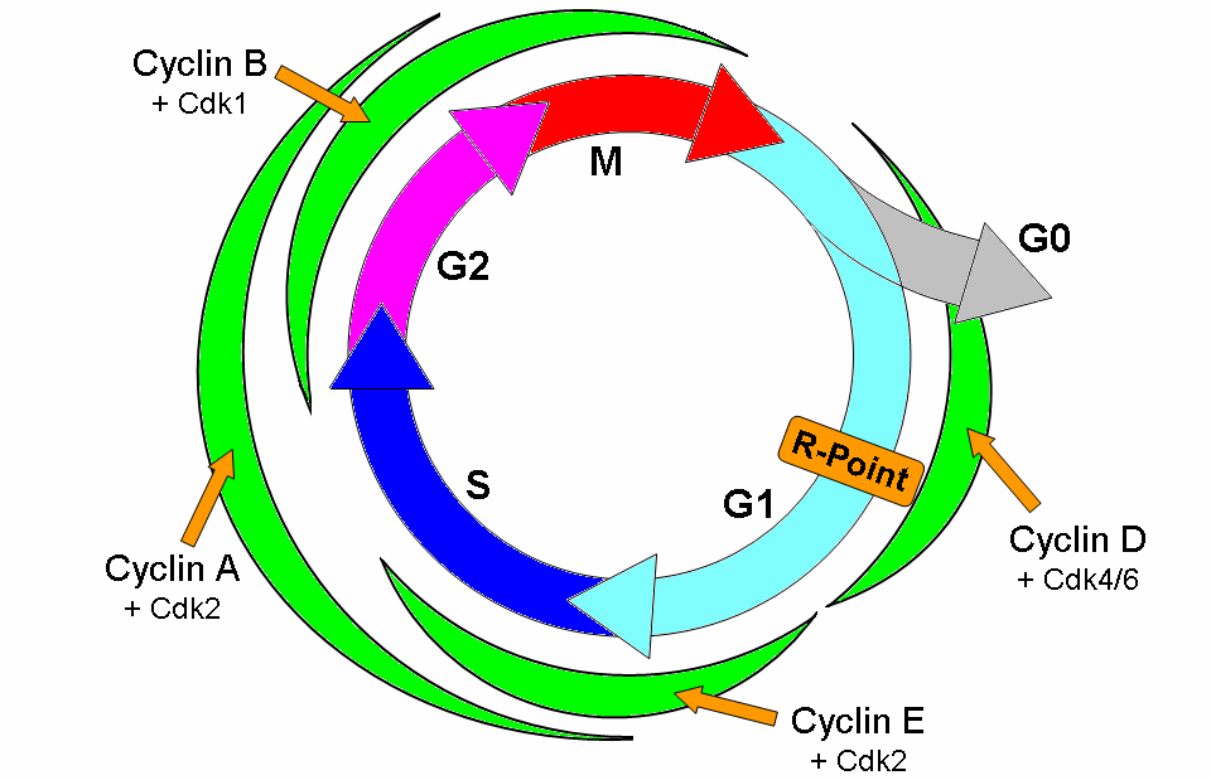

Figure 5.5. Cell cycle progression, as is catalyzed by the concentration levels of cyclin proteins (indicated by the thickness of the green sickle-shaped objects) that form specific complexes with cdks. The restriction point ("R-Point") in G1 phase is shown. The schematic is based on figures and descriptions in 13, 76 and 83.

In principle, cell cycle progression is primarily mediated by several so-called cyclin proteins and cyclin-dependent kinases (cdks). Cdks and cyclins form a variety of different protein complexes that catalyze the transition from one cell cycle phase to the next. The underlying mechanism is based on several parameters and events (13, 83): Firstly, the activity of the cdks is regulated through chemical modification such as phosphorylation,

which may be either inhibitory or stimulating. Thus, the correct phosphorylation status is obligatory for initializing transition to the next cell cycle phase. Secondly, synthesis and degradation of a particular cyclin is phase-specific, thus setting the maximum concentration of each cyclin to a defined point in the cell cycle. Simply put, cyclins "work" in alternating shifts that match cell cycle phases.

Concentration levels of the cyclins A, B, D and E as well as the cdks involved in the formation of the specific complex are indicated in figure 5.5. Apart from the obvious and already discussed points that mark the transition from one phase to the next (see chapter 4.3), the so-called restriction (R)-point is of interest: As a general rule, whether a cell that has ceased cell cycle progression and adopted the G0 state resumes proliferation (thus re-entering G1) or not is mediated by the presence of growth factors. While still being in the earlier part of the G1 phase, withdrawal of growth factors results in returning of the reactivated cells to G0. However, after passing the restriction point, progression to S-phase can no longer be prevented by removal of growth factors, which is also due to regulatory mechanisms involving cyclin D and the cdks 4 and 6.

In the following, the pathways that link radiation induced DNA damage to the cell cycle machinery shall be introduced. A more detailed discussion of basic cell cycle regulation including upstream effectors of the cyclins and cdks as well as downstream target proteins is beyond the scope of this work, and can be found in many recent reviews (13, 82, 83, 84). Basically, the DNA damage signalling network can influence cell cycle progression on any of the so-called "checkpoints" that are regulated by cyclin/cdk complexes – i.e. the restriction point in G1, the initialization of DNA synthesis (G1/S), completion of DNA synthesis in S and the induction of mitosis (G2/M) – by either chemically altering the particular cyclin and cdk or by affecting cyclin expression before reaching the corresponding checkpoint. Of course, these regulatory mechanisms need not necessarily include a direct interaction with cyclins or cdks, but may be limited to other players in cell cycle regulation.

As has been described in section 5.2, ATM is activated in response to DSBs. Other types of DNA damage, as are mainly induced by UV radiation or by treatment with certain drugs (aphidicolin, hydroxyurea), lead to the activation of another PIKK-type kinase, ATR (85). ATM and ATR share a number of substrate proteins involved in cell cycle regulation, and therefore exhibit an overlap in their functionality in the cellular response to DNA damaging agents (76). Even though the contribution of ATM and ATR varies depending on the type of DNA damage (and, therefore, the genotoxic agent), the substrate protein of interest as well as the point in time after the damaging incident, this shall be neglected in the following for reasons of simplification.

Among the substrates that are phosphorylated redundantly by ATM and ATR are the so-called "checkpoint kinases" Chk1 and Chk2. As suggested by their designation, Chk1 and Chk2 fulfil a variety of roles in checkpoint signalling. Inactive Chk2 monomers are phosphorylated on threonine 68 in an ATM/ATR dependent manner, and consecutively undergo autophosphorylation on various sites through dimerization with other monomers

phosphorylated at threonine 68. Thereby, the Chk2 kinase is activated and either persists as a dimer or is retransformed to its monomeric form (77). The event of phosphorylating Chk2 at threonine 68 will feature in some of the results presented in later chapters (see sections 11.1.1 and 13.1.5). Chk1 is also phosphorylated by ATM/ATR on the sites serine 317 and 345, thereby increasing its kinase activity (78) and improving its binding abilities to specific proteins (87). Known targets of active Chk1 and Chk2 include serine residues in members of the Cdc25 family, namely Cdc25A and Cdc25C (86). Phosphorylation of Cdc25A results in its degradation, thus preventing Cdc25A from activating Cdk2, which is involved in the transition from G1 to S phase (in the Cdk2/cyclin E complex) and the progression through DNA synthesis (in the Cdk2/cyclin A complex). Regarding this so-called intra-S checkpoint, there is indication of a parallel signalling pathway involving the Nbs1 protein of the MRN complex and the SMC1 protein (76). In a way similar to Cdc25A, phosphorylation of Cdc25C inhibits activation of Cdk1, which governs the initialization of mitosis at the G2/M checkpoint (in the Cdk1/cyclin B complex). However, this pathway has proven to be not as straightforward as incidentally suspected, since Cdc25A and – most likely – also Cdc25B as well as several other factors (such as 53BP1, BRCA1) and upstream regulators of the Cdc25A/B/C or the Cdk1 proteins (Plk1 and Plk3) possibly contribute to the G2/M transition machinery (76).

Essentially, radiation induced cell cycle mediation involving the Cdc25 proteins is intended to rapidly initialize a cell cycle delay or transient halt, but usually does not suffice and is not meant to cause a sustained cell cycle arrest. In contrast, there are slower paced, Cdc25-independent pathways featuring the P53 protein, which may finally culminate in the induction of apoptosis (see chapter 5.8) or permanent growth arrest (88). P53 is phosphorylated by both ATM/ATR and Chk1/Chk2 at several sites, among them being threonine 18 as well as serine 15, 20, 33 and 37 (89). Furthermore, ATM/ATR also mediates MDM2 activity, the key negative regulator of P53 that not only catalyzes P53 degradation, but also impairs its function as a transcription factor (90). Essentially, MDM2 and P53 are connected via an autoregulatory feedback loop, with P53 enhancing expression of the mdm2 gene and MDM2 impairing P53 levels and functionality (94).

Overall, DNA damage signalling via ATM/ATR and Chk1/Chk2 leads to increased P53 activity over several pathways. P53 initializes enhanced P21 transcription, which leads to the accumulation of high concentration levels of P21 over several hours. In comparison to the Cdc25 pathways that are regulated by rapid chemical alteration processes such as phosphorylation, this mechanism via transcription regulation of P21 is much slower. However, once sufficiently high levels of P21 are reached, P21 blocks Cdk/cyclin complexes that govern cell cycle progression through G1, from G1 to S as well as G2 to M (76). For the latter, the G2/M checkpoint, there is evidence that other factors such as GADD45 and the 14-3-3σ proteins are required (91), and that there may be P53-independent pathways via BRCA1, which also result in P21 accumulation (92). As a basic principle, high levels of P21 eventually lead to the “replacement” of Cdc25 mediated postponement in cell cycle progression with a more sustained delay or permanent cell cycle arrest (76).

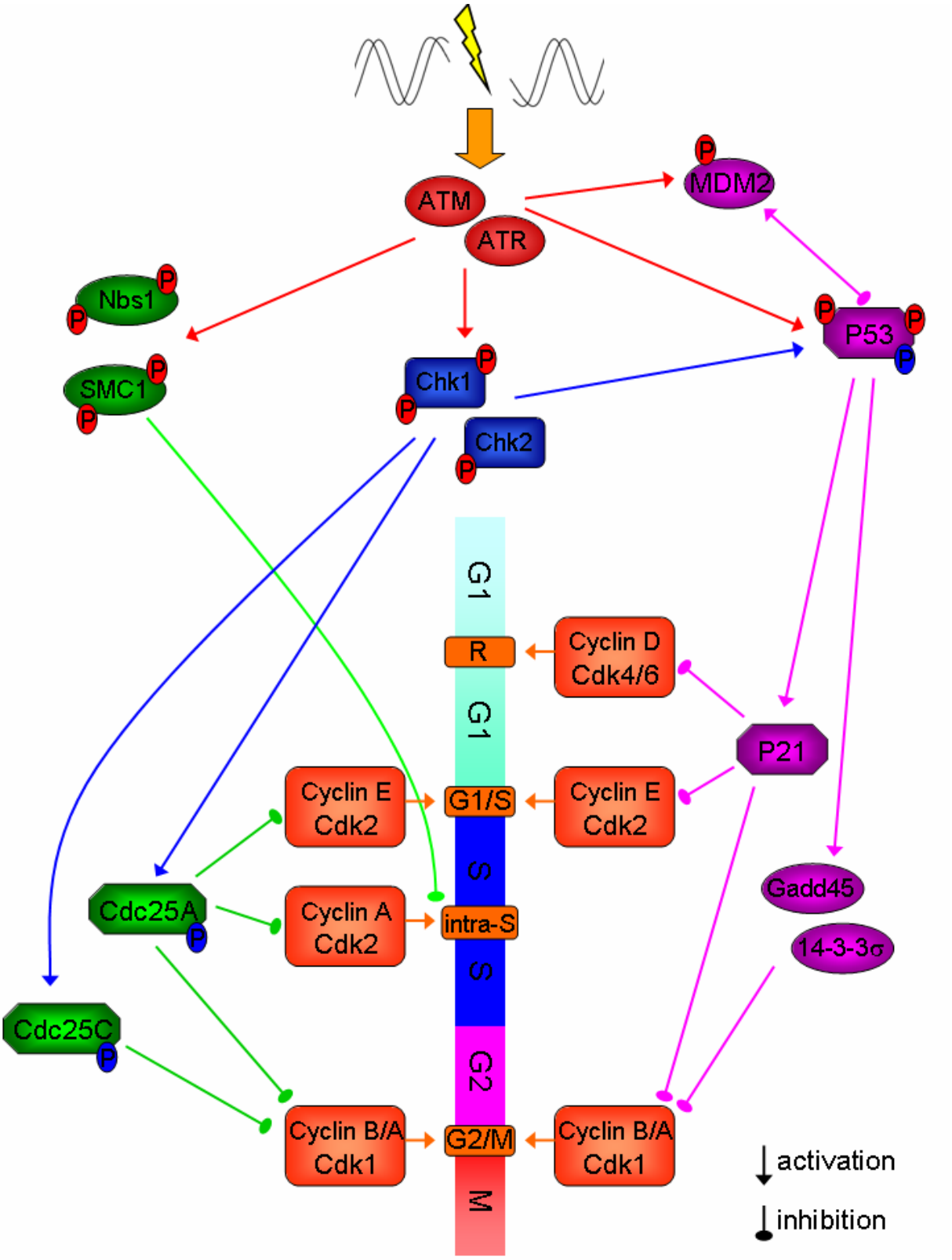

Figure 5.6. ATM/ATR mediated cell cycle checkpoints R, G1/S, intra-S, G2/M (based on descriptions and figures in 22, 76 and 83). Pathways leading to a delay in cell cycle progression are indicated green, signalling towards sustained cell cycle arrest is coloured purple. Given phosphorylation events are either mediated by ATM/ATR (red) or Chk1/Chk2 (blue).

On a side note, some of the mentioned cell cycle regulatory events involving Cdc25 and P53 can also be found in the upper right corner of the "ATM-signalling-network" as depicted in figure 5.3.

For better readability, figure 5.6 provides an overview of the checkpoint pathways according to the discussion above. It needs to be stressed that both text and figure do not include all known events involved in the cell cycle response to DNA damage. Instead, the presented information is intended to provide a general idea of cellular signalling and is meant to be a guideline for understanding of experimental results in later chapters.

5.8. The P53-Mediated Response

Several of the key functions of P53 have already been discussed in the last section. However, P53 is not only involved in cell cycle signalling, but also features in the apoptotic response in case of extensive DNA damage or other types of stress. It is still not totally understood how it is decided whether P53 initializes prolonged or permanent cell cycle arrest, or apoptosis, and why different cell types exhibit greatly varying damage thresholds for apoptosis induction. However, there are hints and theoretical models that shed some light on this decisive event: Basically, the choice whether an apoptotic or arresting response is to be initialized depends on the ability of P53 to selectively promote the transcription of genes that feature in one or the other pathway (88). As has already been mentioned, overall P53 activity is regulated by MDM2 as well as phosphorylation events on a large number of sites in response to cellular damage. One of them, serine 46, is supposed to be of special importance, since it is only phosphorylated at high damage levels that are estimated to lead to cell death, and is furthermore specifically involved in the transcriptional regulation of the P53AIP1 protein that is known to induce apoptosis (93). Thus, it seems plausible that as a general rule, the discrimination between the different pathways may be achieved by specific post-translational modification of P53 that leads either to favouring or disregarding the promotion of pro-apoptotic genes encoding for proteins such as BAX, PUMA or ATAF1 (88).

However, due to the large number of known upstream proteins and pathways involved in direct or indirect P53 regulation and modification, including ATM/ATR, Chk1/Chk2 and (possibly) DNA-PK (32), it is yet to be elucidated how specific lesions or the extent of DNA damage may finally lead to the induction of one or the other response. In case of fibroblasts used in the frame of this thesis, the predominant p53-mediated response to DNA damage is growth arrest (81) due to very high damage thresholds for initialization of apoptosis.

5.9. The Histone H2AX

Double-stranded DNA molecules are wound around spherical core consisting of proteins termed histones, which support the complex, super-coiled structure of chromatin and are essential in maintaining the genomic integrity of the DNA molecule as well as its structural three-dimensional configuration (see also chapter 4.2). A H2A variant, which represents approximately 10 percent of the total number of core histone H2A proteins (99), is termed H2AX and exclusively contains a COOH terminal tail that is not found in other human H2A isoforms (96). The region before this terminus contains an SQ motif that is of particular interest because it contains a serine amino acid on residue 139 that has been observed to be phosphorylated in the presence of DNA DSBs (97).

H2AX histones phosphorylated at serine 139 (then termed γH2AX) can already be found a few minutes after the occurrence of DSBs, and may persist in their phosphorylated state for several hours (98), depending on the course of DSB repair. These phosphorylated H2AX histones have been determined to be located within comparably large regions of chromatin with a length of approximately two megabases that surround each DSB (100), and that are commonly referred to as "nuclear foci". These foci can be stained with immunocytochemical methods (see chapter 8.4) and detected under microscopic magnification. Due to the great correlation between the number of foci and the number of DSBs, γH2AX-staining has become a standard for DSB detection, with γH2AX being widely considered a reliable DSB marker (95).

It is now known that the event of H2AX phosphorylation at serine 139 is involved in both DSB repair pathways (NHEJ and HR) and, to a lesser extent, also in cell cycle signalling (95). Since γH2AX will feature in several later chapters (see chapters 11.1.3, 13.1.3, 13.1.4, 13.1.7, 13.2.3 to 13.2.5) in the presentation of experimental results, cause and impact of this phosphorylation event shall be discussed in more detail in this separate section:

The SQ motif in the terminal tail of H2AX can be targeted by several key players of in the cellular response to DNA damage, which all belong to the PIKK family: Active ATM is well known to catalyze H2AX phosphorylation on serine 139 in response to ionizing radiation shortly after DSB incidence (26, 104, see also figure 5.3 in the upper right), and has been found to colocalize with γH2AX (65, own results, see section 13.1.3 and 13.2.3) at sites of DSBs. Furthermore, replicational stress due to exposure to UV radiation leads to γH2AX phosphorylation mainly through the ATR pathway (102). Even though ATM seems to play the dominant role in γH2AX phosphorylation after DSBs (104), there is evidence that DNA-PK performs the same task in a redundant manner (42). Finally, in the process of DNA fragmentation, which is an integral step in cellular apoptosis, breaks in the DNA molecule are generated which lead to γH2AX phosphorylation that has been determined to exclusively depend on the kinase activity of DNA-PKcs (103).

H2AX-deficiency, though not lethal, leads to severe, detrimental health effects, as has been established in mouse models: H2AX deficient mice exhibit increased radiosensitivity

and chromosomal instability, tumor susceptibility, below-average size as well as male infertility (95). This may be explained by the specific function of γH2AX in DSB-repair: While phosphorylation on serine 139 is not required for activation and initial recruitment of the DSB repair machinery, it is essential for prolonged accumulation of the involved factors at sites of DSBs, as is indicated by the formation of the so-called "irradiation induced foci" (IRIF). This has been demonstrated for a number of proteins that feature in NHEJ and HR repair such as Nbs1, Brca1 and 53BP1 (98). Thus, even though DSB repair is still possible in principle in H2AX deficient cells, sustained local retention of repair proteins facilitates a fast and complete formation of the repair complexes. Therefore, capability of faithful DSB repair is severely hampered in cells with H2AX deficiency.

Furthermore, lack of functional H2AX may influence activation of cell cycle checkpoints in specific exposure situations. It has been demonstrated that low numbers of DSBs, as are generated by low doses of ionizing radiation, fail to arrest H2AX deficient cells at the G2/M checkpoint in contrast to wild-type cells, suggesting a role of H2AX in amplification of signals mediating radiation induced cell cycle regulation (105). However, since the initialization of cell cycle checkpoints is intrinsically linked to the level of DSB repair, as has been discussed in chapter 5.7, this influence of H2AX on checkpoint signalling is likely to be interpreted as a direct result of impaired repair capability due to H2AX deficiency.

Overall, experimental data that has been accumulated so far clearly supports the role of H2AX in DSB repair, namely the accumulation and retention of repair factors. On the other hand, the underlying mechanism is still to be investigated, since as of yet, it is not clear whether IRIF are formed due to direct interaction with γH2AX, a γH2AX-mediated reconfiguration of chromatin structure or a mixture of both (95). Apart from that, due to its intrinsic properties, observation of γH2AX phosphorylation at serine 139 serves as a powerful and precise tool in DSB studies (106), as is also used in the work presented here (see chapters 9.5 and 9.7).

6. Non-Targeted Radiation Effects

The last few chapters have been dealing with cellular damage as a direct result of deposition of radiation energy and a variety of mechanisms that are applied by the cell in order to cope with this situation. What has been discussed so far shall be summed up in brief: Cells that are traversed by ionizing radiation are subject to chemical alteration of their components due to direct interaction with radiation or via generation of secondary radicals. Damage to DNA molecules poses an exceptional threat due to the intrinsic properties and functions of DNA and may lead to cell death, genetic mutation or tumorigenesis as a long term effect. Depending on the extent and the type of DNA damage, different repair mechanisms are applied. The repair of DNA double-strand breaks, which are considered the most dangerous lesions, is performed via the error-prone non-homologous end-joining pathway or by homologous recombination, a high-fidelity mechanism that is only available in specific cell cycle phases. As further measures, progression through the cell cycle may be delayed or halted in order to gain more time for damage repair if necessary or to suspend cell division in case of a large damage amount. The last resort in response to irreparable damage is the initialization of apoptosis in order to minimize the risk of neoplastic transformation.

This model description of events is based on the fundamental idea that most biologic effects, even long-term consequences such as oncogenic transformation, may be traced back to DNA damage that has been induced either through direct interaction with ionizing radiation, or by radicals resulting from ionizing tracks through the nucleus of a cell. However, while this description of radiation induced cellular effects, which has been a longstanding dogma in radiation biology throughout several decades, is capable of explaining a variety of effects and mechanisms, it is not complete. Since the last decade of the 20th century, evidence has been accumulated that specific radiation induced effects are not limited to cells with nuclear traversals of radiation tracks. In fact, cells that have not been subject to any deposition of radiation energy at all, but are merely located in proximity to exposed cells, display certain effects that are similar to those observed after direct irradiation. Furthermore, specific DNA damage patterns have been demonstrated to emerge after several cellular generations (i.e. after a certain number of cell divisions), even though the initial radiation damage has long before been successfully repaired and has yielded no obvious, sustained damage. Clearly, all these surprising effects, which are termed “non-targeted” due to their occurrence off the primary target cell, cannot be explained by any of the models or mechanisms that consider chromatin as the single, most important target of ionizing radiation, as has been presented in the last few chapters. Thus, especially at low radiation doses, where most cells of an organism are not directly affected by radiation, a refined view of cellular events needs to be applied. In the

following, the evidence gathered so far and implications on the assessment of health risks due to non-targeted effects shall be discussed.

6.1. The Bystander Response

Radiation-induced bystander effects refer to effects that are detected in cells which have not been traversed by an ionizing radiation track, but are localized in the vicinity of one or more directly "hit" cells. In the last few years, a bystander response has been demonstrated for a variety of biologic parameters associated with DNA damage: Micronucleation and clonogenic survival (111), sister chromatid exchanges (112), chromosomal aberrations (113), an increased apoptosis rate (115), the occurrence of DNA DSBs (117), mutation (127) as well as oncogenic transformation (116) have been observed in cell culture experiments.

The methods applied in these studies differ greatly, and may basically be attributed to four different types of experiments:

(A) Medium transfer protocols

(B) Co-cultivation of irradiated cells

(C) Exposure to low fluences of high energy charged particles

(D) Precise cell targeting with microbeams

In medium transfer experiments (A), cultivated cells are exposed to (usually high doses of) ionizing radiation or damaging agents and are afterwards kept in a humidified incubator for duration of a few hours. Then, culture medium is gathered from the exposed cells and transferred to samples of cultivated cells that have not been irradiated. After another period of incubation, a bystander response may possibly be observed, which would have been induced by factors released into the medium by irradiated cells. Of course, special filtering techniques need to be applied to avoid contamination of unexposed samples with irradiated cells, and additional control experiments must be performed that include the irradiation and transfer of bare culture medium without cells in order to rule out any systematic errors due to background effects (108, 109, 110, 117).

Co-cultivation protocols (B) rely on irradiating cultivated cells that may be "relocalized" to the immediate vicinity of non-exposed cells, which is typically accomplished by use specifically designed exposure dishes that may be inserted into larger containers with non-exposed cells. Sophisticated assemblies are required to prevent cross-contamination while still allowing for medium flow that transports bystander factors released by irradiated cells to the bystander group (117, 113). Thus, in principle, co-cultivation experiments are similar to medium transfer methods.

With high-energy proton and ion accelerators becoming more easily available, bystander studies were also conducted in beam lines of this type (C). As a basic common strategy, layers of cultivated cells are exposed to low particle fluences that result in a certain percentage of cells being either traversed through their nucleus, through the cytoplasm or not directly hit at all. Therefore, as an ideal solution cell layers are to be placed perpendicular to the incident beam in order to minimize scattering or LET variation. Obviously, cells with nuclear particle hits cannot be easily distinguished from non-hit cells due to the stochastic nature of the particle distribution of the cell layer. Therefore, any results concerning bystander effects need to be derived from geometric considerations and statistical analyses (112, 118, 126, 128). This procedure leads to comparably high thresholds for the determination of bystander effects, since biologic events of interest will also be observed in hit cells with a (higher) probability that is difficult to assess. Thus, as is common experimental practise, all hit cells will be expected to positively display a given effect (unless determined otherwise), and only if the number of affected cells exceeds the number of hit cells, this can be interpreted as a bystander response.

The most elegant and sophisticated way to study bystander effects is accomplished with so-called microbeams (D). Facilities of this type allow precise delivery of ionizing radiation (photons or light charged particles) to small, defined target volumes with diameters in the micrometer range. Thus, when cell monolayers are irradiated with a microbeam at an incident angle close to 90 degree, single cells or even subcellular compartments may be targeted. This allows for direct discrimination between hit and non-hit cells and, therefore, for a straightforward observation of a bystander response (114, 117, 119, 120, 121).

Furthermore, there are a few other methods, which – though not as frequently applied – are suited for bystander experiments as well. As a basic common principle, they aim at inducing DNA damage and/or apoptosis in a defined subpopulation of cells, which may give rise to a spread of the damaging signal via a bystander response. This is, however, achieved by varying means: For instance, Auger electron emitting ^{125}I may be incorporated into DNA molecules of a defined percentage of cells, which leads to a highly localized concentration of ionization events in or in the immediate vicinity of DNA molecules, thus inducing diverse forms of DNA damage inside the target cell without directly damaging surrounding tissue (123, 124). As another alternative, cytotoxic agents may be introduced by single-cell microinjection (125).

By use of the methods described, a significant amount of knowledge has been accumulated as to the nature, biologic effects and consequences of the bystander response as well as to the signalling pathways involved. Some of the insights shall be presented in the following:

Several damage indicators (that have already been listed in the introductory paragraph) have been demonstrated to be found in bystander cells. As a self-suggesting next step, the questions as to how the bystander signal is transmitted from initially affected to bystander cells as well as what factors are involved, need to be answered. It is now known that

different pathways contribute to the communication of the bystander signal either in an exclusive or a cooperating way (see figure 6.1 for a schematic depiction of involved mechanisms):

Firstly, the initial damaging signal can lead to the secretion of soluble messenger proteins (cytokines, growth factors) into the culture medium as is the basis of various bystander studies that rely on harvesting medium from exposed cultures followed by transfer to unexposed cells. These proteins are often referred to as "clastogenic factors" due to the fact that they may eventually cause the induction of chromatin damage in bystander cells. This pathway has been demonstrated for various cell types including normal human fibroblasts (111, 117), which is of importance since cells of this type were used in the presented thesis (see chapter 8.1).

Furthermore, the bystander signal may be transmitted via direct cell-to-cell communication, as is mediated by "gap junctions" (126, 128), which basically represent channels that allow for a bi-directional exchange of cytoplasmic molecules between two adjacent cells across both cell membranes and a very short intracellular distance. The evidence presented for this mechanism was also gathered using normal human fibroblasts and includes micronucleation as well as enhanced expression of proteins involved in the apoptotic pathway, both directly depending on the capability of the cells for intercellular communication via gap junctions.

Finally, the bystander signal has also been suggested to be transmitted by the release of reactive oxygen species (ROS) into the culture medium (129, 130). During the cellular oxidative metabolism, ROS such as hydrogen peroxide, superoxide anions and hydroxyl radicals are formed and may be transmitted to the culture medium. It is known that ROS are involved in the cellular response to radiation in hit as well as in bystander cells (111, 118, 131), as it was found that bystander cells show increased levels of ROS when incubated with medium from irradiated cells and also cell-free medium containing serum that has been exposed to α-particles. However, the mechanism that leads to a sustained increase of ROS production in bystander cells still in need of a more detailed elucidation.

Above all, it needs to be stressed that a particular bystander effect of interest may well be specific as to the pathway used for signal transmission (or, as a matter of fact, as is permitted by the corresponding experimental protocol). For human fibroblasts, it has been demonstrated that some effects can be triggered by transmissible factors (111, 117), whereas others are caused exclusively by signal transfer via gap junctions, as has been shown by preventing cell-to-cell communication with the gap junction inhibitor lindane, thereby eliminating the investigated bystander effect (126). Furthermore, there is evidence that the capability of participating in a certain pathway for transmitting or receiving the bystander signal depends on cell type (109).

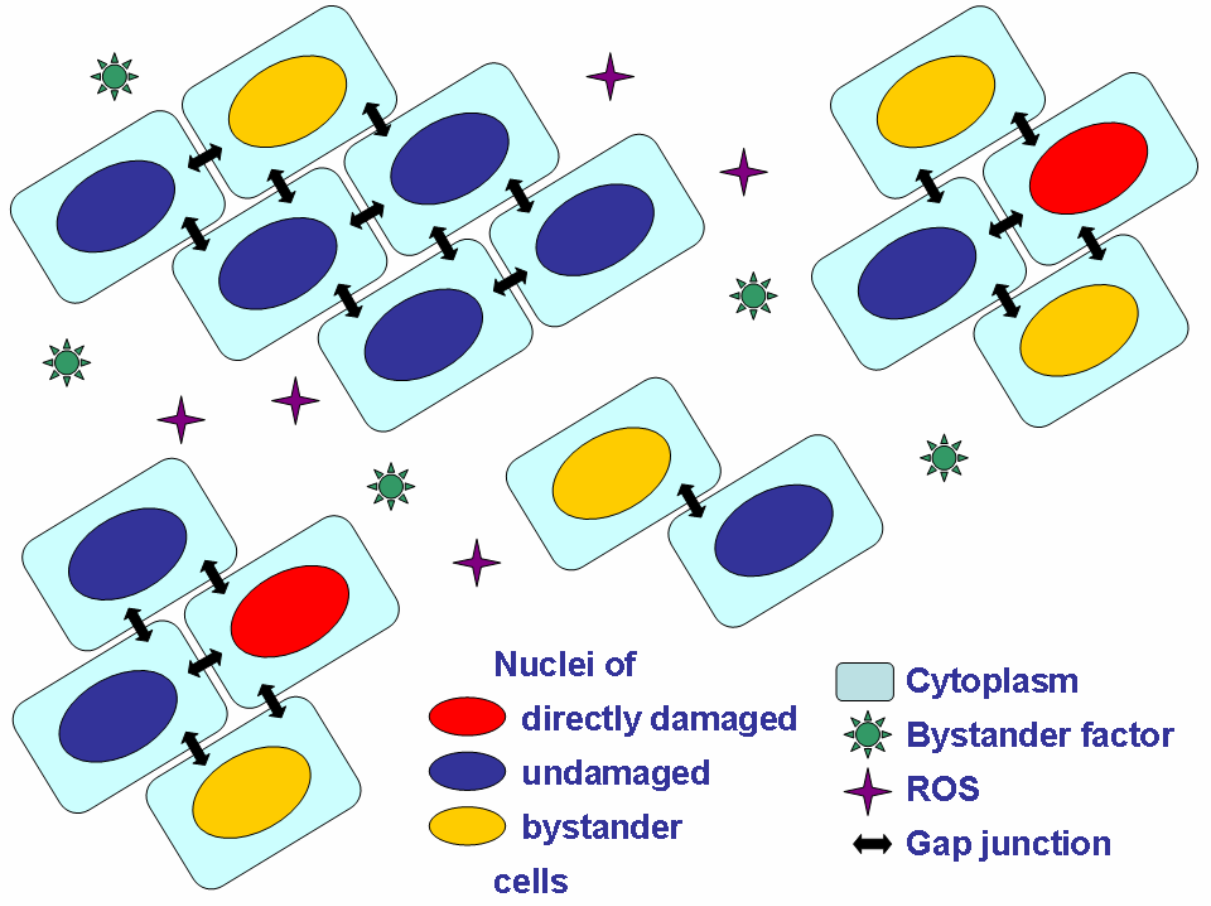

Figure 6.1. The various ways of transmitting the bystander signal – via proteins secreted to the culture medium (cytokine, growth factors, reactive oxygen species) or direct cell-to-cell communication (gap junctions).

On the protein level, several events are known to be triggered due to a bystander response. Some of them are linked to DSB repair, cell cycle signalling and apoptotic pathways, as are of importance for this thesis, and shall therefore be discussed briefly: Most obviously, the incidence of DNA DSBs in bystander cells, as has been found in human fibroblasts using medium transfer protocols (111) and exposure to counted numbers of a-particles (117), leads to the induction of DSB repair mechanisms, as has been demonstrated by observation of H2AX phosphorylation, which is thought to be involved in both NHEJ and HR repair pathways (see section 5.9). Furthermore, accumulation of other key players in DSB repair, such as ATM (phosphorylated at serine 1981), Nbs1, Bp53, Rad50 and Mre11, has been observed at γH2AX foci located in bystander cells, indicating DSB repair activity (117). As far as protein synthesis is concerned, upregulation of p21 and p53 expression in bystander cells has been observed for human fibroblasts, which indicates the activation of stress-inducible pathways that are directly connected to cell cycle regulation and initialization of apoptosis (118). Moreover, elevated levels of RPA and APE (a key player in the base excision mechanism that governs repair of single-base damage) expression were found in normal human fibroblasts that were incubated in culture medium harvested from γ-irradiated cultures, thus providing evidence for the

induction of DNA repair pathways, presumably as a result of induced DNA strand breaks and oxidized base lesions due to oxidative stress (108).

However, a lot of questions still remain unanswered. Since by far the greatest number of studies have been performed using cultivated cells that can only mimic the complexity of an organism or the human body to a very limited extent, the influence of bystander effects on radiation induced health risks is debatable. Secondly, the mechanism itself is not well understood, as far as its biochemical basics and its dependence on biological as well as radiation field parameters are concerned. Above all, there is indication that bystander effects may be linked to or even directly induce an adaptive response (133, 138, 176), a mechanism whereby cells react to a hazardous environmental situation (such as radiation) by processes intended to render them more resistant to the threat. Thus, transmitting a damaging (bystander) signal might not only lead to a spread of damage, but may possibly be interpreted as a signal of warning intended to trigger a state of alert, thus shielding an organism or a group of cells against further assaults. Some of the points mentioned here, combined with recent experimental approaches, will be discussed below (see chapter 6.3).

6.2. Genomic Instability

Radiation induced genomic instability is characterized by an increased rate of genomic alterations encountered in the progeny of irradiated as well as bystander cells. Thus, while genomic instability is listed here as a separate chapter, it is directly connected to the bystander phenomenon. Although this thesis focuses on the immediate cellular response to low doses of ionizing radiation as can be observed within a few hours after exposure, it is important to also understand the long term consequences of initial effects. Since in specific exposure situations such as low fluences of high-LET particles, as are the main topic of this thesis, DNA alteration due to genomic instability is known to greatly exceed initial damage levels (107), this effect shall be discussed in the following in order to put experimental results presented later into a greater context.

As already denoted, bystander effects and genomic instability are closely associated: In both cases, observed effects include various forms of DNA damage, mutation, transformation and, as a result, cell death in cells that have not been subjected to direct chemical alteration due to ionizing radiation. Secondly, both are already (but not exclusively) encountered at low radiation doses in the mGy range that are of special importance for radiation protection. Furthermore, it is known that genomic instability is not limited to induction by radiation, but is caused by chemical carcinogens as well (136), which has also been demonstrated for the bystander response (125).

Due to the intrinsic property of the genomic instability phenomenon that mutations occur in offspring in a non-clonal manner (i.e. specific mutations found in daughter cells have not been inherited), and due to the high frequency of this events, it seems reasonable to

assume that genomic instability needs to be sustained by epigenetic processes that may include cell-to-cell communication and environmental factors (107). Thus, because of the intrinsic requirement of communicating or preserving the initial damage signal as well as due to comparable effects and initializing events, it is speculated that similar factors may be involved in the processes of bystander signalling and genomic instability (133).

Until now, a number of studies have excelled at demonstrating the occurrence of the non-targeted effects such as genomic instability under various circumstances. However, there is still a considerable lack of understanding as to the underlying mechanism, and in particular as to the implications on the quantitative assessment of health risks due to low radiation doses.

6.3. Implications of Non-Targeted Effects and Future Perspectives

The potential impact of radiation induced non-targeted effects on health risk assessment and, as a direct consequence, on thresholds in radiation protection, is a highly controversial topic, which is due to several reasons. Firstly, knowledge about the underlying mechanism is still developing and may be considered far from complete. Some insights have already been gained on the importance of ROS generated in oxidative metabolism, as has been elaborated in section 6.1. Furthermore, evidence has been found that the radiation induced response in bystander cells follows specific pathways that may be different from signal transduction due to direct radiation damage, despite similarities in observed damage patterns. For instance, in bystander cells (normal human astrocytes and T98G glioma cells) formation of γH2AX (serine 139) foci, which indicate the presence of DSBs, has been identified to depend on functional ATR and not ATM or DNA-PK, as would have been expected from cellular events initialized by DSBs in directly irradiated cells (see chapter 5), and was restricted to S phase (122).

Generally speaking, cellular effects due to exposure to low doses of ionizing radiation are highly diverse and depend on a manifold of parameters. Several seemingly opposed effects are observed that include genomic instability, a damage spread to bystander cells as well as protective effects that increase resistance to further exposure, which are generally summarized to the so-called adaptive response. Currently, these issues are frequently discussed and are the topic of many recent reviews (129, 133, 135, 137). Additionally, it is even yet to be clarified whether bystander effects are purely detrimental or may, in fact, also contribute to beneficial adaptive mechanisms. For instance, elevated numbers of apoptotic cells in the bystander population may, at first sight, be interpreted as an increase in the overall radiation damage, but can, on the contrary, have a protective impact, if only those cells that are damaged or defective in a specific response pathway have been eliminated (133). As a consequence, cell death as a commonly used indicator for the negative implications of a bystander response needs to be very critically viewed, especially

when larger biologic units such as organs or a whole human-being are considered. On a side note, all types of low dose effects seem to be, in principle (and not quantitatively), independent of radiation quality, since, as is rather unexpected, even a low dose of high-LET particles has been demonstrated to induce an adaptive response (138).

Finally – as is likely the most important issue – almost all insights on non-targeted effects have been gained through cell culture experiments. It is one of the major drawbacks in radiation biology that results gathered in cell culture experiments may possibly be of limited applicability to the in vivo-situation, and especially to the human-being. Whereas non-targeted phenomena such as bystander effects and genomic instability are in principle already well established in vitro, investigation in animal models as a logical next step is difficult due to experimental reasons. There are, however, different approaches aimed at demonstrating the occurrence of non-targeted effects in vivo, which have already led to further insights:

Watson et al (134) reported indication of a bystander response and chromosomal instability in vivo. In this study, a mixture of (distinguishable) neutron-irradiated and non-irradiated bone marrow cells was transplanted into female mice. A control group received only non-irradiated bone marrow cells. Increased chromosomal instability was found to persist in the bone marrow of mice that were transplanted with mixed cells throughout a period of 3 to 13 months after transplantation. Furthermore, chromosomal aberrations were also found in the progeny of non-irradiated cells, arguing for a bystander response.

In another mouse study, Xue et al (124) observed significantly inhibited growth in bystander tumor cells in the vicinity of labelled cells supplemented with DNA-bound ^{125}I, an Auger emitter. The corresponding electrons have ranges below 0.5 μm and can therefore not enter neighbouring cells.

As yet another step towards true in vivo observation of non-targeted effects, 3D cell culture models were used in order to extend investigation of the well established two-dimensional bystander response by allowing intercellular communication in all directions. Thereby, using PCR methods, Persaud et al (132) demonstrated an increase in mutation rate of non-irradiated cells located near cells irradiated due to labelling with thymidine containing ^{3}H.

Overall, current understanding of non-targeted effects, the underlying mechanisms and especially their significance for in vivo cancerogenesis is still limited. However, future advances regarding the biologic response to low radiation doses may well lead to a refinement of our current view of the dose-effect relationship, which may eventually pivot in the development of new and further improved thresholds in radiation protection.

Part II:
Materials and Methods

Part II of this thesis includes a detailed description of the methodology applied in all experiments of radiobiologic and dosimetric nature. It is divided into several subsections: The first few chapters are dedicated to TL measurements, used dosemeter materials and calibration, annealing as well as TL read-out procedures and systems.

Further on, basic cell culture protocols, chosen configurations for exposures and the characteristics of used different radiation sources are introduced. Exposed biologic samples were subjected to various biochemical techniques in order to investigate radiobiologic parameters of interest on the single cell level. The underlying basics of these procedures will be elucidated in a separate section.

The final part deals with the acquisition, processing and analysis of biologic data, including a brief introduction to used specialized personal computer-based applications and developed half-automated picture processing and analysis procedures.

7. Thermoluminescence Dosimetry

The basic principles of dosimetry on the basis of the thermoluminescence phenomenon have already been outlined in chapter 3. In the following, TL measurement techniques and materials that have been applied in this thesis shall be introduced. Furthermore, devices that have been employed for read-out procedures and dosemeter preparation will be described.

7.1. Properties of Applied Dosemeter Types

As has already been explained, TL materials require allowed energy levels between the conduction and valence band for trapping of electrons and electron holes (see section 3.1). In commercially available TL dosemeters, this energy band structure is usually accomplished by intentionally inserting deviating atoms into pure crystals (i.e. "doping" bulk material). TL dosemeters available include a manifold of materials such as LiF, CaF_2, $CaSo_4$, $Li_2B_4O_7$ and others, supplemented with different types and concentrations of dopants.

In the presented thesis, used dosemeter chips are composed of LiF doped with Mg (330 ppm) and Ti (11 ppm). Of these, two types were employed - one enriched with ^{6}Li, the other with ^{7}Li (see table 7.4 for details). Both types of TL dosemeters have been obtained from Thermo Fisher Scientific Inc. (B-1, former Saint-Gobain/Norton Industrial Ceramics Co. or Harshaw Chemical Co., respectively) and shall further on be referred to by their trade names TLD-600 and TLD-700. All used dosemeter chips are of the same approximate size of 6.4x6.4x0.9 mm³.

Type	^{6}Li [%]	^{7}Li [%]
TLD-600	95.62	4.38
TLD-700	0.07	99.93

Table 7.4: Content of different Li isotopes in TLD 600 and 700.

Properties of TLD-600 and 700 dosemeters have been extensively investigated by W. Schöner (140). His insights on their experimental behavior shall be summarized briefly in the following, and their implications on experiments within the frame of this thesis will be discussed:

Generally speaking, the overall TL output of a material is required to be dependent on absorbed dose in order to qualify for dosimetric applications. Ideally, the relationship between absorbed dose and TL output (i.e. the so-called "dose response") would be linear over the whole dose region of interest. However, real TL materials usually only exhibit a linear dose response in the lower dose region and may show saturation effects at higher radiation doses, which essentially corresponds to occupation of all available traps. For the dosemeter types used in this thesis (LiF doped with Mg and Ti) such as TLD-600, a linear dose response has been demonstrated for doses between 10 μGy and 10 Gy (regarding the dominant peak 5 of the glow curve of LiF that is commonly used for dose determination), which is followed by a supralinear region up to 1000 Gy, where saturation is reached (140). All radiation doses that have been delivered to TLD-600 and TLD-700 in the presented experiments are well within the linear range of LiF:Mg,Ti detectors, since most exposures have been selected to be at or below 60 mGy (see section 10.3).

Furthermore, the intensity of TL-emission is also dependent on the energy of the absorbed radiation, which is termed the "energy response" of a detector. For radiation protection purposes, it is most essential to determine the dose absorbed in human tissue. Therefore, it is advantageous to use TL detectors that exhibit an energy response similar to tissue over the radiation energy range of interest. For photon radiation, the (photon) energy response s(E) is given by

$$s(E) = \frac{(\mu_{en}/\rho)_{TL}}{(\mu_{en}/\rho)_{ref}} \quad , \tag{7.11}$$

where (μ_{en}/ρ) is the mass energy absorption coefficient in the thermoluminescent material (TL) and a reference substance (ref), which is commonly chosen to be tissue or air. Thus, a "tissue-equivalent" detector material is required to show an identical energy dependence of the mass energy absorption coefficient compared to tissue, which corresponds to s(E) = 1 over the whole spectrum of photon energies. As a consequence, a detector with this properties absorbs exactly the same dose as tissue in a given photon field.

According to the energy response curve for LiF as calculated by W. Schöner (140) that shows values for s(E) close to 1 for all relevant photon energies, it is reasonable to consider TL dosemeters based on LiF such as TLD-600 and TLD-700 as tissue-equivalent with good approximation for photons.

Another important property of TL materials is the stability of trapped charges over time and under external influences such as light, moisture and moderate heating. The loss of trapped charges is termed fading, which may result in a decay of the TL-signal and, thus, in an underestimation of the dose absorbed by the TLD. For the dosemeter types TLD-600 and TLD-700, the peak 5 used for dose assessment and especially the higher temperature peaks that feature in the HTR method (see section 7.5) are sufficiently stable at room temperature, where thermal fading of the TL signal has been determined to be below 5% per year (140). For all experiments, exposed dosemeters where generally read out within

several weeks after exposure, and only a few were stored for a few months. Thereby, the influence of fading on the TL measurements was minimized.

The dependence of TL-emission on radiation LET constitutes the fundamental principle of the HTR-method and will be discussed in the corresponding paragraph (see section 7.5).

7.2. The TL-Dat II Reader

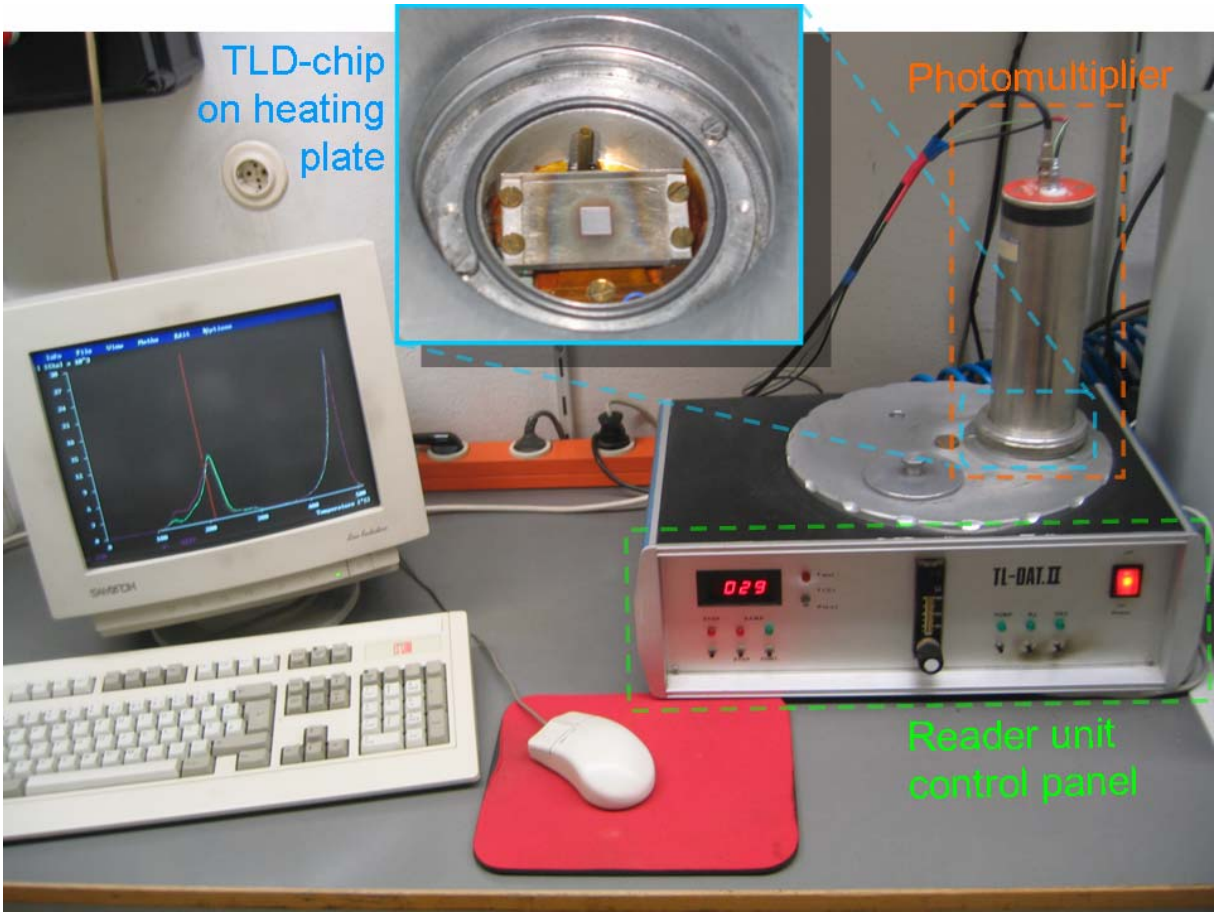

Figure 7.1. The TL-Dat II system and its components.

All TL dosemeters were read out with the "TL-Dat II" Reader, a computerized system that has been developed at the Atomic Institute of the Austrian Universities and is designed to pick up and process the glow curves of TLD chips (139). Its configuration and function shall be described briefly (see also figure 7. for a photograph of the TL-Dat II system): A single TL dosemeter is placed on a heating plate made of Nikrothal 80 that is connected to a thermocouple for heating regulation. The heating plate is located in an aluminium chamber, which can be sealed and evacuated. Measurements are performed under floating of pure nitrogen in order to avoid picking up any parasitic luminescence emissions from normal atmosphere. TL photons are detected with a photomultiplier in single-photon counting mode, which is mounted on a turntable allowing for easy exchange of the

measured TL dosemeters. Both the electronics for heating control and the photomultiplier are connected to a specially designed interface card that is fitted into a standard personal computer, which enables real time on-screen monitoring, processing and storage of glow curves.

For read-out of the applied TLD-600 and TLD-700 detectors, the same well established standard parameters for the heating cycle have been used in all measurements: The chips were heated from room temperature up to a maximum of 480 °C at a heating rate of 5 °C/s. The following rapid decrease in temperature to room levels is achieved by water cooling of the heating unit.

7.3. The TLD Software for Glow Curve Analysis

Even though the MS-DOS based TL-Dat II software is in principle capable of measurement controlling as well as processing and analyzing TL glow curves, a more convenient programme based on Microsoft Windows has been developed in recent years. This piece of software, which has been given the simple name "TLD" (even though it is also capable of and used for processing data from dosemeters based on OSL – optically stimulated luminescence) allows for parallel visualization, manipulation and analysis of multiple glow curves as well as easy data exportation and features a user interface that may be customized to individual needs (1).

The TLD software includes a routine for subtracting the background signal (which is mainly due to black body radiation) from a recorded glow curve by means of a synthetic iterative algorithm for background fitting. The fit function for the TL-light equivalent background intensity y consists of a term exponentially growing with temperature and an offset y_0 (141):

$$y = y_0 + a \cdot \exp\left(\frac{b - T}{c}\right) \tag{7.12}$$

Fit parameters are a, b and c. The value for y_0 is commonly derived from the glow curve in the temperature interval between 21 and 60 °C, where the contribution of the exponential term to y is minimal. The temperature interval for background fitting by variation of a, b and c is user-defined and is generally chosen somewhere between 300 and 480 °C, thus relying on the experience of the experimentalist to a certain extent. Corresponding starting values of a = 1, b = 180, and c = 25 have proven to be preferable. Figure 7.2 illustrates the fitting process.

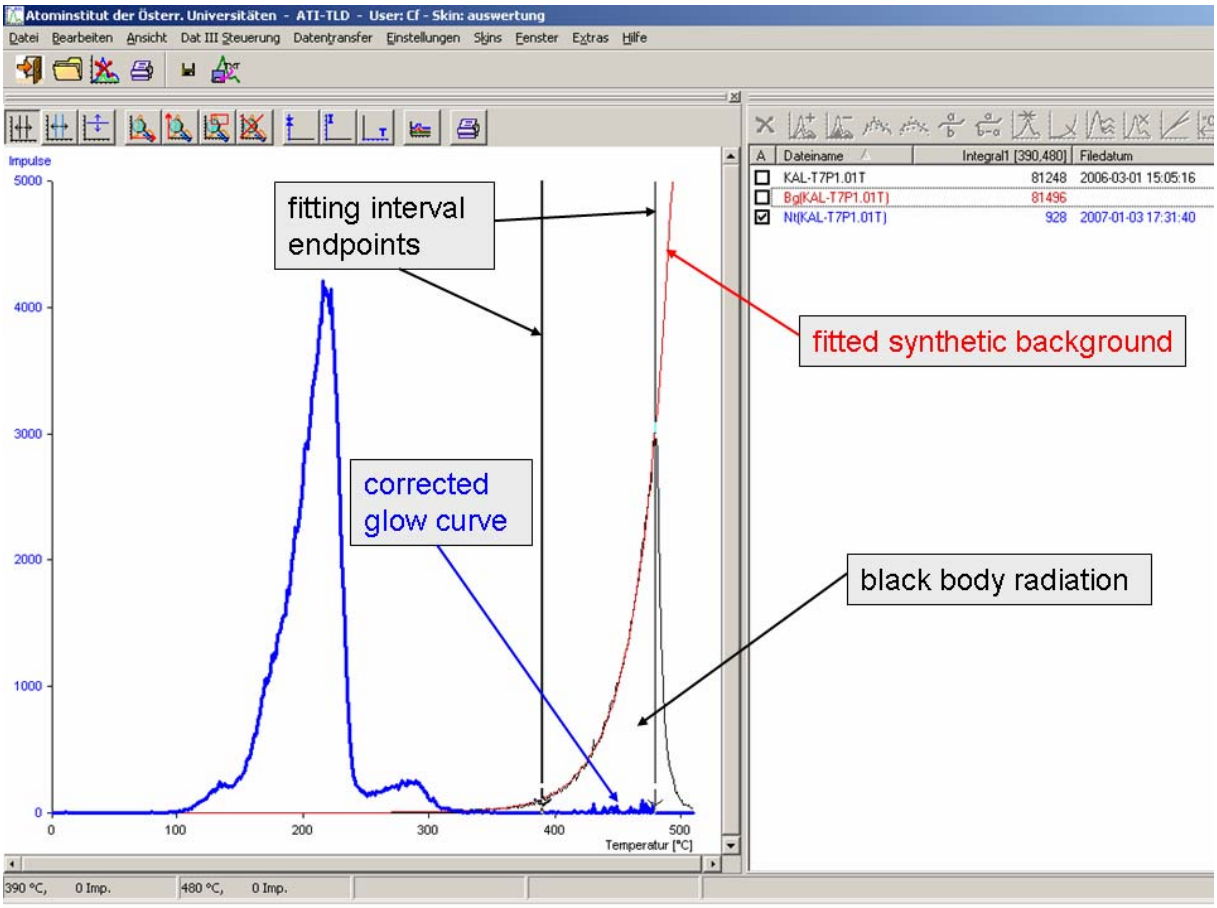

Figure 7.2. Background subtraction by means of a synthetic iterative algorithm, as provided by the Wegs data TLD software. The given glow curve corresponds to a TLD-700 chip exposed to 61.7 mGy of ^{60}Co γ-radiation. In this case, the fitting interval was chosen from 390 to 470 °C.

7.4. Calibration and Annealing Procedures

After read-out and before their next exposure, TLD-600 and TLD-700 are treated with an annealing procedure that represents a standard process applied at the Atomic Institute for measurements with these types of TLDs. Thereby, remaining occupied traps are emptied and a standardized status of the TLD detectors is reconstituted. For this purpose, the oven available in the TL laboratory of the Atomic Institute is preheated to 400 °C. Then, the TLD chips, which have been placed on a fused quartz plate to prevent surface contamination during annealing, are put into the oven and kept at 400 °C for one hour. After that, the oven is switched off and the dosemeters are allowed to cool down inside as defined by the thermal capacity of the oven.

Dose calibration of used TLD-600 and TLD-700 chips has been achieved by exposure to a reference field of γ-radiation. All calibration irradiations have been performed at the Calibration Theratron of the Clinic for Radiotherapy and Radiobiology (Vienna Medical

University, Austria), which contains a ^{60}Co source routinely used for dosemeter calibration and radiobiologic experiments. The corresponding doses have been monitored with ionisation chamber detectors kindly provided by the physics department of the clinic.

Different TL detectors of the same type may display a varying overall TL-efficiency when exposed to the same radiation dose of a reference field, as is likely depending on manufacturing and the experimental "history" of each single chip. Therefore, it has become a common and advantageous practise to group TL detectors into "packages" for exposure, which consist of several chips that share similar efficiency characteristics. Dosemeter packages used in the frame of this thesis (each consisting of 3 to 5 detectors of both TLD-600 and TLD-700 types) have already been pre-selected for measurements in a former study, the so-called PHANTOM project (151), according to their determined properties and were reused without further rearrangement. Each of these groups of TL-detectors was packed into a polystyrene matrix (see figure 7.3) for exposure, transportation and storage.

Figure 7.3. Two packages of TL dosemeters. 4 TLD-600 (upper row) and 4 TLD-700 (lower row) detectors in a polystyrene matrix (left) and an identical, closed and sealed package labelled for exposure at the HIMAC facility (right). A cm-scale is viewed as size reference.

7.5. The HTR-Method

It has long been known that the high temperature TL-emission of LiF detectors (i.e. the area above peak 5 of the glow curve) is dependent on radiation quality (143). Basically, it has been found that, for equal radiation doses, higher LET values up to 100 keV/µm result in a decrease in the sensitivity of the main peak 5 and an increase in the sensitivity of higher temperature peaks (144). These insights suggest a possibility to not only determine the absorbed dose from the TL glow curve, but also obtain information on radiation LET. This is of special interest for applications in radiation protection, since the LET is considered the essential physical parameter that may be directly linked to the relative biologic effectiveness of the corresponding radiation field (see section 2.1.4).

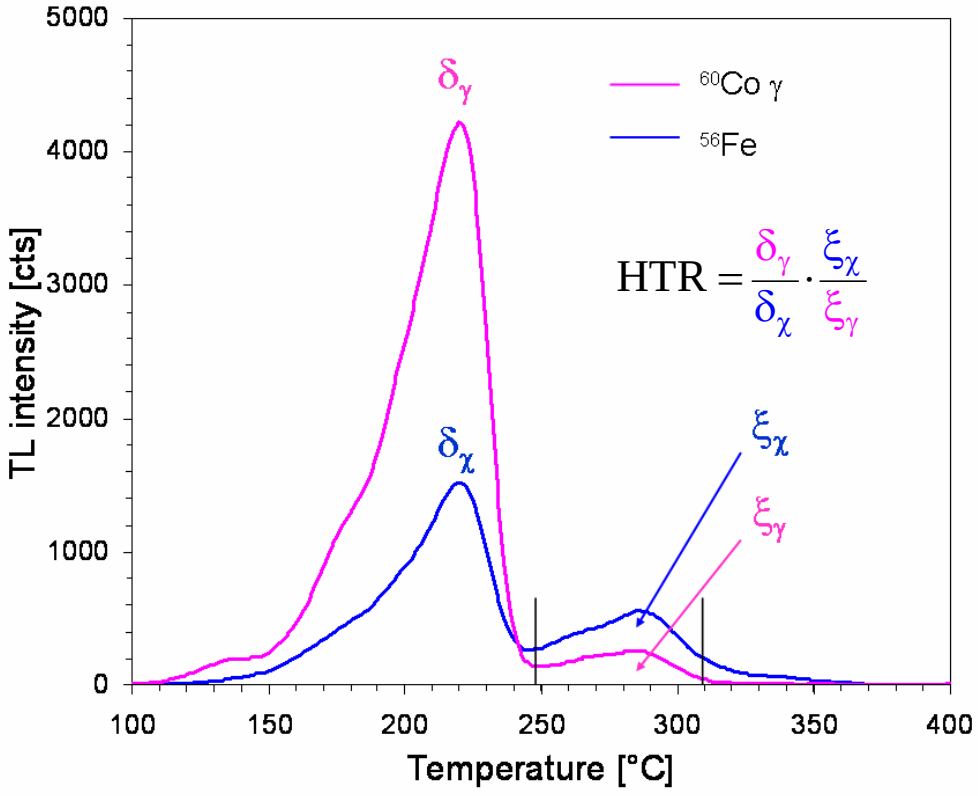

Figure 7.4. The High Temperature Ratio (HTR). Given glow curves correspond to the same TLD-700 chip (6.4×6.4×0.9 mm³) exposed to approximately 60 mGy of either ^{60}Co γ-radiation (γ) or ^{56}Fe (500 MeV/n) particles (χ).

The so-called High Temperature Ratio (HTR)-method, which has been developed at the Atomic Institute of the Austrian Universities, represents a sophisticated procedure of glow curve evaluation that allows for the determination of LET in addition to absorbed dose, thus providing the means for calculation of dose equivalent according to equation (2.6). The underlying principles as well as the practical realization of this method shall be outlined in the following:

According to (145), the HTR is defined for glow curves recorded from a LiF:Mg,Ti detector by

$$\mathrm{HTR} = \frac{\delta_\gamma}{\delta_\chi} \cdot \frac{\xi_\chi}{\xi_\gamma}, \tag{7.13}$$

where δ corresponds to the height of the main peak 5 and ξ to the integral over the high temperature region of the glow curve (from 248 to 310 °C, with the maximum of peak 5 at 220 °C), which essentially includes the peaks 6 and 7, accordingly (see figure 7.4 for illustration). The index γ indicates exposure to a γ-reference field, χ to a field of unknown composition.

Therefore, by normalization of glow curves to peak 5 height (as is accomplished by the first factor in equation (7.13)), which have been obtained after exposure of the same detector to a γ-radiation reference field as well as to various fields of interest, the HTR may be directly visualized for easy comparison (see figure 7.5).

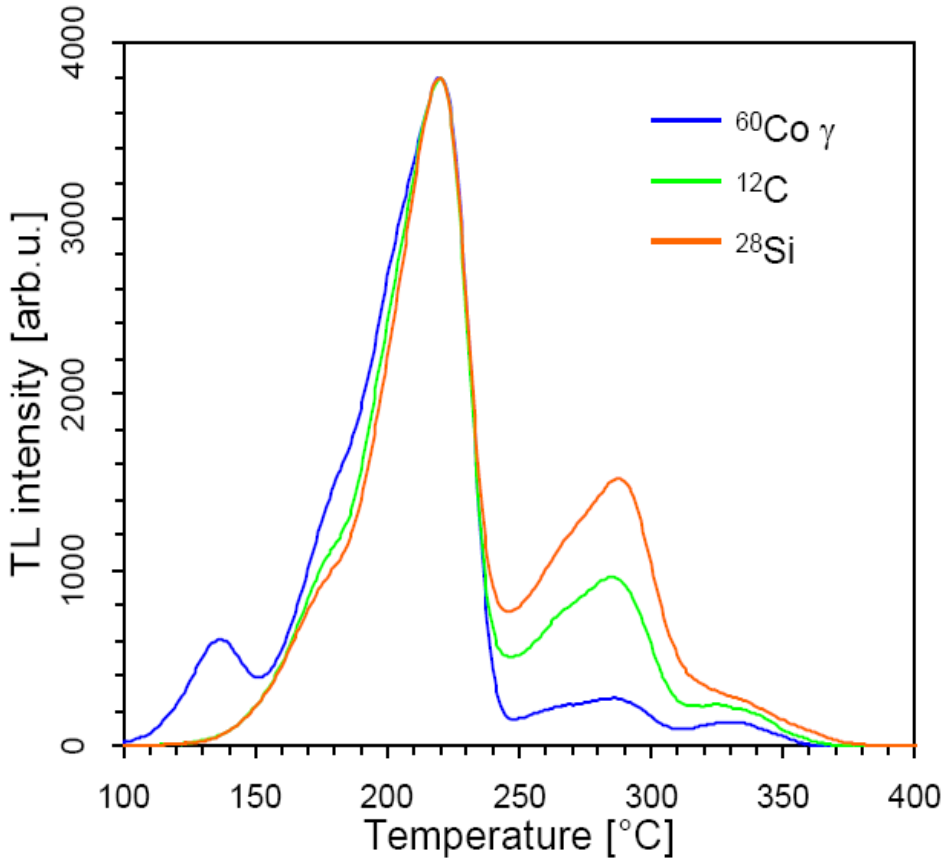

Figure 7.5. TLD-600 glow curves normalized to peak 5 maximum, which were obtained after exposure to γ-radiation, Carbon (with an LET of 13 keV/µm) and Silicon (100 keV/µm) particles. The LET dependence of the TL high temperature emission (248-310 °C) is clearly visible.

In recent years, a multitude of experiments have been performed that were aimed at gathering TL data on LiF detectors in order to gain profound insights on the dependence of TL-efficiency, glow curve structure and, thus, the HTR on radiation field parameters. In exposures at several ion accelerator facilities (most notably, at the Heavy Ion Medical Accelerator HIMAC of the National Institute of Radiological Sciences, Chiba, Japan) a wide range of particle species and LET values up to a few hundred keV/µm could be covered. Thereby, it has been found that TL-efficiency as indicated by the height of the main dosimetry peak 5 depends on particle species and LET (see figure 7.7), and that the LET of the incident radiation correlates with the HTR.

Furthermore, the HTR has been demonstrated to be independent of dose over at least two orders of magnitude (from 1 to 100 mGy, see figure 7.6). The generated data allowed for establishment of a HTR vs. LET calibration function (figure 7.6) for several TL detector types, among them TLD-600 and TLD-700. More exactly, LET, in this case, refers to the "effective" (or formerly: "averaged") LET in the detector volume. In mixed radiation fields (i.e. combined photon and particle fields, or incident particles of different species and LET values), all components and their corresponding LET values contribute to effective LET in accordance with their specific TL-efficiencies.

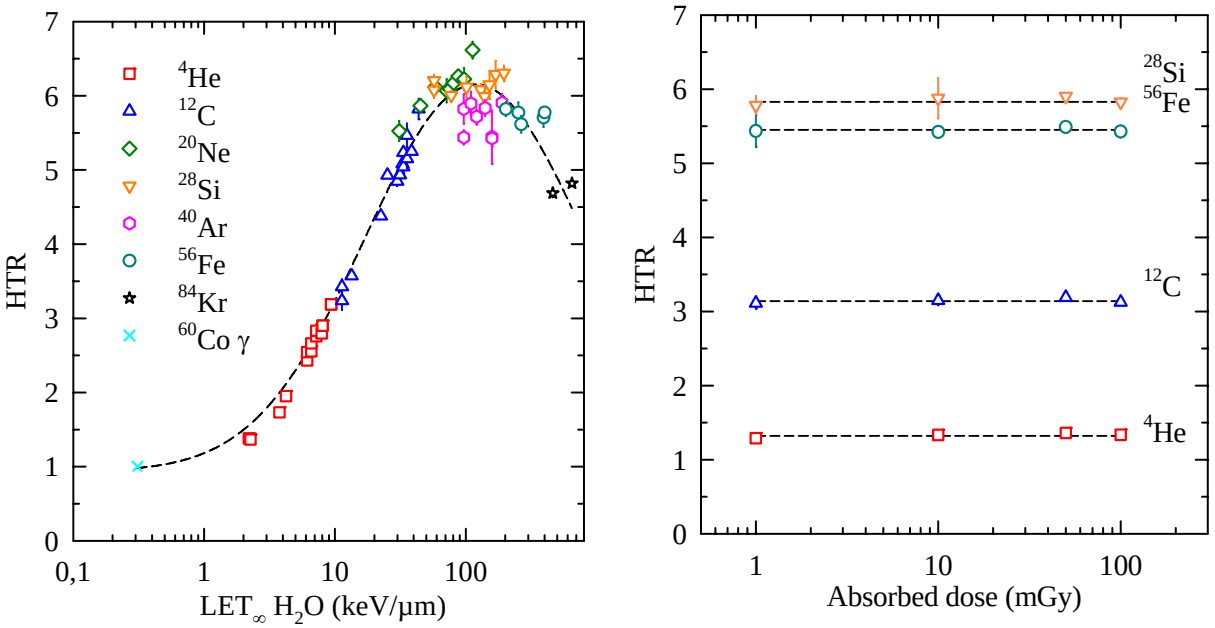

Figure 7.6. HTR vs. LET relationship (left) and demonstration of the linearity of the HTR with dose (right) for TLD-700 (adapted from 153).

Current HTR vs. LET (figure 7.6) and peak 5 efficiency vs. LET (figure 7.7) curves for TLD-700 detectors are given that have been published recently (153, 154, 155). Equivalent curves for TLD-600 dosemeters are supposedly very similar, as is backed up by all TL data gathered and evaluated until today (155). In principle, knowledge of these functional relationships allows for determination of absorbed dose and effective LET from TL glow curves with a low margin of error and thus, calculation of the dose equivalent H (according to equation (2.6)), the essential quantity for personal dosimetry. However, due

to intrinsic properties of LiF detectors such as a dependence of TL-intensity not only on LET, but also on particle species (as illustrated in figure 7.7) and a non-monotonous HTR vs. LET relationship (due to a decrease of HTR above approximately 100 keV/µm), precise determination of equivalent dose in unknown and mixed radiation fields still remains a difficult task.

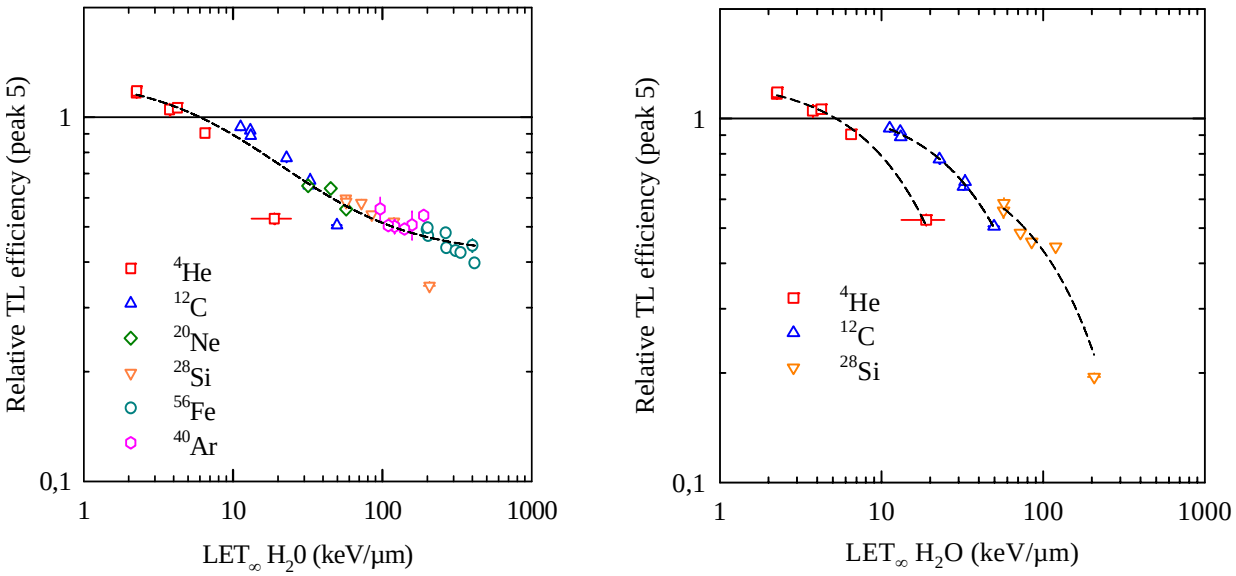

Figure 7.7. Different fit functions for efficiency of the main peak 5 in glow curves of TLD-700, independent from particle species (left, adapted from 153), and separate fits for ^{4}He, ^{12}C and ^{28}Si (right, adapted from 155). Different sets of TL data have been used, as is most obvious from the higher LET silicon results.

Strikingly, a surprising resemblance in the functionality of HTR(LET) and Q(LET) (see figure 7.6 and figure 2.1) suggests the possibility of correlating the HTR with Q or RBE values, eventually allowing for a direct and more effective determination of equivalent dose from a LiF TL glow curve without "taking the detour" via calculation of LET. Comparison of specific biologic effects with TL results, as is the topic of this thesis, represents an essential step towards achieving this ultimate goal.

8. Microbiological and Biochemical Methodology

This chapter is dedicated to the methods used in the radiobiological part of this thesis. The gathering of quantitative data on cellular signal transduction events as a final step requires a series of procedures ranging from cultivation of cells to radiation exposure and biochemical staining techniques. The different methods applied as well as materials and chemicals used shall be introduced in the following.

8.1. Cell Cultivation and Exposure Preparations

In the human body, fibroblasts are part of many types of tissues and organs and may therefore be found not only on the body surface, the skin, but also in various depths inside the human body. Thus, due to their abundance throughout a human-being, they are frequently used as a general model for normal human tissue. Furthermore, a large amount of knowledge has been generated on cellular signal transduction events in fibroblasts as a response to damage induced by radiation and other hazards. Therefore, human fibroblasts where selected as model cells for the radiobiologic experiments in the frame of this thesis.

Normal human foreskin fibroblasts of a low passage (i.e. cells that have yet only performed a small number of divisions in culture) have been kindly provided by the Children's Cancer Research Institute (CCRI) St. Anna, Vienna, Austria. They were cultured in a medium of RPMI 1640 (Sigma-Aldrich, B-2) supplemented with 10% foetal calf serum, 100 U/ml penicillin and 100 µg/ml streptomycin for prohibition of bacterial infection. For cultivation, the fibroblasts were kept in plastic culture flasks (Nunc GmbH & Co, B-4) of varying sizes: Generally, single-layered flasks with a growth area of 25 or 75 cm^2 were used, which were exchanged for triple-layered flasks with a total growth area of 500 cm^2 when large amounts of cells were needed. Cultivated cells were stored in an incubator at a temperature of 37 °C in a humidified mixture of 95% air and 5% CO_2, thus guaranteeing optimal growth conditions.

For clarification purposes, some basic properties of cultivated fibroblasts shall be outlined briefly: Firstly, fibroblasts are adherent cells, which means that they require attachment to a surface like collagen (in vivo) or plastic (in vitro) in order to form a layer of cells through ongoing division (in contrast to suspension cultures that consist of cells floating around in the culture medium). For this purpose, a level of medium is to be provided

above the cell layer that prevents drying and provides nutrients as well as growth factors, but still allows for supply with molecular oxygen through diffusion, which generally corresponds to a height of about 3 to 5 mm. Furthermore, fibroblasts do not grow to unlimited numbers, but are "density-inhibited", which corresponds to the fact that division of fibroblasts slows down in denser cultures and comes to a complete halt (i.e. all cells enter the G0 phase) when a complete cell monolayer has been formed, a status that is also referred to as "100% confluence". Additionally, fibroblasts are best seeded at a cell density of higher than 10 to 20% confluence to achieve fast and continuous growth. Since fibroblasts adhere to the culture flask through extracellular proteins, the protease Trypsin (Invitrogen, B-3) is commonly used to detach the cells from their substrate for harvesting or transfer to another container.

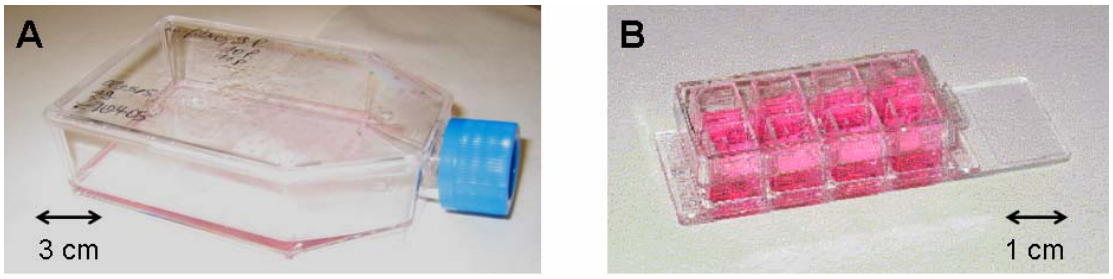

Figure 8.1. Cell culture containers: 75 cm² culture flasks (A) and 8-chamber slides (B). Referential size markers are indicated.

Approximately 48 hours before irradiation, fibroblasts were harvested from culture flasks and seeded into LabTek chamber slides (with 4 or 8 chambers, B-4). These types of cell culture containers are composed of a lower part, a slide made of Permanox™ developed for attachment of adherent cells, a set of caskets for containing the culture medium, which is glued onto the slide, and a loosely covering lid. The "chambered" part may be easily removed from the slide without residues, allowing for comfortable immuno-staining of the cells attached to the slide (see section 8.4) and microscopic visualization.

For all exposures, cells were selected to grow to about 60% confluence by appropriately choosing the concentration of seeded fibroblasts. The dilution factor was determined by counting of suspended cells with a standard counting chamber (hemacytometer) before seeding them into the chamber slides. Fibroblasts where stored in an incubator under the described conditions until a few minutes before irradiation.

8.2. Exposure to High-Energy Charged Particle Beams – the HIMAC Facility

Irradiation of cultivated cells with high energy charged particles has been performed at the Heavy Ion Medical Accelerator (HIMAC) facility of the National Institute of Radiological Sciences (NIRS), Chiba, Japan. This facility was constructed primarily for the

purpose of cancer treatment with high-energy carbon ions and protons as an alternative to conventional, photon-based radiotherapy. After its completion in 1993, the HIMAC has been successfully operated for use in clinical studies since 1994. More recently, clinical therapy has been expanded to treatment of hundreds of patients per year, having reached a total of 2800 treated patients as of March 2006 (147).

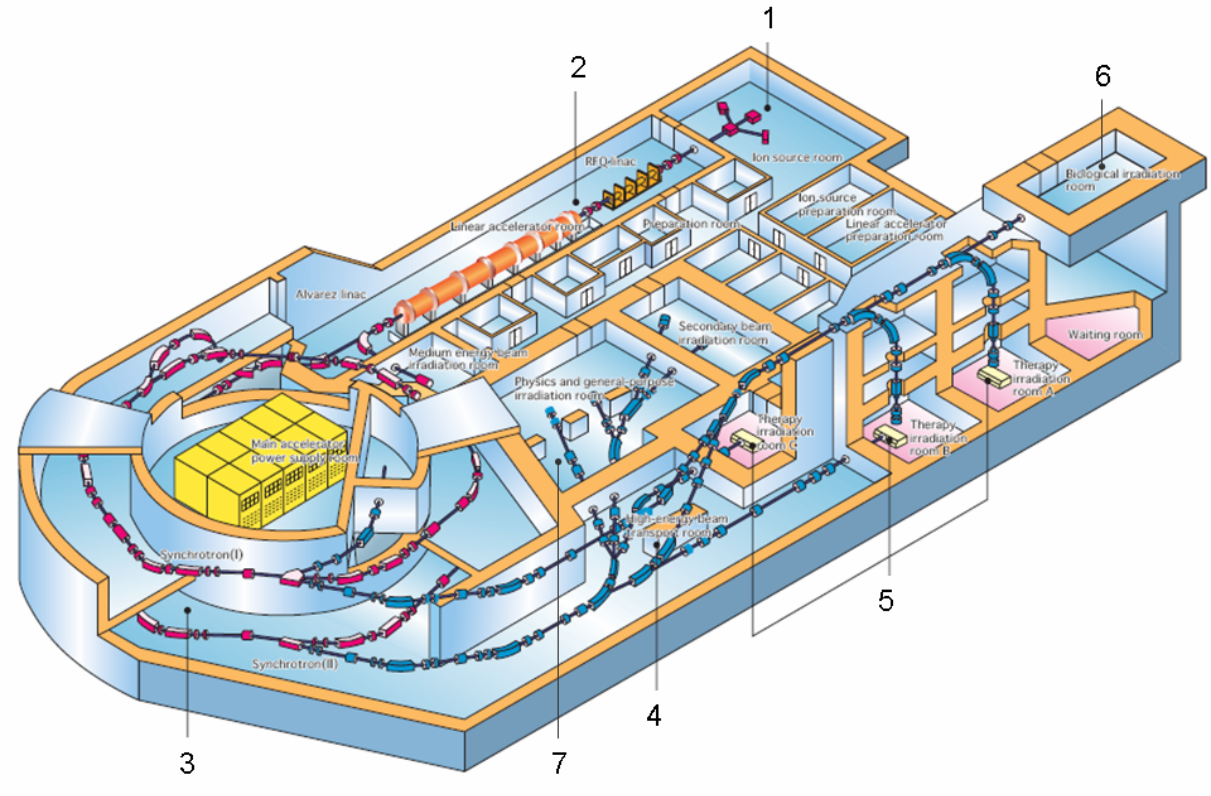

Figure 8.2. Cross-sectional view of the HIMAC building (adopted from 1, with slight modifications). Several essential compartments are indicated: 1 – ion source room, 2 – linear accelerators, 3 – synchrotron rings, 4 – high energy beam transport room, 5 – therapy rooms A, B, and C, 6 – biology exposure room, 7 – physics exposure room.

In the HIMAC facility, acceleration and delivery of charged particles is accomplished by application of the following means (see figure 8.2 for a schematic view): Ions, as provided by different ion sources, are pre-accelerated by two linear accelerators, where they reach energies up to 6 MeV/n (173). They are then stripped off their remaining electrons by passing through a thin Carbon foil (100 µg/cm²). After leaving the second linac, ions are injected into the synchrotron, which consists of an upper and a lower ring suited for parallel operation, where they can be accelerated to particle energies up to a maximum of 800 MeV/n. In the beam transport room, channelling of the particles to the desired exit location of the beam is achieved.

In routine operation, the HIMAC is employed for therapeutic purposes during daytime from Mondays to Fridays, and delivers proton and carbon beams to three therapy stations in an alternating manner. At night time and on weekends, the HIMAC beamline is

available for scientific studies that include various physical and radiobiological experiments. For this reason, the HIMAC building also contains separate exposure rooms suited for scientific exposures. One of them, the so-called "biology exposure room", is supplied with a broad and homogenous particle beam that has been widened to a diameter of 10 cm, and is connected to two laboratories that include a complete set of standard equipment for cell culture studies. Therefore, the HIMAC facility was found to be highly adequate for achieving the goals set for this thesis.

For foreign researchers, access to the HIMAC facility is limited. In order to be granted beam time at the HIMAC, submission of a project proposal is compulsory, which needs to be approved by the NIRS authorities after extensive evaluation. Therefore, in a combined effort, the Atomic Institute of the Austrian Universities and the Clinic for Radiotherapy and Radiobiology have formulated a proposal for radiobiological and dosimetric experiments, which was accepted in 2004. In three exposure series at HIMAC, each lasting for 3 to 4 weeks (see table 8.1), a large number of fibroblast samples and TLD-600 and TLD-700 were targeted with different types of ion beams, as will be described in chapter 10.1 in more detail.

Series	Timeframe
I	January – February 2005
II	June – July 2005
III	January – February 2006

Table 8.1: Exposure series at the NIRS-HIMAC facility.

In the biology exposure room of the HIMAC-facility, the particle beam is delivered to the exposure position in horizontal direction. At this exit location, the beam is highly uniform within a diameter of 10 cm, with rapidly decreasing intensity outside of this area (148). Several samples can be mounted on up to five sample holders that can be attached to a movable sleigh by insertion into sockets. This configuration allows for transportation of single samples into the particle beam via remote control (see figure 8.3), thus eliminating the need to enter the exposure room for exchange of every single sample. Furthermore, reduction of particle energies and, thus, an increase in particle LET up to the Bragg peak is achieved by use of so-called "binary filters" made of PMMA, which are available in varying thicknesses and may be moved into the beam line as absorbers in front of the sample holders. During exposure, correct sample positioning and binary filter insertion can be supervised on several surveillance monitors.

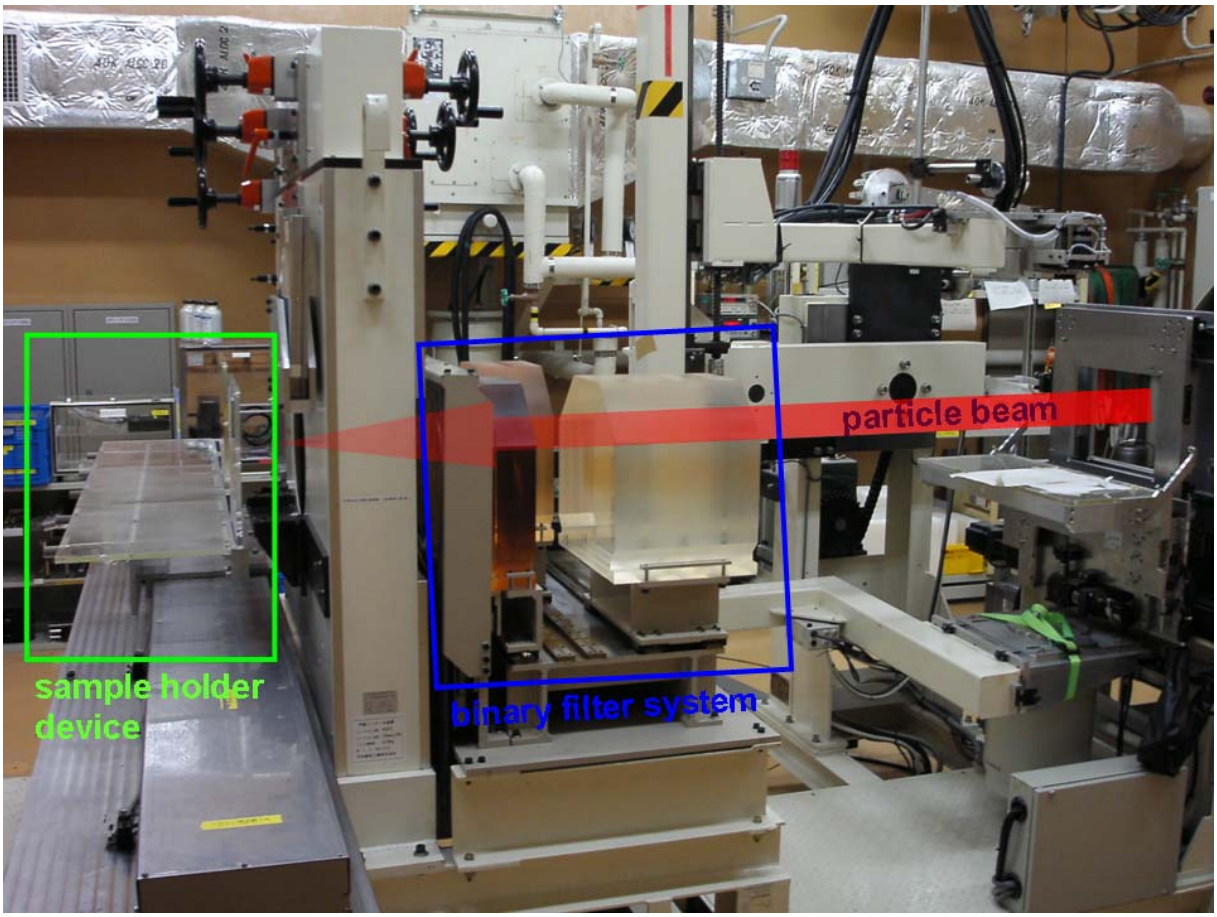

Figure 8.3. The beamline in the biology exposure room.

In order to achieve the specific irradiation patterns at the single cell level as given by the developed exposure plan (see section 10.3), the cell layers had to be set up in a perpendicular direction to the incident beam, corresponding to a vertical positioning of the chamber slides. For this purpose, it is necessary to fill up the chambers with culture medium and seal them with sticky tape in order to prevent drying of the cells during exposure. This was done immediately before sticking the sealed slides onto planar perspex sample holders (with up to two chamber slides per perspex plate, for optimal use of the fixed 10 cm beam diameter) in an upside-down position. Thus, upon inserting the sample holders into the sockets of the sleigh, the chamber slides were set up with the slides facing towards and the caskets facing away from the beam. Thereby, cell layers are positioned perpendicular to the horizontal beam as required, shielded only by the PermanoxTM slide of 1 mm thickness (see figure 8.4 for photographs and figure 8.5 for a schematic depiction of the exposure configuration).

Directly after irradiation of all mounted samples, chamber slides were removed from the sample holders. The usual amount of medium was restored as fast as possible and cells were left to recover in an incubator at 37 °C in a humidified mixture of 95% air and 5% CO_2 for incubation times between 20 minutes and three hours as chosen according to the experimental plan. On a side note, because of the rather short incubation period after

irradiation, loss of sample sterility due to sealing with unsterile standard sticky tape is not an issue.

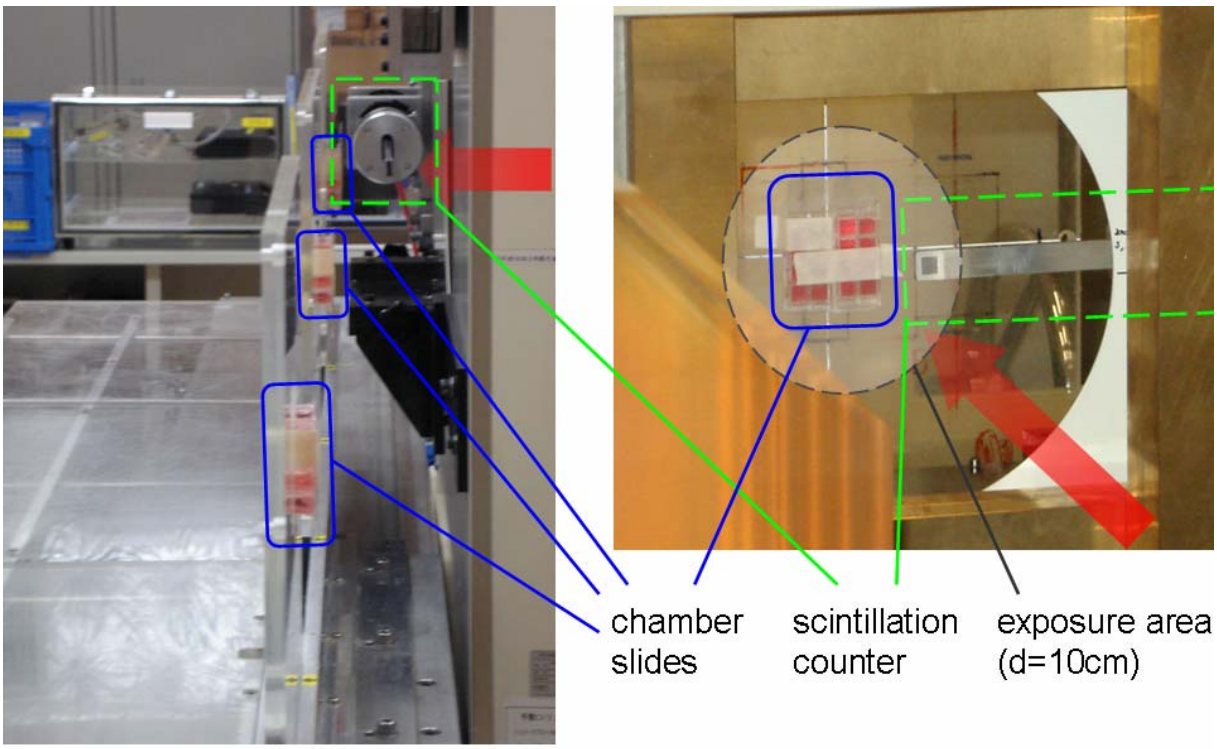

Figure 8.4. Exposure of cells in chamber slides to the HIMAC particle beam with parallel measurement of particle fluence with a scintillation counter, shown from two different angles. Beam directions are indicated with red arrows. Pairs of 8-chamber slides (blue) are mounted on three perspex sample holders. The estimated area of uniform beam intensity is indicated (corresponding to the sample plane) and contains both samples and the active detection area of the scintillation counter.

In every HIMAC exposure series, a sufficient number of control samples (approximately representing 20% of the total sample number) were prepared according to the same procedures as exposed cells, and mock-irradiated, including all essential steps such as filling of the chamber slides with culture medium, sealing, sticking them to sample holder perspex plates and setting them up in a vertical position for an amount of time comparable to usual exposure times.

For the majority of exposure parameters (i.e. particle species, fluence and binary filter thickness) selected for irradiation of cultivated cells, at least one package of TL-detectors was exposed under the same conditions, allowing for direct comparison of TL- and radiobiologic results. For this purpose, the detector packages were set up in a configuration similar to the cells in chamber slides and were thus mounted on the same perspex plates with the lid of the polystyrene matrix perpendicular to the incident particle beam.

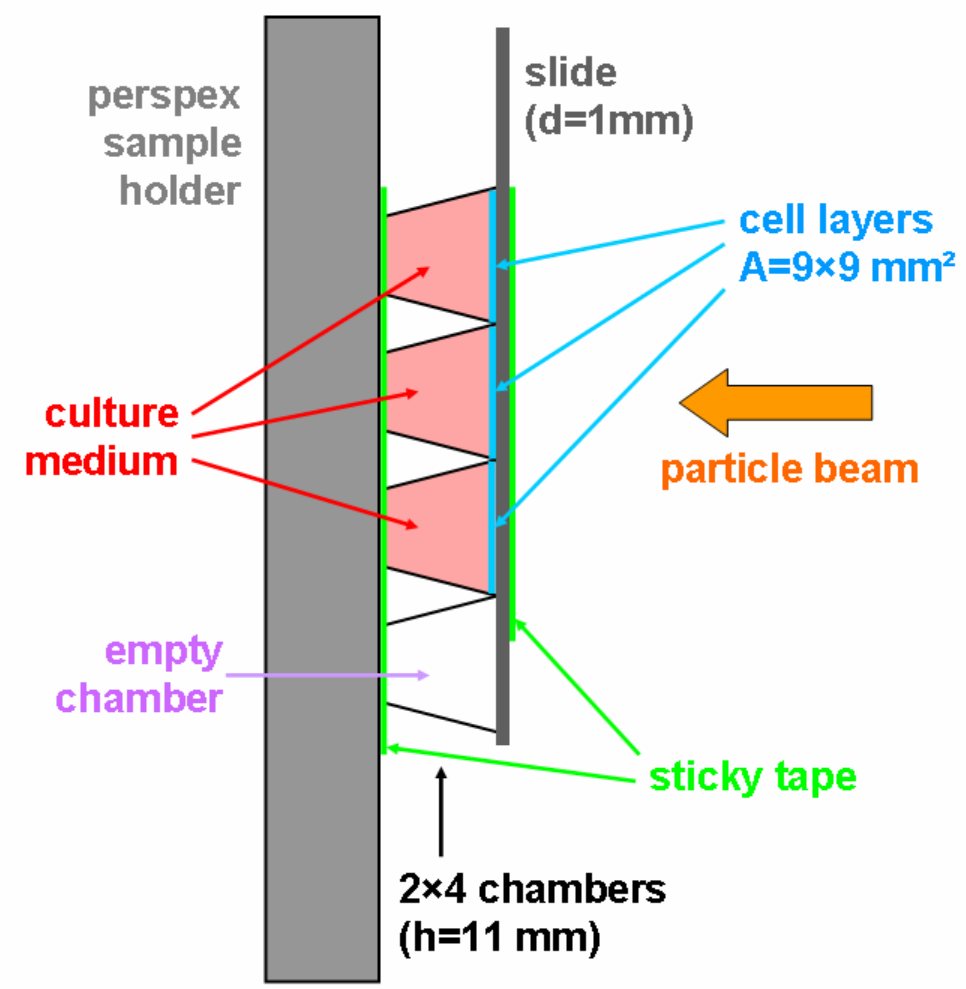

Figure 8.5. Configuration for exposure of an 8-chamber slide in the particle beam in side view. As indicated, the particles only need to traverse a Permanox™ slide of 1 mm thickness (plus one layer of sticky tape) before reaching the cells. For most exposed 8-chamber slides, the lower pair of chambers was kept empty, since this part of the slide cannot be observed properly with the used microscope system.

For most irradiations, low particle fluences below 10^5 ions/cm² were chosen. In these exposures, the number of particles was directly counted by means of different scintillation counters with active detection areas between 0.95 and 1.24 cm² (see figure 8.4), which were used depending on particle type. For higher particle fluences, readings of the integrated "Main Monitor" ionisation chamber were utilized for dose determination. Furthermore, for some exposures, binary filters of varying thickness were applied for LET variation. In these cases, particle LET was calculated with the SRIM/TRIM Monte Carlo code (149). For this purpose, it has to be paid attention to the fact that particle energies are lower at the beam exit in the HIMAC biology exposure room than nominal energies due to matter (such as detectors) in the beam line. Results and parameters of SRIM/TRIM calculations can be found in chapter 10.2.

Generally, the HIMAC delivers accelerated particles in "packages", the so-called spills, which are separated from each other by a short pause of a few seconds. The number of ions per spill is adjustable and has proven to be highly stable throughout several minutes of exposure, and its absolute variation decreases with decreasing spill size. With this in mind, the beam intensity (i.e. the number of ions per spill) was selected according to the following considerations: A low number of ions per spill allows for a more precise delivery of an equal number ions to a series of samples that are all intended to receive the same nominal number of ions. On the other hand, exposure times are to be kept short in order to minimize any further detrimental effects on exposed cells (as well as mock-irradiated control samples) due to a prolonged stay outside the incubator and due to being covered by a higher than ideal level of culture medium. For these reasons, spill sizes where chosen as low as reasonable while keeping exposure times per sample position well below 10 minutes. Furthermore, only up to three of five sample positions were used, thus limiting the stay of cell containers inside the biology exposure room to a maximum of half an hour, which was rarely reached. For by far the greatest percentage of fibroblast samples, the whole procedure (starting with taking the chamber slides out of the incubator, followed by preparation and set-up, exposure, restoring of the optimal level of medium, and ending with their return to the incubator) lasted between 20 and 25 minutes.

8.3. Exposures to low-LET photon radiation

The main experimental part of this thesis is dedicated to exposures of cultivated cells and TL detectors to high-energy charged particles. However, on several occasions, irradiation experiments using X- and γ-rays have also been performed for a variety of purposes: Before the first HIMAC run in January 2005, all biochemical procedures have been established, tested, and optimized utilizing cultivated cells irradiated with X-rays. This includes observation of all events in the cellular response to ionizing radiation that were also scheduled to be investigated after exposure to high-energy charged particles, and the development of basic concepts for quantitative sample analysis, even though these had to be greatly refined and adjusted according to the eventual staining patterns observed in cells exposed to low fluences of high-LET particles. In most X-ray experiments, comparably large doses between 1 and 10 Gy have been delivered to the samples, which result in a strong cellular radiation response, thus facilitating initial testing and refining of different biochemical methods as well as comparing results with data from literature, where a large amount of information on cellular signal transduction events caused by several Gy of low-LET radiation is available.

All X-ray exposures were performed using the Philips RT-100 (kV) X-ray device of the Clinic for Radiotherapy and Radiobiology. Doses were calculated according to the supplied documentation. The characteristics of this device are routinely checked by the physics department of the clinic in regular inspection intervals. Regarding the corresponding exposure configuration, cells in 25 cm² or 75 cm² flasks and chamber slides

were irradiated with X-rays from below, thus avoiding the need to fill up cell containers with culture medium as well as additional supporting measures.

Furthermore, as has already been mentioned, all calibration exposures of TL detectors have been performed at the Co-60 γ-source of the Clinic for Radiotherapy and Radiobiology. Additionally, a smaller number of fibroblast samples have also been irradiated with low doses of γ-radiation (below 200 mGy) for estimation of methodical limitations under most ideal conditions, and also for qualitative comparison with high-LET results. In these experiments, fibroblasts were seeded into chamber slides and an experimental procedure similar to exposures at the HIMAC facility was chosen, which includes filling up and sealing of the chamber slides and positioning of the cell layers in a vertical direction, perpendicular to the incident, quasi-horizontal γ-radiation, followed by restoration of the initial level of culture medium and incubation. The duration of the complete process was comparable to HIMAC experiments. Mock-irradiation of control samples was performed accordingly.

8.4. Immunocytochemistry

8.4.1. Basic Concept

In general, immunocytochemical staining techniques are procedures suited for detection of one or more targets ("antigens") of interest in single cells and cell layers. These methods are based on the exploitation of highly specific antibody-antigen interactions. Basically, most common protocols for immunocytochemical staining rely on the application of a "primary" antibody that reacts specifically with a defined "epitope" of the target antigen, i.e. particular sequences of amino acids and/or the corresponding three-dimensional configuration of a protein. Antibodies are generated in different kinds of animals and are therefore distinguished according to their origin (e.g. goat, rabbit, mouse, donkey etc.) For each species, antibodies contain typical, constant regions that may, again, serve as targets for further immunological reactions. Therefore, primary antibodies that have successfully bound to the corresponding antigen of interest (or in a non-specific manner, to other proteins, as is not desirable, but cannot be avoided completely) may be detected by a secondary antibody designed against these species-specific sequences. Thus, in this secondary antibody-antigen reaction, the primary antibody acts as antigen, effectively. Secondary antibodies are either labelled with a fluorescent dye (with the procedure then being referred to as "immunofluorescence") that may be visualized by excitation with light of a suitable wavelength or, alternatively, may be conjugated to an enzyme (e.g. peroxidase) that is able to catalyze a colour reaction. This two-step mechanism (illustrated in figure 8.6) is preferable to (less common) direct staining with dye-labelled or enzyme-conjugated primary antibodies, since binding of several secondary antibodies to one primary antibody may lead to signal amplification, and an overall much lower number of labelled antibodies are needed (essentially, one per target species compared to one for

each target protein), especially when several parallel stainings of more than one target protein with differently coloured dyes (dual-, triple-staining, etc.) are to be performed for reasons of direct comparison.

In both cases of labelling, the signal is retained at the binding sites of primary antibodies and, thus, confined to the location of the target of interest. Therefore, immunostaining techniques are capable of providing information not only on concentration of the antigen in the cell or tissue, as is corresponding to staining intensity, but also on the local antigen distribution, which is indicated by distribution patterns of the colour signal.

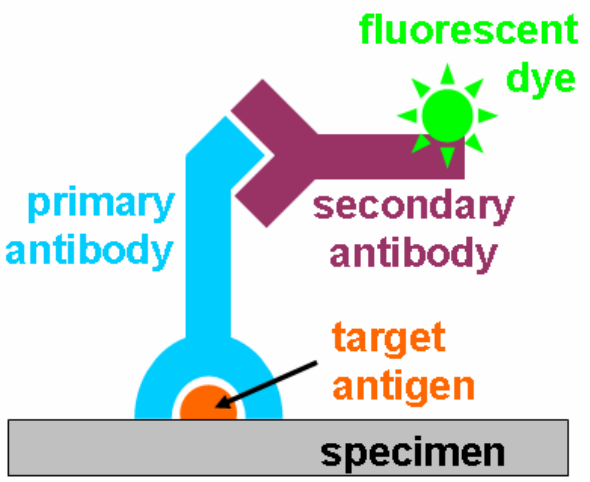

Figure 8.6. Detection of specific targets via two-step immunofluorescence staining.

In principle, detection and visualization of target proteins that are localized inside cells or even their nuclei, and conservation of stained layers for extensive microscopic observation requires several methodical steps: After incubation, the culture medium is removed. Then, the cell layer is "fixated" by use of chemical means, which are suited to abruptly end all biochemical processes while still preserving cellular structure and composition for further investigation, as is achieved by displacing the water contained in the cells and cross-linking of the protein content. Consecutively, cells are incubated with a solution containing the primary antibody, allowing for its binding to the antigen of interest. Afterwards, the secondary antibody is applied for detection and staining of the target-bound primary antibody. Counter-staining of cellular parts with different chromogens may be performed for more efficient interpretation of staining patterns. Finally, stained samples are set up for microscopic analysis and storage by application of a small amount of so-called mounting medium and covering with thin cover glasses.

Obviously, there are certain parameters that limit resolution and detection limits of immunostaining methods. Firstly, suboptimal binding specificity of both primary and secondary antibodies results in unspecific background staining, which may be observed as a low-intensity colour signal that is homogenously distributed across the stained sample, or as localized, dot- or spot-like artefacts. Furthermore, access of the antibody to its target

may be pro- or inhibited, leading to a decrease in detection efficiency. For these reasons, further measures may be taken as part of the staining procedure, which are aimed at facilitating antibody access (by chemical permeabilization of membranes that enclose cells and cellular compartments), or at reducing unspecific background staining by optimization of antibody concentration, additives, and blocking of unspecific targets prior to antibody application.

8.4.2. Long-term Fixation of Cell Layers on Chamber Slides

Common fixation techniques for cultivated cells on microscope slides or cover glasses are generally designed for immediate follow-up of staining procedures and not for extended storage of samples months before further treatment. However, within the experimental plan of this thesis, storage of fixed cell layers up to several months was unavoidable, since all exposures of cells to the HIMAC particle beam had to be fitted into three, rather short periods of a few weeks. Thereby, large numbers of samples were generated in each run, which could by no means be processed and analyzed immediately, as is intended according to standard immunocytochemical methodology. Furthermore, especially for the first series, it was preferable to regularly adapt experimental procedures, analysis techniques and the focus on signalling events of interest to the continuously gathered insights, thus supporting the need for the possibility to adequately conserve samples over longer periods.

For this purpose, several methods have been tested according to the following requirements: Storage of fixed samples may exceed several months without significant reduction in signal strength and increase of artefacts and unspecific background when immunostaining is performed. Additionally, since all samples exposed to the HIMAC particle beam have to be fixated at the NIRS, transportation of fixed samples, either in dried state or in liquid-filled containers, from Japan to Austria, where further sample processing was scheduled, should be viable, preferably without the need of cooling.

Finally, the following fixation protocol for cells in chamber slides has proven adequate, and was used throughout all experiments at HIMAC and after X-ray and γ-exposure at the Clinic for Radiotherapy and Radiobiology:

- Culture medium and polystyrene caskets are removed.
- Slides are briefly rinsed twice with cooled (4 °C) phosphate buffered saline (PBS).
- Slides are kept in fresh paraformaldehyde (4%, in PBS) for 10 minutes at room temperature.
- Slides are put into increasing concentrations of ethanol (70% and 96%, for 3 to 5 minutes each) at room temperature.

- Slides are finally placed in sealed containers filled up with absolute (>99.5%) ethanol and stored in this condition at or close to room temperature until further use.

Using this protocol, sample transportation from Japan to Austria was realised in ethanol as fixative solution. Fluctuation of temperature during transport has not been found to lead to alterations in the immunostaining signal and was similar for all samples exposed at the HIMAC facility.

8.4.3. Immunofluorescence Staining

As has already been covered in section 8.4.3, immunofluorescence staining (IF) is a technique for visualization of cellular targets with fluorescent dyes by use of target specific antibodies. In this thesis, a two-step method has been used for all IF stainings: Target proteins are recognised and bound by a primary antibody, which then may be detected with a dye-conjugated secondary antibody. Furthermore, additional dyes are available for specific staining of cellular parts such as DNA or the cytoplasm, which may be applied for geometric reference or, in case of DNA-staining, to gain information on cell cycle and account for micro-nucleated as well as apoptotic cells. Moreover, by using primary antibodies originating from different species and secondary antibodies coupled to dyes that may be distinguished by optical filtering of the fluorescent signal, two (or, rarely, three) different targets may be staining in a parallel manner, allowing for direct comparison.

In detail, IF staining of cells on chamber slides, which have been stored in ethanol, has been achieved according to the following protocol, which represents an adaptation of procedures suggested by the manufacturers of primary antibodies and online sources for biochemical methodology (156):

- Slides are taken from absolute (>99.5%) ethanol and put into decreasing concentrations of ethanol (96% and 70%, for 3 to 5 minutes each) at room temperature.
- Slides are rinsed with a solution of 0.01% Triton X-100 in deionised water for 3 to 5 minutes.
- For the purpose of membrane permeabilization, slides are put into PBS supplemented with 1% Triton X-100 for 10 minutes, which is followed by 5 minutes in 0.01% Triton in PBS, both at room temperature.
- Slides are incubated with blocking buffer, a solution of 1% bovine serum albumin (BSA) in 0.01% Triton/PBS, for 30 minutes at room temperature for blocking of unspecific binding sites of antibodies.
- Slides are incubated with primary antibodies diluted in blocking buffer over night in a cooled (4 °C) environment.

- Slides are rinsed with washing buffer (0.01% Triton in PBS) 3 times for 5 minutes each at room temperature.
- Slides are incubated with secondary antibodies diluted in blocking buffer for one hour at room temperature.
- Slides are rinsed with washing buffer (0.01% Triton in PBS) 2 times for 5 minutes each at room temperature.
- For DNA-counterstaining, slides are incubated with approximately 10 mg/ml of HOECHST 33342 (B-2) in washing buffer for 5 minutes at room temperature.
- Slides are mounted for fluorescence microscopy using FluorSave™ reagent (Calbiochem, B-5), an aqueous mounting medium, and standard cover glasses of varying sizes, and are allowed to dry for half an hour.
- For further storage, samples are kept at 4 °C in a dark environment in order to minimize photo-bleaching.

Dilution factors for primary and secondary antibodies vary for each antibody and have been optimized for good signal-to-background ratio and for equal signal strength in case of dual-stainings, as has been achieved in pre-experiments with X-ray irradiated cultures.

8.4.4. Immunocytochemical Staining with Signal Amplification

In principle, this method is very similar to IF, with the exception that secondary antibodies are not conjugated with fluorescent dyes, but eventually catalyse a colour reaction. The corresponding staining patterns may be observed with conventional light microscopy. Counter-staining can also be performed, but may often not be necessary, since subcellular parts of many cell types (such as fibroblasts) are easily recognised in phase contrast, and was therefore neglected for this thesis.

For practical purposes, several reagent kits are commercially available that rely on a two- or three-step cascade of reactions for amplification of the colour signal, which may therefore be initialized by very few bound primary antibodies and thus lead to comparably low detection thresholds. One of these kits, the polymer-based Lab Vision UltraVision LP Detection System combined with the Lab Vision AEC-chromogen single solution (Lab Vision Corporation, B-6), has been used on various occasions throughout this thesis because of its advantageous properties – intense red colour combined with effectively no unspecific background signal due to kit reactions (but, of course, possibly due to primary antibody binding). This system includes a blocking solution termed “Ultra V Block”, a so-called “Primary Antibody Enhancer” and the “HRP Polymer” (which, both together, substitute the secondary antibody in standard immunocytochemical protocols), and the AEC chromogen. It is suited for detection of primary antibodies of mouse and rabbit origin. No further information as to the composition of the kit reagents, which are all supplied in drop dispensers, is available.

Staining of chamber slides stored in ethanol has been performed according to the protocol enclosed by the manufacturer, which was slightly adapted to the specific needs. All washing steps are performed at room temperature.

- Slides are taken from absolute (>99.5%) ethanol and put into decreasing concentrations of ethanol (96% and 70%) followed by 0.01% Triton X-100 in deionised water (for 3 to 5 minutes each) at room temperature.
- For membrane permeabilization, slides are put into 1% Triton X-100 in Tris buffered saline (TBS) for 10 minutes, which is followed by 5 minutes in washing buffer (0.01% Triton in TBS), both at room temperature.
- Slides are incubated with the "Ultra V Block" solution for 5 minutes at room temperature.
- Slides are incubated with primary antibodies diluted in washing buffer over night in a cooled (4 °C) environment.
- Slides are rinsed with washing buffer 4 times for 3 minutes each.
- Slides are incubated with the "Primary Antibody Enhancer" solution for 20 minutes at room temperature.
- Slides are rinsed with washing buffer 4 times for 3 minutes each.
- Slides are incubated with the "HRP Polymer" for 30 minutes at room temperature.
- Slides are rinsed with washing buffer 4 times for 3 minutes each.
- Slides are incubated with the "AEC Single Solution" at room temperature for up to 10 minutes, depending on staining intensity.
- Slides are rinsed with 0.01% Triton in de-ionized water 4 times for 3 minutes each.
- Slides are mounted for light microscopy using an aqueous mounting medium – either Vision Mount (Lab Vision Corporation, B-6) or Aquatex (Merck KGaA, B-14) – and standard cover glasses of varying sizes, and are allowed to dry for half an hour.
- Within three days after staining, digital pictures of samples are taken (see section 9.2) to avoid any influence on results due to degradation of the colour signal.

In contrast to IF, this protocol is not suited for parallel staining of multiple proteins of interest, but provides greater sensitivity for detection of some targets. Dilution factors for primary antibodies vary for each antibody and have been optimized for good signal-to-background ratio in X-ray experiments.

8.4.5. Primary and Secondary Antibodies

This section gives an overview of all primary and fluorescent-labelled secondary antibodies used in the course of this thesis for staining of samples exposed to high-energy

charged particle beams. In pre-experiments with X-ray irradiated cells, a larger number of antibodies were tested for selection of those with most preferable properties. Primary antibodies were purchased from different manufacturers, including Rockland Immunochemicals (B-7), Cell Signaling Technologies (B-8), and Upstate Cell Signalling Solutions (B-9). The following table 8.2 contains a listing of these selected primary antibodies and provide information as to target, origin, type and manufacturer.

Product	Type	Origin	Manufacturer
Anti-phospho-Histone H2AX (Ser139)	monoclonal IgG_1, clone JBW301	mouse	Upstate
Anti-phospho-Histone H2AX (Ser139)	polyclonal IgG	rabbit	Upstate
Anti-phospho-ATM (Ser1981)	polyclonal IgG	rabbit	Rockland Inc.
Anti-phospho-DNA PKcs (Thr2609)	polyclonal IgG	rabbit	Rockland Inc.
Anti-phospho-Chk2 (Thr68)	polyclonal IgG	rabbit	Cell Signaling

Table 8.2: Primary antibodies

All fluorescent-labelled secondary antibodies were purchased from Jackson ImmunoResearch (B-10). In detail, three different types, all of donkey origin, were used in order to achieve the required distinction of primary targets in dual-stainings, which correspond to the following products: Anti-rabbit IgG (H+L) Cy™2-conjugated, Anti-rabbit IgG (H+L) Rhodamine Red™-X-conjugated, Anti-mouse IgG (H+L) Rhodamine Red™-X-conjugated.

8.5. Sample Transportation

Since it was decided to use cells of the same origin (i.e. descendants of normal human skin fibroblasts originally provided by the CCRI) for exposures at the HIMAC facility, some of these cells had to be transferred to the NIRS. There, the large amounts of fibroblasts needed for irradiation experiments were accumulated via further cultivation on-site.

Cell transportation was realised in the following manner: At the Clinic for Radiotherapy and Radiobiology, large numbers of fibroblasts were cultivated in three-layered flasks with a growth area of 500 cm^2 each. These containers were filled up completely with culture medium (approximately 750 ml per flask) and sealed immediately before departure. For transportation by plane, the flasks were wrapped in pulp in order to avoid breakage and for absorption of medium in case of leakage. Immediately upon their arrival at the NIRS, the optimal level of medium was restored, and the cells were allowed to recover in an incubator at usual conditions (humidified, 37 °C, 5% CO_2). Overall, the

duration for cell transfer (i.e. from taking cells out of the incubator at the Clinic for Radiotherapy and Radiobiology until insertion into the one at the NIRS) amounts to around 24 hours. This procedure was adequately tested before the first cell transfer, and was found to yield excellent cell survival in all HIMAC runs.

As has already been mentioned above, transport of irradiated and fixed samples back to Austria was performed with the chamber slides placed in sealed plastic jars (10 slides per jar) filled with absolute ethanol. Upon arrival, these containers were immediately checked for leaks.

8.6. Other Methods

On a few occasions, especially during testing of primary antibodies, "western blotting" has been performed for the purpose of comparison with literature data and own immunocytochemical stainings. This method relies on gel electrophoresis of denatured cellular proteins, thus separating them by mass, which are then transferred to a membrane. Afterwards, by application of specific primary and secondary antibodies, targets of interest may be detected via an immuno- and dye-reaction similar to immunostaining of a cell layer (see section 8.4.1). Overall, due to the much lower sensitivity of this method compared to immunostaining of fixed cell layers and due to the loss of important structural information, western blotting has not been used for evaluation of samples exposed to high-energy charged particles.

9. Quantitative Analysis of Biological Samples

9.1. Basic Concepts of Staining Analysis and Quantification

As has been elaborated so far, particular cellular signal transduction events, as indicated by phosphorylation of involved proteins, are investigated and observed by staining fibroblasts cultures, which have been exposed to radiation of different quality and dose, using immunocytochemical methods. Thus, quantitative or qualitative differences in biologic effects due to differing exposure parameters, which represent the main topic of this thesis, are visualized via these cell immuno-stainings, or, more precisely, are contained within the characteristics of sample stainings, which display different colour intensities and signal patterns. It was therefore both a major experimental and analytical challenge to transform these differences into "measurable" quantities, which allow for quantitative comparison between samples as well as with dosimetric results and, furthermore, represent "sensible" parameters from the viewpoint of radiation protection and risk assessment.

In general, all of the radiation induced events of interest for this thesis may be easily observed in immuno-stainings after high radiation doses above 1 Gy, and in a wide time window from at least one until several hours after exposure, as has been demonstrated in test experiments with X-rays before the first HIMAC irradiation series. In some cases (mainly for pChk2, pChk1, pp53), radiation exposure results in a strong and homogeneous, overall increase in staining intensity of the nuclei, whereas in others (pATM, pDNA-PKcs, γH2AX), a high number of clearly defined foci may be observed in nuclei of exposed cells. As an illustrative example, figure 9.1 shows ATM phosphorylation (Ser1981) three hours after exposure to 5 Gy of X-rays.

However, at low radiation doses, the situation is much more difficult. Basically, a lesser extent of cellular damage is induced, which either may lead to a less pronounced signal transduction response or to no effects at all (see section 4.5 for further thoughts on this matter). For immuno-staining of these phospho-proteins that have been listed above, this translates into a lesser or no increase in staining intensity or in the number of detectable foci. However, the margin of error for immuno-staining is rather high due to a varying, unspecific background, staining artefacts, and slight differences in sample handling that

cannot be totally avoided. Thus, a low but nevertheless existent cellular response may easily lie below the detection threshold. It is therefore imperative to precisely adhere to biochemical protocols and develop standardized analysis procedures in order to minimize errors and lower detection limits, which must also include a highly similar treatment of control samples (see also section 8.2). Furthermore, in order to allow for good inter-comparison between samples exposed to different radiation fields, all samples gathered in one HIMAC run have been divided in groups of 4 to 15 slides. All slides of one group were stained simultaneously, thereby achieving maximal coherence in handling and staining conditions within each group. Apart from that, it needs to be stressed that in principle, immunocytochemical staining methods are still considered to be one of, if not the most precise tools for visualization of low dose effects, as has been demonstrated by detection of an increase in γH2AX foci formation via immunofluorescence after X-ray doses as low as 1 mGy (157).

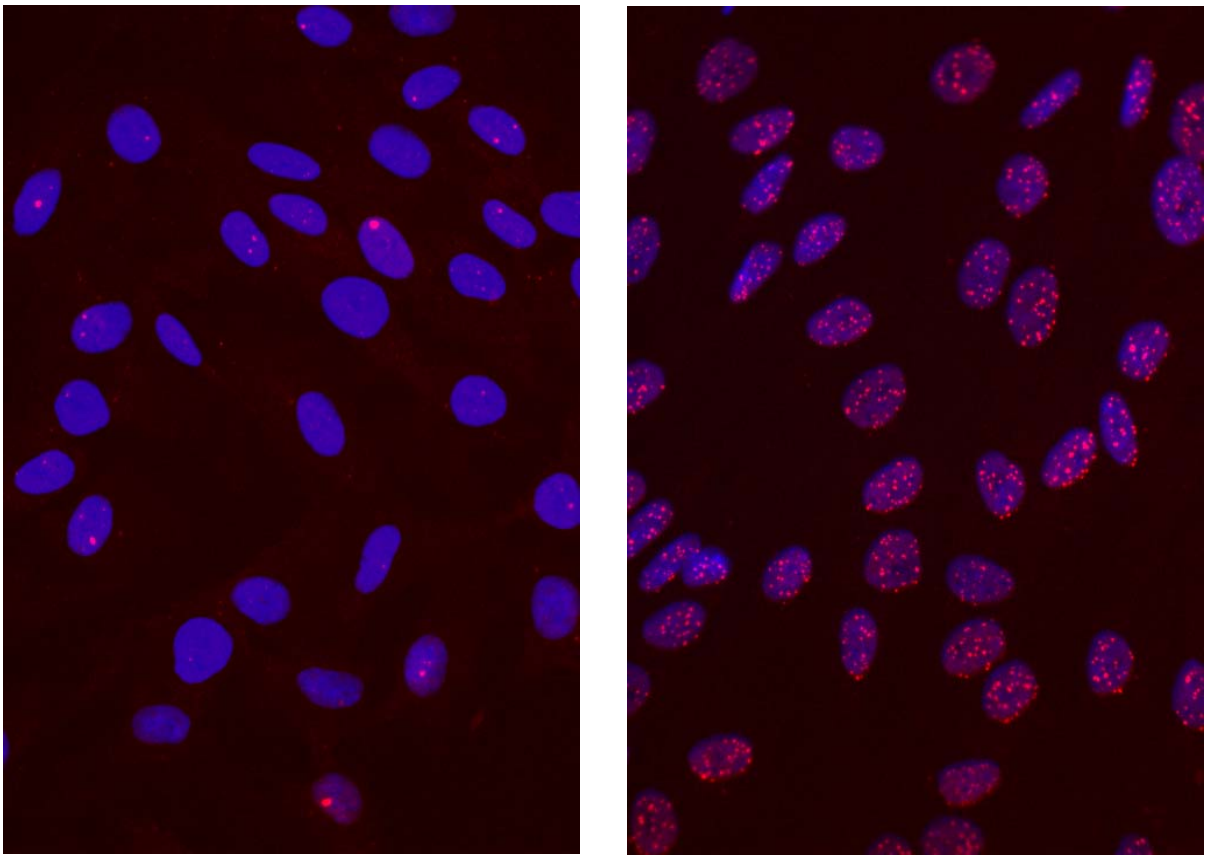

Figure 9.1. ATM phosphorylation (Ser1981) in human fibroblasts after 5 Gy of X-rays (right), compared to a mock-irradiated control sample (left). Nuclei are indicated blue, pATM is stained red. Phosphorylated ATM is found accumulated in a large number of foci at sites of DNA damage.

Basically, analysis of immuno-stained samples has been performed in three parts: Firstly, digital pictures of stained samples need to be acquired and transferred to a personal computer. These images are then processed according to standardized procedures, and are thereby prepared for quantitative analysis as a final step. In the following sections, the involved processes and devices shall be elaborated in detail.

9.2. Picture Acquisition

Immuno-stained and mounted layers of fibroblasts were visualized with an Olympus BH2-RFCA microscope (B-11), which is suited for light and fluorescence microscopy and equipped with oil-immersion lenses of different magnification. Excitation of fluorescent samples is achieved by use of a UV-lamp and a set of combined optical filters for selective excitation and observation of different common fluorescent dyes.

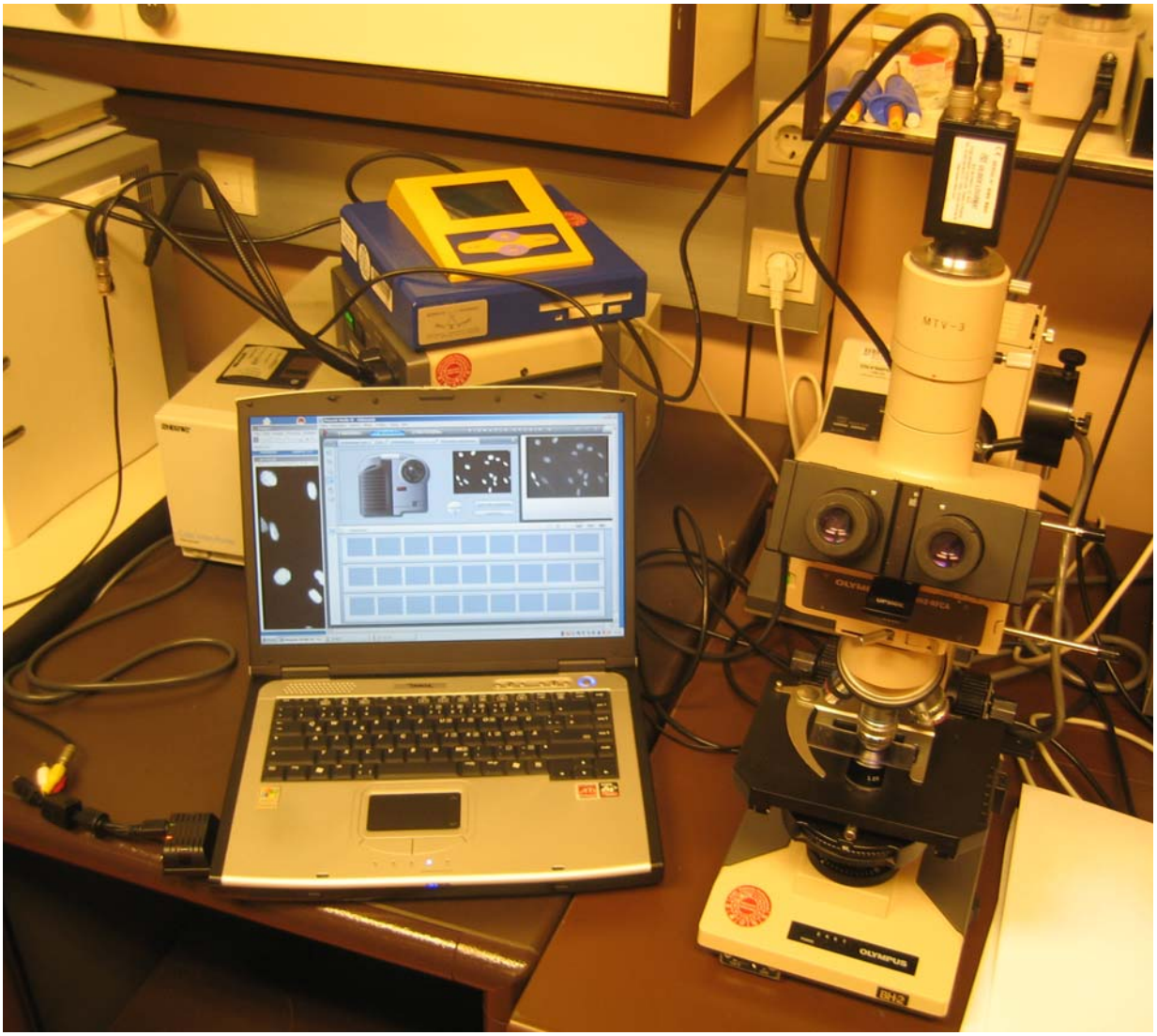

Figure 9.2. The image acquisition system (Clinic for Radiotherapy and Radiobiology, Vienna Medical University).

The microscope is connected to a highly sensitive Vilber Lourmat CCD-Camera (B-12), which is capable of picking up 8-bit (values from 0 to 255) greyscale images with a resolution of 752×575 pixel. The camera signal is transmitted to a standard TV-card (Pinnacle Systems, B-13) of PCMCIA format, which is inserted into a PC notebook operated with Microsoft Windows XP. Images are taken and stored in *.tif file format using the snapshot-tool of the Pinnacle Studio 9 application that is included in the TV-

card software package for operation of its video management functions. Figure 9.2 shows a photograph of the completely assembled devices for digital image acquisition.

As has been described in the last section, samples were grouped for staining procedures. From each such group, all images were taken within two days in order to minimize any influence of photo bleaching or colour degradation on results. Furthermore, in case of dual or triple immunofluorescence stainings, two or three pictures were taken for each field of view, corresponding to the used dyes of different colour. As a basic rule, between 9 and 15 fields of view were stored as digital images per sample and stained protein.

9.3. Personal Computer Based Image Processing and Analysis

The following section is intended to provide insights on principles, methods and algorithms applied in processing and analysis of cell images and the combined evaluation of results gathered in this manner. For the purpose of clarity, the basic concepts that have been explained so far shall be summed up briefly:

- Cultivated and exposed cells are stained via immunocytochemical methods
- For signal-enhanced staining with AEC red, phospho-proteins of interest are observed one by one without counter-staining. In immunofluorescence, DNA and, therefore, nuclei are counter-stained as reference, and one or two target proteins are stained with different dyes for direct comparison of geometric patterns.
- Slides are grouped for staining, allowing for direct comparison within one group due to minimal differences in handling and, therefore, background effects.
- Digital greyscale images of 9 to 15 fields of view per sample and stained target are taken.
- Staining characteristics differ depending on the target phospho-protein, which may be homogenously distributed across the nucleus, or found accumulated in foci.

Keeping these principles in mind, it is obvious that different procedures for picture processing and analysis had to be developed in correspondence with staining patterns and staining methods, which will be described separately later on. However, these applied procedures share some similarities: Firstly, all are based on the ImageJ software (v1.35p, 158), a java-based public domain application developed by the National Institutes of Health, USA. This programme features various tools for image manipulation and analysis, and includes a multitude of plug-ins that have been specifically designed for evaluation of microbiological images. Therefore, ImageJ and its predecessor NIH Image for Apple Macintosh may be considered a standard for analysis of microbiological images.

Furthermore, since thousands of pictures had to be assessed by repeating identical or, at least, similar steps for file sorting in Microsoft Windows Explorer, image processing as well as analysis in ImageJ, and data transfer to Microsoft Excel data sheets, a solution needed to be developed that was capable of facilitating and accelerating these highly time-consuming and tedious procedures. As a first approach, extensive use of the ImageJ macro function allowed for contraction of several different steps to single commands. However, ImageJ macros are not designed for automating processes that include more than one programme, such as data transfer to Excel, and do not allow for halts in execution, as are intended and needed for user interaction such as manual input of intensity thresholds, selection of regions of interest, intermediate file re-sorting or change of filenames, during runtime.

AutoIt (v3.1.1, 159) is a freeware general-purpose scripting language that includes most common concepts of a programming language such as different types of variables, arrays, loops, conditional clauses, functions, string manipulation and more. It is specifically designed for automating the Microsoft Windows Graphical User Interface (GUI) and, therefore, especially excels at simulating keystrokes and mouse commands, window handling, and direct interaction with Microsoft Windows controls. Because of its advantageous properties, scripts written in this language are routinely applied by IT technicians for repetitive tasks that require interaction with the Microsoft Windows GUI, such as installing and updating applications on a large number of PCs, and general maintenance procedures.

AutoIt is also ideally suited for the task at hand, the automation of processing and analysis of image sets as well as data and file management. Therefore, for all extensively applied analysis procedures, an AutoIt script has been designed correspondingly, which performs the intended tasks while requiring as little as possible user interaction. Thereby, the overall analysis speed is greatly increased, and is essentially limited by the computing power of the PC. Furthermore, due to the fully automated execution of most repetitive tasks, possible sources for human errors, as are rather likely due to the tiresome nature of these procedures if done by hand, are largely eliminated. It needs to be stressed that the large amount of data could not have been gathered by a single experimenter in the given timeframe without use of PC and script-based automation.

As has already been anticipated above, different target proteins of interest and staining procedures require different analysis techniques. Thus, these different procedures are discussed below in separate sections.

9.4. Determination of the Amount of Phospho-Chk2 (Thr68) per Cell

In response to DNA damage, the cell cycle regulating Chk2 protein is phosphorylated at threonine 68 (see section 5.7). Phosphorylated Chk2 is mainly found homogenously distributed across the nucleus, while only a smaller part of total pChk2 is accumulated at sites of DNA damage. Thus, when cells are immuno-stained for pChk2 (thr68), the overall staining intensity of the nuclei is an indicator for Chk2 activity, thus representing a cellular quantity of interest, with the staining patterns or intranuclear distribution of pChk2 playing a minor role. Basically, the amount of stain may be considered proportional to the amount of the target protein present (neglecting unspecific staining that may be corrected for during image processing), as long as intrinsic methodical limits of the immuno-staining process are not reached, such as an extremely high local concentration of the target that may lead to a local shortage of antibodies or chromogen during staining, resulting in below-linear behavior of staining intensity.

Following van der Laak et al (160), the intensity $I_t(\lambda)$of light of wavelength λ transmitted through a specimen is given by

$$I_t(\lambda) = I_0(\lambda) \cdot \exp\left[-A \cdot c(\lambda)\right], \tag{9.1}$$

where $I_0(\lambda)$ corresponds to the light of wavelength λ entering the specimen, A is the amount of stain per unit area of the specimen, and $c(\lambda)$ is a factor that describes the wavelength dependent absorption characteristics of a specific dye.

The absorbance is defined as the common logarithm of the quotient of the incident divided by the transmitted light intensity. In quantitative microscopy, this quantity is also commonly referred to as “optical density” (OD), even though, strictly speaking, optical density is the absorbance per unit length. Following this custom, the optical density, or absorbance, $OD(\lambda)$ can be written as

$$OD(\lambda) = \log_{10}\left[\frac{I_o(\lambda)}{I_t(\lambda)}\right] = k \cdot A \cdot c(\lambda), \tag{9.2}$$

where the constant factor k equals $\log_{10}(e)$. As has been elaborated above, the amount of stain A present in a specific part of the specimen is proportional to the amount of the target protein in the same volume. Therefore, equation (9.2) indicates that the local optical density is a measure for the amount of protein at that position.

In the following, the concept of OD-measurement for determination of the concentration and the amount of the target protein shall be assessed on the basis of sample characteristics and the configuration of the image acquisition system used in this thesis.

Samples are single layers of fibroblasts, which are to be described as very flat cells covering an area of a few hundred μm² each with a thickness of only two to three μm, as has been visualized by application of confocal microscopy. Thus, for simple model descriptions, the nucleus of a fibroblast may be described by a very flat cylinder as a good approximation, which is embedded in two – even thinner – layers of cytoplasm above and below.

Now, the functional relationship given by equation (9.1) shall be adapted to the used system for image acquisition as describe above, thus accounting for characteristic properties of the device for detecting the light intensities. Furthermore, as a specimen, a layer of cells immunocytochemically stained for pChk2 (thr68) shall be considered, which is traversed by a parallel beam of light that is incident on the layer in perpendicular direction and is eventually detected by a greyscale CCD camera. Generally, neglecting deviations from detector linearity with light intensity due to detection limits or saturation effects for lowest and high light intensities beyond the linear range of the CCD element, the camera output signal I_{grey} of each pixel is given by

$$I_{grey} = \int_0^\infty S(\lambda) \cdot I'_0(\lambda) \cdot \exp\left[-A \cdot c(\lambda)\right] d\lambda , \tag{9.3}$$

where $S(\lambda)$ is the wavelength dependent sensitivity of the camera. Ideally, $S(\lambda)$ would be constant for all (optical) wavelengths emitted by the light source for illumination of the specimen. Furthermore, $I_0(\lambda)$ has been replaced with $I'_0(\lambda)$, which represents the light intensity transmitted through an unstained specimen of equal configuration (or an unstained part of a stained sample), thus accounting for the slight decrease in light intensity upon traversing a specimen even in the absence of stain. Therefore, the output signal $I_{0,grey}$ of a pixel corresponding to an unstained area with $A = 0$ may be written as

$$I_{0,grey} = \int_0^\infty S(\lambda) \cdot I'_0(\lambda) d\lambda . \tag{9.4}$$

In case of optimal staining of pChk2, where no unspecific background is present, an output signal of $I_{0,grey}$ is detected in all but the nuclear areas, since the cytoplasm, which contains practically no pChk2, appears transparent. In analogy to equation (9.2), the integral optical density $\overline{OD}$, which is independent of wavelength and based on quantities measured with the CCD camera, is given by

$$\overline{OD} = \log_{10}\left(\frac{I_{0,grey}}{I_{grey}}\right). \tag{9.5}$$

Without any assumptions as to the functional dependence of $S(\lambda)$, $I_0(\lambda)$ or $c(\lambda)$, this expression cannot be simplified further. However, as can easily be seen, when $c(\lambda)$ is a

constant value c' for all wavelengths detected by the CCD element, the integral optical density $\overline{OD}$ amounts to

$$\overline{OD} = k \cdot A \cdot c' \tag{9.6}$$

in a manner similar to equation (9.2). Thus, for dye absorption characteristics independent of wavelength, which essentially correspond to a grey staining colour, the integral optical density $\overline{OD}$ is directly proportional to the concentration of the target antigen. Obviously, equation (9.6) is only a crude approximation of a real immuno-stained sample, with its applicability depending on the dye and the degree of staining specificity. Nevertheless, as has been elucidated above, the general method of measuring optical density may be exploited for direct comparison of antigen concentrations as indicated by colour staining of varying intensity, and has been covered and applied in many studies (e.g. 160), using different methods for "read-out" of stained samples. However, it needs to be stressed that due to intrinsic uncertainties in the staining process, this method is to be considered semi-quantitative, thus posing limits to comparison of results gained by different working groups due to application of different biochemical protocols and read-out procedures.

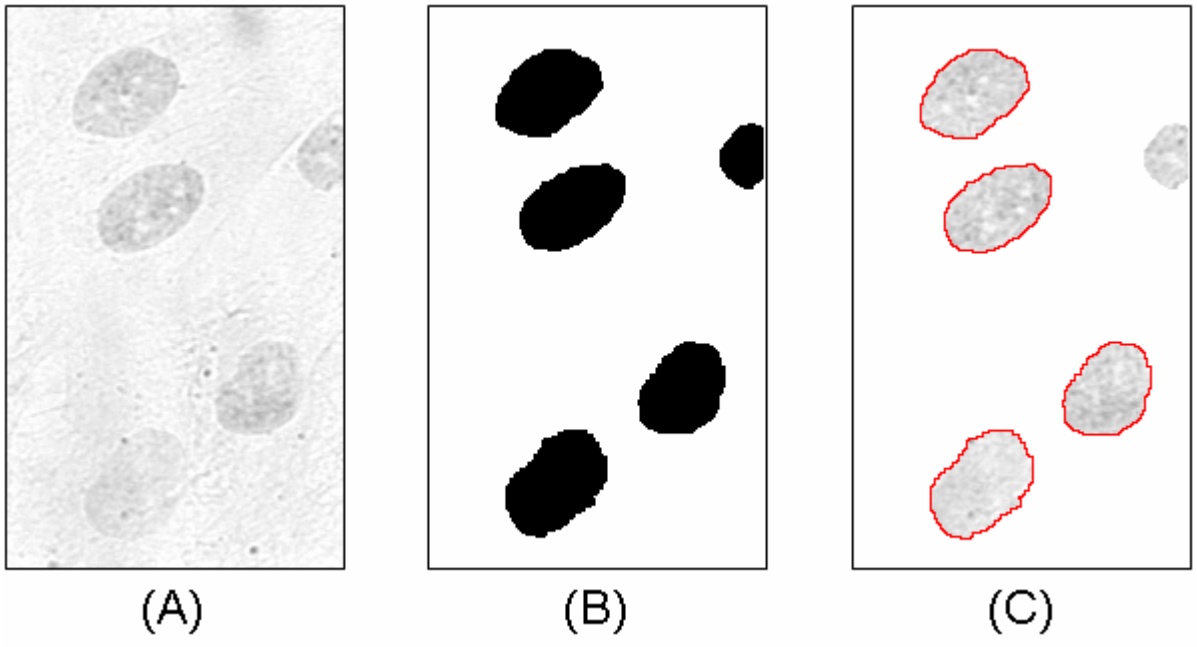

Figure 9.3. Steps in image processing for pChk2 quantification. From an image that has already undergone background homogenization (A), a black-and-white template for nuclei (B) is generated that is used for definition of areas of interest (C, marked red), for each of which A_{total} is then determined. Images correspond to a fibroblast sample that has been exposed to 7.3×10^4 cm^{-2} ^{28}Si (490 MeV/u) particles and immunostained for pChk2 (thr68) using AEC red.

The practical evaluation of a digital image from a sample stained for pChk2 is performed in several steps that are incorporated into an AutoIt script as described above: Firstly, the

image is processed with the ImageJ "Pseudo Flat Field" plug-in, which "flattens" the background, thus correcting for inhomogeneous sample illumination. From this corrected image, a histogram (number of pixels vs. greyscale value) is obtained. The maximum of this histogram indicates the most frequent grey value of background pixels, and thus corresponds to $I_{0,grey}$.

Then, by automated application of a variety of image processing "tricks" (including background subtraction, adjustment of minimum and maximum grey values, hole-filling and other algorithms for black-and-white images, and even manual editing if necessary, especially for very weakly stained cells due to low concentrations of pChk2) a black-and-white template is generated that allows for direct selection and marking of single nuclei as areas of interest. Thus, for every nucleus a measure for the total amount of pChk2, A_{total}, is calculated by summing up the integral optical densities of all pixels in the respective area of interest,

$$A_{total} = \sum_{k=1}^{K} \overline{OD_k}\,, \tag{9.7}$$

where k represents the pixel index and K the total number of pixels corresponding to the particular nucleus.

Even though this method is not fully suited for absolute quantification of the concentration or the amount of target antigen in a cell, the detection system must still fulfil a few requirements in order to guarantee consistent semi-quantitative results. First of all, it needs to be considered that the CCD element essentially maps all "real" light intensities on discrete grey values from 0 to 255. Thus, obviously, the real detector output signal unavoidably deviates from the theoretical detector output function as given in equation (9.3), since only integer output values are allowed for each pixel and all light intensities above a certain threshold will be mapped on 255. However, this does not pose a problem, as long as all realistically occurring light intensities (due to various degrees of staining intensity) and their corresponding output values adhere to a linear relationship within an acceptable margin of error. The validity of this requirement is best tested with a configuration similar to the actual measurement situation, and therefore, with a real sample. For this purpose, the following procedure has been applied:

A number of N pairs of nuclei shall be considered, with each pair being observed under identical illumination conditions. Assuming a constant value of c', the detector signal output for each pixel should be given by

$$I_{n,1/2} = I_{0,n} \cdot \exp\left(-A_{n,1/2} \cdot c'\right) \tag{9.8}$$

in accordance with equation (9.3), with n as the pair index and 1 or 2 indicating the two paired nuclei. Thus, the average output signal per pixel $\overline{I_{n,1/2}}$ for each nucleus may be written as

$$\overline{I_{n,1/2}} = \frac{\sum_{P_{n,1/2}} I_{p,n,1/2}}{P_{n,1/2}} = I_{0,n} \cdot \exp\left(-\overline{A_{n,1/2}} \cdot c'\right) \tag{9.9}$$

with $P_{n,1/2}$ as the number of pixels in the nucleus, p as the pixel index, and $\overline{A_{n,1/2}}$ as the "averaged" staining concentration attributed to the nucleus. The N pairs are chosen so that

$$\frac{\overline{I_{n,2}}}{\overline{I_{n,1}}} = \exp\left[\left(\overline{A_{n,1}} - \overline{A_{n,2}}\right) \cdot c'\right] = \exp\left(\Delta A \cdot c'\right) \tag{9.10}$$

with ΔA being constant for all pairs, which essentially means that each pair of nuclei differs by the same amount of dye.

In the last relation, equation (9.10), the quotient on the left side represents a measurable quantity, which is to be found constant for all N pairs, if the applied image acquisition process transforms the corresponding light intensities into greyscale values in a sufficiently linear manner as required. So far, the characteristics of the N pairs of nuclei have only been defined by the right expression in equation (9.10) and according to the initial declaration that each pair has been observed under identical illumination, but no further details have been provided as to their origin. However, since equation (9.10) is independent of $I_{0,n}$ and, therefore, the incident light intensity, an arbitrary number of such pairs may be easily generated by observation of two differently stained nuclei in the same field of view for varying illumination intensities.

For practical realisation, instead of pairs, a field of view containing three nuclei (with intense, medium and light staining, numbered from 1 to 3) in close proximity to each other has been selected. Digital images have been acquired for five different incident light intensities, thereby covering more than the complete range of greyscale values expected during standard quantitative evaluation, which is almost exclusively limited to values of I_t>100. For all images the quotients $\overline{I_{n,2}}/\overline{I_{n,1}}$ and $\overline{I_{n,3}}/\overline{I_{n,2}}$ have been calculated in an analogous way to equation (9.10) and compared. The gathered data is illustrated in figure 9.4 and demonstrates that, within reasonable approximation and under usual image acquisition conditions, identical results may be obtained independent of the intensity of the transmitted light, thus supporting the applicability of this method of OD determination for comparative quantification of the amount of staining.

On a side note, this procedure also directly elucidates that for the applied experimental protocol, OD results are largely independent of the selected light intensity for specimen

illumination. Due to intrinsic limits in stability and precision in tuning of the light source integrated into the used microscope, this insight has greatly facilitated and accelerated image acquisition, since time-consuming and continuous determination of background grey values and illumination readjustments could be neglected.

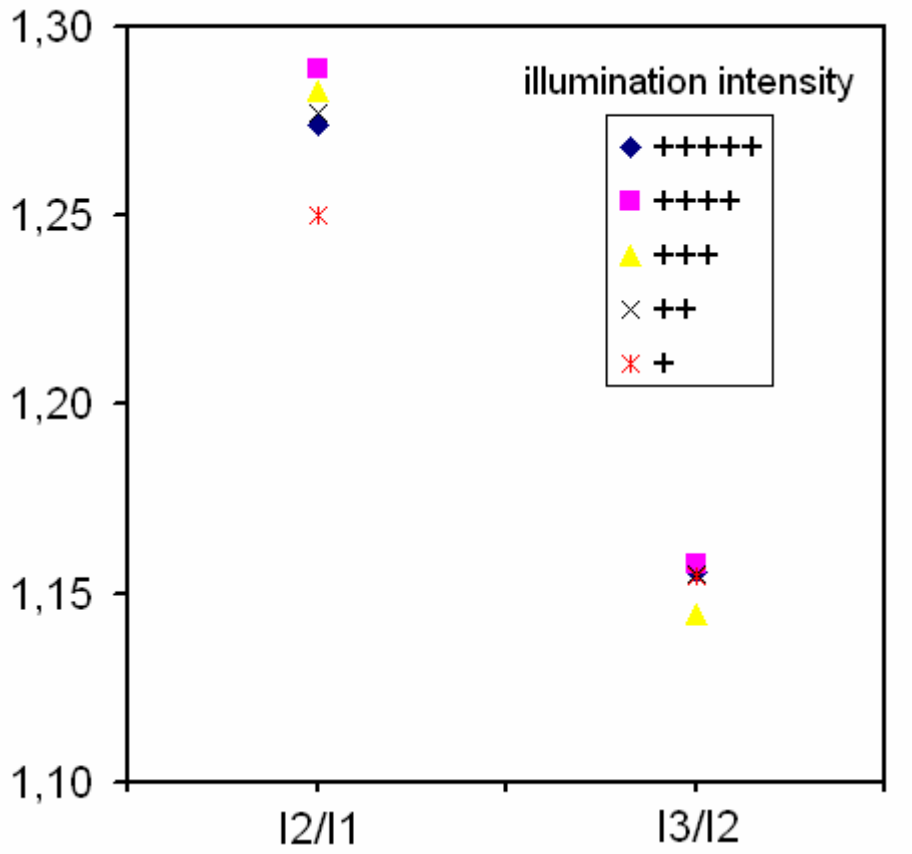

Figure 9.4. Quotients of averaged CCD output signals $\overline{I_{n,2}}/\overline{I_{n,1}}$ *and* $\overline{I_{n,3}}/\overline{I_{n,2}}$ *as obtained by observation of three nuclei under various illumination conditions (more + indicate higher light intensities). Good consistency of data is found for all ranges of greyscale values. Only the value for* $\overline{I_{n,2}}/\overline{I_{n,1}}$ *corresponding to the higher stained nuclei observed under the lowest illumination level (red, left) is found slightly off the rest of the group, indicating a deviation from detector linearity in the lowest part of the scale (*I_t*<80), which is practically never reached under normal staining evaluation conditions due to higher light intensities used and mostly lower dye concentrations encountered.*

As a final conclusion, the application of the described optical density based evaluation procedure to a sufficient number of nuclei allows for determination of the mean value as well as a distribution function for A_{total} for every sample. However, as has been outlined in section 9.1, direct comparison of these parameters between different samples is only advisable within the same staining series. For combination of data originating from different staining series, adequate correction factors are to be derived.

9.5. γH2AX (Ser139) in Hit and Bystander Cells

In a chromatin region of 1-2 megabases length surrounding a DNA DSB, the core histone H2AX is phosphorylated at serine 139 (see section 5.9). Thus, irradiated samples that have been immuno-stained for γH2AX (ser139) exhibit distinct foci, which mark the presence of DSBs. As has been demonstrated (95), the number of γH2AX foci correlates well with the number of DSBs. Therefore, immuno-staining of γH2AX (ser139) may be considered an ideal tool for quantification of radiation-induced DNA damage.

At low doses in the mGy range, only few DSBs are caused. Correspondingly, a lot of cells may show no γH2AX-foci at all, whereas in others one up to a few foci may be observed. For exposure to high-LET charged particles, cells with nuclear particle traversals are likely to experience DSBs and can therefore be expected to show γH2AX foci. Cells with no direct particle hits either remain undamaged, exhibit a bystander response or suffer from endogenous DNA damage. Therefore, for low doses of ionizing radiation, the most straightforward indicator for the extent of the overall cellular damage is to determine the fraction of cells with DSBs compared to cells without. As a next step, the percentage of damaged cells above the level of a corresponding control sample can be interpreted as caused by radiation exposure.

For exclusive assessment of phosphorylated H2AX, immunocytochemical staining with Labvision reagents for signal amplification has been found to be advantageous. For distinction of cells with and without γH2AX foci, all images of a staining series are subjected to background correction and contrast enhancement in ImageJ, using identical sets of processing parameters. Then, all images are scored by a human observer in a blinded fashion, i.e. all images are numbered in a random manner before evaluation. Only after blinded scoring of one staining series is fully completed, the gathered results are attributed to the corresponding sample.

Sample examination in a blinded fashion is generally considered an adequate tool for quantitative evaluation of biological specimens, which, as is quite obvious, requires a certain amount of practise and experience from the experimenter in order to gain reproducible results. As a drawback, direct comparison of quantitative data gathered by different observers is to be done very carefully and may expose limited agreement due to the subjective nature of this evaluation process.

9.6. Evaluation of Foci Sizes for Phospho-ATM (Ser1981) and Phospho-DNA-PKcs (Ser2609)

Both ATM and DNA-PKcs are phosphorylated in response to DNA DSBs, thereby mediating their activity in DSB repair and cell cycle control (see sections 5.2 to 5.8). Furthermore, the phosphorylated forms of both kinases (ATM at serine 1981, DNA-PKcs

at threonine 2609) have been found to stay predominantly located at sites of DSBs over an extended period of time, starting several minutes after DSB incidence and lasting for at least several hours.

In section 2.3, it has been elaborated that high-energy charged particles initially deposit most of their energy along their tracks in volumes that are small compared to cells, a nucleus or even other organelles. Correspondingly, most of the induced DNA damage such as DSBs is found concentrated along these tracks, as has been demonstrated recently (161). Therefore, after visualization via immuno-fluorescence, it is to be expected that pATM (ser1981) and pDNA-PKcs (thr2609) are also found localized along these tracks. Thus, when observing exposed and stained cell layers from the direction of the incident beam, as is performed within the frame of this work, these phosphorylated kinases will appear as fluorescent foci of varying sizes, corresponding to different amounts of target antigens concentrated at these sites. It is plausible to assume that the size of a pATM or pDNA-PKcs focus may be interpreted as an indicator for the extent of damage at this particular site, which may range from a single DSB to a cluster of many. For this reason, a method for evaluation of fluorescent images has been developed, which allows for foci counting and size determination in order to investigate possible differences in the focal size distribution for exposures to particle fields of varying microdosimetric properties.

The procedure for gathering data on foci sizes from immuno-fluorescent samples relies on several steps: Firstly, for all sample from a staining series, digital images are acquired from both the immuno-fluorescent dye as well as the HOECHST 33342 DNA counter-staining for each of several fields of view, as has been described above. According to the mean staining intensity of the corresponding series, a mean greyscale cut-off value C is chosen that serves to separate high-intensity focal areas from the rest of the image using ImageJ software. Since variation of staining characteristics between sample series is a frequently encountered problem in semi-quantitative immunocytochemistry, similar procedures are also applied by other groups (162). For each sample, the value C is slightly adapted to the individual background intensity, thus accounting for minor variations within the same staining series due to antibody binding or photo-bleaching. This is achieved by generating the sample specific cut-off value C_s according to

$$C_s = 255 - \frac{255 - h}{255 - h_s} \cdot \left(255 - C\right), \tag{9.11}$$

where h corresponds to the (mean) maximum of the intensity histograms (number of pixel vs. greyscale values from 0 to 255) of all images from one series, which indicates the most frequent grey value of background pixels. In an analogous manner, h_s corresponds to all fields of view for one particular sample.

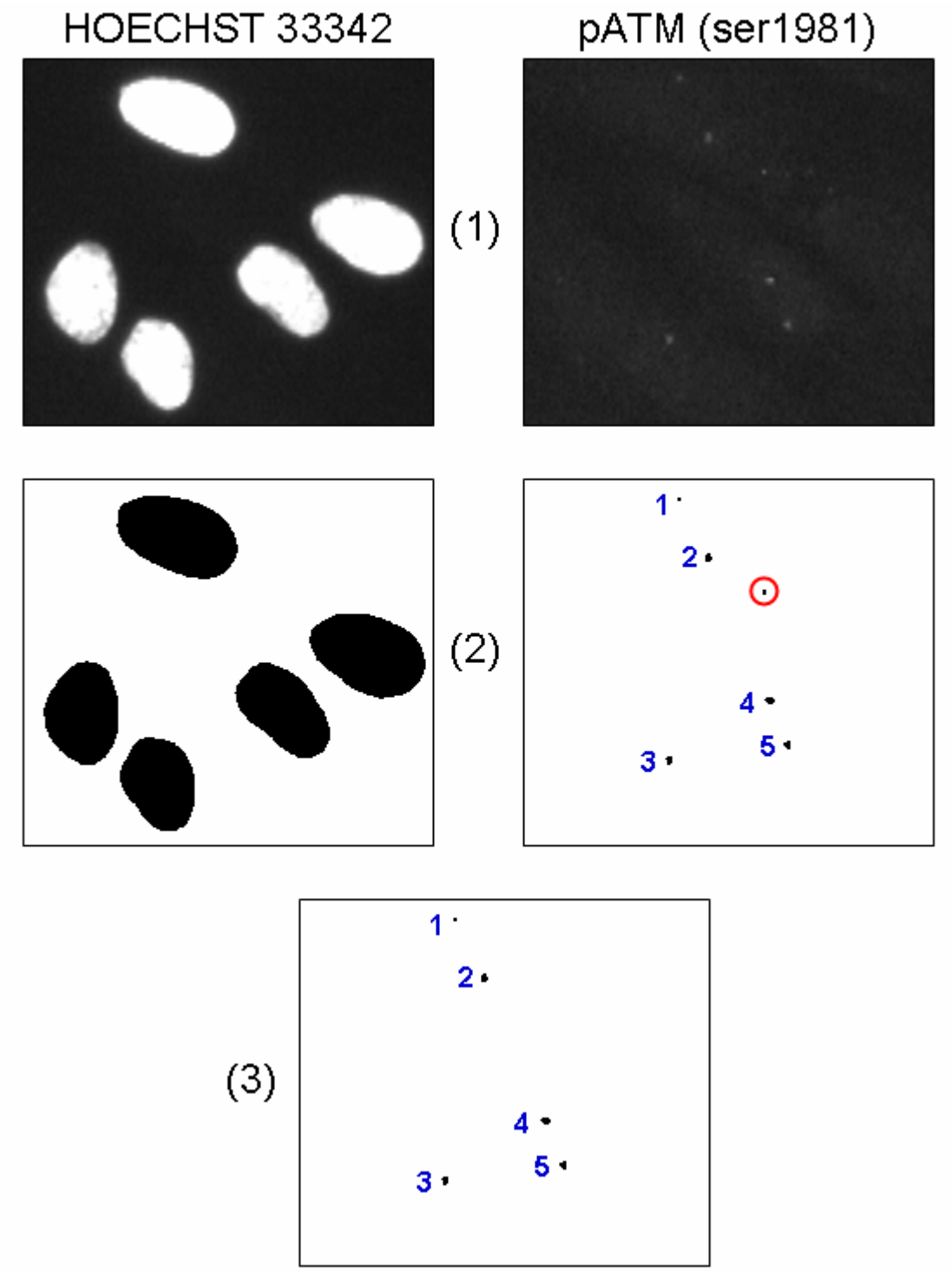

Figure 9.5. Illustration of the image manipulation procedure for determination of foci sizes. As an example, five fibroblasts from a sample exposed to 7.3×10^{4} cm^{-2} ^{56}Fe (500 MeV/u) particles and stained for pATM (ser1981) are shown. From the original greyscale pictures (1), black and white images of nuclei and foci (2) are obtained, which are overlaid for correction of unspecific artefacts (3). For better readability, "real" pATM foci are numbered (from 1 to 5) and an extra-nuclear artefact is marked with a red circle.

Essentially, equation (9.11) represents a purely phenomenological approximation that rescales the "real" signal interval from [h; 255] to [h_s; 255] and adjusts the cut-off threshold accordingly. However, since the usual difference between C and C_s does not exceed one or two greyscale channels, any other roughly similar functional relationship for C_s would lead to identical distribution functions for pATM and pDNA-PKcs foci sizes as presented in chapter 13 within the margin of error.

After calculation of C_s, it is applied as an intensity cut-off threshold, thus reducing the corresponding (inverted) image to black and white only, with black foci on a white background. As a next step, for each field of view a black and white template is generated from the corresponding HOECHST 33342 image. The blue fluorescent dye HOECHST 33342 stains DNA with high specificity and is therefore exclusively located in the nuclei. Thus, by use of an additional inversion step, the generated template consists of black nuclei on a white background. By overlaying, or multiplying, the foci image with the nuclear template, unspecific artefacts (i.e. dots of high fluorescence intensity outside of nuclear areas that may otherwise be misinterpreted as foci) are eliminated. The resulting picture is utilized to determine the area (in numbers of pixel) of every individual remaining focus, thus generating a size distribution function. Under standard magnification that has been applied for by far most of the samples, one pixel corresponds to an area of 0.11 μm^2. For clarification purposes, figure 9.5 elucidates the image processing steps involved.

9.7. Colocalization of Foci in Immunofluorescence Dual-Stainings

It is well established that phosphorylated ATM (ser1981) and DNA-PKcs (thr2609) is found predominately located at sites of DSBs (68, 31, own results) in order to fulfil their functions in DSB repair. This is visually demonstrated by a high degree of colocalization of pATM and pDNA-PKcs with γH2AX, since γH2AX (ser139) precisely marks the location of a DSB (95). Furthermore, both ATM and DNA-PKcs are involved in phosphorylation of H2AX as a response to DNA damage (42, see also section 5.9 for further explanation).

The investigation of colocalization of these proteins is of interest for several reasons: Firstly, a focus where both γH2AX and another player involved in DSB repair are found represents an actual DSB with much higher certainty than any single DSB indicator observed (106). Therefore, these colocalizing foci may be considered a most reliable tool for DSB recognition, and are thus perfectly suited for quantification of radiation induced DNA damage. Furthermore, it seems plausible that radiation of different quality (which induces specific damage patterns), as investigated in this thesis, may well lead to a variation in the extent of colocalization, thus indicating alterations in the cellular response dependent on particular exposure parameters.

For investigation of colocalization, cell layers are co-stained for γH2AX (ser139) and pATM (ser1981) or pDNA-PKcs (thr2609) using different fluorescent dyes (green and red, or Cy™2 and Rhodamine Red™-X, respectively), and HOECHST 33342 (blue) for positional reference. Antibody concentrations have been optimized for similar fluorescence intensity of red and green stained targets in order to avoid misinterpretation due to imperfect separation of the fluorescence signal by the applied optical filter sets. For each field of view, greyscale digital images of all three dyes are acquired. These pictures are processed using AutoIt scripts and ImageJ as described above, starting with false colouring of the greyscale images (red, green, blue) in correspondence to each dye, thus mimicking the visual impression under the microscope. This is followed by background subtraction and contrast enhancement according to a set of parameters that is used unchanged throughout a complete staining series and has been selected by the experimenter for optimal subjective visibility of staining patterns. Finally, the three differently coloured images are overlaid in several combinations (red + blue, green + blue, red + green + blue) allowing for easy assessment of single or combined targets of interest. A set of these finalized images are provided in figure 9.6 as an illustrative example.

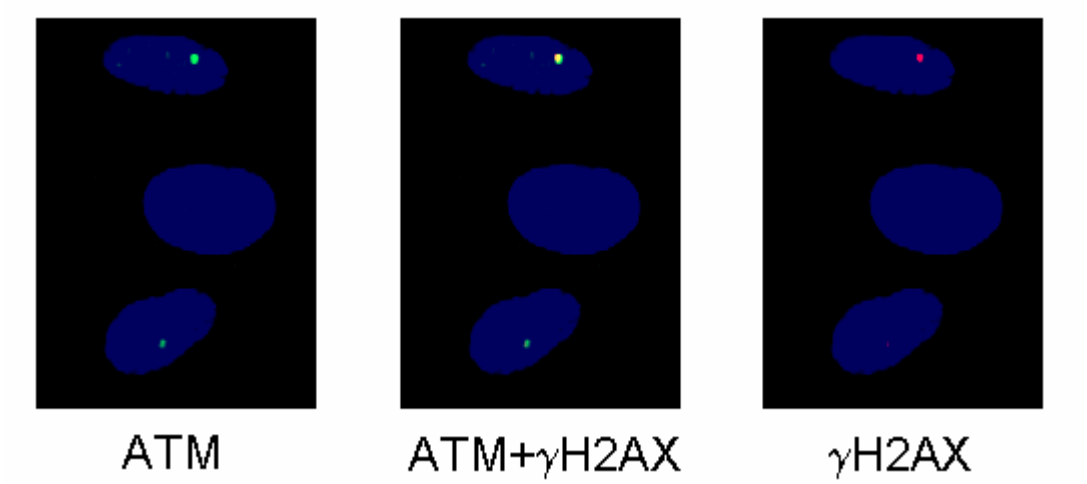

Figure 9.6. Illustration of the evaluation of a dual-stained sample. Three fibroblasts from a sample that has been exposed to 7.3×10⁴ cm⁻² ⁵⁶Fe (500 MeV/u) particles and co-stained for pATM (ser1981, green) and γH2AX (ser139, red) are shown. The uppermost nucleus exhibits a site of colocalization, the middle shows no focus at all and the lower contains one pATM focus.

In analogy to the evaluation of samples stained for γH2AX with the AEC chromogen, all fields of view (represented by three images with different dye combinations, see above) are scored by a human observer in a blinded fashion, i.e. all fields of view are numbered in a random manner before evaluation and the gathered data is attributed to the corresponding samples after scoring has been fully completed.

Thereby, fibroblasts are attributed to four fractions:

- Cells with at least one focus with both proteins colocalizing
- Cells with no site of colocalization, but one or more γH2AX foci
- Cells with no site of colocalization, but one or more pATM/pDNA-PKcs foci
- Cells without any visible foci

Again, due to the subjective nature of this evaluation method, reproducibility of results relies heavily on the experimenter, and quantitative comparison with data gathered by other researchers may prove to be difficult. As a consequence, the assessment of potential systematic errors in the used methodology is almost impossible to achieve due to the lack of "absolute" reference data, which applies to all (semi-) quantitative analysis techniques presented in the last few sections. Despite these issues, it needs to be stressed that all performed procedures are commonly considered highly reliable and sensitive tools in the investigation of cellular signalling events, even though their inherent limitations are to be kept in mind.

Part III:
Results and Discussion

In this chapter, radiobiologic and dosimetric data generated by application of the methods described above will be presented. For this purpose, the experimental plan, exposure parameters and the corresponding implications on interpretation of results shall be outlined in detail.

Next, a few selected, illustrative pre-experiments performed with X-rays and γ-radiation at the Clinic for Radiotherapy and Radiobiology will be presented that represent essential steps in the development of quantitative methods eventually applied for samples exposed to high-LET charged particles.

This is followed by several sections dedicated to the exposures at the HIMAC of NIRS, which include the analysis of TL-measurements as well as radiobiologic results.

Finally, all gained insights shall be summarized by detailed comparison of TL- and biologic data and put into the context of current literature. Implications on the current status of knowledge and on radiation protection will be discussed and suggestions for future experiments will be outlined.

10. Exposure Plan

This section is intended to provide detailed information on the experiments performed at the HIMAC facility of NIRS. For this purpose, samples numbers, exposure parameters (such as particle species, fluence, absorber materials) are described in detail, and the conditions at the target, i.e. a layer of cells or a TL-chip, will be derived by Monte Carlo simulation. Finally, the chosen exposure parameters will be interpreted from the viewpoint of a cell layer in order to provide a basis for analysis of radiobiologic results presented in the next chapters.

10.1. Exposure Series at HIMAC

In three runs at the HIMAC facility of NIRS that were spread across the years 2005 and 2006, exposures of TL-dosemeters and cultivated cells have been performed. According to the experimental schedule of HIMAC, different types of particle beams were available for each series, which allowed for covering an LET range from 2.2 up to 300 keV/µm in H_2O as required. The granted machine time and particle species were in good agreement with the proposed exposure plan, thus resulting in the need to only very slightly adjust the experimental schedule in order to meet the desired objectives. Table 10.1 lists the available HIMAC machine time for each beam type, distributed over three series.

For the first HIMAC run, not only human fibroblasts were exposed as described in section 8.2, but also a number of chamber slides containing HeLa cells, a human cervical tumor cell line, with the intention of qualitative comparison of cellular signal transduction events in normal and tumor cells. However, due to their intrinsic properties, HeLa cells exhibit a high overall level of endogenously occurring DNA damage compared to a normal cell line such as fibroblasts, which furthermore varies greatly from cell to cell. Because of these characteristics, they were found to be inadequate for studying low radiation doses, and, therefore, small biologic effects, during evaluation of samples exposed in HIMAC series I. Since cells from other tumor types can be expected to display a similar extent and inhomogeneity of endogenous DNA damage, all further experiments have focused on the radiation response of normal cells such as human skin fibroblasts, which represent the only cell line exposed during HIMAC runs II and III.

Particle species	^{4}He	^{12}C	^{20}Ne	^{28}Si	^{56}Fe
Nom. energy [MeV/u]	150	290	400	490	500
HIMAC I	X	X		X	X
HIMAC II	X			X	X
HIMAC III		X	X	X	X

Table 10.1: Granted HIMAC machine time for each exposure series. Each marked case corresponds to three hours of beamtime, which were used to full extent for irradiation of cultivated cells, TL-chips and tuning of the particle beam.

Overall, more than 300 chamber slides with fibroblasts have been exposed to high-energy charged particles that were suited for immunological evaluation. In accordance with the selected exposure parameters, these samples may essentially be attributed to two different approaches that are intended to elucidate different aspects of the dependence of the cellular response on radiation quality:

(A) **Comparison of cellular effects after exposure to a chosen particle fluence for different particle species and lineal energies.** This experimental setup allows for investigation of differences caused by the characteristics of a single particle track, since the average number of particle traversals per cell or the number of cells with particle hits, respectively, is kept constant while only the properties of the incident particle are varied. Furthermore, this approach is preferable for the observation and comparison of bystander effects, since, when a sufficiently low particle fluence is chosen, the spatial distribution of ionization events is kept similar from a cellular viewpoint.

(B) **Comparison of cellular effects after exposure to a chosen dose for different particle species, lineal energies and recovery times for damage repair.** In reference to the concept of quality factors (see section 2.1.4), this approach is based on exposures to equal radiation doses of different quality. In the low dose range, the situation on the cellular level varies greatly, with quasi-homogenous distribution of ionization events for low-LET radiation to energy deposition patterns corresponding to only a fraction of cells being directly affected. By selecting an "interesting" dose value that covers a wide range of qualitatively different spatial distributions of ionization events depending on the radiation field, characteristic differences may be highlighted on a quantitative basis. Furthermore, varying temporal dynamics in the cellular response are to be expected that may be investigated by allowing for different recovery times.

In section 10.3, more details as to the selected exposure parameters for both experimental series will be provided and their implications on the damage distribution on the cellular level will be discussed

10.2. LET Calculation with SRIM

At the beam exit location in the HIMAC biology exposure room, the particle energies are lower than the nominal energies, which is due to beam transport and widening as well as a number of detectors in the beamline that act as absorber material. This small deviation has to be taken into account when determining LET and absorbed dose at the sample position using a Monte Carlo code such as SRIM 2003 (149), which has been demonstrated to yield satisfying agreement with practical LET measurements in previous experiments at HIMAC (148) for all regions of the Bragg curve except in close proximity to the peak.

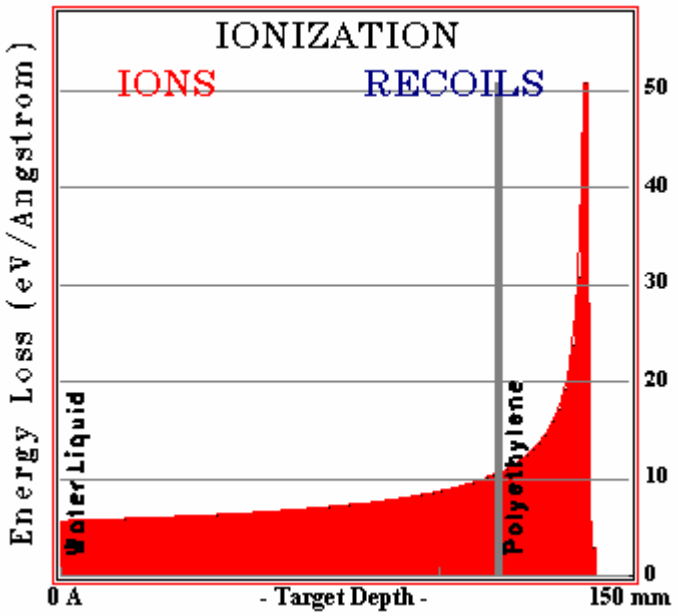

Figure 10.1. Simulation of the exposure configuration for cells in chamber slides with SRIM 2006 for LET determination: As an example, ^{28}Si ions (443.8 MeV/n) are shown that are traversing 115.35 mm of water-equivalent PMMA and a 1 mm slide of polyethylene, with the cell layer being located immediately after the slide. The indicated quantity "Energy Loss (eV/Angstrom)" is to be multiplied by 10 to get the LET in keV/µm.

For most exposures, samples have been exposed directly in the beam line without application of additional absorber material. However, on some occasions, the binary filter system in the biology exposure room, which inserts a layer of water-equivalent PMMA of selected thickness into the beam line in front of the sample position, has been used for LET variation. For all chosen exposure conditions, LET values have been calculated with SRIM by simulating the incident beam, PMMA filters and absorption by the material of

the cell containers. As has been illustrated under "materials and methods", the incident particles have to traverse a Permanox™ slide of 1 mm thickness before reaching the cell layer (see figure 8.4). Since no information as to the exact elemental composition of Permanox is available (except from being classified as a member of the polyolefin family), a 1 mm thick layer of polyethylene (another polyolefin) as a "generic" type of plastic of supposedly similar composition and characteristics has been simulated instead. For calculation purposes, the additional sheet of sticky tape is not simulated, since its contribution to the beam modulation can safely be neglected in comparison to statistical errors of the biologic experiments. The cell layer is chosen to be directly adjacent to the slide. Figure 10.1 shows an example of this procedure for LET determination. Analogous SRIM results for all other used particle beams and chosen absorbers can be found in appendix A. An overview of SRIM results that cover all used exposure setups is presented in table 10.2.

Ion	E_{nom} [MeV/n]	E_{target} [MeV/n]	Range [mm] H_2O	Absorber [mm PMMA]	LET at sample [keV/µm] in H_2O
^{4}He	150	144.2	145.9	–	2.24
^{12}C	290	273.3	148.9	–	13.0
				128.74	29.8
^{20}Ne	400	367.9	144.4	–	30.9
^{28}Si	490	443.8	137.8	–	56.0
				115.35	108.0
^{56}Fe	500	414.7	73.5	–	197.8
				53.62	307.4

Table 10.2: Particle species, energies, absorber thickness and LET at the sample position. E_{target} corresponds to the particle energy before traversing water-equivalent PMMA absorber material. For calculation of the LET at the sample position (i.e. the cell layer) using the SRIM code, 1 mm of polyethylene is selected for simulation of the Permanox™ slide. At least 3000 particles have been simulated for each data point.

10.3. Dose Distribution on the Cellular Level

High-energy charged particles deposit comparably large amounts of energy in small volumes along their tracks while causing a negligible number of (primary) ionization events a few µm off track, as has already been discussed (see section 2.3). Thus, when a low fluence of high-energy charged particles is incident perpendicularly on a layer of cells, direct radiation damage is limited to the fraction of cells that has been traversed by

one or more particles, since the volumes of high dose deposition inside the cell layer are small in comparison to the size of a nucleus or a cell (see also figure 2.2).

In the following, a simple mathematical description of the exposure situation on the cell layer level shall be derived: A layer of cells (of the same type) is traversed by particles fluence Φ that are incident in a direction perpendicular to the cell layer. The particles are distributed randomly across the layer, which resembles the situation in a broad ion beam such as the one available at the beam exit in the HIMAC biology exposure room. Since the DNA represents the most essential target for direct radiation effects, cells with particle traversals through their nucleus, where the DNA molecules are located, shall be considered directly "hit", cells with cytoplasmic or no particle traversals at all as "non-hit".

Furthermore, the nuclei (and thus, the nuclear areas) are allowed to differ in size in order to account for random variation and differences due to cell cycle progression. Thus, the nuclear area A adheres to a distribution function f(A)dA, so that the mean nuclear area $\overline{A}$ is given by

$$\overline{A} = \int_0^\infty A \cdot f(A) dA . \tag{10.1}$$

Furthermore, the average number of particle traversals per nucleus with an area A may be simply written as

$$n_A = \Phi \cdot A . \tag{10.2}$$

In accordance with equation (10.1), the overall average of particle traversals per nucleus, $\overline{n}$, amounts to

$$\overline{n} = \int_0^\infty \Phi \cdot A \cdot f(A) dA = \Phi \cdot \overline{A} . \tag{10.3}$$

Due to the random allocation of particle traversals across the cell layer and the low number of particle per cell, the fraction of nuclei receiving a particular number of hits may best be described with a Poisson distribution. Therefore, for cells with a nuclear area A, the probability to receive a number of k hits is given by

$$P_{n_A}(k) = \frac{n_A^k}{k!} \cdot \exp(-n_A) \tag{10.4}$$

with n_A from equation (10.2) as the expectation value of the Poisson distribution. However, as has been outlined above, the nuclear area A is not constant for all cells, but varies according to f(A)dA. Since A is derived from digital images by pixel counting, only

integer values need to be considered. Taking this into account in the interpretation of f(A), the overall distribution of nuclear particle hits is given by a summation over all occurring pixel values for the nuclear area A, and may thus be written as

$$P(k) = \sum_{A=A_{min}}^{A_{max}} f(A) \cdot \frac{n_A^k}{k!} \cdot \exp(-n_A) \qquad (10.5)$$

with A_{min} as the area pixel value for the smallest, A_{max} for the largest nucleus. f(A) has been obtained experimentally by size determination of more than 1000 HOECHST 33342 stained nuclei originating from several different samples exposed at HIMAC. The normalized size distribution function is shown in figure 10.2. Interestingly, this distribution can be approximated very well by summation of two adequately weighed Gaussian distribution functions as is also illustrated in figure 10.2. This indicates the presence of (at least) two populations of cells, which agrees well with the properties of cultivated fibroblasts at a confluence level between 50 and 100% (see also section 4.3), where a large number of cells are found to be in G0/G1 phase (corresponding to the smaller nuclei represented in Gaussian function 1), whereas a lesser number of cells are progressing towards mitosis, which is accompanied by an increase in nuclei sizes due to a larger amount of DNA content (Gaussian function 2). A tiny fraction of even larger nuclei is detected (at close to 400 μm²), which may be attributed to partly overlapping cells, so that their nuclei cannot be distinguished from the HOECHST 33342 picture.

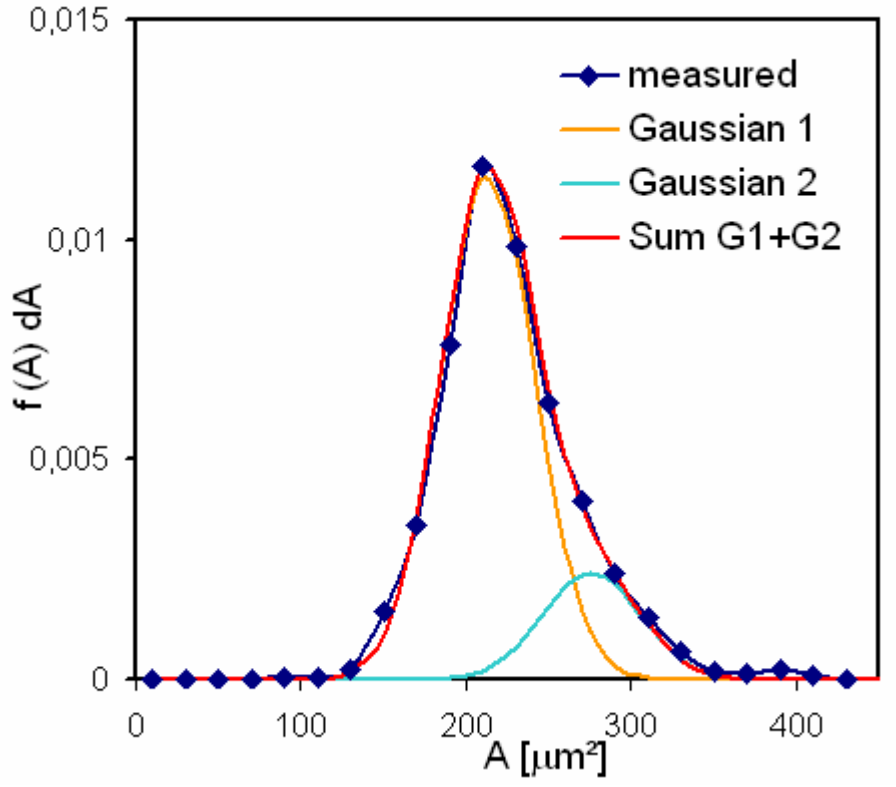

Figure 10.2: Size distribution of fibroblast nuclei: Measured sizes by evaluation of HOECHST stained cells compared to a fit with two Gaussian distributions.

As has been elaborated in section 10.1, one extensive experimental series was dedicated to the comparison of samples that have been exposed to a constant fluence of particles differing in species and LET. For this setup, the presumably most important parameter, from a radiobiologic point of view, is the ratio between cells that received a direct particle hit in their nucleus to cells that did not, or as an equivalent measure, the number of non-traversed cells per one hit cell. This approach is essential in order to be able to demonstrate whether any radiation-induced effects are found in a fraction of cells that exceeds the number of hit cells, thus indicating a bystander effect or a response to cytoplasmic exposure. For this purpose, the quantity N_b has been assessed as given by

$$N_b = \frac{1}{1-P(0)} - 1, \tag{10.6}$$

which corresponds to the number of non-hit cells per cell with a particle traversal through its nucleus. Therein, the expression [1-P(0)] with P(0) according to equation (10.5) represents the probability for a cell to be subjected to a nuclear traversal by at least one particle. Obviously, in order to be able to observe non-targeted radiation-induced effects in a reasonable number of cells, particle fluences are required to be small so that $\bar{n}$ is well below 1, which results in a value of 5 or larger for N_b.

Particle	^{4}He	^{12}C	^{20}Ne	^{28}Si	^{28}Si*	^{56}Fe	^{56}Fe*
LET at target [keV/µm] in H_2O	2.24	13.0	30.9	56.0	108.0	197.8	307.4
Φ [10^4 cm^{-2}]	7.43	7.40	7.33	7.34	7.32	7.34	7.37
± [10^4 cm^{-2}]	0.09	0.03	0.06	0.06	0.07	0.10	0.07
$\bar{n}$	0.168	0.168	0.166	0.166	0.166	0.166	0.167
±	0.002	0.001	0.001	0.001	0.002	0.002	0.002
N_b	5.47	5.49	5.55	5.54	5.56	5.55	5.52
±	0.07	0.02	0.05	0.05	0.06	0.08	0.06
hit nuclei [%]	15.4	15.4	15.3	15.3	15.2	15.3	15.3
±	0.2	0.1	0.1	0.1	0.1	0.2	0.1

Table 10.3: Exposures to an equal fluence of different particles beams. Indicators for the particle distribution across the cell layer, based on particle fluence measurements with a scintillation counter and calculations according to equations (10.1) to (10.6), are given. Asterisks (*) indicate the use of PMMA binary filters for LET modulation. For all derived quantities, σ was obtained according to error propagation of measured fluence values.

Adhering to this principle, it was aimed to deliver a particle fluence close to 7.3×10^4 cm^{-2} to each sample, which was measured by use of a scintillation counter at HIMAC as described in section 8.2. This value was initially chosen for both human fibroblasts and HeLa cells (which are much smaller than the former), so that the fraction of hit nuclei was reasonably close to 10 percent, with more hit nuclei for fibroblasts and less for HeLa. Although further experiments with HeLa were ceased after the first HIMAC exposure run, the same fluence value was applied for experiments with fibroblasts in the runs II and III for the reason of consistency.

Table 10.3 gives an overview of the particles fluences measured in each case, and the resulting values for $\bar{n}$ and N_b as well as the percentage of hit nuclei according to the described formalism. As intended, only a slight variation of particle fluence was encountered across all exposures, corresponding to qualitatively very similar distribution patterns of particles for all samples. In this manner, a solid basis for direct comparison of radiobiologic effects between samples could be established.

Particles	^{12}C	^{12}C*	^{20}Ne	^{28}Si	^{56}Fe
LET at target [keV/µm] in H_2O	13.0	29.8	30.9	56.0	197.8
$\bar{n}$	6.59	2.82	2.81	1.49	0.430
±	0.01	0.01	0.02	0.03	0.001
N_b	<0.003	0.072	0.073	0.30	1.88
±	-	0.001	0.001	0.01	0.01
hit nuclei [%]	>99.7	93.3	93.2	76.7	34.7
±	-	0.1	0.1	0.6	0.1
D [mGy]	60.5	60.1	61.4	59.1	60.2
±	0.1	0.1	0.4	1.0	0.2

Table 10.4: Exposures to equal radiation doses delivered with different particle beams. Absorbed doses were determined using the calculated LET values (see section 10.2) and particle counts measured either with the HIMAC main monitor for higher or a scintillation counter for lower beam intensities. The asterisk (*) indicate the use of a PMMA binary filter for LET modulation. For all derived quantities, σ was obtained according to error propagation of measured fluence values

The second series was aimed at delivering a constant dose of approximately 60 mGy to the cell layer using different particle beams and binary filters. In this dose range, only the ^{56}Fe-500 and – to a lesser extent – the ^{28}Si-490 beams yield a significant fraction of fibroblasts that were not subjected to a particle traversal through their nuclei. For other

beams, the average number of particle hits per nucleus is higher than 1, and thus, no biologic effects may be directly attributed to a non-targeted cellular response.

Particles	^{12}C	$^{12}C^*$	^{20}Ne	^{28}Si	^{56}Fe
LET at target [keV/µm] in H_2O	13.0	29.8	30.9	56.0	197.8
$\bar{n}$	6.59	2.82	2.81	1.49	0.430
±	0.01	0.01	0.02	0.03	0.001
N_b	<0.003	0.072	0.073	0.30	1.88
±	-	0.001	0.001	0.01	0.01
hit nuclei [%]	>99.7	93.3	93.2	76.7	34.7
±	-	0.1	0.1	0.6	0.1
D [mGy]	60.5	60.1	61.4	59.1	60.2
±	0.1	0.1	0.4	1.0	0.2

Table 10.5: Exposures to equal radiation doses delivered with different particle beams. Absorbed doses were determined using the calculated LET values (see section 10.2) and particle counts measured either with the HIMAC main monitor for higher or a scintillation counter for lower beam intensities. The asterisk (*) indicate the use of a PMMA binary filter for LET modulation. For all derived quantities, σ was obtained according to error propagation of measured fluence values

Table 10.5 is dedicated to this second exposure series and provides a listing of particle beams, corresponding LET values and the mean number of particle traversals per nucleus $\bar{n}$. Additionally, the quantities described above, N_b and the percentage of hit nuclei, have been calculated. For exposures to the higher-LET ^{28}Si and ^{56}Fe ions, significant fractions of nuclei (approx. 23 and 65%) are not hit, whereas in the lower-LET ^{12}C and ^{20}Ne exposures, by far the greatest fraction of cells (>93%) is subjected to nuclear particle traversals. These specific, LET-dependent characteristics in the distribution of radiation energy across a cell layer argue for intrinsic differences to be expected as to the number of affected cells, damage patterns, and, therefore, the overall extent of detrimental effects, despite of equal doses being delivered to all samples of this series.

11. Radiobiological Pre-Experiments

Before the first HIMAC exposure series scheduled for January 2005, a multitude of pre-experiments has been performed throughout the year 2004. This work was mainly aimed at refining and optimizing the biochemical methods applied and evaluating their general suitability for low-dose experiments, where small biologic effects are to be studied and a high degree of reproducibility is required in order to allow for quantification of results with a reasonably small experimental error.

In the following, a few selected experimental results among the many that originate from this period shall be presented, which are intended to illustrate general methodology and to provide further clarification for interpretation of experiments with high-energy charged particles in later sections. However, it needs to be stressed that direct comparison between observations shown in this chapter and the samples exposed at HIMAC is limited due to fundamental or qualitative variations in the applied methods, since many procedures used in this period before HIMAC series I where still subject to further improvements or were later found to be inadequate for evaluation of HIMAC samples due to various reasons.

11.1. Exposures to Low-LET Radiation – Results from Immunocytochemical Staining

In preparation of the first exposure series at HIMAC, more than 100 chamber slides with cultivated cells have been immuno-stained. The major part of these experiments was dedicated to refinement of staining procedures and development of an adequate protocol for fixation, transportation and long-term conservation of exposed cell layers. Furthermore, various combinations of primary and secondary antibodies as well as detection kits have been tested for observation of all selected radiation-induced signal transduction events of interest. In detail, these have included phosphorylation of ATM (ser 1981), DNA-PKcs (thr 2609), Chk1 (ser 317 and 345), Chk2 (thr 68), Nbs1 (ser 343), P53 (ser 15 and 37), H2AX (ser 139) and Cdc25c (ser 216). For all these targets, antibody dilutions have been optimized and staining intensities and patterns have been assessed for X-ray doses above 1 Gy and compared to control cells. Recovery times of up to two hours

were considered, which correspond to the "early" cellular response to radiation, the main timeframe of interest within the scope of this work. Based on staining characteristics, intensities and time-dependent activation patterns, ATM, DNA-PKcs, H2AX, Chk2 and P53 have been pre-selected as promising targets for low dose studies with high energy charged particles.

11.1.1. pChk2 (thr 68) in HeLa Cells Irradiated with X-Rays

Eventually, a first, more pronounced attempt (than subjective optical comparison by the experimenter) in quantification of a particular signaling event induced by comparably huge radiation doses has been made using HeLa cells, which have been cultivated in five 8-chamber slides. For each slide, two chambers have been irradiated with an X-ray dose of 10 Gy, two more chambers with 1 Gy and the rest has been shielded during the exposure procedure to serve as control group. The HeLa cells were allowed to recover for one hour and were then immuno-stained with the AEC chromogen (see section 8.4.4) for pChk2 (thr 68), which is found exclusively located in the nuclei. Figure 11.1 shows representative pictures of control and exposed cells captured with an RGB camera.

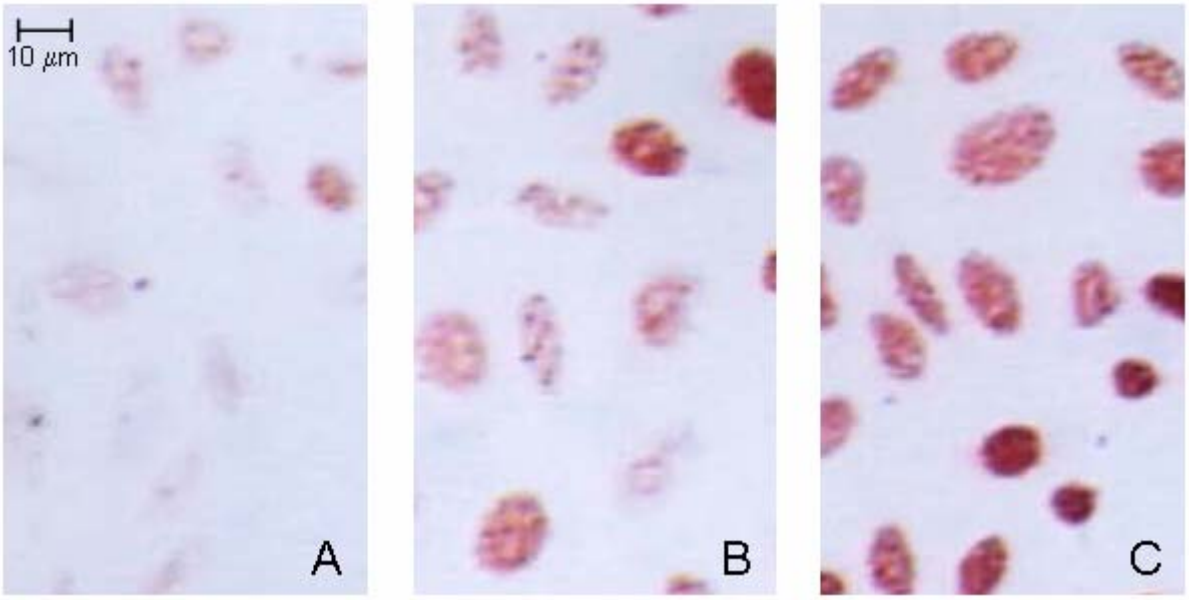

Figure 11.1: HeLa cells immunocytochemically stained for pChk2 (thr 68) that have been exposed to X-ray doses of 1 Gy (B) and 10 Gy (C) compared to an unirradiated control sample (A) after an incubation time of one hour.

For quantification of staining intensity as a measure for pChk2 concentration, greyscale images have been obtained from all samples. By application of a simplified method for determination of optical density based on the principles described in section 9.4, but with less sophisticated and precise determination of nuclear areas, rudimentary background correction and lacking any automation of repetitive procedures, a distribution of the pChk2-concentration per nucleus has been determined for all three groups, which is

shown in figure 11.2. In agreement with the cell images given in figure 11.1, which exhibit a clear increase of staining intensity with radiation dose, the pChk2-concentration has been found to be highest in samples exposed to 10 Gy and lowest for the control group, as has been determined by analysis of optical density.

Obviously, this result is hardly surprising, since doses of a few Gray are to be expected to induce a pronounced effect on cell cycle progression, as is indicated by Chk2 phosphorylation on threonine 68. Nevertheless, this experiment has successfully demonstrated the general applicability of the applied biochemical staining method for quantification of radiation-induced signal transduction events, which requires sufficient reproducibility of staining intensity in order to obtain a similar dose response from evaluation of different samples. Therefore, the used procedures have essentially formed the basis for all further attempts of quantification and the development of more refined and precise evaluation procedures.

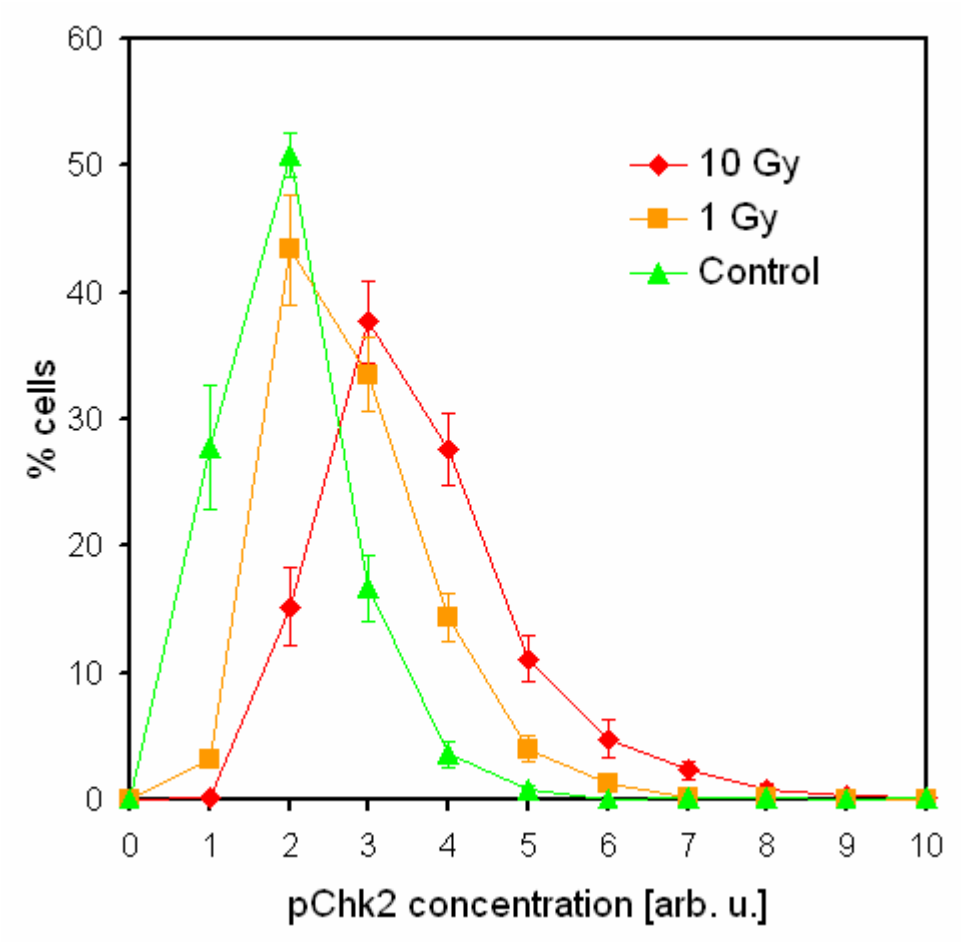

Figure 11.2: pChk2 (thr 68)-concentration (± s.e.) in HeLa cells exposed to an X-ray dose of 1 and 10 Gy compared to a control sample.

On a side note, the dose value of 10 Gy has been deliberately chosen to induce a very intense response, which may likely be close to the theoretical maximum of Chk2 activation due to radiation for proliferating HeLa cells. Therefore, the given result does by

no means imply a linear increase in pChk2 concentration with increasing dose from 1 to 10 Gy. In fact, it is very plausible that 5 Gy of X-rays would have lead to a distribution of pChk2-concentration that is very similar to the curve for the 10 Gy exposures.

11.1.2. ATM Activation after Low-Dose γ-Exposure

Obviously, being able to quantify signal transduction events initialized by radiation doses above 1 Gy of X-rays is not sufficient for investigation of effects induced by a few mGy of high-energy charged particles. Even though these particles are generally exhibit a high relative biologic effectiveness, a dose of e.g. 20 mGy of ^{56}Fe-ions with an LET of approximately 200 keV/µm H_2O can still only be expected to result in a radiobiologic response equivalent to a few hundred mGy of low-LET photon radiation at most.

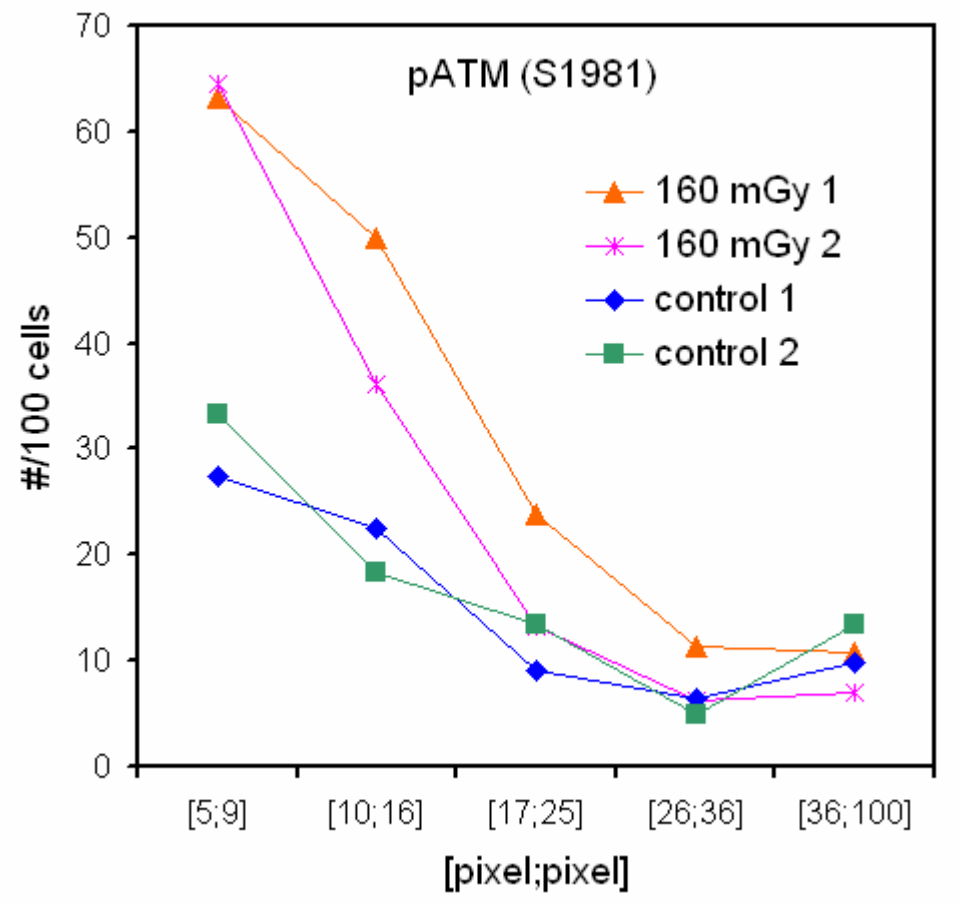

Figure 11.3: Distribution of pATM (ser 1981) foci sizes in human fibroblasts exposed to 160 mGy of γ-radiation (^{60}Co) compared to control samples. Foci sizes are given in [pixel;pixel] intervals, with one pixel corresponding to an area of 0.11 µm².

Therefore, as another test experiment, two chamber slides with human skin fibroblasts have been exposed to 160 mGy of γ-radiation (^{60}Co) and left to recover for two hours. The radiation-induced ATM activity was evaluated by assessment of the formation of pATM

(ser 1981)-foci using IF and comparison of results with two unirradiated control slides. For this purpose, a similar protocol for determination of focus sizes was applied as described in chapter 9.6, which was still – to a certain extent – lacking in optimized correction procedures for unspecific background staining. All image manipulation steps were performed "by hand", since no scripts for automation had yet been developed at that time point.

For both exposed samples, a clear increase in ATM activity is detected, which is demonstrated by a rise in the total number of pATM-foci to almost twice the level of control samples (see figure 11.3). This increase is especially pronounced for the smaller sized foci, which is consistent with DNA damage patterns generally attributed to exposures to low-LET radiation, where individual DSBs arise randomly distributed across the nuclei and no additional, tightly packed damage "clusters" are to be expected, which would appear as larger foci under microscopic view.

It needs to be stressed that a seemingly huge increase in the number of foci as illustrated in figure 11.3 is already difficult to determine by simple subjective optical analysis of stained samples under the microscope (except by counting a large number of cells and foci in a blinded manner). Therefore, it can be concluded that the determination of foci and their sizes from digital images has proven to be an adequate and advantageous tool for sample evaluation, which is able to provide additional insights on the cellular distribution of the target protein and may – in case of ATM (or DNA-PKcs, γH2AX) – allow for further conclusions on DNA damage patterns.

11.1.3. γH2AX in Human Fibroblasts Exposed to 60 mGy of X-Rays

Finally, an experiment with low-LET radiation shall be presented that may be used as a basic reference for the γH2AX (ser 139)-results for exposures to high-energy charged particles: Human skin fibroblasts have been seeded into two 8-chamber slides and grown to approximately 60% confluence. Two chambers of each slide have been exposed to 60 mGy of X-rays (100kV) while shielding the other chambers to serve as control groups. After an incubation period of two hours, the cell layers have been fixated and immunocytochemically stained for γH2AX (ser 139) with the AEC chromogen as described in section 8.4.4. Digital images have been obtained and scored for cells with at least one and without visible γH2AX-foci in a blinded manner.

The results are illustrated in figure 11.4: On both slides, the exposed layers contain an increased number of cells with γH2AX foci. Due to γH2AX representing a marker for DNA DSBs, these additional foci may be interpreted as radiation-induced DNA damage. Since an equal fraction of cells with foci as found in the control groups can be expected to be present in the exposed samples as well, which are always scored positive whether they exhibit an additional γH2AX focus or not, the absolute increase in cells with foci is to be related (or normalized) to the fraction of cells without foci in the control samples in order to obtain the corrected fraction of cells with radiation-induced foci. Therefore, according

to this principle and taking both samples together, a mean fraction of approximately 8% of all cells exhibit at least one detectable γH2AX focus as a result of the exposure to 60 mGy of X-rays.

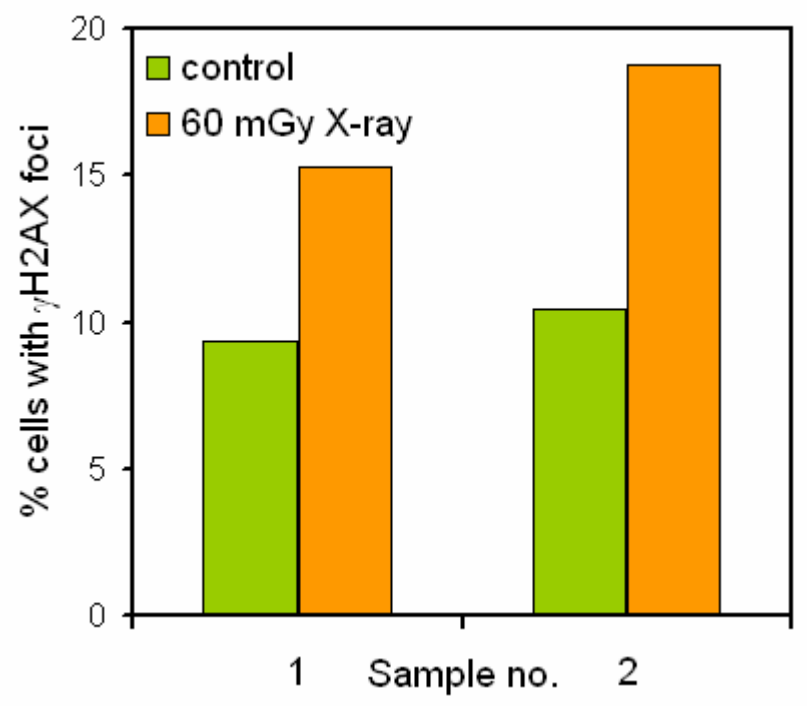

Figure 11.4: Fraction of human fibroblasts with visible γH2AX-foci after exposure to an X-ray dose of 60 mGy and an incubation time of 2 hours, compared to control cells. Cells on two chamber slides have been scored, each containing control and exposed cultures.

11.2. Western Blotting – pP53 (Ser15)

On several occasions in the phase prior to the first exposure series at HIMAC, the specificity of primary antibodies used in immunocytochemical stainings and the induction of chosen signal transduction event at time points of interest have been verified with the western blotting (WB) technique (see section 8.6). One exemplary result is given in figure 11.5: Human fibroblasts cultivated in 25 cm² flasks have been irradiated with a high X-ray dose (10 Gy) and harvested two hours after exposure. As expected, comparison to a control sample shows that large amounts of P53 is phosphorylated at serine 15 in response to radiation, arguing for the triggering of P53-dependent cell cycle arrest in a large fraction of cells.

In this preliminary experimental phase, it has furthermore been tried to roughly "simulate" the damage patterns expected in cell layers due to low fluences of high-energy charged particles by means available at the Atomic Institute of the Austrian Universities. For this purpose, a few samples have been exposed to neutrons with energies up to about

10 MeV, which are emitted by a $^{239}Pu^{9}Be$ source via an (α,n)-reaction. However, due to the low source strength, no modulation of cellular signalling activity could be detected for any of the selected exposure geometries and durations, even though different methods such as immunocytochemical staining or western blotting have been applied. Sample B indicated in figure 11.5 has been exposed in very close proximity to the source for about one hour, which may be interpreted as the maximal dose reasonably achievable with this experimental setup, and, accordingly, shows no increase in the level of pP53 (ser 15) compared to control cells. Therefore, futile efforts of precisely determining the physical exposure parameters for this difficult configuration have been ceased in favor of more rewarding experiments.

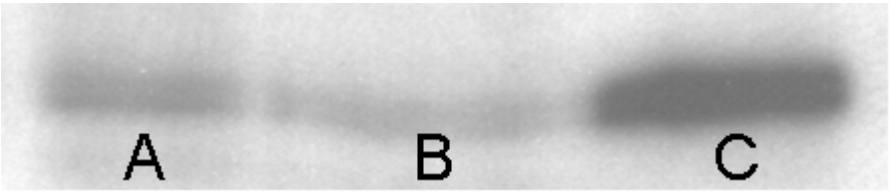

Figure 11.5: pP53 (ser 15) in normal human fibroblasts two hours after exposure. A mock-irradiated sample (A) is compared to cells exposed to a low dose of neutrons (a few mGy) from a PuBe source (B) and to 10 Gy of 100 kV X-rays (C).

Overall, western blotting has served as a useful tool in test experiments, but has not been applied for samples exposed to low doses of high-energy charged particles because of the much lower sensitivity and the inherent lack of information on the intranuclear localization of targets.

12. TL-Measurements at HIMAC

In all experimental runs at HIMAC, irradiation of cultivated cells has been accompanied by parallel exposures of TL-detector packages to an identical radiation field. Therefore, for all exposure conditions that have been outlined in the experimental plan in section 10.3, at least one package including both TLD-600 and TLD-700 dosemeter types has been exposed, γ-calibrated and evaluated as described in sections 7 and 8.2.

Parallel TL-measurements have been performed for several purposes: Firstly, obtained TL glow curves are utilized for verification of values for absorbed dose calculated by use of Monte Carlo simulation and particle fluence measured by means of a scintillation counter. Furthermore, it is one of the main goals of this thesis to investigate the correlation of the HTR with radiobiologic events of interest, which is intended to provide insights on the possibility of determining the extent of radiation-induced biologic effects with a physical measurement system and may eventually peak in the application of TL-detectors for direct estimation of radiation health risks. Therefore, comparison of gathered HTR data with the most recent HTR vs. LET calibration curve is warranted as a prerequisite for correlation with biologic results as a final step in order to guarantee a high degree of consistency with previous studies performed by the working group "Radiation physics, protection and measurements" at the Atomic Institute.

12.1. Determination of absorbed dose

Dose measuring methods based on the TL-effect as applied in the frame of this thesis rely on standardized procedures for preparation of detectors, read-out, mathematical evaluation of acquired glow curves and calibration in reference fields, as has been described in section 7. In principle, the outlined methods using LiF:Mg,Ti-detectors are suited for determination of absorbed dose and effective LET in radiation fields of variable composition with a reasonable margin of error, as has been demonstrated (153). Essentially, when a radiation dose delivered by an unknown field is to be assessed, the HTR is calculated and used for determination of the expected TL-efficiency based on current HTR(LET)-data (see figure 7.6) and the peak 5 TL-efficiency as a function of LET (see figure 7.7). A detailed discussion of this procedure may be found in (154). However,

while this approach allows for the determination of absorbed dose based exclusively on TL-measurements, especially for HTR values around 6 the variation for calculated TL-efficiencies of peak 5 will be rather great due to the characteristics of the HTR(LET)-curve for LET values above 50 keV/µm H_2O (figure 7.6).

Yet, it is to be kept in mind that the primary objective of this work is to investigate the relationship between observed radiobiologic effects with dosimetric quantities, as measured with TL-detectors. While this path may, in the future, possibly lead to a TL-based method for estimation of the biologic consequences due to any radiation field of interest, it is neither necessary nor reasonable to interpret the particle beams used for this thesis as "fields of unknown composition", thus deliberately suffering from a higher margin of error for the determination of absorbed dose due to greater uncertainties in the assumed peak 5 efficiencies. Whereas this matter may have to be dealt with eventually, at this early status the particle LET as calculated with SRIM (see section 10.2) will be used for determination of TL-efficiencies for peak 5, thus obtaining more precise TL-results for absorbed dose. However, since the assessment of overall health risks in complex radiation fields is considered to be exceptionally difficult and, therefore, even more error-prone, moderate deviations in dose measurement may likely prove to be of minor significance.

Both cell layers and TL-detectors have been exposed to HIMAC particle beams in a very similar configuration as described in section 8.2, with the cells being "shielded" from the beam by a 1 mm thick Permanox slide and the TL-chips by the equally thick lid of the polystyrene matrix. Thus, due to this particular geometry and the (expectedly, see section 10.2) similar shielding characteristics of both plastics, the dosimetric quantities measured with the TL-chips (which are to be interpreted as averaged over the detector volume) are ideally suited for direct comparison with effects in the cell layers, which, in an analogous view, would be located inside the TL material. For the same reason, LET values calculated for the location of the cell layers, which are given in table 10.2, can directly be reused for determination of the LET-dependent TL-efficiencies of peak 5 as a sufficiently satisfying approximation. Furthermore, even in exposures using PMMA binary filters, absorber thicknesses have been selected for the sample positions to be still significantly off the Bragg peak. Therefore, comparison of selected particles and LET values with the left-hand side of figure 7.7 shows that, for all used radiation fields, TL-efficiencies $\eta_{k,\gamma}$ for peak 5 are well approximated by the included fit function

$$\eta_{k,\gamma} = \frac{1 + 0.0275 \cdot \overline{LET_k}}{0.7749 + 0.06474 \cdot \overline{LET_k}}, \tag{12.1}$$

where k symbolizes the radiation field of interest and $\overline{LET_k}$ denotes the effective LET of field k.

In the experimental series with exposures to an equal fluence of approximately 7.3×10^4 cm^{-2} using different particle beams and absorbers thicknesses, dose determination by means of TL detectors was mainly performed in order to provide further verification of

exposure conditions in addition to LET calculation by Monte Carlo simulation and scintillation counter measurements. Since the deviations in measured particle fluence from the nominal value (or the mean of 7.36×10^4 cm^{-2}) are very small, the deviations from the corresponding nominal dose values are well within the expected statistical error of absorbed dose measurements with TLD-600 and TLD-700. Therefore, for comparison and verification purposes, the mean fluence may safely be used for all LET values. By doing this, the absorbed dose at the target position is only dependent on particle LET in a linear manner, putting all exposure conditions on a straight line in an absorbed dose vs. LET graph, as is illustrated in figure 12.1.

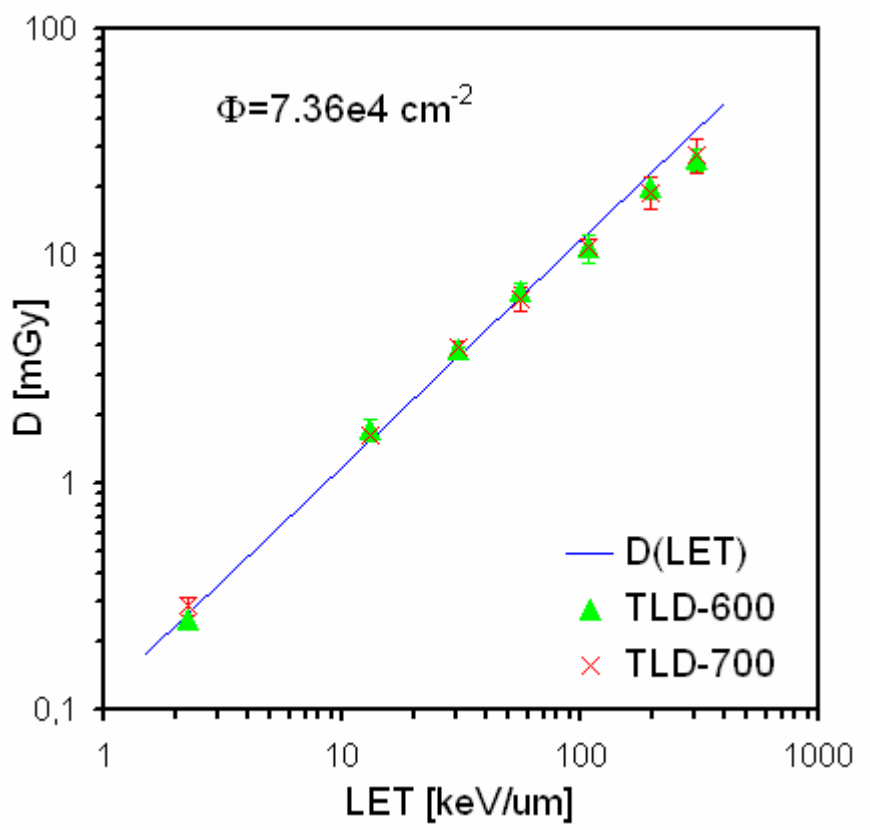

Figure 12.1: Absorbed dose measured with TLD-600 and TLD-700 detectors vs. calculated LET for a constant particle fluence of $\Phi=7.36\times10^4$ cm^{-2}.

Good agreement between dose values, calculated from particle fluence and LET, and TL-measurements was found, which only exhibit a slight deviation at the highest LET values, which may be partly attributed to uncertainties in the TL-efficiencies $\eta_{k,\gamma}$ and statistics. Furthermore, limited particle discrimination capabilities of the used HIMAC scintillation counters may contribute to a certain extent, which lead to misinterpretation of contaminating particles from other species than the primary beam particles, thus slightly overestimating fluence and, therefore, calculated dose values especially for the heavy ion beams.

The results of the TLD-600 and TLD-700 dose-measurements for exposures to an equal dose of approximately 60 mGy are given in table 12.1, where they are also compared to calculated values. Again, slightly larger deviations between measured and calculated values are found for the high-LET exposure to ^{56}Fe particles, which may be explained by the reasons given above.

Particle	^{12}C	^{12}C	^{20}Ne	^{28}Si	^{56}Fe
LET [keV/mm] H_2O	13.0	29.8	30.9	56.0	197.8
Dose, calc. [mGy]	60.6	59.7	61.4	59.1	60.2
Dose, TLD-600 [mGy]	56.5	54.0	64.4	63.7	53.4
σ [mGy]	1.1	0.8	0.7	1.5	1.8
Dose, TLD-700 [mGy]	55.9	53.2	61.1	64.0	48.2
σ [mGy]	1.9	1.9	1.0	1.8	0.9

Table 12.1: Absorbed dose at the target position for the 60 mGy exposures. Results correspond to one package of 4 to 5 detectors of both TLD-600 and TLD-700 types for each LET value.

12.2. HTR vs. LET results

As one of the major objectives, the High Temperature Ratio measured in radiation fields of different quality is to be compared with radiobiologic events of interest, as will follow in section 14. For this purpose, the HTR results generated from TL-detectors that have been exposed as a dosimetric reference shall be compared to recent data in order to demonstrate the consistency of measurements performed for this thesis with established knowledge. Therefore, for each LET value selected for the cell exposures, the HTR averaged over a few (1 to 5) TL-detector packages, which have been exposed to varying doses, has been determined and inserted into the published HTR(LET) curve (154, see also section 7.5), as is illustrated in figure 12.2.

As required, the obtained HTR results are in good agreement with data gathered in former studies, and are thus suited for use in correlation of TL measurements with the radiation-induced biologic effects investigated.

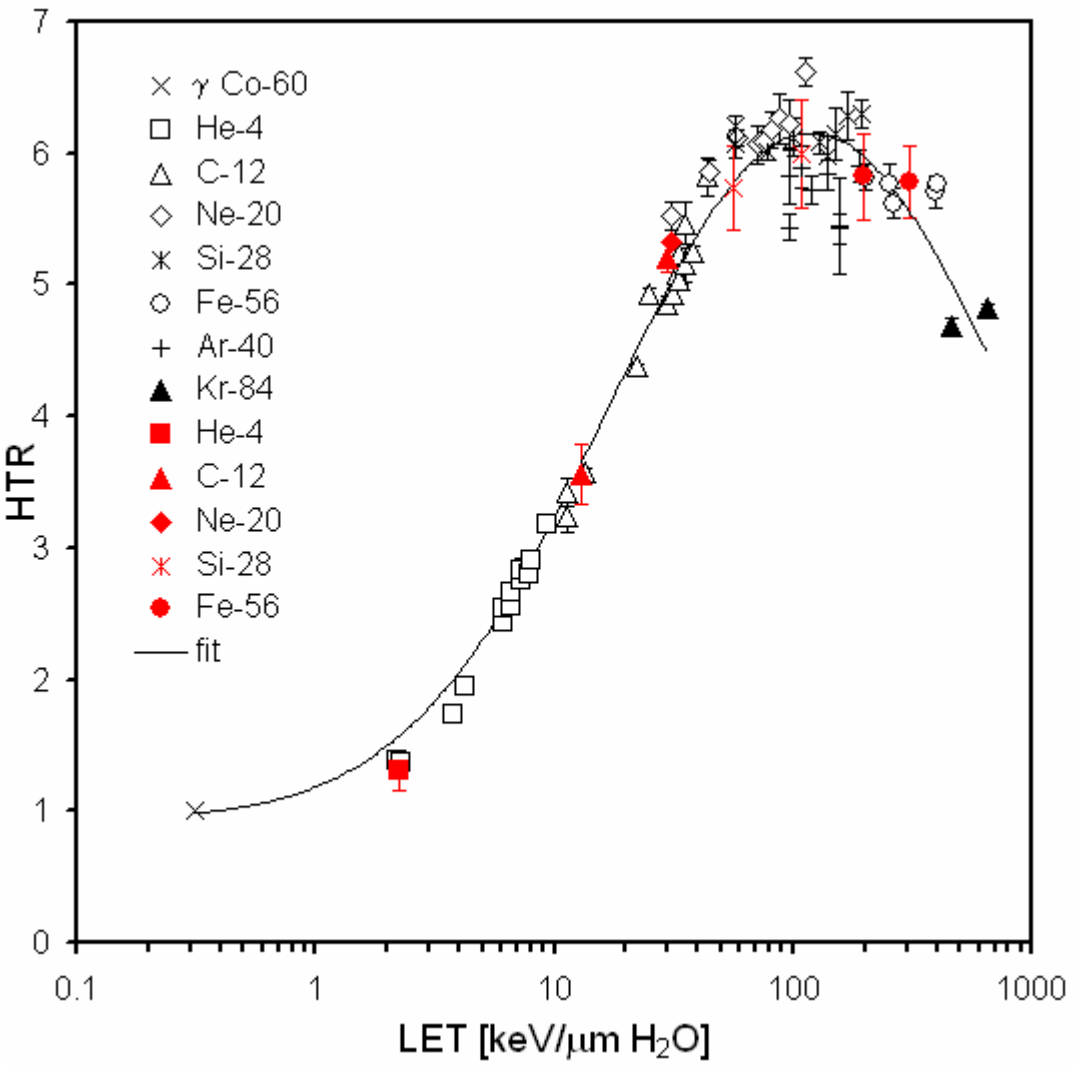

Figure 12.2: Comparison of HTR results for LiF:Mg,Ti detectors (TLD-600 and 700 combined) gathered in the HIMAC runs I to III (red) with established TLD-700 data (black) and the recent HTR vs. LET calibration curve (154). Standard deviations are given and, in case of the new results, indicate variation between different TL-packages.

13. Cellular Response to High-LET Charged Particles

So far, parameters for the exposures to charged particle beams at HIMAC have been introduced from both a macro- and microscopic viewpoint, results from pre-experiments have been presented and a description of results for dose and HTR measurements with TL detectors has been given, which have been performed accompanying cell exposures as a dosimetric reference. On this basis, insights gained from these experiments with cultivated cells shall now be thoroughly discussed in the following sections.

The first part of chapter 13 will be dedicated to a series of samples exposed to an equal fluence of particles that differ in species and LET. Therein, implications on several cellular signal transduction events such as the formation of pATM (ser 1981), pDNA-PKcs (thr 2609) and γH2AX (ser 139) foci as well as the accumulation of pChk2 (thr 68) will be described for a selected time point of two hours after irradiation.

In the second part, the cellular response to an equal dose of approximately 60 mGy delivered by different particle beams will be elucidated, focusing on ATM and DNA-PKcs activation and H2AX phosphorylation. Data will be presented for three time points – 20 minutes, 1 and 2 hours after exposure – allowing for conclusion on the time course of the cellular response and the kinetics of focus formation and dissolution for the targets of interest.

13.1. Cell Effects Induced by Equal Fluences of Different Particles

Exposure of a single-layered culture of cells to a low fluence of particles that are incident in perpendicular direction results in a defined fraction of cells being subjected to a particle traversal through their nucleus, which may yield direct damage in DNA molecules due to radiation. The remaining fraction of cells is either not hit at all or traversed only in their extranuclear volume, where radiation induced ionization events may not directly impair the genomic integrity of a cell.

In three runs at the HIMAC facility, more than a hundred chamber slides containing cultivated diploid human skin fibroblasts were exposed to a fluence of approximately 7.3 to 7.4×10^4 cm^{-2} using varying particle beams with different lineal energies. On the cellular level, this configuration corresponds to approximately 15% of all cells receiving a particle hit in their nucleus, as has been elaborated in section 10.3. By keeping the fluence at a constant value, differences in the cellular response may be traced back to the characteristics of a single particle track, since, essentially, the statistical spatial distribution of tracks across the cell layer is highly similar for all samples. Below, various signal transduction events initialized in these experiments shall be discussed. Several of the following results are expected to be published in 2007 (163).

13.1.1. Formation of pATM (Ser 1981) Foci

After exposure to particle beams as described above, normal human skin fibroblasts were allowed to repair DNA damage for two hours. This time point was chosen because at two hours after irradiation, significant activity of ATM and DNA-PKcs could be observed in pre-experiments with higher doses of low-LET photon radiation, as indicated by the presence of their phosphorylated forms and the phosphorylation of several downstream targets, which corresponds well with established knowledge. After incubation, cell layers were fixed and stored. Samples were eventually stained for pATM (ser 1981) via immunofluorescence according to the protocols supplied in chapter 8.4.3. Acquisition of digital images of the cell layers was followed by an analysis procedure for determination of pATM foci sizes (see section 9.6).

More than a hundred cells per sample were evaluated. For presentation of results, pATM (ser 1981) foci for each exposure condition have been grouped according to their size and their numbers have been normalized to 100 cells (see figure 13.1). For LET values up to about 30 keV/µm (corresponding to the ^{4}He-, ^{12}C-, and ^{20}Ne-exposures), no significant dependence of pATM focus formation on particle LET could be observed, since the number of detected foci was found to remain at the control level of mock-irradiated samples for all foci sizes. A slight increase in the number of pATM foci is exhibited by samples irradiated with ^{28}Si particles (with an LET of 56.0 and 108.0 keV/µm H_2O), which, while not being found for all foci sizes, is more obvious when comparing the total number of foci per 100 cells, as will be done later on (see figure 13.2). Samples exposed to ^{56}Fe ions (both LET values of 197.8 and 307.4) yielded a significantly higher number of pATM foci throughout all foci sizes, which is especially pronounced for the larger foci with areas above 2.7 μm^2 (corresponding to the [26;36] and [37;max] pixel intervals), where three or more times the number of foci were detected in ^{56}Fe-exposed samples compared to the control group.

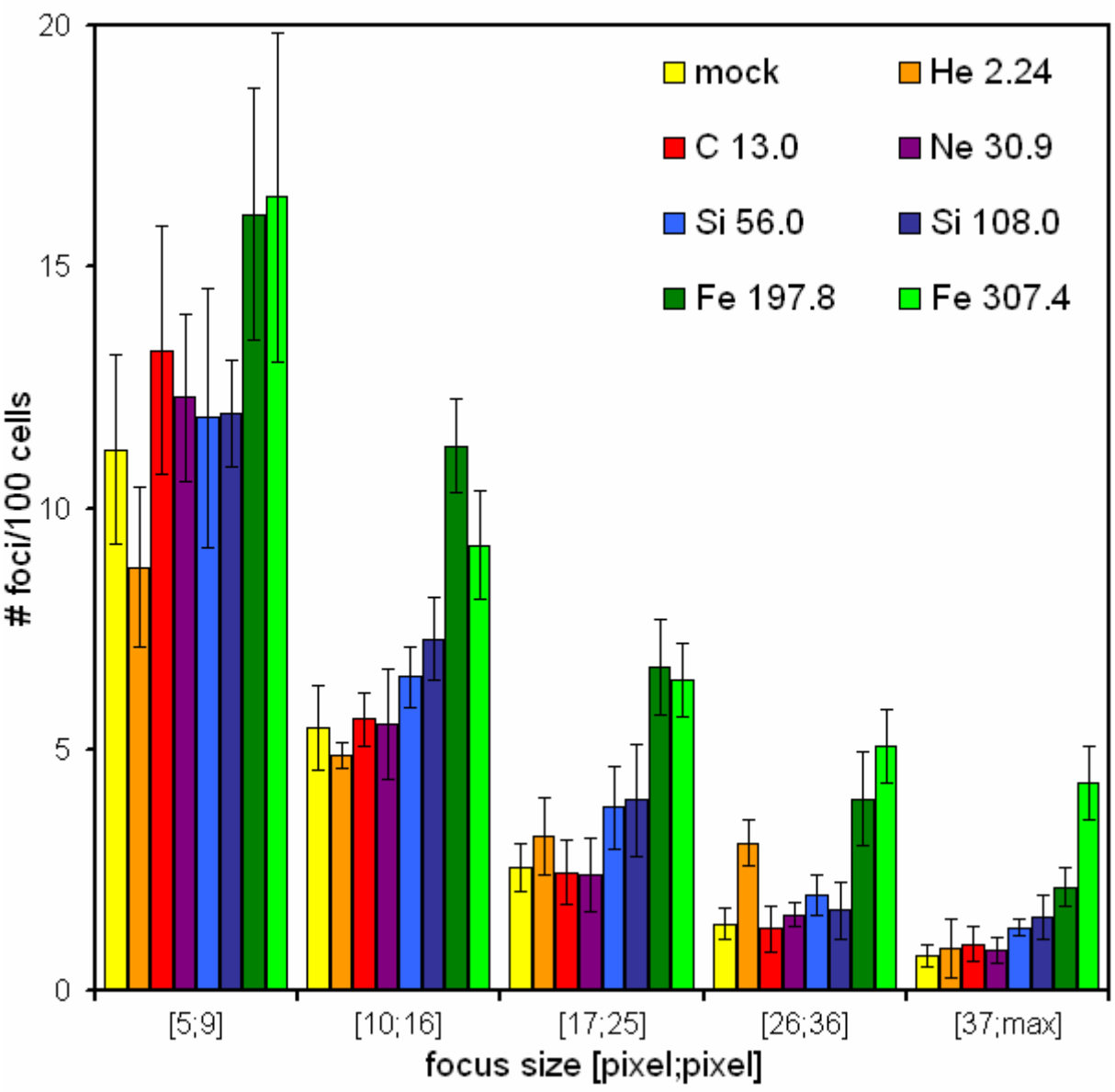

Figure 13.1: Different sizes of detected pATM (ser 1981) foci per 100 human skin fibroblasts after exposure to an equal fluence of varying particles. Foci sizes are given in [pixel; pixel] intervals (1 pixel ≈ 0.11 µm²). Results are means of at least 4 samples per LET value ± s.e.. Particle species and LET values (in [keV/µm] H_2O) are included in the picture legend.

The total number of pATM foci per 100 cells independent of size has been determined for each exposure condition by summation over all foci sizes. The results are presented in figure 13.2: In correspondence with the size distribution results, samples exposed to beams with LET values up to about 30 keV/µm exhibit no increase in the total number of pATM foci. As has already been announced above, fibroblasts exposed to ^{28}Si particles (56.0 and 108.0 keV/µm H_2O) contain slightly more foci than controls. Irradiation with ^{56}Fe ion beams (197.8 and 307.4 keV/µm H_2O) results in an increase of pATM foci to about twice the control level.

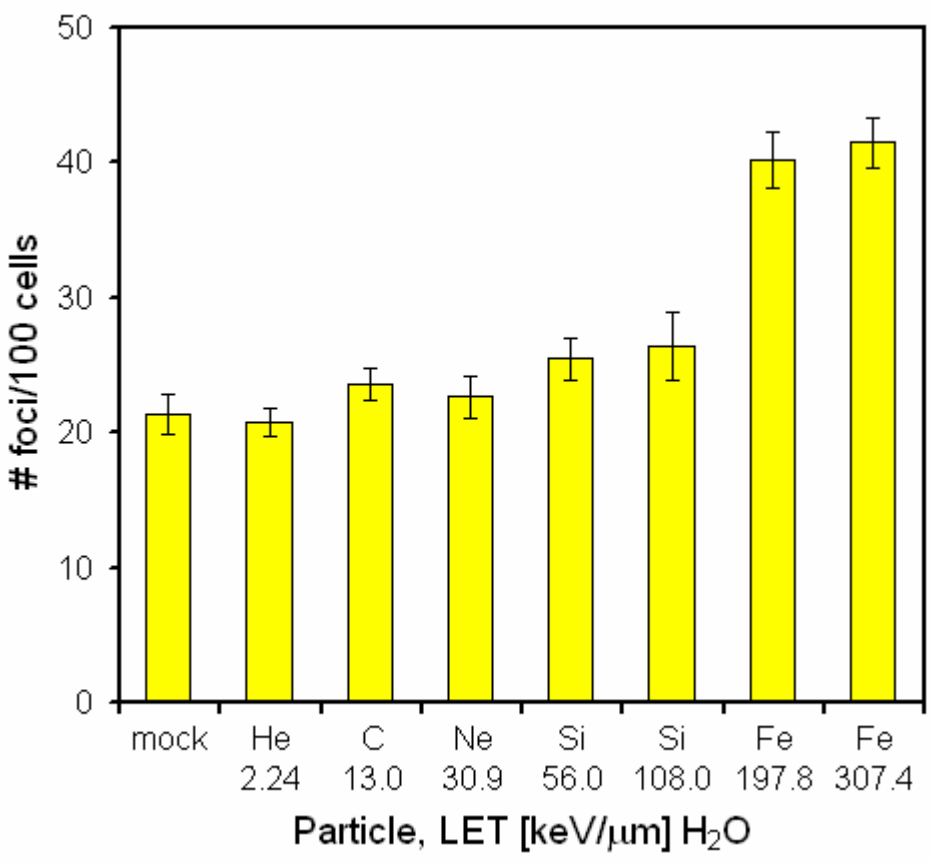

Figure 13.2: Total number of pATM (ser 1981) foci per 100 human skin fibroblasts after exposure to an equal fluence of varying particles. Results are means of at least 4 samples per LET value ± s.e..

Interestingly, the difference between the number of pATM foci in ^{56}Fe exposed and control samples amounts to about 15 to 22 foci per 100 cells. Comparison with the microscopic distribution of particles shows that the calculated number of particles traversing nuclear areas, which is given by 16.7 per 100 cells (see table 10.3), lies well within this interval. It is thus tempting to speculate that practically every nuclear hit by a ^{56}Fe ion results in the formation of a pATM focus, which is successfully detected using the applied staining and evaluation methods.

As a summary, ATM activity persisting until two hours after irradiation, as indicated by the formation of pATM (ser 1981) foci, is clearly modulated by radiation LET under the given exposure conditions. An increase in the number of pATM foci compared to the control group has been detected for radiation with LET values above 50 keV/µm H_2O. Analysis of foci sizes shows that exposure to beams of the highest LET values (about 200 keV/µm H_2O and above) yields a highly increased number of larger pATM foci, arguing for the induction of extensive clustered DNA damage by these types of particles, which is not found to be fully repaired at the two hours time point after irradiation.

13.1.2. Formation of pDNA-PKcs (Thr 2609) Foci

Human fibroblasts that were treated in a manner identical to the pATM-samples as described in the last chapter were stained for pDNA-PKcs (thr 2609) according to immunofluorescence protocols. Again, digital images were acquired and used for detection of pDNA-PKcs foci. The number and size of pDNA-PKcs foci were evaluated in more than a hundred cells per sample.

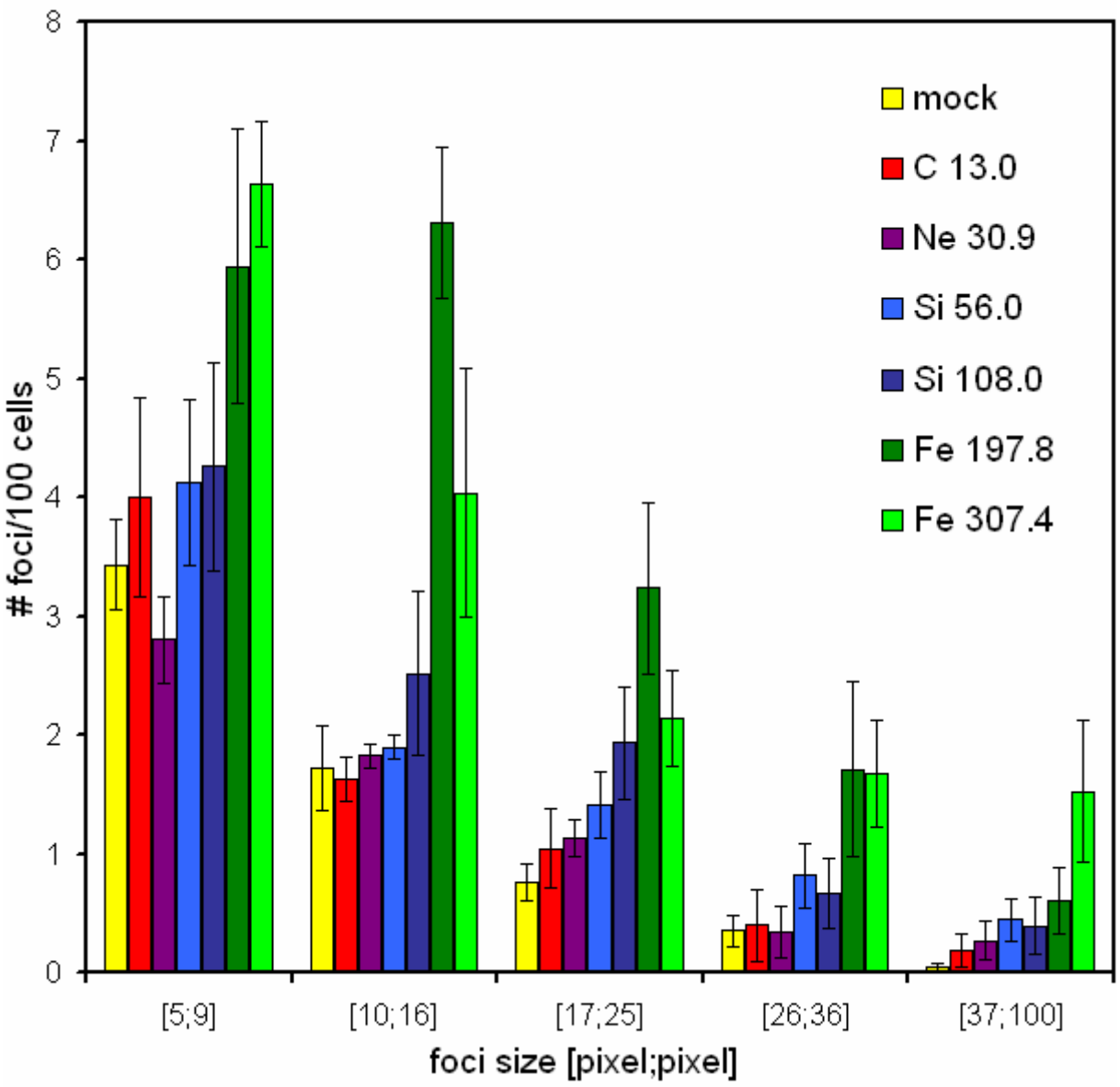

Figure 13.3: Different sizes of detected pDNA-PKcs (thr 2609) foci per 100 human skin fibroblasts after exposure to an equal fluence of varying particles. Foci sizes are given in [pixel; pixel] intervals (1 pixel ≈ 0.11 µm²). Results are means of at least 4 samples per LET value ± s.e.. Particle species and LET values (in [keV/µm] H_2O) are included in the picture legend.

Figure 13.3 shows the detected number of foci, which have been grouped according to their size and normalized to 100 cells per exposure condition. In analogy to the pATM-results, no increase in DNA-PKcs phosphorylation compared to the mock-irradiated control group is found in cells that have been exposed to particle beams with LET values below 50 keV/µm H_2O, corresponding to the ^{12}C and ^{20}Ne exposures. However, irradiation with higher-LET ^{28}Si-particles (56.0 and 108.0 keV/µm H_2O) shows a slight rise in the extent of DNA-PKcs phosphorylation above control levels. Again, both ^{56}Fe-exposures yield a much higher number of foci of up to four times the number in unirradiated samples, depending on the regarding size interval.

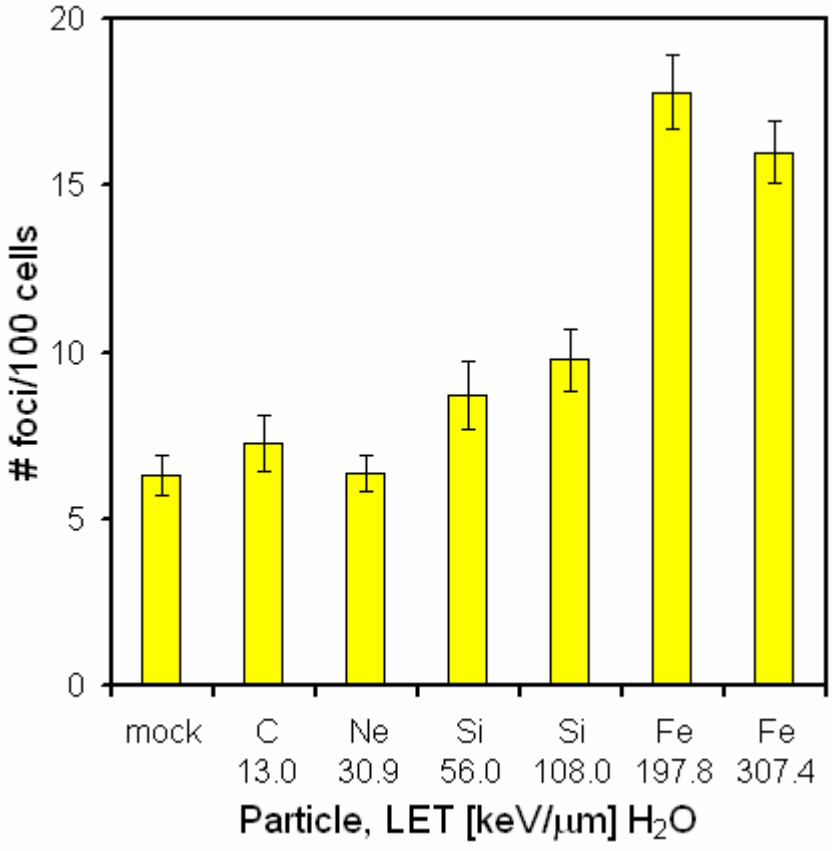

Figure 13.4: Total number of pDNA-PKcs (thr 2609) foci per 100 human skin fibroblasts after exposure to an equal fluence of varying particles. Results are means of at least 4 samples per LET value ± s.e..

The total number of DNA-PKcs foci per 100 human fibroblasts, which is determined by summation over all foci sizes for each exposure condition, is illustrated in figure 13.4. The results precisely reflect the insights gained from the foci size distribution graph, showing an increase in the amount of pDNA-PKcs with increasing LET, starting with the ^{28}Si-exposure of 56.0 keV/µm H_2O. Both ^{56}Fe exposures are found to yield the same total number of foci within experimental accuracy limits. However, detailed examination of the distribution of foci sizes given in figure 13.3 shows that the pDNA-PKcs foci induced by the 197.8 keV/µm ^{56}Fe beam are, on average, of smaller size than those due to the 307.4 keV/µm ions. Comparison with the size distribution of pATM foci (figure 13.1) shows that

a similar, yet not as pronounced effect may also be found for ATM phosphorylation. In the author's opinion, while these observations may possibly hint at an induction of slightly different damage patterns along the particle tracks due to a varying local density of ionization events, more extensive studies of this potential effect would be required to support this hypothesis.

Overall, elevated levels of pDNA-PKcs (thr 2609), which is observed to be concentrated at localized sites, have been demonstrated to persist until two hours after irradiation for particle beams with LET values above 50 keV/µm in water. The number of detected pDNA-PKcs foci has been found to increases up to an LET value of about 200 keV/µm H_2O. A further increase of particle LET does not result in the formation of additional foci, but rather in a change of their size distribution to larger foci. Since DNA-PKcs is one of the major players in DSB repair via non-homologous end joining, these data provides evidence that the characteristics of single particles translate into specific patterns of DNA damage. The shown differences in DNA-PKcs activation at the two hours time point argue for a particle-specific repair response that varies in extent or duration.

13.1.3. Colocalization of γH2AX and pATM

In order to simultaneously assess ATM- and H2AX-phosphorylation, cells were exposed under the conditions described above and co-immunostained for pATM (ser 1981) and γH2AX (ser 139) using Cy2- and Rhodamine Red-X conjugated secondary antibodies. Digital images were taken, processed and overlaid. The percentages of cells with one or more γH2AX- and pATM-foci as well as of cells with at least one colocalization site of both types of foci were determined by an observer in a blinded fashion. For a detailed description of the steps involved, see sections 8.4 and 9.7.

Results are illustrated in figure 13.5, which shows the percentage of cells with at least one "radiation-induced" focus of the different types. This value is obtained by subtracting the fraction of foci-exhibiting cells in a control sample (which are, per definition, not caused by radiation exposure) from the determined fraction in exposed samples, since the same number of cells with foci can also be expected in the irradiated cell layers. Hence, the presence of an additional number of foci may be attributed to radiation-induced effects. Since the overall number of cells has been reduced due to this subtraction, results need to be renormalized to a total of 100% to finalize calculation of this quantity, namely the fraction of cells exhibiting radiation-induced foci, as is used in figure 13.5.

For pATM foci, γH2AX foci, as well as for the colocalization of both types, a clear increase in number with increasing radiation LET has been detected for values above 100 keV/µm H_2O. For the exposures to lower-LET beams (^{12}C, ^{20}Ne, and ^{28}Si without binary filter), no significant radiation-induced increase in focus formation could be demonstrated, since the numbers of cells with foci of different types closely resemble the situation in control layers.

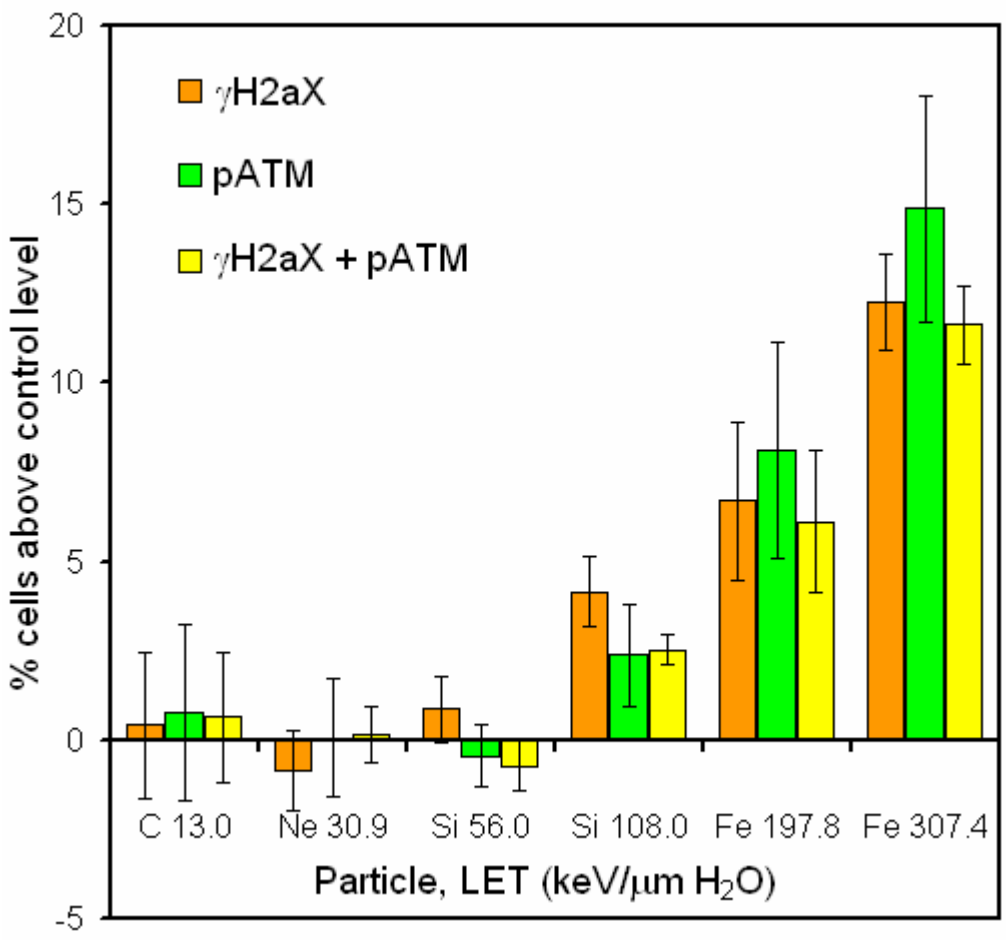

Figure 13.5: Percentage of human fibroblasts with at least one radiation-induced γH2AX-, pATM-focus or colocalization of both, after exposure to an equal fluence of varying particles. Results are means of at least 4 samples per LET value ± s.e..

As mentioned above, approximately 15% of the fibroblasts are subjected to a particle traversal through their nucleus. Comparison of this value with figure 13.5 shows that for the highest-LET particles (^{56}Fe, 307.4 keV/µm H_2O), exactly the same percentage of cells exhibit at least one additional pATM (ser 1981) focus, with the other types of foci being found, on average, in a slightly lower number of nuclei (12 to 13%). Thus, in consistency with the pATM results for ^{56}Fe (307.4 keV/µm) discussed in section 13.1.1, it seems plausible to assume that for these particles, every nuclear traversal causes the formation of one pATM focus that is still visible two hours after irradiation. In the ^{56}Fe (197.4 keV/µm)-exposed samples, a lower number of cells have been scored positive for pATM foci than what would have been expected from the evaluation of the pATM focus size distribution in section 13.1.1. However, this deviation may be easily explained by the fact that "counting" by an observer is an intrinsically different evaluation method that is likely less precise especially for smaller sized foci, which are a bit more abundant in samples irradiated in the bare ^{56}Fe (197.4 keV/µm)-beam.

On a side note, as is also, to a certain extent, indicated by the relative differences between the three types of foci for each exposure condition, pATM and γH2AX foci have been found not to colocalize in all cases. This difference can be explained by the fact that even though both pATM- and γH2AX-foci are linked to DSBs, they correspond to different signal transduction events that may differ in extent and their time point of initialization. Dual-stainings of pATM (ser 1981) and γH2AX (ser 139) published by Bakkenist and Kastan (68) also agree with this finding and show good yet not perfect colocalization of both phosphorylated targets in fibroblasts after different treatments.

13.1.4. Colocalization of γH2AX and pDNA-PKcs

For parallel observation of the phosphorylation status of DNA-PKcs and H2AX, exposed and mock-irradiated layers of fibroblasts were co-immunostained for pDNA-PKcs (thr 2609) and γH2AX (ser 139) using Cy2- and Rhodamine Red-X conjugated secondary antibodies. Quantitative analysis and calculation of the percentage of cells with radiation-induced foci (i.e. the corrected fraction of cells with foci above the control level) has been performed in analogy to dual-stainings of pATM and γH2AX as covered in the last subsection 13.1.3.

The results are illustrated in figure 13.6: In agreement with other data presented so far, no radiation-induced cellular response as indicated by DNA-PKcs- or γH2AX-phosphorylation is exhibited by cells exposed to the lower-LET ^{12}C and ^{20}Ne (13.0 and 30.9 keV/μm H_2O) beams at the two hours time point, whereas a clear increase in the fraction of foci-containing cells with particle LET from 100 up to 300 keV/μm is seen for all types of foci. Somewhat surprisingly, both ^{28}Si exposures (56.0 and 108.0 keV/μm H_2O) have been found to yield the same number of cells with foci within statistical uncertainties. However, since standard deviations for both the fraction of cells with γH2AX and with pDNA-PKcs foci in these particular samples (56 keV/μm) are comparably high (about 70% of the mean value), these values do not contradict other results depicted in figure 13.5 and figure 13.4.

In current literature, some controversial findings have been reported as to the subcellular distribution of DNA-PKcs that has been subjected to autophosphorylation at threonine 2609 in response to radiation-induced DSBs. Phosphorylated DNA-PKcs has also been reported to be found distributed homogeneously across the nucleus (45) rather than being exclusively or, at least, predominantly located at sites of DSBs, which would correspond to the more common opinion presented in various papers and reviews (e.g. 31, 38, 103). In any case, the experimental results gathered within the frame of this thesis argue for the latter option, since a large number of sites, where pDNA-PKcs foci colocalize with the DSB marker γH2AX, could be observed in cells exposed to high-energy charged particles, as has been shown above. However, in analogy to the pATM-gH2AX dual-staining, not all pDNA-PKcs and γH2AX foci have been found to colocalize. Again, this is rather easily understood, since both types of foci generally indicate the presence of a DSB, but

represent different events in the cellular response to DNA damage, which may very well vary in extent and time course.

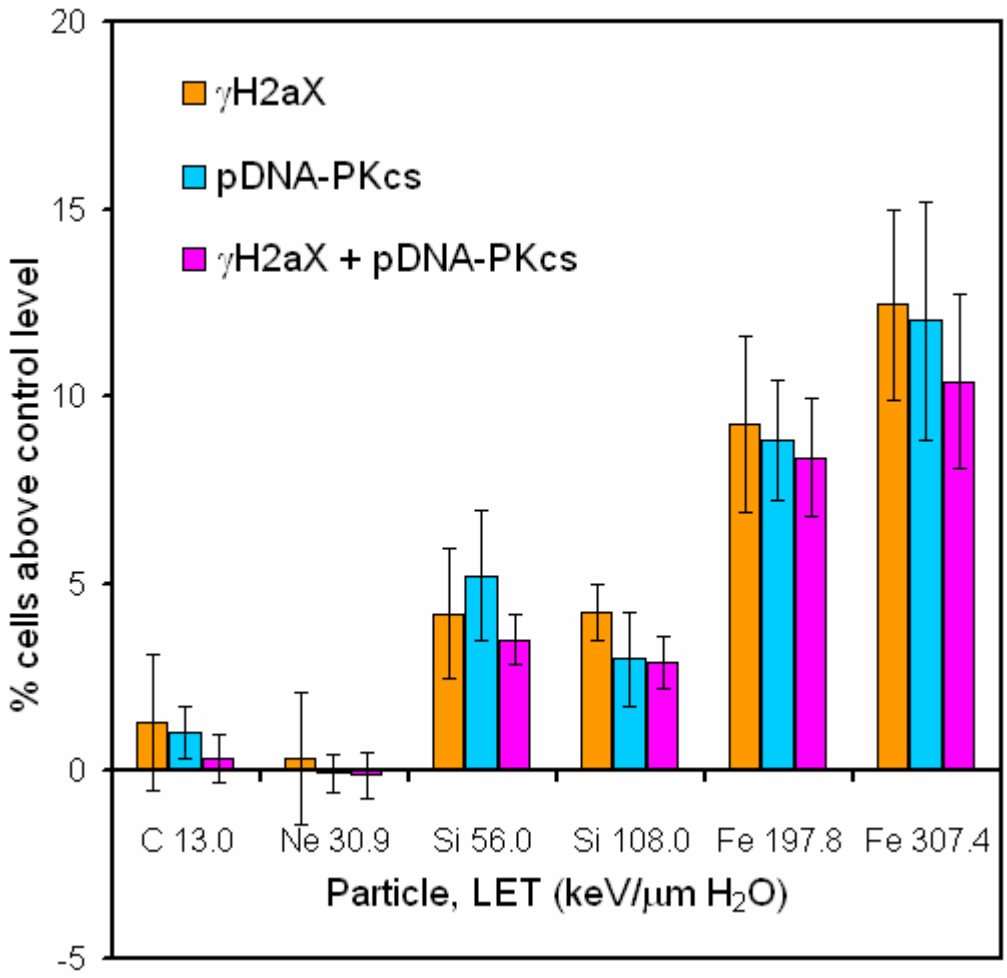

Figure 13.6: Percentage of human fibroblasts with at least one radiation-induced γH2AX-, pDNA-PKcs-focus or colocalization of both, after exposure to an equal fluence of varying particles. Results are means of at least 4 samples per LET value ± s.e..

The results from both the pATM-γH2AX- and the pDNA-PKcs-γH2AX-dualstainings have been gained by relying on identical methods for staining and evaluation. Therefore, data on γH2AX-foci from both experiments may be directly combined to further decrease uncertainties of mean values due to larger sample numbers (see figure 13.7). Clearly, a monotonous increase in the number of cells with radiation-induced γH2AX-foci or DSBs, respectively, with LET is shown for exposures to charged particle beams with LET values greater than 50 keV/µm H_2O, whereas lower-LET beams are not able to induce a visible increase in H2AX phosphorylation at the same particle fluence.

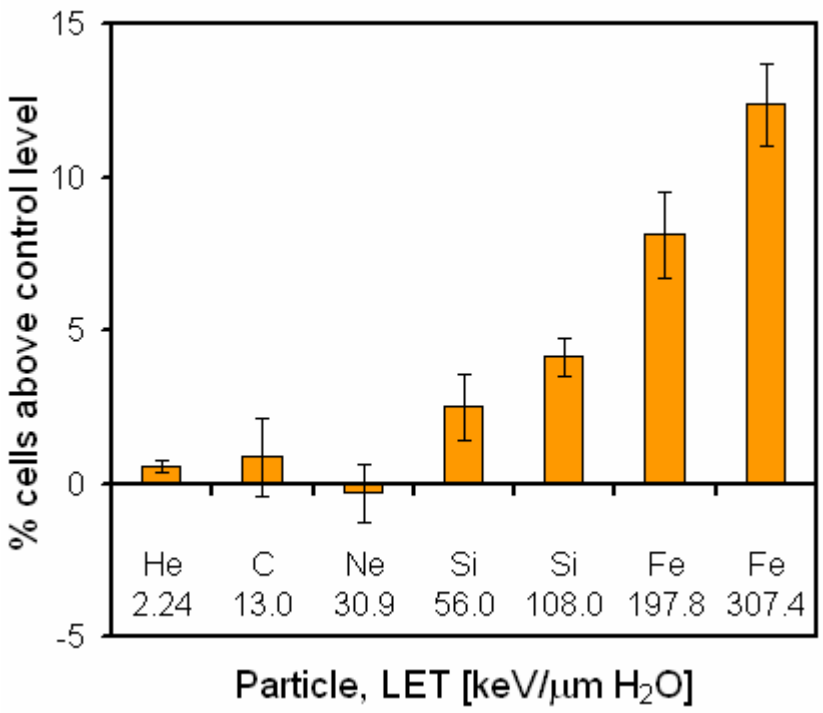

Figure 13.7: Fraction of human fibroblasts with at least one radiation-induced γH2AX (ser 139)-focus, after exposure to an equal fluence of varying particles. Results are means of at least 8 samples per LET value ± s.e. (with the exception of He 2.24, where only 2 samples have been available).

For the sake of completeness, results for ^{4}He (2.24 keV/µm H_2O) have been added, even though they are only based on two samples. Further verification could not have been achieved because no beam time for ^{4}He has been available in the third HIMAC run. However, since both samples exhibit staining patterns very similar to mock-irradiated samples, and no increase in either ATM, or DNA-PKcs and H2AX phosphorylation could be detected even for comparably higher-LET particles such as ^{12}C and ^{20}Ne, no significant insights are to be expected from further exposures to ^{4}He ions for the selected experimental parameters, which may therefore very well be omitted.

13.1.5. Checkpoint Signalling – pChk2 (Thr 68)

As has been elaborated in the introductory part (chapters 5.2 and 5.7), DNA damage caused by ionizing radiation leads to the activation of ATM at sites of DSBs. Active ATM (phosphorylated at ser 1981) is known to be the central player in cell cycle mediation in response to ionizing radiation and triggers various pathways that result in a transient halt or even a sustained arrest of cell cycle progression at specific checkpoints. Furthermore, cell cycle regulation pathways are intertwined with the P53-mediated apoptotic response, with both mechanisms essentially being selectively initialized depending on the extent and type of stress.

In the last sections, the presence of DSBs as shown by γH2AX foci and phosphorylated DNA-PKcs, which indicates the activation of the NHEJ repair mechanism, has been demonstrated for some of the selected exposure conditions. Furthermore, kinase-active ATM has been found at an increased number of sites. As a foremost ATM-dependent event, the observed phosphorylation of H2AX is already a direct consequence of increased ATM activity. Thus, it remains to be shown whether this degree of ATM activation may also be sufficient to induce other downstream events and have a pronounced effect on the regulation of key proteins in the cell cycle regulatory network as well.

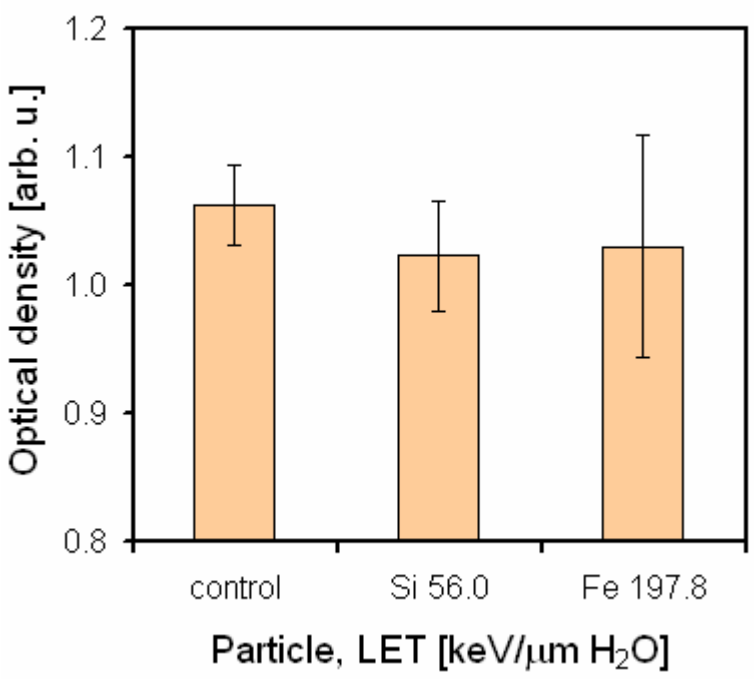

Figure 13.8: The mean concentration of pChk2 (thr 68) in human fibroblasts after exposure to an equal fluence of ^{28}Si or ^{56}Fe ions compared to a control group. Results are means of at least 4 samples per LET value ± s.e..

Pre-experiments (see sections 11.1.1 and 11.2) and current literature (165) show that the Chk2 protein is phosphorylated rapidly at threonine 68 in response to ionizing radiation, leading to the presence of a significant amount of nuclear pChk2 already at one to two hours after irradiation. Due to ATM activity being a prerequisite for Chk2-phosphorylation, samples exposed to the higher-LET ^{28}Si and ^{56}Fe beams (56.0 and 197.8 keV/µm H_2O), which have been demonstrated to exhibit an increased number of pATM foci, have been immunocytochemically stained for pChk2 (thr 68) according to the protocol supplied in section 8.4.4. Digital images have been acquired for determination of the pChk2 concentration in single nuclei as described by equation (9.10) in section 9.4.

The determined mean optical densities are compared to control samples and are illustrated in figure 13.8. As is very obvious, no radiation-induced increase in pChk2 (thr 68) concentration could be observed under the given circumstances and within the methodical limitations. However, a few points need to be kept in mind when interpreting

these results: Firstly, a much larger increase in the amount of stain is necessary to be successfully detected when it is distributed over the whole nucleus rather than being localized at small focal sites. Thus, a higher threshold for the detection of increased pChk2 may be expected than for pATM, pDNA-PKcs or γH2AX. Furthermore, it cannot be safely assumed that the ATM-dependent phosphorylation of Chk2 in response to a low fluence of high-LET particles takes place following the same time course as for higher doses of low-LET photon radiation, which were delivered in pre-experiments and many published studies on cell cycle regulation, due to different patterns of DNA damage. On the other hand, a significant increase in pChk2 is observed in response to DNA damage, which was induced by various treatments, over a long period of time, starting a few minutes up to several hours after damage occurrence (79, 164, 165, 166). From this point of view, the chosen two hours time point is well within this limits, and any damage induced activation of the ATM-Chk2 signalling pathway should very likely lead to the presence of an increased amount of pChk2 (thr 68) at this time.

Overall, the detected concentrations of pChk2 (thr 68) for both exposed groups suggest that short-term effects on cell cycle progression due to the traversing particles can be expected to be minimal. However, this result does not contradict published data on Chk2 activation in response to IR exposure, which have been obtained using much larger radiation doses of at least several hundred mGy.

13.1.6. P53-Mediated Signalling – pP53 (Ser 15)

Extensive DNA damage is known to lead to the initiation of growth arrest or cell death via a mechanism featuring the apoptosis-promoting P53 protein, with arrest being the dominating reaction in human fibroblasts, as has been discussed in section 5.8. In this process, P53 is phosphorylated on several locations, among them being serine 15, which is targeted by both activated ATM as well as Chk2 and plays an essential role in cell cycle regulation and apoptotic pathways. Therefore, the amount of pP53 (ser 15) present in a single cell or culture at a defined time point after exposure may be interpreted as a measure for cell inactivation or apoptosis induction by the corresponding radiation hazard.

In pre-experiments, chamber slides containing human skin fibroblasts were exposed to 100 kV X-rays and incubated for one hour. Afterwards, they were stained for pP53 (ser 15) using colour signal amplification methods as described in section 8.4.4, and compared to control samples. It was found that control cells exhibit no visible colour staining at all due to a negligible amount of P53 being phosphorylated at serine 15 in the absence of radiation-induced DNA damage. In comparison, an X-ray dose of 500 mGy yielded a weak, yet clearly visible nuclear staining signal, whereas for higher radiation doses of a few Gy, the pP53 (ser 15)-concentration was observed to increase with dose.

On this basis, several slides with fibroblasts, which had been exposed to an equal fluence of different particle beams at HIMAC as described above, were immunocytochemically

stained for pP53 (ser 15) with the AEC chromogen and visually assessed under the microscope. In all cases, no colour staining could be observed in the exposed cells at all, which perfectly mirrored the condition of mock-irradiated control samples. Therefore, it has to be concluded that no detectable amount of pP53 (ser 15) is present at the two hours time point after irradiation. However, since phosphorylation at this site is mediated by Chk2, which was not found to be significantly activated under the selected exposure parameters, and ATM, which also failed to induce a pronounced increase in pChk2 (thr 68), this insight is in good agreement with the other results and fits the general picture.

13.1.7. Double-Strand Breaks in Hit and Bystander Cells

As the last series for evaluation of human fibroblasts that were exposed to equal particle fluences delivered by different beams, cell layers were immunocytochemically stained for γH2AX (ser 139) using AEC red according to the protocol given in section 8.4.4. Digital images were acquired and evaluated by an observer in a blinded manner in order to determine the fraction of cells with at least one and without visible γH2AX foci, and the percentage of cells with radiation-induced foci was calculated as described in section 13.1.3. In principle, this method of γH2AX assessment is very similar to the γH2AX-experiments based on immunofluorescence that were, as part of a dual-staining with either pATM or pDNA-PKcs, presented in sections 13.1.3 and 13.1.4. However, advantageous staining characteristics of this staining method such as an extremely low unspecific background and high colour intensities outweigh the greater flexibility of IF in some cases. For the task at hand, the evaluation of γH2AX, the signal enhancement protocol based on the Labvision reagents exhibited greater sensitivity than IF and was therefore applied for an in-depth assessment of a few selected exposure conditions that were deliberately limited to bare particle beams without PMMA layers for LET modulation.

The percentage of cells with radiation-induced γH2AX foci may be directly judged against the fraction of cells with nuclear particle traversals, as is illustrated in figure 13.9. First of all, comparison of these γH2AX-results with data from IF co-staining (figure 13.7) shows that the overall number of cells with detected foci is significantly higher in AEC-stained samples, which is due to the better signal-to-background ratio of this method as announced above. As could be expected from the γH2AX and pATM IF experiments, exposures in the ^{4}He beamline (2.24 keV/µm H_2O) yield no detectable increase in H2AX phosphorylation compared to the mock-irradiated group. Rather surprisingly, the number of γH2AX foci scored in ^{20}Ne exposed samples slightly exceeds control levels, which is the first indication of a biologic response induced by these particles under the given exposure conditions and may, again, be attributed to the higher sensitivity of the applied staining method.

In good agreement with the IF results presented in chapters 13.1.3 and 13.1.4, a clear increase in the formation of γH2AX (ser 139) foci with radiation LET is observed. Moreover, for the samples exposed to ^{56}Fe ions, the highest-LET beam (197.8 keV/µm

H_2O) used in this experimental series, the average fraction of cells with one or more γH2AX foci amounts to nearly 20 percent, which exceeds the calculated fraction of cells subjected to nuclear particle hits that is given by approximately 15 percent. Therefore, when it is assumed that every ^{56}Fe particle traversing a nucleus induces the formation of a γH2AX focus that persists until two hours after irradiation and is also successfully detected with the applied staining and analysis procedures, an additional group of cells (>4%), which have either been subjected to a cytoplasmic particle traversal or not hit at all, exhibit nuclear γH2AX foci that mark the presence of DSBs.

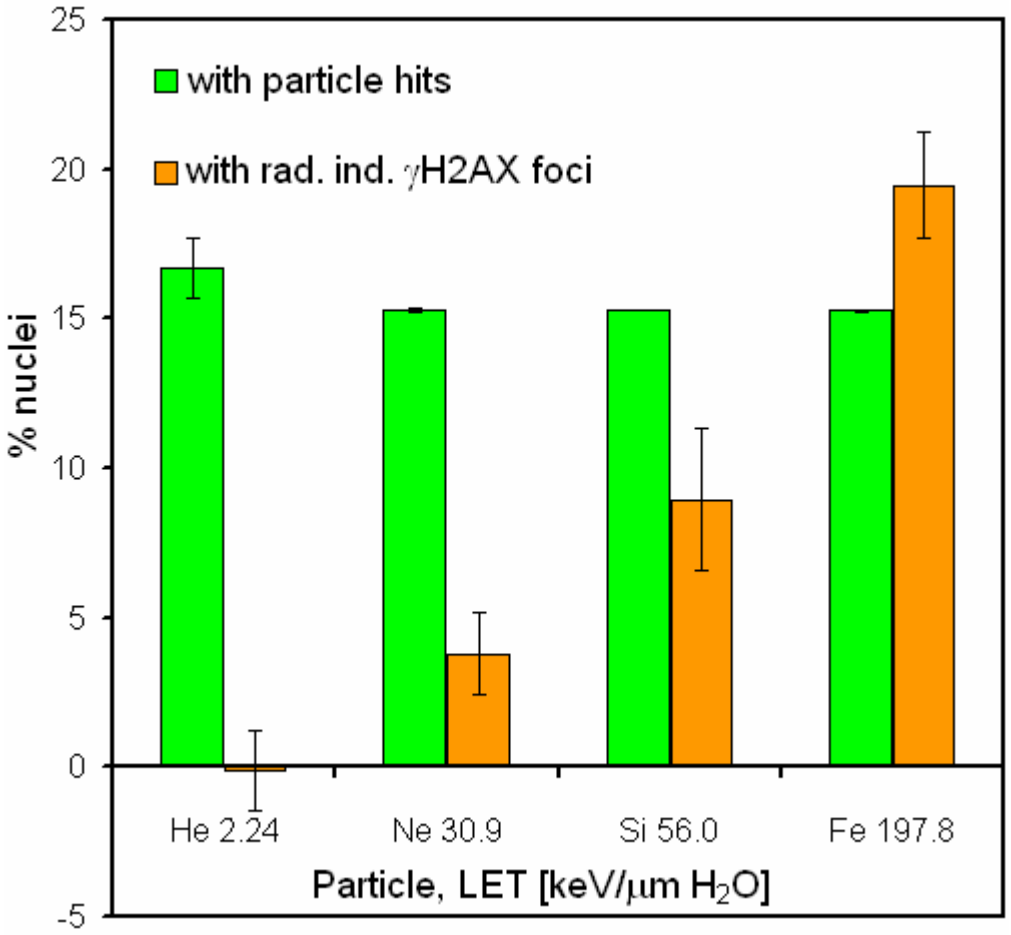

Figure 13.9: Fraction of human fibroblasts exposed to an equal fluence of varying particles with at least one radiation-induced γH2AX-focus compared to the fraction of cells subjected to nuclear particle traversals. Results are means of 4 samples per LET value (3 for "Ne 30.9" due to limited availability of the ^{20}Ne beam) ± s.e.. The deviation in the percentage of hit cells indicates slightly different particle fluences delivered to individual samples. In case of He 2.24, the greater variation is due to a higher than nominal fluence for two samples exposed in HIMAC series I.

Considering recent findings that γH2AX foci are also formed in human fibroblasts after medium transfer from a low-LET irradiated culture (111), it seems plausible that the

detected surplus foci may be attributed to a bystander response. Furthermore, by assuming that every single nuclear particle track is represented by and detected positively as a γH2AX focus for determination of the "bystander" group, this fraction is rather underestimated, since a detection efficiency of less than 100 percent is to be expected. However, while these findings and considerations strongly argue for the spread of DNA damage by a bystander effect in the ^{56}Fe exposed samples, it cannot be unequivocally proven from the data presented because of insufficient statistical significance ($t = 0.066$) due to the small data set when the fractions of cells with nuclear hits and with γH2AX foci are directly compared, and due to limited knowledge on the exact locations of the particle traversals in the cell layer.

13.2. Time-Dependence of the Cellular Response to Equal Doses of Different Particles

So far, all presented experimental results were dedicated to exposures to equal, low particle fluences delivered with different high energy ion beams, resulting in statistically similar relation between non-hit and cells with nuclear or cytoplasmic particle traversals. Thus, they were aimed at the characterization of effects due to the intrinsic properties of single particles and the detection of a damage spread to bystander cells. However, while the concept of fluence may likely be advantageous when discussing cellular effects of very low doses of particle radiation, these results may not be easily related to dose limits in current operational radiation protection or used for RBE assessment, since, obviously, very different radiation doses have been delivered to each group of samples.

Therefore, a second experimental approach has been adopted for this thesis, which allows for the comparison of biologic effects at a defined, low dose level and, thus, RBE, while still accounting for fundamental, qualitative differences in the biologic response at the cellular level. This is achieved by two means: Firstly, a dose value of approximately 60 mGy has been chosen for this experimental series, which especially highlights specific differences in the distribution of damaging events across the cell layer. In detail, the absorption of 60 mGy of the highest LET ^{56}Fe particles (197.8 keV/µm H_2O] incident perpendicular on the cell layer corresponds to about one third of the fibroblast nuclei being traversed by a particle. For ^{28}Si [56.0 keV/µm H_2O], about three fourth of all cells are subjected to nuclear particle hits, whereas the fraction of hit cells exceeds 90 percent in the samples exposed to the lower LET ^{12}C and ^{20}Ne beams (see table 10.5). Therefore, at a dose of 60 mGy, the available particle beams at HIMAC were ideally suited for a thorough elucidation of specific biologic effects due to different distribution patterns of ionization events. Secondly, there is evidence that the time course of DNA damage repair and triggering of particular molecular events in the cellular signal transduction network is dependent on radiation quality (167). According to these findings, differences in the cellular response are already to be expected in the early phase after irradiation, which represents the period of interest for this thesis. Therefore, all investigated cellular events,

namely the formation of pATM (ser 1981), pDNA-PKcs (thr 2609) and γH2AX (ser 139) foci, have been assessed at three different time points after exposure (20', 1 and 2 hours) in order to draw conclusions on the time course of the cellular response and the kinetics of focus formation and dissolution for the targets of interest.

In the following sections, results for the given signalling events shall be presented according to the applied evaluation method. In the final part, the influence of particle species on radiation-induced effects will be discussed by comparison of samples exposed to different particle beams with an equal LET of approximately 30 keV/µm H_2O, which was realized by application of PMMA binary filter of appropriate thickness.

13.2.1. Formation and Persistence of pATM (Ser 1981) Foci

Normal human skin fibroblasts were exposed to 60 mGy of high-energy charged particle radiation as described above. After irradiation, cells were allowed to recover in an incubator. At three different time points, a sufficient number of samples were fixed and stored. The cell layers were eventually stained for pATM (ser 1981) via immunofluorescence (see figure 13.10 for a representative example) according to the protocols supplied in chapter 8.4.3. Acquired digital images of all samples were used for determination of pATM foci sizes as outlined in section 9.6.

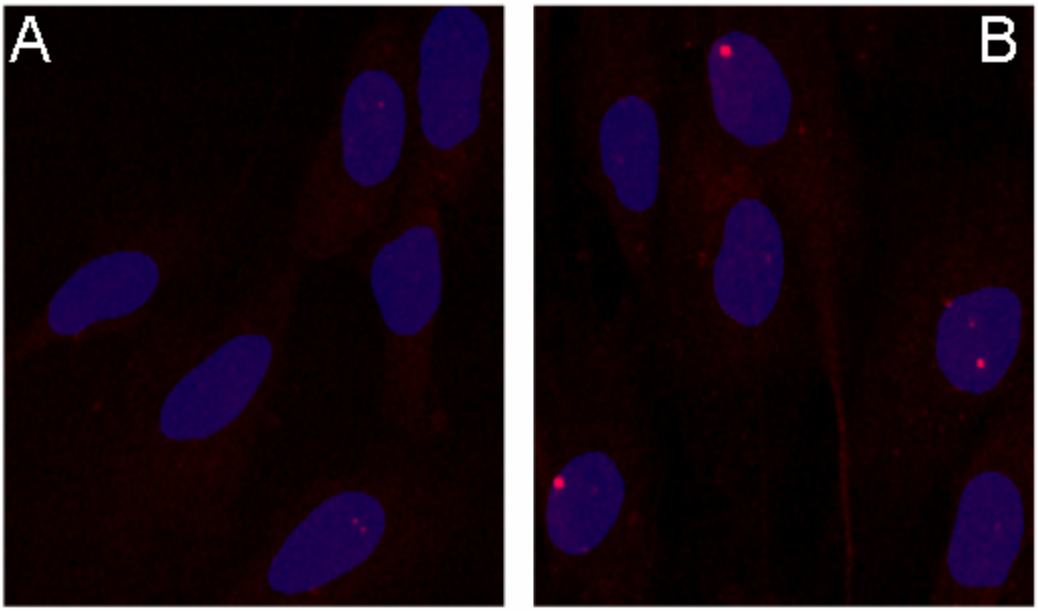

Figure 13.10: Human fibroblasts IF-stained for pATM (ser 1981) two hours after exposure to 60 mGy of ^{56}Fe-ions (B, 197.8 keV/µm H_2O) compared to mock-irradiated cells (A). Pictures have been generated by false-colouring and overlaying greyscale images from the Rhodamine Red-X-marked target and HOECHST 33342 nuclear counter-stain.

The total number of pATM (ser 1981)-foci per 100 fibroblasts, independent of size, has been obtained for the different particle beams and is illustrated in figure 13.11 as a function of time after irradiation. At the 20' time point, the highest number of foci is found in ^{28}Si exposed samples followed by ^{20}Ne and ^{56}Fe. However, whereas ATM activity significantly decreases with time in cells exposed to particle beams with an LET below 100 keV/µm H_2O (^{12}C, ^{20}Ne and ^{28}Si) until two hours after irradiation, the number of pATM-foci stays at a constant level in Fe-exposed samples during the same period. As a consequence of this behavior, at the 2h time point ATM activity is observed to be highest in cells irradiated with ^{56}Fe ions.

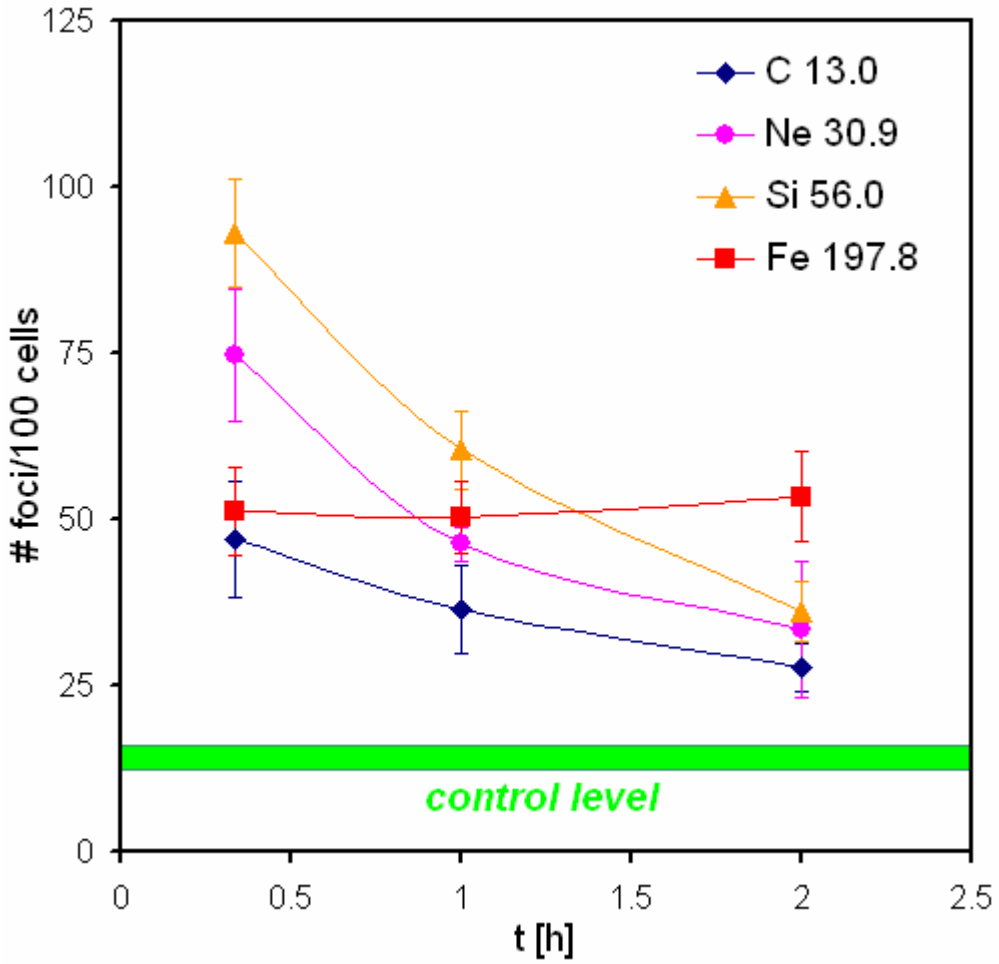

Figure 13.11: Total number of pATM (ser 1981) foci per 100 human skin fibroblasts as a function of time after exposure to 60 mGy of varying particles. Results are means of 4 to 6 samples per LET value and time point ± s.e.. Particle species, LET values [keV/µm H_2O] and the level of pATM foci in control samples (± s.e.) are indicated.

Furthermore, comparison with the control group shows that the number of foci in ^{56}Fe-exposed cells above the pATM-level in mock-irradiated cells amounts to around 40 foci per 100 fibroblasts. This value concurs very well with the number of ^{56}Fe particles traversing nuclear areas as calculated from particle fluence and the average size of a

fibroblast nucleus, which corresponds to 43 per 100 cells (see table 10.5). In contrast, the number of detected pATM-foci in cells irradiated with the lower LET beams lies well below the calculated number of particle hits. Taken together, these results support the view that single particles of sufficiently high lineal energy are able to trigger cellular signal transduction mechanisms whereas lower ionization densities along the particle tracks may fail to do so. Thus, this finding fully agrees with analogous insights obtained from pATM (ser 1981) data for a recovery time of two hours, which were gathered in the exposures to equal particle fluences (section 13.1.1).

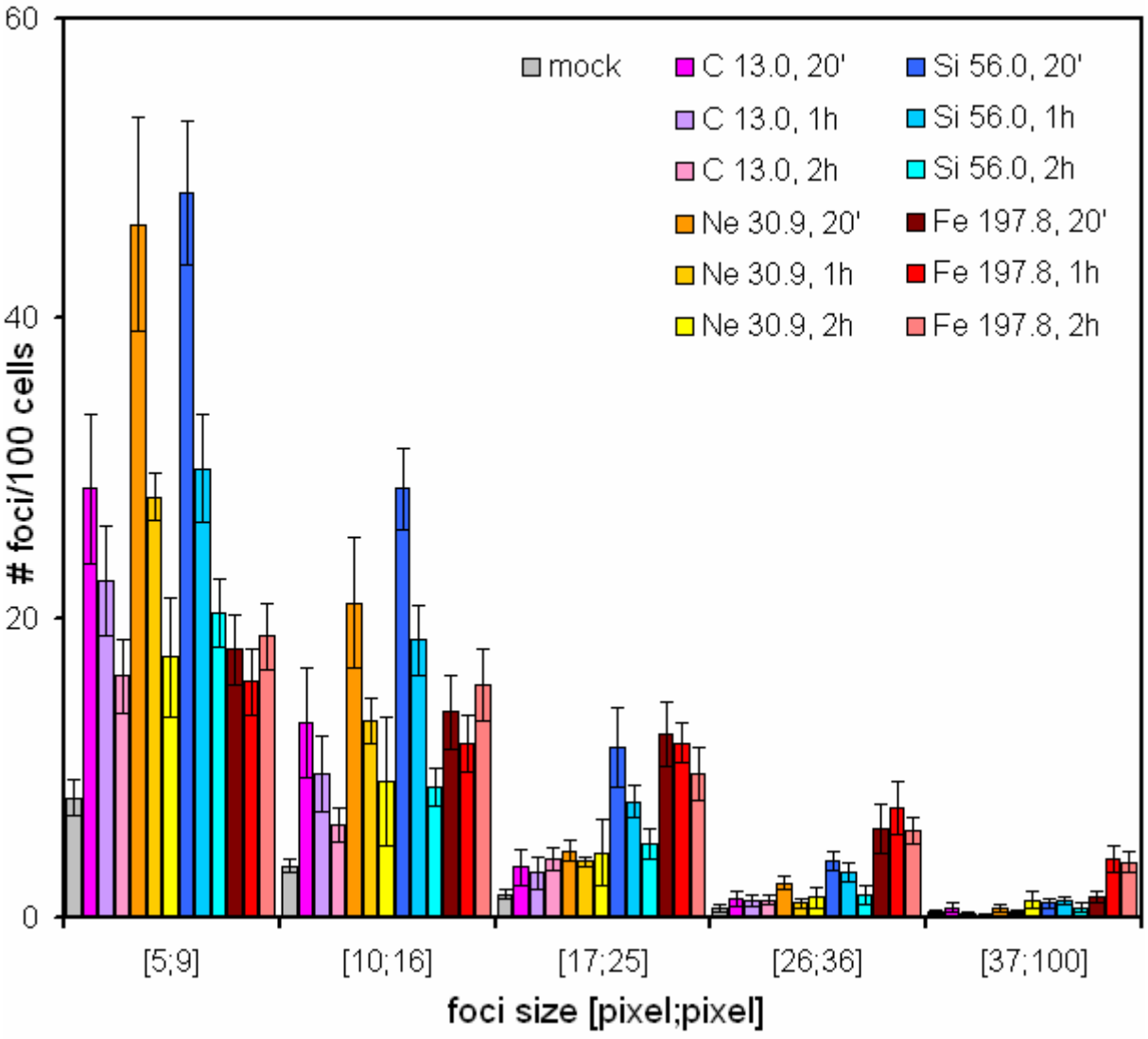

Figure 13.12: Different sizes of detected pATM (ser 1981) foci per 100 human skin fibroblasts after exposure to 60 mGy delivered with different particle beams. Foci sizes are given in [pixel; pixel] intervals (1 pixel ≈ 0.11 µm²). Particle species, LET values (in [keV/µm] H_2O) and recovery times are indicated in the picture legend. Results are means of 4 to 6 samples per particle type and time point ± s.e..

Since the time-dependence of the total number of pATM (ser 1981) foci has been found to exhibit a rather curious behavior, this phenomenon shall be elucidated in more detail. For

this purpose, pATM foci were grouped according to their size, as is illustrated in figure 13.12. For better readability, the data sets have been arranged so that each three consecutive bars correspond to the same particle type, with increasing recovery time from left to right.

Several insights may be derived from figure 13.12: Firstly, the decrease in ATM activity observed in samples exposed to the lower LET ^{12}C, ^{20}Ne and ^{28}Si beams is especially pronounced for the smaller sized foci. In contrast, the number of smaller sized pATM foci stays at the same level in the ^{56}Fe-irradiated cells, whereas slight indication for an increase of the largest pATM foci is found from the 20' to the 2 hours time point. Furthermore, higher-LET radiation (^{56}Fe and, to a lesser extent, ^{28}Si) clearly yields a relatively greater portion of larger pATM foci.

Taken together, due to pATM being predominantly located at DNA DSBs, these findings suggest that smaller sized pATM (ser 1981) foci may be interpreted as sites of less extensive DNA damage that is successfully repaired in a short period after exposure. Basically, the "dissolution rate" of the smallest detected pATM foci present is even higher than indicated by the bars referring to the pixel interval [5;9], since it is plausible to assume that a significant number of pATM foci will still form at a later time point than 20' after irradiation, and that the larger foci do not dissolve instantly and, thus, essentially have to "progress" through smaller sizes with ongoing repair. Keeping this in mind, the seemingly constant ATM activity in ^{56}Fe-exposed fibroblasts from 20' to 2 hours after irradiation may also be due to a state close to equilibrium between forming, growing, shrinking and dissolving pATM foci, which would also account for the smaller number of the largest pATM foci at the 20' time point. Moreover, the increase in the mean size of pATM foci with LET strongly argues for the induction of locally confined, extensive DNA damage along the tracks of particles with high lineal energies, which agrees well with findings presented in section 13.1.1. Especially the results from ^{56}Fe-irradiated cells elucidate that these damage clusters cannot be successfully dealt with within two hours after exposure, arguing for a less efficient repair of this type of damage.

Overall, the presented pATM (ser 1981) data shows that in the low dose range, the time-dependent cellular response to particle radiation is modulated by the energy deposition of single particles. The specific behavior in formation and persistence of pATM foci induced by different particle beams illustrate that both the initial extent of radiation-induced damage and repair kinetics are greatly depending on radiation quality.

13.2.2. Formation and Persistence of pDNA-PKcs (Thr 2609) Foci

In analogy to the assessment of ATM activation in the last section, layers of normal human skin fibroblasts that had been exposed to 60 mGy of different high-energy charged particles were fixed at three different time points after exposure. Digital images of samples IF-stained for pDNA-PKcs (thr 2609) were utilized for evaluation of pDNA-PKcs foci sizes (section 9.6).

By summation over all foci sizes, the total number of pDNA-PKcs (thr 2609) foci per 100 fibroblasts has been determined for the different exposure conditions. The results are depicted in figure 13.13 as a function of the recovery time after irradiation. Comparison with pATM (ser 1981) data (figure 13.11) shows that the event of pDNA-PKcs focus formation shares several qualitative similarities with ATM in its time and LET dependent behavior: The total number of pDNA-PKcs foci induced by the three lower LET exposures (^{12}C, ^{20}Ne and ^{28}Si) decreases significantly from the 20' to the 2 hours time point. In contrast, the number of foci in ^{56}Fe-irradiated cells stays at a constant level within statistical uncertainties in the same timeframe. In analogy to the pATM results, the number of pDNA-PKcs foci at the 20' time point is highest in ^{28}Si-exposed cells, whereas the ^{56}Fe-exposed samples come out on top at two hours due to the rapid decrease of DNA-PKcs activity in fibroblasts subjected to ^{28}Si ions. Furthermore, for both pATM and pDNA-PKcs, exposure to ^{12}C particles yields the lowest number of foci at all investigated time points.

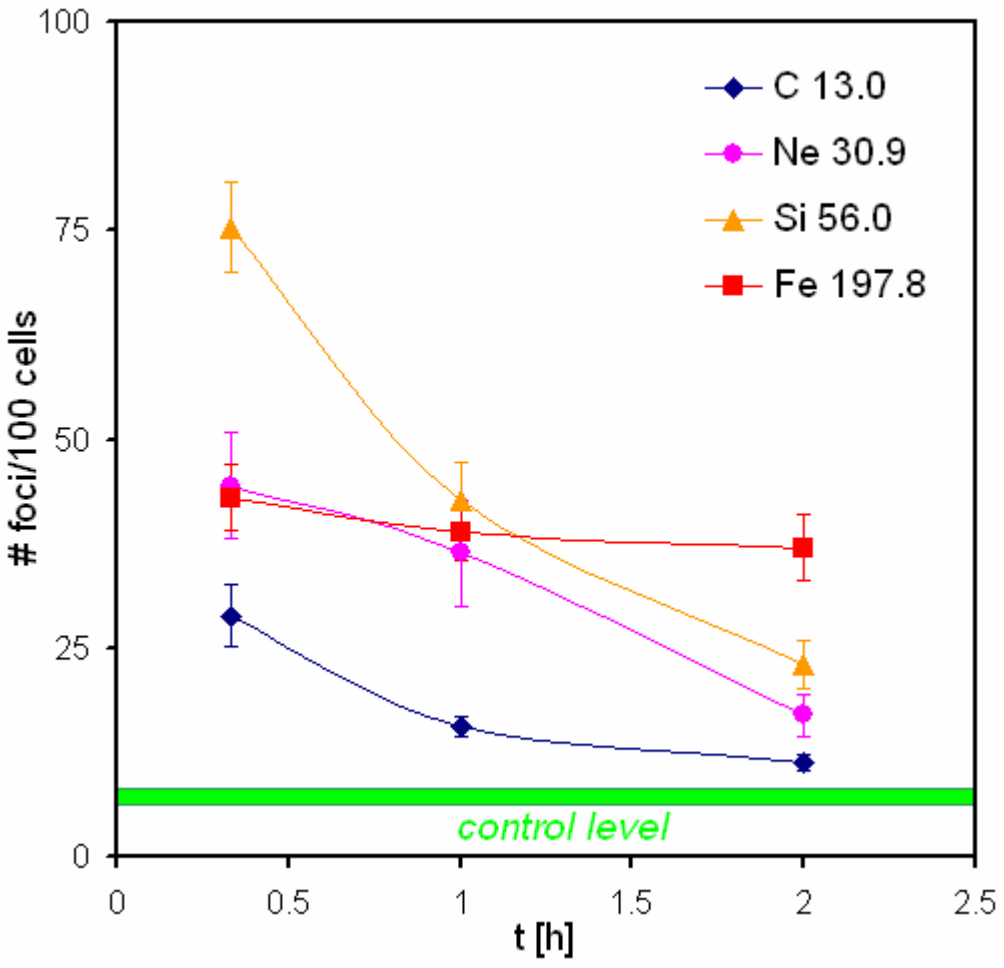

Figure 13.13: Total number of pDNA-PKcs (thr 2609) foci per 100 human skin fibroblasts as a function of time after exposure to 60 mGy of varying particles. Results are means of 5 to 6 samples per LET value and time point ± s.e.. Particle species, LET values [keV/µm H_2O] and the level of pDNA-PKcs foci in control samples (± s.e.) are indicated.

The most obvious difference between pATM and pDNA-PKcs is found at 20', the earliest time point investigated, when samples exposed to ^{20}Ne and ^{56}Fe are compared: Whereas both beams yield about the same initial number of pDNA-PKcs foci, the early ATM activity is observed to be significantly higher in cells irradiated with ^{20}Ne particles. However, association of the pDNA-PKcs data for ^{20}Ne with ^{12}C and ^{28}Si suggests that the mean total number of pDNA-PKcs foci in ^{20}Ne exposed samples given for the 20' time point may be slightly underestimated when a qualitatively similar time-dependence for all three particle beams is assumed. It needs to be stressed that this assumption is valid within the statistical uncertainties of the presented pDNA-PKcs data, which do by no means imply significantly different patterns in DNA-PKcs phosphorylation due to ^{20}Ne ions.

In analogy to ATM, the absolute number of pDNA-PKcs (thr 2609) foci in samples exposed to the three lower LET beams above the control level is well below the calculated number of nuclear particle traversals, which amounts to about 43 per 100 fibroblasts. In cell layers irradiated with ^{56}Fe ions, approximately 30 to 35 radiation-induced pDNA-PKcs foci per 100 cells are detected, which is a bit less than the number of pATM foci under identical exposure conditions. This observation may be explained in different ways: Firstly, while both types of foci can be expected to predominantly colocalize with DNA DSBs, they correspond to different events in the cellular signalling mechanism. Besides, cell layers of about 60 percent confluence have been used for exposure, which include a large number of cells in G0/G1 phase as well as another fraction of cells that are progressing through the different cell cycle towards mitosis. As outlined in section 5.6, the two known mechanisms for DSB repair, NHEJ and HR, contribute to a varying extent, depending on the position in cell cycle. With DNA-PK being one of the major players in NHEJ (chapter 5.4), the presence of a pDNA-PKcs (thr 2609) foci may basically be interpreted as DNA DSBs that are repaired via NHEJ, which is the dominant repair pathway in the G0/G1 phase. Obviously, while this includes the major portion of all radiation-induced DSBs in this setup, DSBs in cells proceeding through other phases such as G2 will likely initialize an HR response, thus avoiding the formation of a pDNA-PKcs (thr 2609) focus. Therefore, the detected number of pDNA-PKcs foci in ^{56}Fe exposed fibroblasts is well in line with results presented in former sections, which suggest that every nuclear traversal by a particle of high lineal energy such as the applied ^{56}Fe ions yields DSBs along its track, thus triggering a pronounced signalling response.

A more detailed assessment of pDNA-PKcs (thr 2609) focus formation in dependence of the recovery time after exposure is provided in figure 13.14, were the detected pDNA-PKcs foci are grouped according to their size. Each three consecutive bars refer to identical exposure conditions and are arranged with increasing time after irradiation from left to right. In similarity to pATM, a significant decrease in the number of smaller sized pDNA-PKcs foci is found in samples exposed to the lower-LET ^{12}C, ^{20}Ne and ^{28}Si beams. The situation is clearly different in ^{56}Fe-irradiated cells, where the number of foci stays at roughly the same level for all foci sizes. Furthermore, in samples exposed to the ^{56}Fe beam, there is a slight tendency towards larger foci at the one hour time point, which results in an average size of about 1.3 μm^2 compared to 1.0 μm^2 at both 20' and 2 hours, respectively.

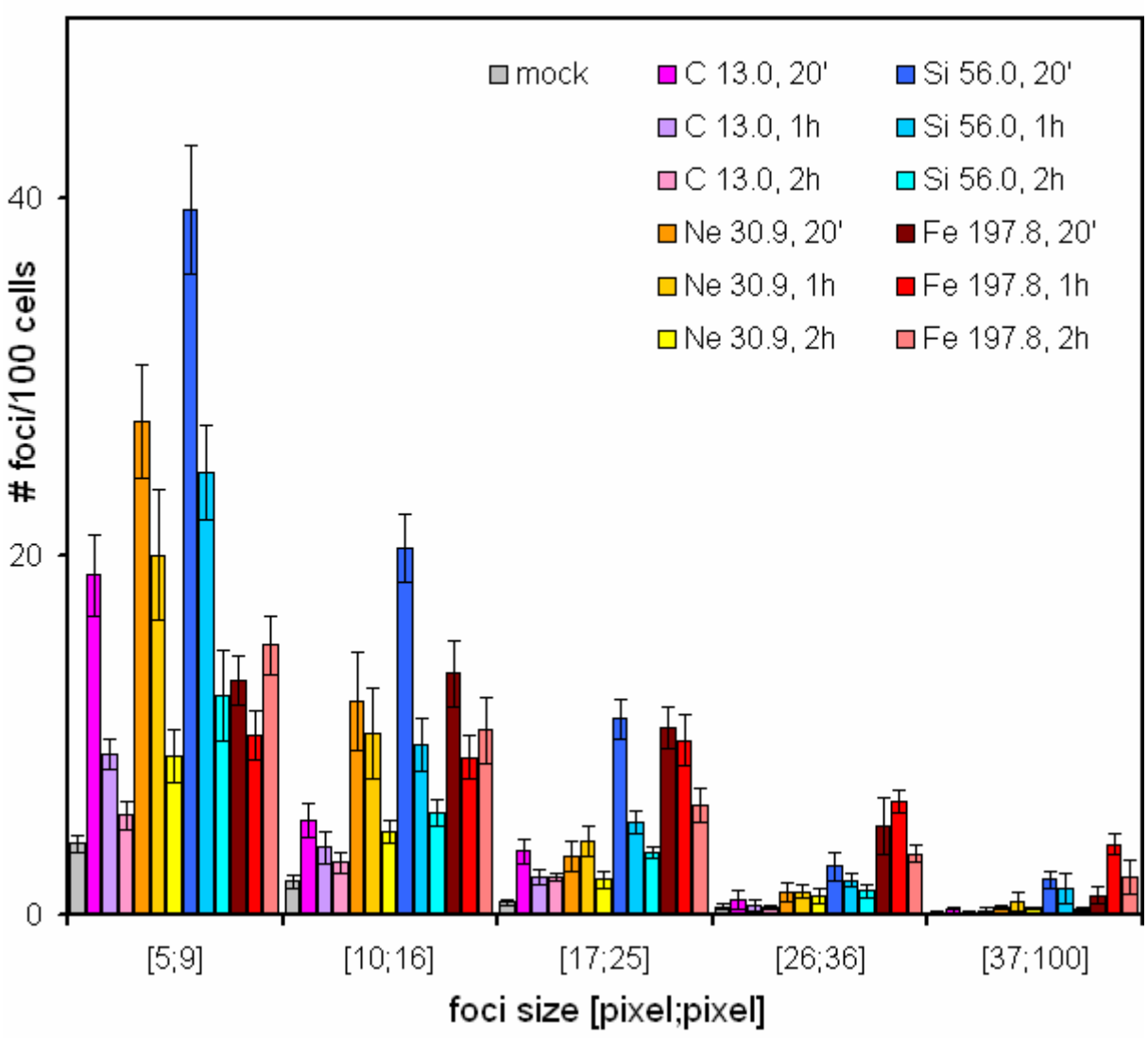

Figure 13.14: Different sizes of detected pDNA-PKcs (thr 2609) foci per 100 human skin fibroblasts after exposure to 60 mGy delivered with different particle beams. Foci sizes are given in [pixel; pixel] intervals (1 pixel ≈ 0.11 µm2). Particle species, LET values (in [keV/µm H_2O]) and recovery times are indicated in the picture legend. Results are means of 5 to 6 samples per particle

Keeping this in mind, the presented pDNA-PKcs (thr 2609) data shows that a large portion of DNA damage caused by 60 mGy delivered with different ion beams is readily dealt with via the NHEJ pathway. The time-dependent decrease in the number of foci in cells exposed to the lower-LET ^{12}C, ^{20}Ne and ^{28}Si particles suggests that at a fraction of the initially damaged sites, the processing and rejoining of DNA ends is being successfully performed, showing significant progress until the two hours time point. In contrast, the almost constant number of pDNA-PKcs foci in ^{56}Fe irradiated fibroblasts at all three time points indicate the quick assembly of the NHEJ machinery at damaged sites, however, these efforts appear to be less rewarding than in cells exposed to lower-LET particles during the investigated time period. It is therefore tempting to speculate that the specific damage clusters induced by particles of sufficiently high lineal energy cannot be easily

repaired via the NHEJ mechanism. Instead, the damaged DNA molecules either require extensive processing over an elongated time period that may eventually allow for a reconnection of free DNA ends or, possibly, cannot be successfully restored at all. This interpretation agrees with results from current literature, were significantly slower kinetics and a lower efficiency of the NHEJ mechanism has been found for DNA damage induced by higher-LET particle irradiation with doses above 2 Gy (167).

Apart from that, it needs to be stressed that the NHEJ pathway is to be considered an error-prone mechanism that may introduce deviating base sequences into the genome at the location of the DSB (see section 5.4). From this point of view, all selected exposure conditions result in an increased probability for mutation, which appear to be lowest in the ^{12}C followed by the ^{20}Ne exposed cells. Due to the curious differences in the initial extent and the time-dependent behavior of DNA-PKcs phosphorylation in samples irradiated with ^{28}Si and ^{56}Fe particles, conclusions on the relative mutation risk, which would be of importance for radiation protection purposes, cannot be drawn in a simple way.

As a fundamental insight in analogy to the interpretation of pATM (ser 1981) data, the presented results for pDNA-PKcs (thr 2609) show that for low doses, the time-dependent initialization and persistence of specific radiation-induced cellular signalling events are greatly influenced by radiation quality.

13.2.3. Colocalization of γH2AX and pATM

A detailed description of the assessment of colocalization of pATM and γH2AX has been given in section 9.7. Briefly, irradiated (60 mGy) and control samples of fibroblasts were co-stained for pATM (ser 1981) and γH2AX (ser 139) using Cy2- and Rhodamine Red-X conjugated secondary antibodies. Processed digital images were scored for cells with one or more pATM-, γH2AX-foci or sites of colocalization of both foci types in a blinded fashion aimed at deriving the fraction of cells with foci that may be attributed to a radiation-induced response.

In this chapter, only the results for pATM and the colocalization of both foci types are presented. For the sake of better statistics, the data on H2AX phosphorylation has been combined with results from pDNA-PKcs (thr 2609) and γH2AX (ser 139) dual-stainings (see chapter 13.2.4) and will be discussed separately in section 13.2.5.

The fractions of cells with visible colocalizing foci of pATM and γH2AX for different particle beams and recovery times are shown in figure 13.15. As is very obvious, the number of cells with detectable foci increases with radiation LET for all three time points. Furthermore, the fraction of cells with foci decreases with time for all selected exposure conditions until two hours after exposure. However, when this time-dependent decrease is viewed relatively to the initial number of cells with foci at the earliest time point of 20', significant differences between different particle types are uncovered: Whereas the

fraction of fibroblasts exposed to the lowest-LET ^{12}C ions that still display sites of colocalization between pATM and γH2AX have been reduced to about one third of the initial value at 20', approximately three fourth of the cells with foci still remain in samples irradiated with ^{56}Fe particles after the same recovery time. Correspondingly, cells exposed to ^{20}Ne and ^{28}Si ions fit in between, exhibiting, on average, around 57 and 68 percent of the initial foci at two hours after treatment.

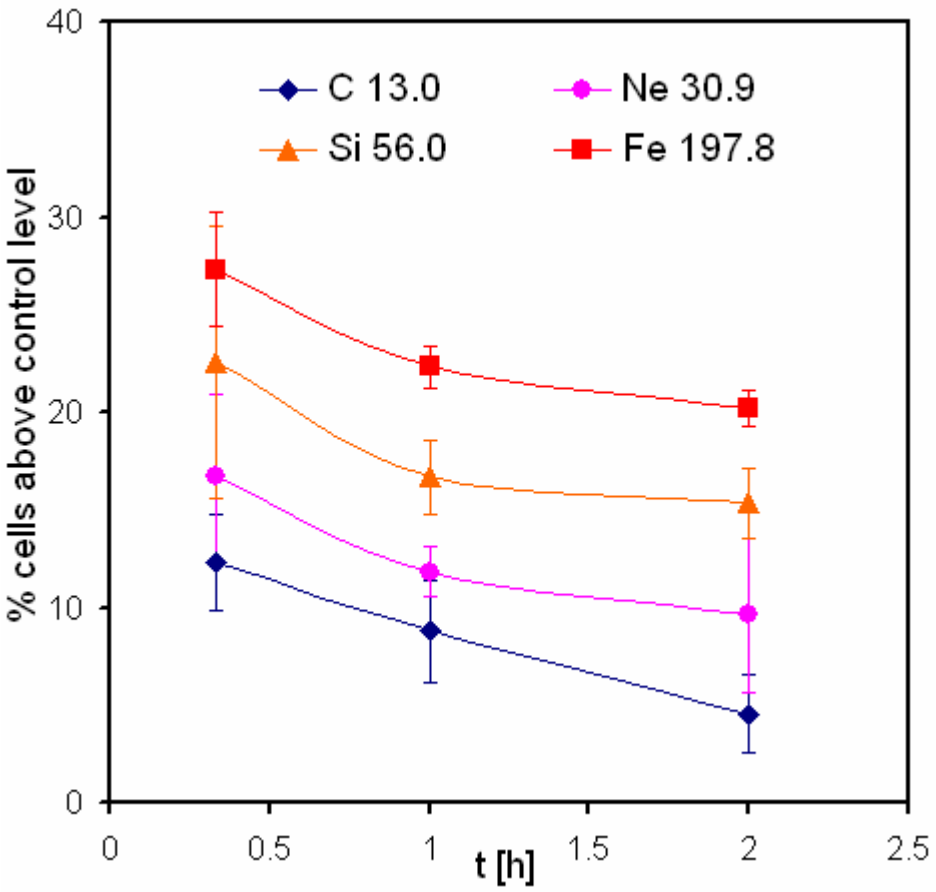

Figure 13.15: Percentage of human fibroblasts with at least one radiation-induced colocalization site of γH2AX and pATM as a function of recovery time. Cells have been exposed to 60 mGy, delivered with different particle beams. Results are means of at least 4 samples per particle type and time point ± s.e..

As has been outlined in section 9.7, co-immunostaining of pATM (ser 1981) and γH2AX (ser 139) is considered to be a most precise and specific tool for detection of DNA DSBs (106), since both targets are found concentrated at sites of DSBs. Therefore, it is permissible to directly interpret the data presented above in terms of DSB incidence, persistence and repair. As a consequence, it can be concluded that the extent of DNA damage increases with radiation LET, and that DNA lesions induced by higher-LET particles are not efficiently repaired within two hours after irradiation and persist over a longer time period than DNA damage cause by lower-LET radiation.

When interpreting figure 13.15 in terms of RBE, a monotonous increase of RBE with LET is advertised for the investigated LET range. Since RBE values contribute to the determination of the quality factor Q, a comparison of this result with Q(LET) as illustrated in figure 2.1 is warranted, which proposes a maximum in the biologic effectiveness at 100 keV/µm H_2O., However, the insights gained from the presented experimental series are, for principle reasons, limited to the utilized beams and the corresponding, discrete LET values, and, thus, do not exclude the presence of a local maximum in DSB incidence in between the used ^{28}Si and ^{56}Fe beams at around 100 keV/µm. As a consequence, the presented data may not be used to argue for a refinement of the current Q(LET) relationship in the low dose range.

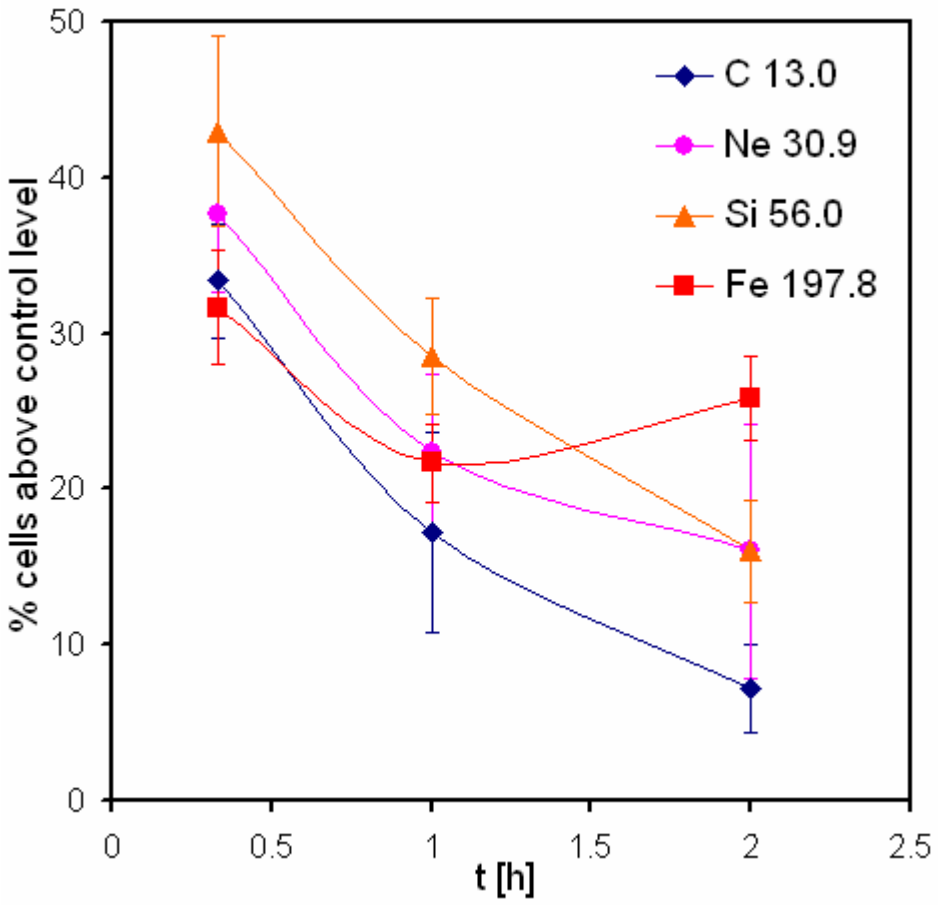

Figure 13.16: Percentage of human fibroblasts with at least one radiation-induced pATM (ser 1981) focus as a function of recovery time. Cells have been exposed to 60 mGy, delivered with different particle beams. Results are means of at least 4 samples per particle type and time point ± s.e..

From the same set of dual-stained samples, the fractions of cells with radiation-induced pATM (ser 1981) foci have been obtained, neglecting optical information from γH2AX staining. The results are illustrated in figure 13.16: Briefly, exposure to ^{28}Si particles yields the largest number of cells with radiation-induced pATM foci at the earliest time point (20'), followed by ^{20}Ne, and, at almost the same value, ^{12}C and ^{56}Fe. With the exception of

the ^{56}Fe-irradiated samples, the fraction of cells with pATM foci is observed to decrease with time until two hours after exposure. Since the average fraction of cells with pATM foci that have been traversed by ^{56}Fe ions is only slightly lower after two hours compared to the initial value, ATM activity is found to be highest in these samples at the two hours time point.

Overall, this behavior of radiation-induced ATM activation excellently agrees with results obtained from the analysis of pATM (ser 1981) foci sizes discussed in section 13.2.1 (figure 13.11). Whereas the absolute numbers are bound to deviate due to different staining and evaluation methods, the qualitative insights on the relationship between ATM activation, LET and time after exposure almost perfectly concur. While there appears to be a local minimum in ATM phosphorylation one hour after exposure to ^{56}Fe particles, when the fraction of cells with radiation-induced pATM foci is assessed, it is not significantly lower than the corresponding value at two hours, and, thus, does not contradict data obtained from the evaluation of foci sizes. Therefore, pATM data presented in this section may be seen as further verification of results and conclusions presented earlier due to different staining and analysis methods applied.

Finally, comparison with the calculated fraction of cells subjected to nuclear particle traversals shows that for both cells with pATM foci or with sites of pATM-γH2AX colocalization, a much lower number of cells exhibit a radiation response than have been directly hit by ^{12}C, ^{20}Ne or ^{28}Si ions. For fibroblasts irradiated with the highest-LET ^{56}Fe beam, about 35 percent of all nuclei have been determined to be traversed by one or more particles. This value is well within the statistical range of the initial fraction of cells with radiation-induced pATM (ser 1981) foci, those with sites of colocalization between pATM and γH2AX being slightly below. Taken together, these data provide yet another indication that sufficiently high ionization densities along single particle tracks are able to trigger a pronounced cellular signalling response.

13.2.4. Colocalization of γH2AX and pDNA-PKcs

In analogy to the evaluation of γH2AX and pATM colocalization, cells exposed to 60 mGy of different particles were co-stained for pDNA-PKcs (thr 2609) and γH2AX (ser 139) using Cy2- and Rhodamine Red-X conjugated secondary antibodies. Cells with one or more pDNA-PKcs-, γH2AX-foci or sites of colocalization of both foci types were counted in a blinded fashion using digitized sample pictures. The percentage of cells with radiation-induced foci has been determined for all types by comparison to equally treated control samples.

In figure 13.17, the time-dependent colocalization of pDNA-PKcs and γH2AX is illustrated for different exposure conditions. From a qualitative viewpoint, the results are rather similar to the assessment of the distribution patterns of pATM and γH2AX: The fraction of cells with colocalizing foci of DNA-PKcs and γH2AX is observed to increase with particle LET at all investigated time points. The average number of these foci is

found to be highest at the earliest time of 20' after exposure. Furthermore, the relative decrease from 20' to two hours is slightly higher in samples irradiated with the lower LET ^{12}C and ^{20}Ne ions and least pronounced in cell layers subjected to ^{56}Fe radiation.

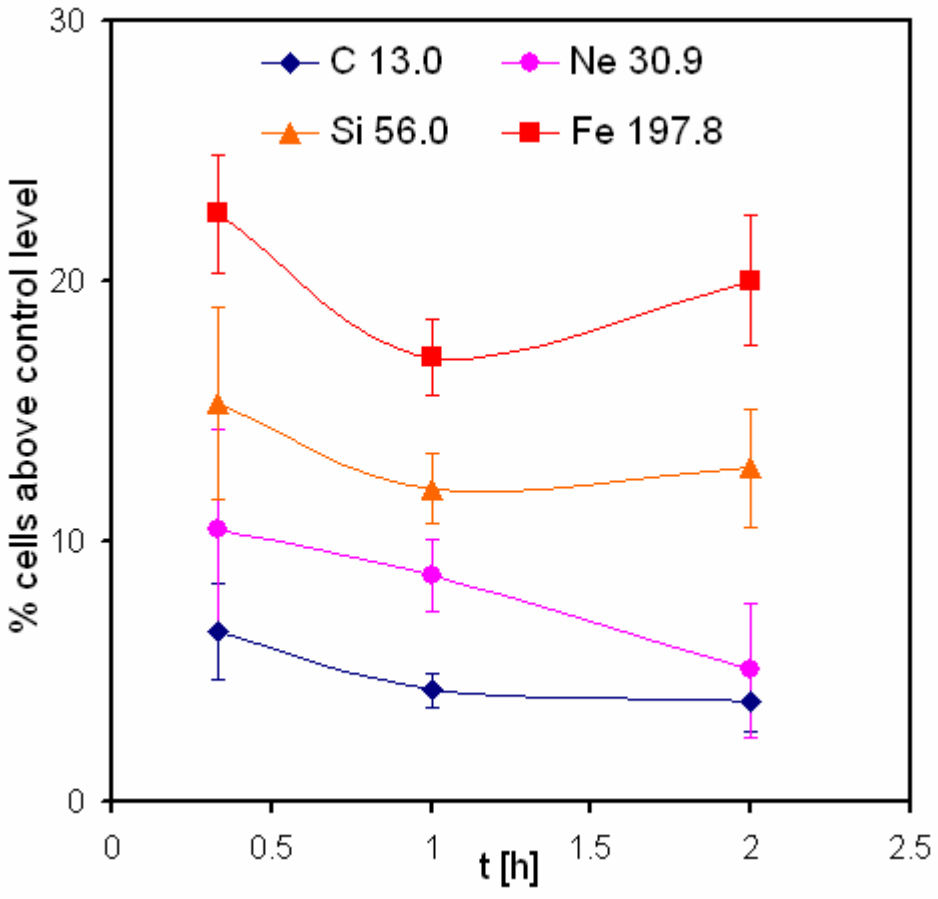

Figure 13.17: Percentage of human fibroblasts with at least one radiation-induced colocalization site of γH2AX and pDNA-PKcs as a function of recovery time. Cells have been exposed to 60 mGy, delivered with different particle beams. Results are means of at least 4 samples per particle type and time point ± s.e..

The perceived differences between colocalization patterns of γH2AX with pDNA-PKcs and γH2AX with pATM may basically be attributed to a varying initiation of ATM and DNA-PKcs autophosphorylation, since the parallel staining of γH2AX (ser 139) should, ideally, be unaffected by the binding of the additional primary antibody and, thus, the selected target for co-staining. This assumption is supported by the results for γH2AX focus formation obtained from both types of co-stainings, which have been found to be identical within statistical errors, and have therefore been combined (see the following section 13.2.5). For further elucidation of the characteristics of DNA-PKcs phosphorylation, the fractions of fibroblasts with pDNA-PKcs (thr 2609) foci are given in figure 13.18 for different particles and repair times.

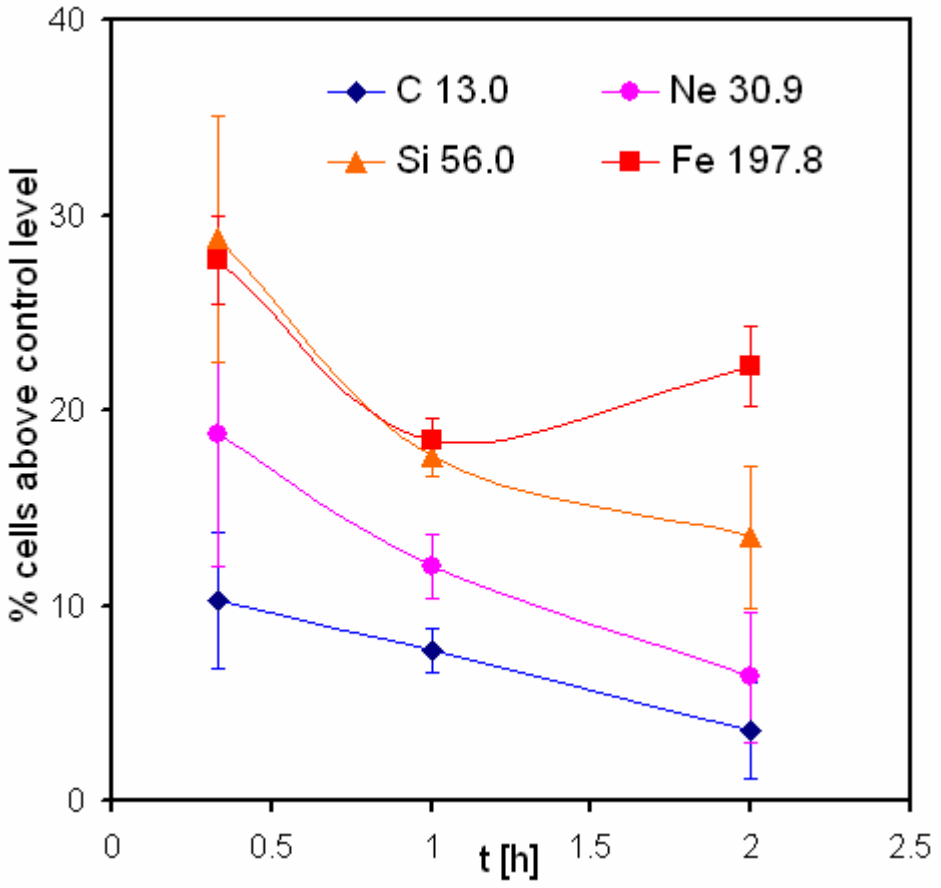

Figure 13.18: Percentage of human fibroblasts with at least one radiation-induced pDNA-PKcs (thr 2609) focus as a function of recovery time. Cells have been exposed to 60 mGy, delivered with different particle beams. Results are means of at least 4 samples per particle type and time point ± s.e..

Overall, exposures to high-energy charged particles cause a more widely spread activation of ATM, whereas a comparably lower number of cells exhibit pDNA-PKcs foci. As a consequence, more γH2AX foci are found "unpaired" in cell layers co-stained for pDNA-PKcs (thr 2609). This observation is in agreement with results originating from the evaluation of pATM and pDNA-PKcs foci sizes (sections 13.2.1 and 13.2.2). There, it has already been explained that due to the distribution of cells over different cell cycle phases, the major yet not the total portion of DSBs will be treated via the NHEJ pathway, which expectedly results in a lower number of pDNA-PKcs foci compared to pATM or γH2AX. Furthermore, for both pDNA-PKcs foci and sites of colocalization with γH2AX, a slight resemblance of the rather curious performance of ATM activity is observed, where a minor increase in or, at least, a constant value for the fraction of cells with pATM foci has been monitored from one to two hours after irradiation to 60 mGy of ^{56}Fe particles. Further thoughts on this issue may be found in chapter 15.

Due to the characteristics and the hypothesized purpose of DNA-PKcs autophosphorylation at threonine 2609, namely the rearrangement of the DNA-PK complex at specific points in the DSB repair process, the author would like to refrain from

raising the question of RBE in this context, since this molecular event may likely prove to be unsuitable or too complex to serve as a cellular parameter for straight-forward estimation of radiation damage potential.

To sum up these results, the assessment of DNA-PKcs phosphorylation (thr 2609) has shown that for the selected experimental configuration, the major fraction of all radiation-induced DSBs as indicated by the presence of γH2AX (ser 139) leads to the initiation of NHEJ repair. Especially in cultures irradiated with the higher-LET ion beams, a large fraction of cells still contains pDNA-PKcs foci two hours after exposure, which strongly suggests the presence of complex DNA lesions that require extensive processing by the NHEJ machinery, obviously resulting in a sustained period of damage repair.

13.2.5. Combined γH2AX (Ser 139) Results

As has already been announced above, the data on γH2AX (ser 139) generated in immunofluorescence dual-stainings with both pATM and pDNA-PKcs (sections 13.2.3 and 13.2.4) have been combined, which is feasible due to sufficiently consistent staining characteristics and quality for both protocols. The results, the fraction of cells with radiation-induced γH2AX (ser 139) foci in dependence of radiation type and incubation time, are visualized in figure 13.19.

The number of cells with γH2AX foci is found to be highest at 20' after exposure for all beams and increases with particle LET at all selected time points. Furthermore, for layers exposed to the lower-LET ^{12}C and ^{20}Ne ions, the percentage of cells monotonously declines from 20' to two hours. Whereas the higher LET ^{28}Si and 56Fe beams yield different numbers of cells with γH2AX foci, the time-dependent behavior of focus formation and persistence appears to be very similar: The average fraction of cells with γH2AX foci are detected to be at roughly the same level at the 20' and the two hours time point, while a slightly lower number of cells are scored positive at one hour after exposure. This curve shape has also been described by the incidence of colocalizing pDNA-PKcs and γH2AX foci (figure 13.17) and, for ^{56}Fe, by pATM (figure 13.16) as well as pDNA-PKcs foci (figure 13.18). This issue will be brought to further attention in section 15.

Comparison of the calculated fraction of cells subjected to nuclear particle traversals with the shown number of cells with γH2AX foci again illustrates that a great fraction of the delivered particles with an LET below 60 keV/μm H_2O does not induce a cellular response that can be detected with the applied methods. The initial number of cells with γH2AX foci due to exposure to ^{56}Fe ions is found to be slightly lower than the calculated number of hit nuclei. However, considering an observation from the evaluation of the experimental series with equal particle fluences (see section 13.1.7), that IF staining is only able to detect a lower number of γH2AX foci than can be demonstrated with signal enhancement staining methods due to worse levels of unspecific background, it may safely be concluded that the actual number of DSBs is very close to the number of particle traversals.

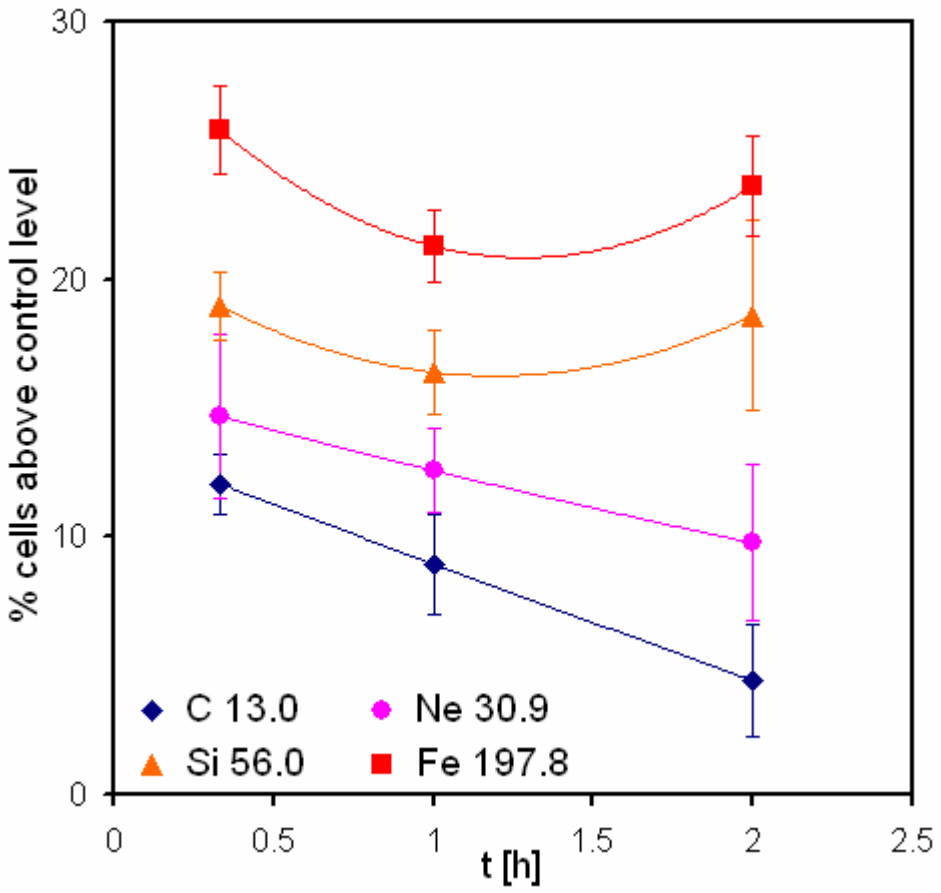

Figure 13.19: Fraction of human fibroblasts with at least one radiation-induced γH2AX (ser 139)-focus as a function of recovery time. Cells have been exposed to 60 mGy, delivered with different particle beams. Results are means of at least 8 samples per particle type and time point ± s.e..

Since a γH2AX (ser 139) focus is generally interpreted as a site of one or more DNA DSBs, it may be concluded from the given results that single particles of higher lineal energy are much more effective at inducing these type of lesions. Furthermore, much higher doses of lower-LET radiation would be needed to induce the same damage extent, which translates into a significant increase of RBE over the investigated LET range.

On a side note, an educating aspect on the concept of RBE may be derived from figure 13.19: It is very obvious that different RBE values would be obtained when investigating DSB incidence with the utilized, common methodology, depending on the time point of observation. Whereas, at first glance, it seems plausible to employ the maximal number of DSBs (and, thus, a very early time point) for each exposure situation in order to determine the "real" RBE value for DSB occurrence, both the LET-dependent persistence of γH2AX and implications on the local concentrations of players in cellular signal (as indicated by different foci sizes) strongly argue for the existence of further parameters with significance for radiation risk assessment that are not effectively accounted for by pure counting of DSBs at any selected time point. Since a prolonged persistence of DSBs for

higher-LET radiation, as shown in this chapter, is to be considered an indicator for less efficient repair, which may very well translate into an increased accumulation of lasting alterations of the genomic information, a restriction to DSB counting for the assessment of radiation damage would likely lead to an underestimation of the damage potential of high-LET charged particles.

13.2.6. The Influence of Particle Species

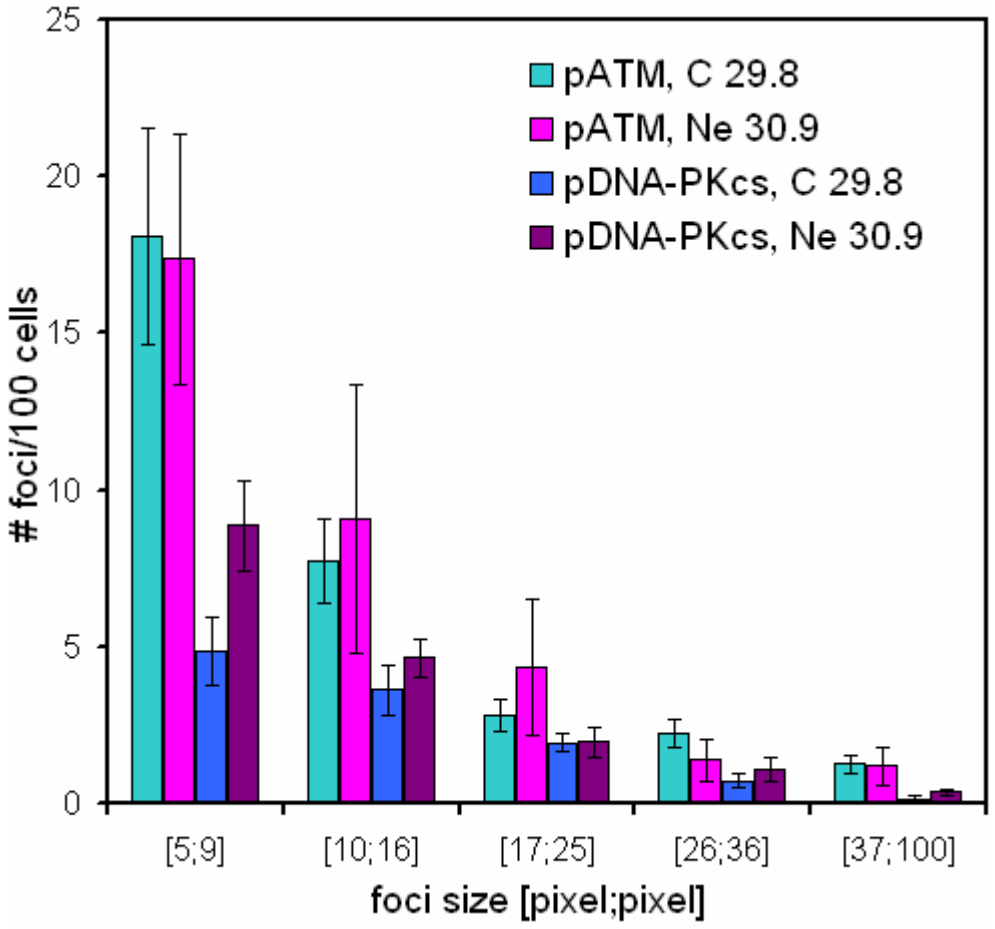

Figure 13.20: Different sizes of detected pDNA-PKcs (thr 2609) and pATM (ser 1981) foci per 100 human skin fibroblasts two hours after exposure to 60 mGy, delivered with ^{12}C and ^{20}Ne ions of similar LET. Foci sizes are given in [pixel; pixel] intervals (1 pixel ≈ 0.11 µm²). IF targets and LET values (in [keV/µm H_2O]) are indicated in the picture legend. Results are means of 5 to 6 samples ± s.e..

The main premise of this thesis is to assess radiobiological effects after exposure to high-energy charged particle beams, which are mainly distinguished by the parameter of LET. However, for fundamental and experimental reasons, the LET range of interest up to 300 keV/µm H_2O cannot be covered using one single particle species or beam type that can be provided by the NIRS HIMAC synchrotron. Since there is indication that particle species has an influence on the TL-emission of LiF:Mg,Ti material (see section 7.5), which,

essentially, represent a manifestation of the energy deposition characteristics of the corresponding particle, a test of the influence of particle species on the investigated radiobiologic events is warranted.

As an exemplary assessment of this matter, samples of diploid human fibroblasts have been exposed to the bare ^{20}Ne beam as well as ^{12}C particles, which have been subjected to LET modulation by application of PMMA binary filters in order to closely resemble the LET of the ^{20}Ne particles. In this manner, doses of approximately 60 mGy have been delivered to the cell layers using ions of different species, but at a similar LET of 30.9 and 29.8 keV/µm H_2O. After irradiation, cells were allowed to recover for two hours and fixed.

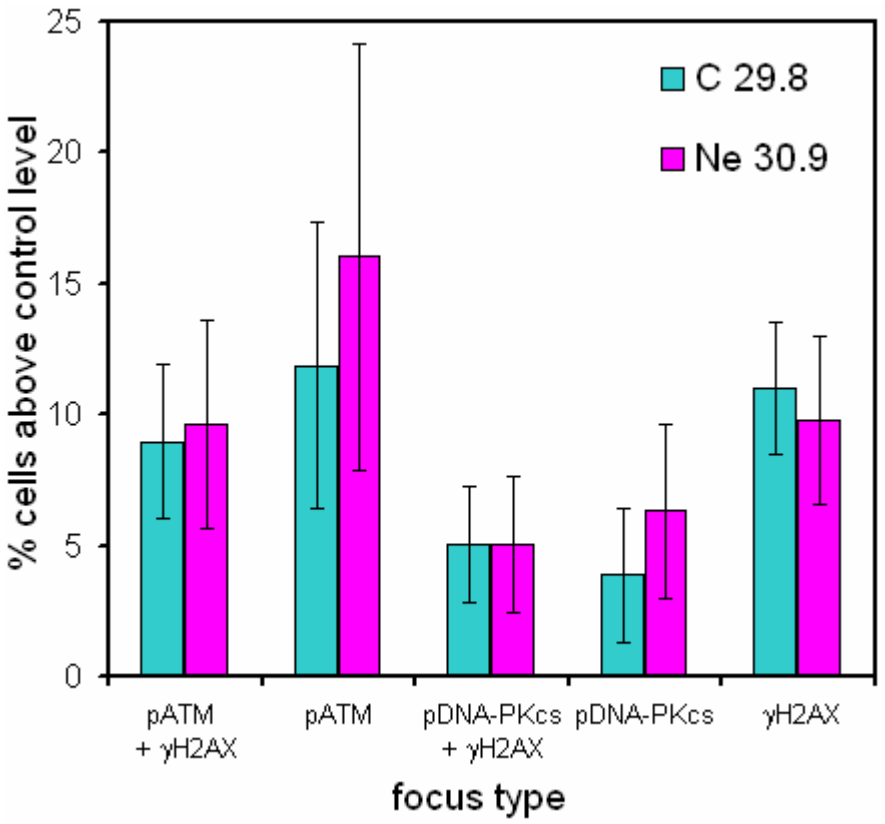

Figure 13.21: Fraction of human fibroblasts with at least one radiation-induced focus of varying type two hours after exposure to 60 mGy, delivered with ^{12}C and ^{20}Ne ions of similar LET. Focus types and LET values (in [keV/µm] H_2O) are indicated. Results are means of 4 to 5 samples ± s.e..

A multitude of parameters have been evaluated, which include the determination of foci sizes for pATM (ser 1981) and pDNA-PKcs (thr 2609), as well as the observation of colocalization of these targets with γH2AX (ser 139). For this purpose, IF staining and analysis procedures were applied as described in the previous sections 13.2.1 to 13.2.4.

Figure 13.20 illustrates the size distributions of both pATM (ser 1981) and pDNA-PKcs (thr 2609) foci two hours after irradiation for the two selected particle beams. Apart from

a slight deviation for the smallest pDNA-PKcs foci, which may well be attributed to insufficient statistics, there is no hint to any variation due to the differing particle types. This finding is further supported by the assessment of cells with several different types of radiation-induced foci, which is presented in figure 13.21. Clearly, the same result, independent of particle species, is obtained for all focus types within the statistical limitations.

Since comparably sized sample groups are used for all analyses throughout this thesis, the data shown here strongly suggests that the actual particle species does not significantly contribute to the findings presented in earlier chapters. However, it needs to be stressed that this comparison of different particles has been deliberately limited to two types of ions and one LET value due to a finite number of available samples. Therefore, it cannot be excluded with absolute certainty that a different behavior would have been found for the higher-LET particles such as ^{28}Si and ^{56}Fe, even though, in the author's opinion, this seems rather unlikely.

14. Comparison of TL- and Radiobiological Results

It is the main goal of this thesis to relate microbiologic measures derived from radiation-induced cellular signal transduction events to physical quantities obtained from TL-measurements. So far, both TL- and radiobiologic results have been presented and analyzed independently in the last chapters. Especially the detailed discussion of the generated cellular data from a strictly biologic viewpoint is of crucial importance in order to understand the meaning of individual parameters of interest and their significance for radiation risk assessment.

In the following, several aspects of radiation quality and its implications on the relation between TL-emissions and DSB signalling shall be elucidated. As a first approach to this matter, results from the experimental series of exposures to equal fluences of different particles will be employed to outline features that may be attributed to properties of single particle tracks. The second part of this chapter is dedicated to an in-depth comparison of the HTR and DSB induction together with consecutive repair and cellular signalling, which is mainly based on the exposures to 60 mGy delivered with different types of particle beams.

14.1. Characteristics of Single Particle Tracks

Basically, the series of exposures to equal particle fluences delivered with varying beam types was performed in order to meet two major goals: Firstly, the occurrence of DSB-mediated early signalling events in bystander cells within the first two hours after irradiation was to be assessed by application of statistical means. A final discussion of this issue can be found in section 15.2. Secondly, apart from a bystander response that may or may not contribute to a significant extent, specific direct effects due to particle traversals through fibroblast nuclei were to be quantitatively evaluated. Since the statistical distribution of particles across the cell layer is highly similar in all exposed samples because of the same particle fluence of approximately $7.36 \times 10^4/cm^2$, differences in the cellular response may be safely attributed to the intrinsic properties of single particles and

their energy deposition characteristics along the tracks. Insights on this matter will be presented below.

Obviously, when the same number of particles are delivered to cells that cover a defined area by using ion beams of various species and/or energy, different radiation doses are absorbed by the samples in correspondence to radiation LET. These doses have been measured using TL-detectors, and have already been shown in figure 12.1. By relating the obtained doses to the percentage of cells with foci of different types at the two hours time point after exposure, the cellular radiation response can be directly illustrated as a function of dose (see figure 14.1). However, it is to be kept in mind that in this case, dose variation is achieved by modulation of LET, or radiation quality, which implies a different biologic effectiveness for all dose points.

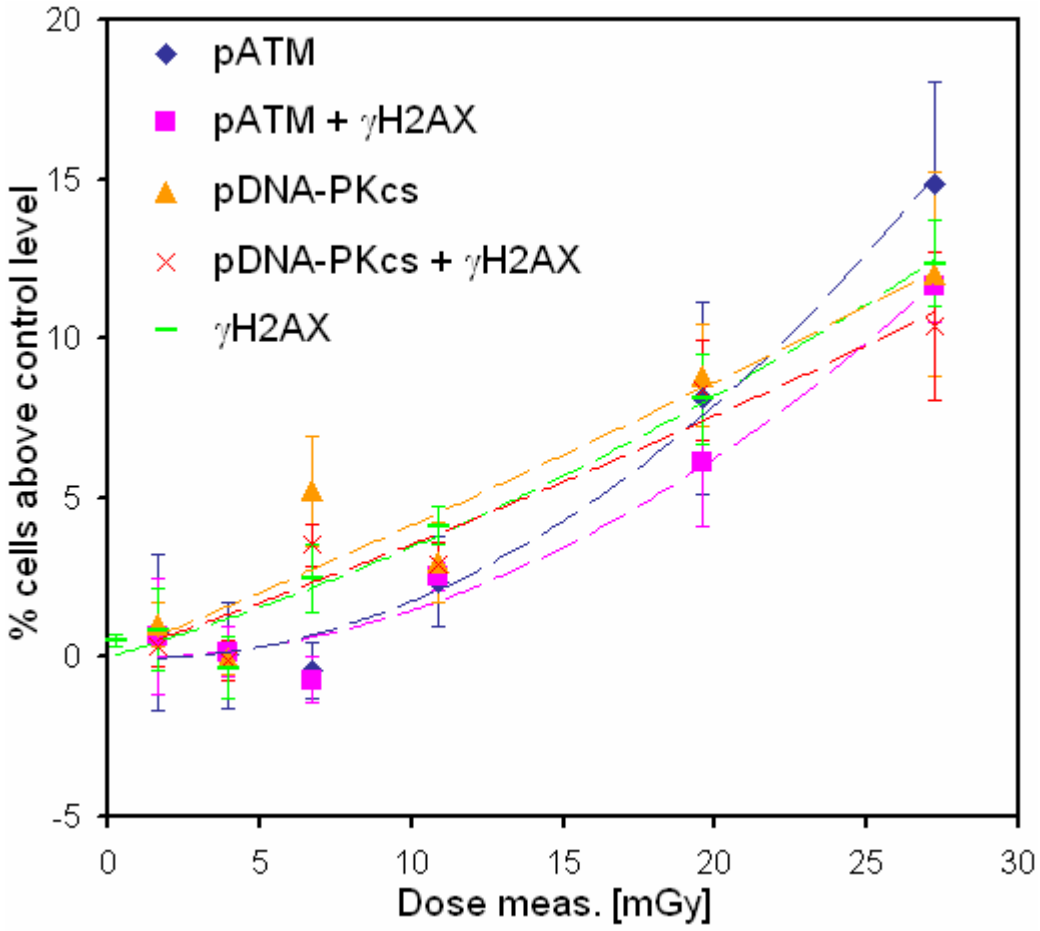

Figure 14.1: Fraction of human fibroblasts with at least one radiation-induced focus of varying type as a function of absorbed dose. Samples have been exposed to equal particle fluences, resulting in higher doses with increasing LET. Focus types are indicated in the legend. Results are means of 4 to 10 samples ± s.e. Doses have been determined with TLD-600 and TLD-700 detector packages.

On many occasions, a higher biologic effectiveness has been reported for particles with LET values exceeding 100 keV/µm H_2O, which can be expected to translate into a

superlinear behavior for the upper dose range in figure 14.1. When fitting all datasets with polynomials of 2nd degree, both pATM (ser 1981) focus formation and colocalization of pATM and γH2AX perfectly fit this picture, while a more linear relationship with dose seems to be valid for pDNA-PKcs (thr 2609) foci and colocalizing sites of pDNA-PKcs and γH2AX.

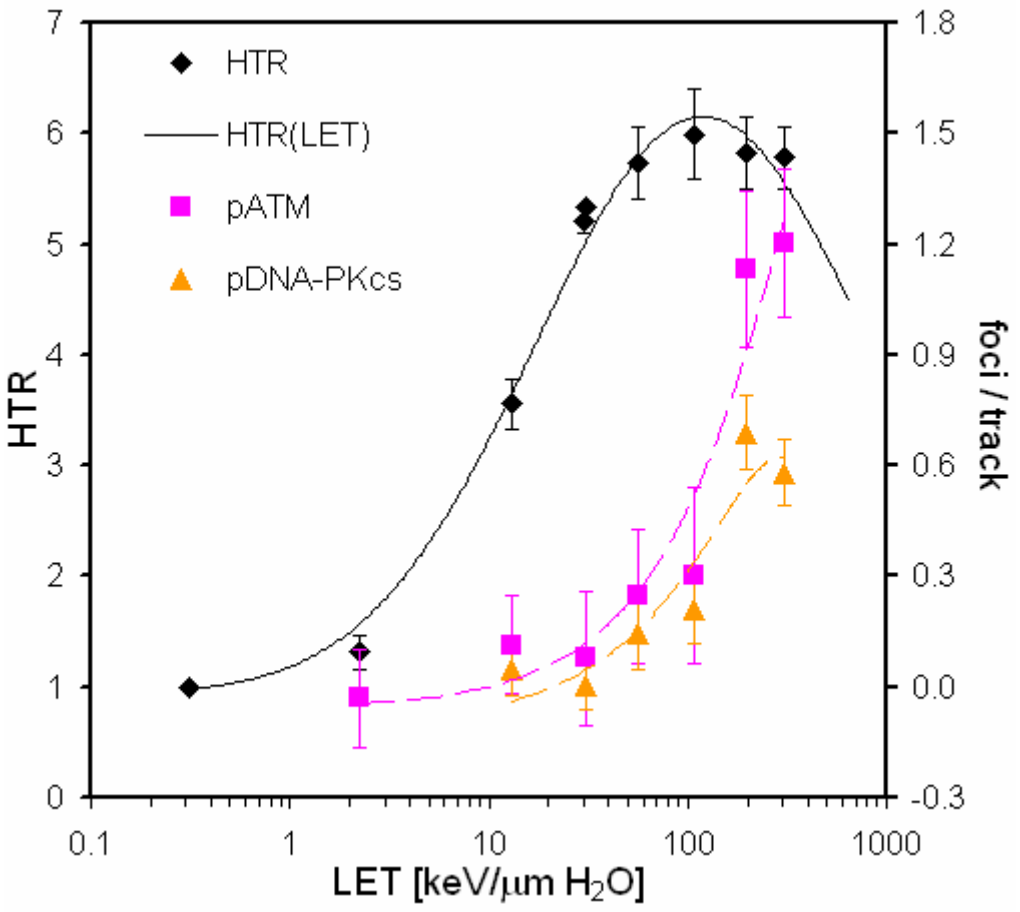

Figure 14.2: The number of pATM (ser 1981) and pDNA-PKcs (thr 2609) foci per nuclear particle traversal compared to HTR(LET) in cells exposed to an equal fluence of particles. Biologic results are means of 4 to 6 samples ± s.e., HTR values are means of up to 5 detector packages ± σ.

Due to high statistic uncertainties and the lack of information on essential quantities such as the actual number of foci and their size in figure 14.1, data from the analysis of the size distribution of pATM and pDNA-PKcs foci (sections 13.1.1 and 13.1.2) two hours after exposure to equal particle fluences are utilized for a further, more concise assessment of effects induced by single particle tracks. From these experiments, the average numbers of pATM and pDNA-PKcs foci (above control levels) per nuclear particle traversal have been calculated and are compared to measured HTR values in the different beam lines, as is illustrated in figure 14.2. Basically, when an increase in the number of radiation-induced foci due to a bystander response or cytoplasmic energy deposition is neglected, the quantity "foci per nuclear track" may be interpreted as the probability for a single particle of a given lineal energy to induce a particular cellular response. Obviously, this

interpretation is only valid for very low particle fluences as used in this series of experiments, where more than 98% of all nuclei are either not hit or traversed by a single ion, thus rendering an overlap of particle tracks extremely unlikely. Therefore, according to this principle, a number of foci/track close to zero means that a single ion track is insufficient to trigger the observed cellular event, whereas a number of one describes a situation, where every single particle causes the particular reaction.

At first glance, comparison of HTR and the number of specific foci per track as functions of LET may seem somewhat arbitrary. However, both share the important property of being independent of dose, which has been experimentally demonstrated for the HTR (154) and is, essentially, included in the definition of "foci/track", when only low particle fluences with negligible track overlap are allowed. Furthermore, as an explanation for the striking resemblance of the Q(LET) function by the HTR, it has been hypothesized that this might be due to radiation energy being deposited in comparable volumes in both TL-material and biological tissue (154). Since the DNA is to be considered the most essential target for radiation energy imparted on tissue and both pATM (ser 1981) and pDNA-PKcs (thr 2609) foci mark events in the cellular response to DNA lesions, the number of foci per nuclear particle track may constitute an ideal quantity for studying energy deposition characteristics of a given type of radiation. Obviously, while radiation of very low LET corresponds to an HTR close to 1, it will yield close to zero foci per track. Therefore, the two y-axes in figure 14.2 have been aligned accordingly.

In fact, a few functional similarities between the HTR data and the number of pATM and pDNA-PKcs are observed: In all cases, a clear increase with radiation LET is observed in the lower-LET range below 100 keV/µm H_2O. This increase leads to a maximum, which is located at around 100 keV/µm H_2O and followed by a decrease in case of the HTR. For both pATM and pDNA-PKcs, the numbers of foci per track are highest for 200 and 300 keV/ µm H_2O, where identical values have been obtained within statistical errors. Due to this behavior, it is tempting to speculate that both the number of pATM and pDNA-PKcs foci may have (almost) reached a saturation level that is exhibited by fibroblasts subjected to particles above 200 keV/ µm H_2O. When it is further assumed that the major part of ATM and DNA-PKcs phosphorylation at two hours after exposure may be attributed to targeted effects found along particle tracks rather than bystander and cytoplasmic effects (see also section 15.2), this hypothesis appears to be even more plausible, since the same number of pATM foci as nuclear particle traversals is already found in the 200 keV/ µm H_2O exposures, complemented by a correspondingly lower number of pDNA-PKcs foci due to the intrinsic characteristics of DSB repair. From this viewpoint, it seems highly improbable that a decrease – in analogy to HTR – may be expected for the number of foci per nuclear track for a higher LET up to reasonable values, since targeted DNA damage is not known to decline at higher ionization densities.

However, despite its qualities for elucidation of effects due to single particles, it needs to be pointed out that the quantity "foci/track" does not contain any information on the actual size distribution or even average sizes of foci types of interest. For further

explanation, figure 14.3 shows the detected mean sizes of pATM (ser 1981) and pDNA-PKcs (thr 2609) foci for the same set of samples as above. For both types, a clear increase in size with LET is exhibited that does not show any signs of saturation in the investigated LET range. This behavior may be interpreted as another hint for most pATM and pDNA-PKcs foci being a consequence of targeted damage, since these clusters of phosphorylated ATM and DNA-PKcs as indicated by larger foci sizes are generally attributed to extensive and highly localized DNA damage along particle tracks rather than more homogenously distributed lesions in bystander nuclei. However, while this LET-dependence of foci size obviously further complicates the use of focus induction as a cellular parameter for radiation risk assessment, it provides the means to "weight" individual foci that are caused by particles of varying lineal energies.

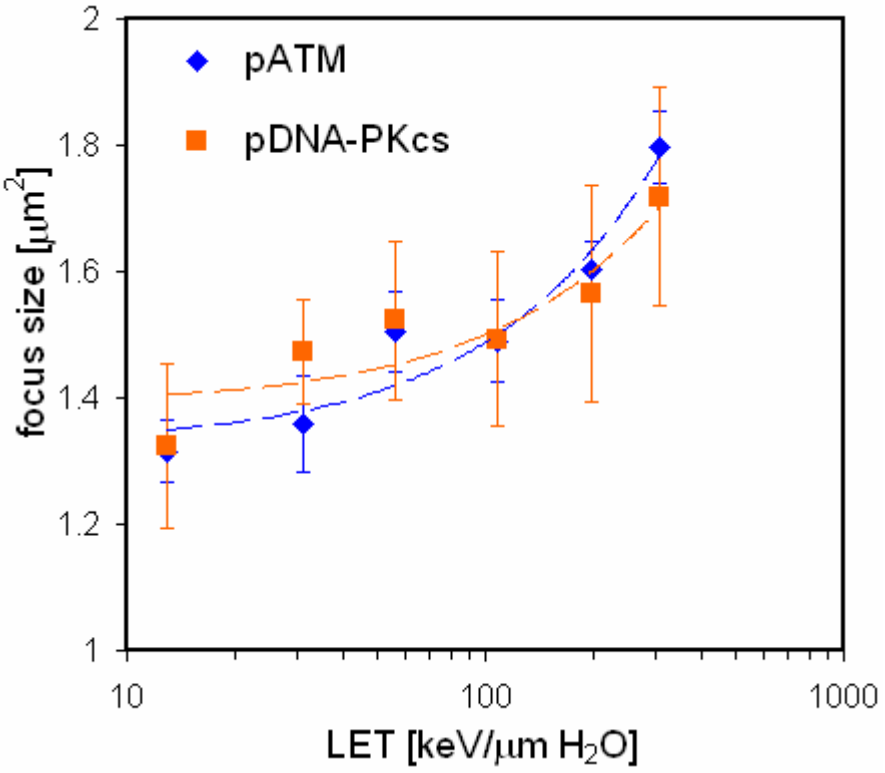

Figure 14.3: The average size of pATM (ser 1981) and pDNA-PKcs (thr 2609) foci as a function of LET in cells exposed to an equal fluence of particles. Results are means of 4 to 6 samples ± s.e..

14.2. HTR(LET) and DSB-Induced Signalling Events

In the second main experimental series of exposures to high-energy charged particles, cultivated cells were subjected to 60 mGy delivered with different particle beams. Therein, energy distribution patterns greatly vary on the cell layer level (see table 10.5) depending on radiation LET, which range from several tracks per nucleus for the ^{12}C beam (13.0 keV/µm H_2O), where ionization events originating from more than one track may

contribute to a particular DNA lesion, to only one third of all nuclei being hit in the ^{56}Fe exposures (197.8 keV/μm H_2O).

With these differences in mind, it is clear that only limited insights on the effects of specific, single particles can be gained, as has been done in the last section 14.1. However, since absorbed dose constitutes the basic quantity in standard dosimetry, which has been kept at the same value throughout these experiments, the generated biological data may be utilized to highlight effects due to varying radiation quality. Furthermore, it needs to be stressed that LiF:Mg,Ti TL-materials exposed to particle radiation are subjected to the same differences in energy deposition patterns, which, essentially, give rise to the LET-specific characteristics of the TL glow curve that are abused in application of the HTR method.

When the focus is moved from the assessment of effects due to single particle tracks to a more general evaluation of the consequences of a given exposure situation on DSB-induced cellular signalling, a refined approach in the interpretation of IF results is warranted. Basically, as has been elucidated in figure 14.3 and in many presentations of foci size distributions in chapter 13, pure counting of pATM and pDNA-PKcs foci is not sufficient to describe ATM and DNA-PKcs activity. Instead, both number and size are to be taken into account, which is most easily achieved by determining the visible area of IF staining that may be attributed to foci. Using the normalized size distribution $f_n(A)$ and focus size A, with n being the sample index of a total of N samples, the focal area A_{foc} is given by

$$A_{foc} = \frac{1}{N} \cdot \sum_{n=1}^{N} \int_0^{\infty} f_n(A) \cdot A \, dA \, . \qquad (14.1)$$

By this definition, A_{foc} corresponds to the mean area of IF-staining per cell localized in foci. For reasons of consistency with size distributions shown in chapters 11 and 13, A_{foc} is renormalized to 100 cells for presentation in the following graphs (figure 14.4 and figure 14.5). In order to refer exclusively to foci induced by particle irradiation, A_{foc} has been determined for a large group of control samples and subtracted from exposed samples. The detected focal area can be expected to be directly proportional to the volume, where radiation-induced ionization events take place, which may best be approximated by cylinders along particle tracks due to sufficiently high energies and beams incident in perpendicular direction.

In this manner, the area per 100 cells corresponding to radiation-induced pATM (ser 1981, figure 14.4) and pDNA-PKcs (thr 2609, figure 14.5) foci is presented for the 60 mGy exposures and three different recovery times of 20', 1 and 2 hours. The data has been fitted with polynomials of 2nd degree on a purely phenomenological basis. Qualitatively, the results for pATM and pDNA-PKcs are amazingly similar – with slightly lower values for pDNA-PKcs as found on various occasions throughout this thesis, which may be attributed to the fact that most but not all of the DSBs are treated via NHEJ repair.

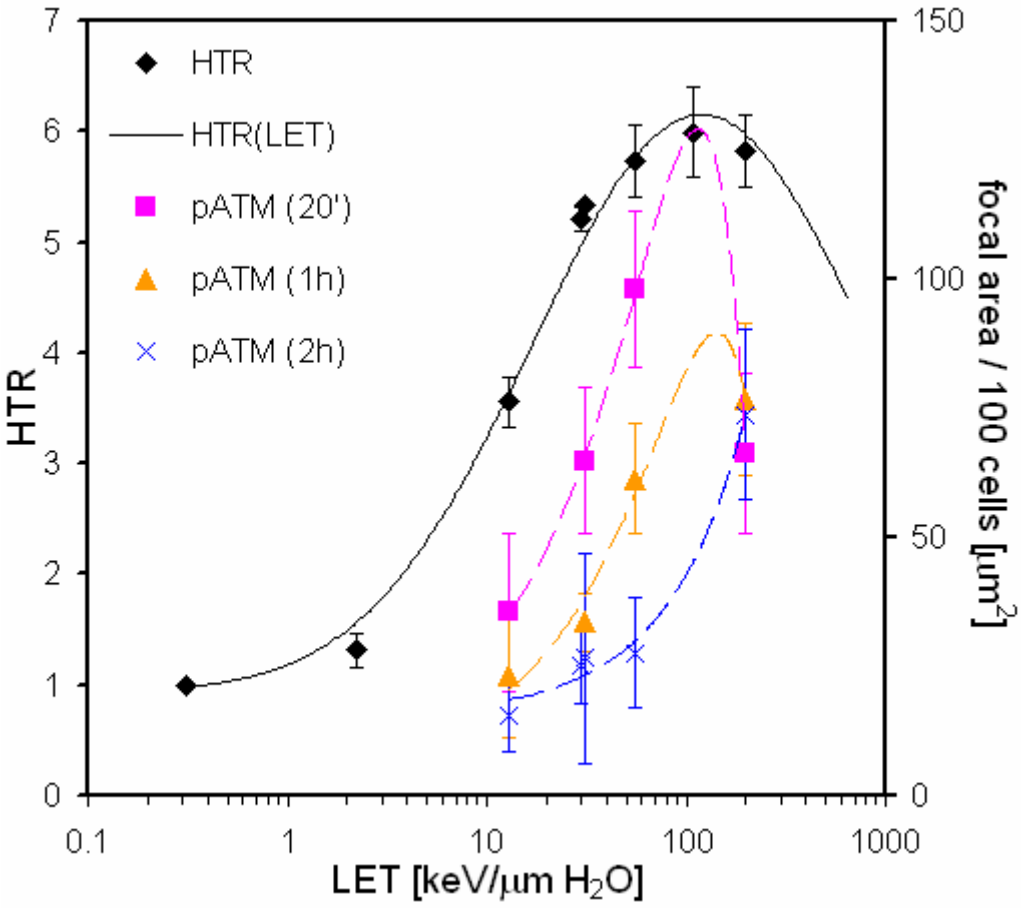

Figure 14.4: The time-dependent area of pATM (ser 1981) foci per 100 fibroblasts (above control) exposed to 60 mGy of different particles, compared to HTR(LET). Biologic results are means of 4 to 6 samples ± s.e., HTR values are means of up to 5 detector packages ± σ. Fit functions for the focal area are 2nd degree polynomials.

For both pATM and pDNA-PKcs, the initial numbers of foci – represented by the 20' time point – clearly exhibit a potential maximum located between the ^{28}Si (56.0 keV/µm H_2O) and the ^{56}Fe (197.8 keV/µm H_2O) exposure, which is put very close to 100 keV/µm H_2O by the fitted curves. It needs to be stressed that, obviously, due to the limitation to four LET values and rather large errors, the exact positions and especially the peak heights of these maxima need to be interpreted as roughly estimated and are only suited for qualitative comparison. Nevertheless, it is striking that this behavior nicely reflects the shape of the HTR(LET) curve, which also features a local maximum at around 100 keV/µm H_2O. Furthermore, the A_{foc}(LET) function can safely be assumed to "end" at values below ^{12}C and above zero for low-LET photon radiation, as can be estimated from pre-experiments with the ^{60}Co source (see section 11.1.2), resulting in a similar shape of A_{foc}(LET) and HTR(LET) in the lower LET range below 30 keV/µm H_2O. Unfortunately, this plausible assumption cannot be conclusively supported by experimental data due to differing staining characteristics of samples that have not been treated at NIRS and, consecutively, subjected to the on-site environment, prolonged transportation and storage.

The situation gradually changes with increasing time after exposure due to ongoing repair of DNA lesions. There is indication from both pATM and pDNA-PKcs data that the DNA damage maximum moves to higher LET values with progressing time, possibly exceeding the investigated LET range of up to 200 keV/µm H_2O at around two hours. Therefore, the overall shape of A_{foc}(LET) increasingly deviates from HTR(LET) for longer repair times.

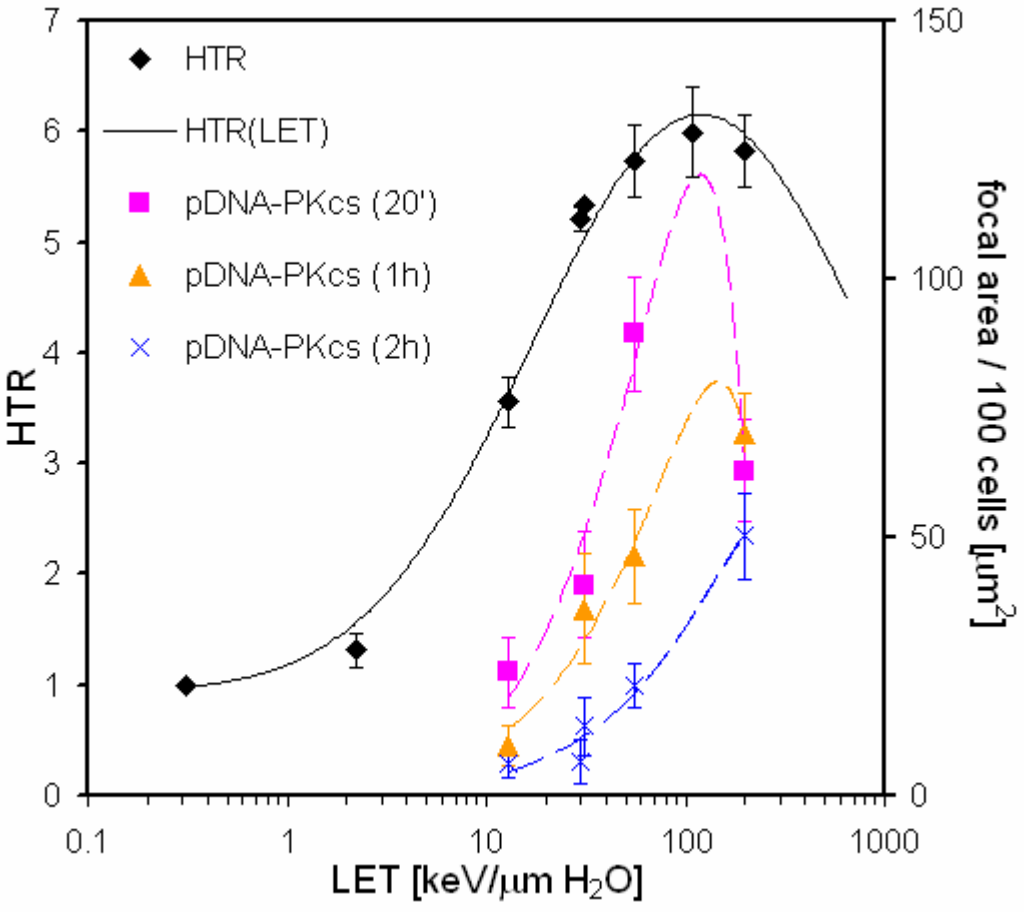

Figure 14.5: The time-dependent area of pDNA-PKcs (thr 2609) foci per 100 fibroblasts (above control) exposed to 60 mGy of different particles, compared to HTR(LET). Biologic results are means of 5 to 6 samples ± s.e., HTR values are means of up to 5 detector packages ± σ. Fit functions for the focal area are 2nd degree polynomials.

For further elucidation of this issue, the occurrence of pATM and pDNA-PKcs foci has also been analyzed on a cell to cell basis (figure 14.6). Again, a data fit with polynomials of 2nd degree hint at the presence of a maximum somewhere around 100 to 200 keV/µm H_2O, depending on repair time. Apart from that, comparison to the results for focal areas shows that the initial number of cells with pATM foci is rather high for lower LET values, which is due to a large number of smaller sized foci that contribute little to focal area and likely correspond to DNA damage that is rapidly repaired within the first two hours. For the sake of completeness, it shall be mentioned that the analysis of cells with radiation-induced γH2AX (ser 139) foci yield qualitatively similar results except for a relatively greater persistence of foci in ^{28}Si (56.0 keV/µm H_2O) exposed cells, which may be easily

explained by a dissimilar time course in the dephosphorylation of the different target proteins after damage repair, as has already been demonstrated for pATM and γH2AX (171), accompanied by varying detection limits for the different types of foci.

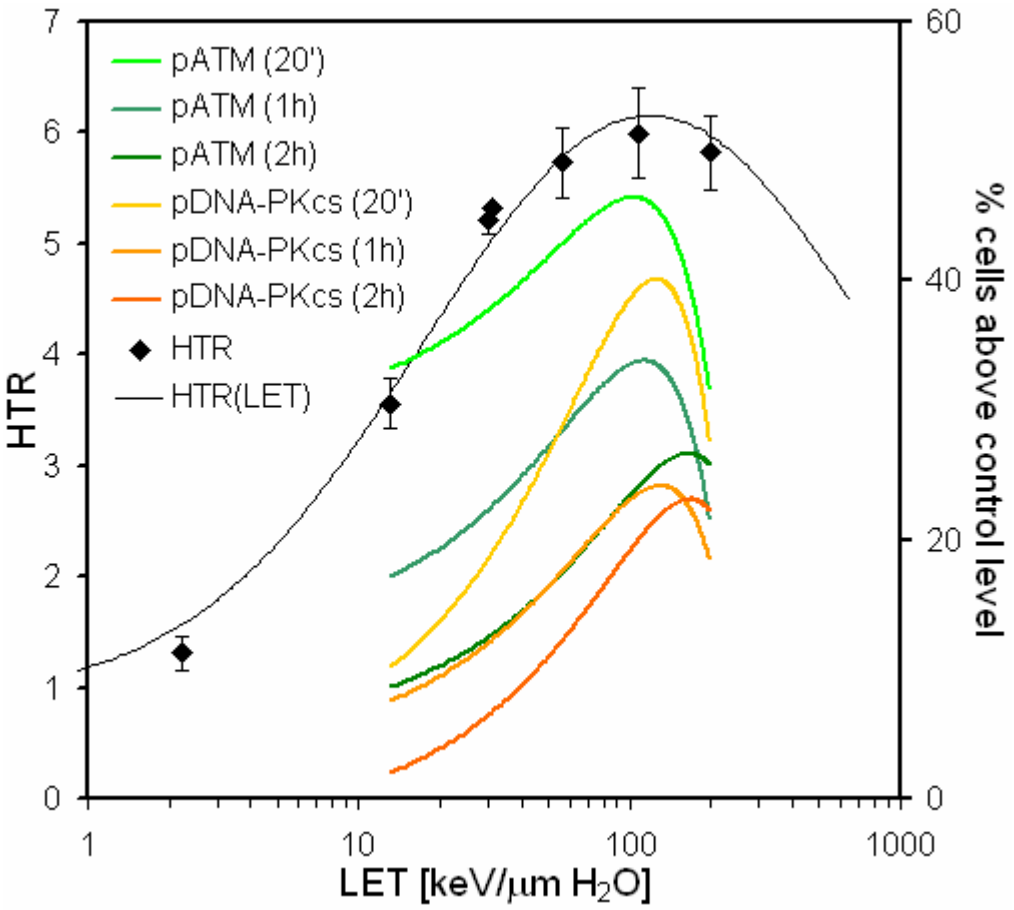

Figure 14.6: The time-dependent fraction of fibroblasts with radiation-induced pATM (ser 1981) and pDNA-PKcs (thr 2609) foci after exposure to 60 mGy of different particles, compared to HTR(LET). For better readability, individual data points are omitted and only 2nd degree polynomial fits are shown. HTR values refer to means of up to 5 detector packages ± σ.

Overall, it has been demonstrated that the initial cellular response to particle radiation as a function of LET shares remarkable similarities with the characteristics of HTR(LET) derived from TL glow curves. This finding is especially impressing for the focal area A_{foc} of pATM and pDNA-PKcs foci induced by radiation exposure, which represents a simple and straightforward concept for quantification of IF-stained target proteins that are found accumulated at sites of varying sizes. While these insights argue for the hypothesis that the energy deposition in LiF:Mg,Ti TL-materials and relevant biologic targets such as DNA may share similar characteristics, the presented data provides evidence that repair kinetics, which may furthermore be overlaid by non-targeted effects, lead to an LET-dependent time course of specific cellular signalling events such as phosphorylation of the particular targets investigated, as well as focus formation and resolution.

15. Conclusions and Discussion

A multitude of experimental data of both radiobiological and dosimetric nature has been presented and interpreted in the last sections. Since different biologic events in cellular signalling have been assessed, many individual conclusions have been drawn from smaller datasets, which shall be briefly summed up in the first subsection of this chapter.

Afterwards, two major issues still remain to be discussed, which require the combined analysis of individual hints and insights that have been outlined throughout this thesis. Firstly, indications on the contribution of non-targeted radiation-induced effects shall be used to draw a picture of the possible influence of bystander signalling on the early cellular response to radiation. Finally, the main question whether TL-dosimetry may be applied for prediction of events on the subcellular level will be critically reviewed. Accompanying this analysis, the necessity of future experimental studies will be outlined by presenting experimental concepts designed to further explore targeted and non-targeted effects of importance for radiation protection, thus gathering the knowledge required to better estimate risks due to high-LET radiation on the basis of physical measurement systems.

15.1. A Brief Summary of Individual Results

As a follow-up to experiments with low-LET photon radiation that have demonstrated the initialization of a manifold of cellular signalling events in the early two hours period after irradiation, exposures of cultivated human fibroblasts to high energy charged particles have been performed at the NIRS-HIMAC facility. In all cases, synchronous exposures of TL-detectors have been carried out for verification of exposure parameters and for comparison of biologic effects with LET-dependent characteristics of TL-emissions, using the HTR as a measure for radiation quality.

In a first approach, cells have been exposed to an equal particle fluence of about 7.36×10^{4} cm^{-2} delivered with beams of different ion species and LET in order to study the effects of individual particle traversals. In these experiments, approximately 15% of all nuclei are traversed by a particle track. Evaluation of pATM (ser 1981), pDNA-PKcs (thr 2609) and

γH2AX (ser 139) focus formation reveals that particles with an LET value as low as 56 keV/μm H_2O, already yield a detectable signal transduction response two hours after treatment, which is even more pronounced for particles of higher LET. However, downstream targets of kinase-active ATM such as P53 and Chk2 were not found to show any detectable increase in phosphorylation at this time point.

In experiments with the highest-LET ions (^{56}Fe, 197.8 and 307.4 keV/μm H_2O), the number of pATM and pDNA-PKcs foci have been found to be similar to the number of nuclear particle traversals. Co-immunostaining of both pATM and pDNA-PKcs with γH2AX (ser 139) shows that both targets are mainly found colocalizing with sites of DNA damage, which agrees well with many recent studies. In the light of contradicting reports that put pDNA-PKcs (thr 2609) either localized in foci at DSBs or rather homogenously distributed across the nucleus, the gathered results strongly support the former opinion.

The radiobiologic response can be characterized by the number of radiation-induced foci of different types per nuclear particle track. The obtained LET-dependent function of pATM and pDNA-PKcs foci per track is found to exhibit similarities to HTR(LET) up to about 200 keV/μm H_2O, but appears to be shifted towards higher LET values. It could be demonstrated that not only the total number of foci, but also their size distribution is modulated by radiation LET. This insight is especially noteworthy since it adds a crucial aspect to the interpretation of DSB signalling and argues for the necessity to weight individual foci instead of relying on pure counting of foci numbers, which are still commonly applied as a measure for radiation damage.

In the second experimental series, cells were subjected to 60 mGy of varying particles in order to draw conclusions on the initial damage extent and repair efforts within the first two hours after exposure. The rapid decrease in the number of foci observed in samples irradiated with the lower-LET beams suggests that DNA damage induced by these particles is efficiently repaired within a short timeframe. In contrast, the same amount of pATM, pDNA-PKcs and γH2AX has been detected in ^{56}Fe (197.8 keV/μm H_2O) exposed samples at 20' and 2 hours after irradiation. This finding impressively illustrates that the time course of the radiation-induced cellular signalling response is gravely modulated by radiation LET.

In order to account for the LET-dependence of focus sizes, the "focal area" has been introduced as a measure for the radiation-induced modification of a target protein. Comparison of this quantity with TL results shows that the early accumulation of pATM and pDNA-PKcs at sites of DNA damage induced by radiation exhibit a functional dependence on LET similar to the HTR. However, as a consequence of the LET-dependent time course of the cellular response due to specific damage patterns, later time points show different characteristics of the focal area. Conclusively, it has been proven that cellular signal pathways must be viewed as time-dependent processes when using the initialization of specific events as benchmarks for radiation damage.

In both experimental series, the number of pATM foci induced by ^{56}Fe (197.8 keV/µm H_2O) particles has been determined to be identical to the calculated number of nuclear particle traversals within statistical errors. These results strongly argue for the hypothesis that a single particle of sufficiently high lineal energy that closely passes DNA molecules is able to trigger a detectable cellular signalling response.

In a contracted manner, the most essential insights are given here:

- **H2AX and upstream kinases ATM and DNA-PKcs are phosphorylated shortly after exposure to charged particles at low doses of a few mGy.**
- **The damage extent along particle tracks is found to increase with LET. At high LET values (197.8 and 307.4 keV/µm), every single nuclear particle traversal induces a biochemical reaction.**
- **DNA damage due to lower-LET particles is efficiently repaired within a short timeframe, whereas DNA damage due to higher-LET radiation requires extensive, prolongued processing.**
- **The extent of the initial cellular response and the HTR show a remarkably similar LET-dependence. Because of the LET-dependent characteristics of DSB repair, this similarity is less pronounced at later timepoints.**

Overall, differences in radiation quality have been found to greatly influence the biologic consequences of radiation on the cellular level. Especially for exposures to low doses of high-energy charged particles in the mGy range, microscopic aspects such as the cellular localization of particle traversals and damage induction characteristics of single particles have been found to be of substantial value for the assessment of biologic radiation effects. In contrast, the macroscopic concept of dose is not well suited to describe microbiological consequences and to serve as a physical measure for the estimation of radiation damage in these important exposure situations.

15.2. Where is the Bystander Effect?

In the introductory part to this thesis, different types of radiation effects on biologic tissue have been distinguished in order to account for the highly localized and non-homogenous deposition of energy in a layer of cells that is traversed by a low number of high-energy charged particles: Firstly, direct damage to DNA due to ionization of the DNA molecule or the production of radicals in close proximity triggers an immediate cellular response that is intended to minimize the detrimental effects of radiation. Secondly, non-targeted effects, which include specific damage patterns in bystander cells that have not been directly subjected to radiation, contribute to the overall cellular response to radiation in a manner that is dependent on a manifold of biological and exposure parameters.

It has been defined as one of the goals of this thesis to investigate a possible contribution of non-targeted effects to the early cellular signal transduction response to high-LET particle radiation. For this purpose, one experimental series has focused on the response to low particle fluences, where only a small fraction (about 15%) of all nuclei is subjected to a particle traversal, thus allowing for the transmission of a bystander signal to the unhit neighbouring cells. For these experiments, a recovery time of two hours after exposure has been deliberately chosen as a point of interest, where the slightly delayed events in bystander cells, which have been demonstrated to occur starting few hours after exposure (118), can already be expected to contribute to a significant extent.

When using a highly sensitive immunocytochemical detection system for signal amplification, the fraction of cells with radiation-induced γH2AX foci has been found to exceed the percentage of traversed nuclei two hours after exposure to high-LET particles of 197.8 keV/µm. While this difference (19.5 to 15.3%) is not significant in terms of statistics due to the small number of samples, additional issues such as progressing repair of direct damage suggest a considerable overestimation of direct radiation effects at this time point, thus augmenting the detected surplus of foci. Therefore, this result may be interpreted as a strong indication for the contribution of an early bystander response, which, however, cannot be directly distinguished from targeted effects due to inherent limitations of broad beam experiments.

Cells irradiated with 60 mGy of ^{56}Fe particles (197.8 keV/µm H_2O, about 65% hit nuclei) have been demonstrated to exhibit a rather peculiar time-dependent behavior in the formation and persistence of the different types of radiation-induced foci: Firstly, the total numbers of both pATM (ser 1981) and pDNA-PKcs (thr 2609) foci per 100 fibroblasts are found to remain at roughly the same level for all three time points of interest (20', 1 and 2 hours) after exposure. Secondly, the fraction of cells with any type of foci (pATM – figure 13.16, pDNA-PKcs – figure 13.18, γH2AX – figure 13.19) is highest at 20' after irradiation, followed by a decrease and yet another increase, resulting in a minimum somewhere between the 20' and the 2 hours time point.

These local minima in the fraction of cells with foci are not very pronounced, and thus, their occurrence cannot be proven individually due to insufficient statistics. However, since all three types of foci are inherently linked to the presence of DSBs, it is permissible to combine the datasets in order to draw conclusions on DSB incidence and repair. Comparison of the individual results shows that the numbers of pATM and γH2AX foci per DSB are virtually identical, whereas DSB incidence is slightly underestimated by pDNA-PKcs due to its specific function in NHEJ repair. As a consequence, the data on pATM and γH2AX have been taken "as is", whereas the fraction of cells with pDNA-PKcs foci had to be multiplied by a constant factor ($k = 1.162$) that accounts for its relatively lower numbers in order to generate a combined measure for the time-dependent presence of DSBs and, consecutively, DSB-induced cellular signalling.

Merging of all data results in a much larger sample count, corresponding to about 20 individual stains per time point. Thereby, the statistical significance of the decrease in the

fraction of cells with foci from 20' to 1h (t = 0.0001) and the increase from 1 to 2 hours (t = 0.013) can be demonstrated, which results in a final level of cells with foci that is a bit below the initial (t = 0.015). It therefore has to be concluded that in response to 60 mGy of ^{56}Fe (197.8 keV/µm H_2O) particles, the fraction of cells engaged in processing of induced DSBs reaches a local minimum at around one hour after exposure.

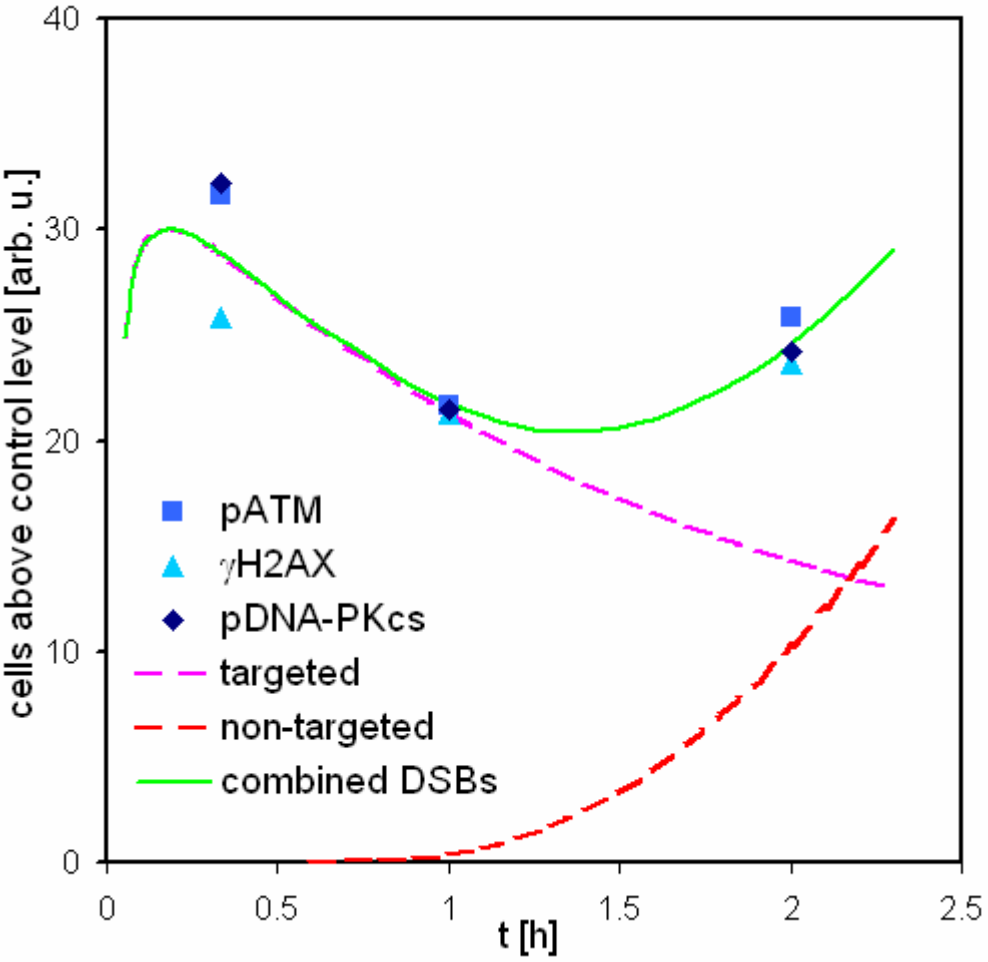

Figure 15.1: Model for the time-dependent contribution of targeted and non-targeted effects to early cellular signalling due to DSBs that have been induced by a low dose of high-LET radiation, based on the occurrence of different types of foci (pATM, γH2AX, pDNA-PKcs) in fibroblasts exposed to 60 mGy of ^{56}Fe ions (197.8 keV/µm H_2O). The fractions of cells with foci are indicated using arbitrary units, since results for pDNA-PKcs had to be multiplied by a constant factor in order to compensate for its inherent underestimation of the actual number of DSBs present at the given time point.

This general behavior is illustrated in figure 15.1: The green line represents the time course of the extent of DSB induced signalling that is suggested by the data on formation and persistence of the different types of foci. Since no radiation-induced foci can be present immediately after exposure, a steep increase in the number of foci has been assumed before the 20' time point, as is backed up by data from recent studies (e.g. 65, 42).

The position of the initial maximum has been put prior to the earliest point of measurement, since ATM phosphorylation has been reported to be already maximal at five minutes after irradiation with 0.5 Gy IR (68).

So the early maximum in signalling activity is easily explained, but where does this curious minimum at around one hour after treatment come from? In response to varying doses of low-LET photon radiation, where only targeted effects contribute to cellular damage due to all cells being subjected to direct ionization events, the number of different types of foci has been found to decrease monotonously after reaching an early maximum (79, 168, 170) using different cell systems. Furthermore, there is evidence that a significant portion of DSBs induced by a higher dose of high-LET radiation cannot be efficiently repaired within 24 hours after exposure, resulting in the sustained presence of radiation-induced foci (167).

Taking these findings into consideration, targeted radiation effects can be expected to result in the rapid formation of various types of foci, which decrease over time due to successful damage repair, but may, in the case of high-LET radiation, eventually remain at an elevated level over an extended time period. Thus, the decrease in the number of foci may well be exclusively accounted for by targeted DNA lesions and their repair, as is illustrated by the purple line in figure 15.1. However, since the distribution of the sample fibroblasts over all cell cycle phases has been promoted by the applied cultivation procedures (see also figure 10.2), the deviation from the monotonous increase suggested by established knowledge about targeted effects cannot be explained by cell cycle progression and, correspondingly, specific repair processes, but instead argues for a contribution via an additional mechanism.

A mechanism that would be able to account for the delayed increase of affected cells is the spread of the initial damaging signal to bystander cells. This hypothesis is supported by current literature: Firstly, the occurrence of bystander effects in diploid human fibroblasts as used in this work has been demonstrated with various experimental setups (e.g. 108, 111, 121, 128). Furthermore, the postponed nature of focus formation in bystander cells, where γH2AX foci could not be detected within the first 30 minutes but reach high numbers at much later time points (117), in comparison to directly targeted nuclei, is well in line with the observed late increase in the number of affected cells starting one hour after irradiation.

However, the early induction of non-targeted DNA damage is not necessarily due to a bystander response that originates exclusively from targeted DNA damage in other cells. In a study by Shao et al (120), evidence is presented which suggests that cytoplasmic traversals of high-LET particles, which have been realized in microbeam exposures, may have a more pronounced impact on both targeted as well as bystander cells as has so far been anticipated, which has been demonstrated by an increase in micronucleation observed in both populations of cells. While further data on the genotoxic effects of cytoplasmic exposure (169) is scarce, implications on DSB induction and focus formation cannot be ruled out. Obviously, the exposure of cultivated cells in a broad ion beam

results not only in a given number of nuclear, but also in cytoplasmic particle traversals, which may initialize a DNA damage response via a yet unknown mechanism. Therefore, the observed time-dependence of ATM, H2AX and DNA-PKcs phosphorylation may also be mediated by the deposition of radiation energy in cytoplasmic areas.

As a consequence, the difference between the observed total and the estimated targeted response in figure 15.1 shall be attributed to "non-targeted" effects in general (represented by the red line). These refer to radiation-induced events in all cells that have not been subjected to nuclear particle hits, and therefore include both bystander as well as effects triggered by cytoplasmic traversals. Thus, based on the exposures to ^{56}Fe (197.8 keV/µm H_2O) ions and current literature, a simple model for the contribution of targeted and non-targeted effects to the incidence and processing of DSBs in response to low doses of high-LET particle radiation is suggested (figure 15.1) by the author, which may be summarized by the following principles:

- **Every particle of sufficiently high lineal energy induces DSBs upon traversal of a nucleus, which quickly leads to the activation of the DSB signalling and repair machinery and the formation of an equivalent number of foci within a few minutes.**
- **Successful repair is accompanied by the dissolution of foci, resulting in a decrease of the number of affected cells over the first one to two hours.**
- **Starting about one hour after exposure, DSBs are generated in cells not subjected to nuclear particle hits due to bystander signals and/or cytoplasmic particle traversals. These cells eventually exhibit foci similar to those with direct hits and increasingly contribute to the total number of affected cells.**

It shall be stressed that the data gathered in this thesis and used as an experimental basis for this model is not suited for a quantitative prediction of the absolute contribution of both types of effects, which is mainly due to the inherent lack of information on the exact locations of particle hits in broad beam experiments. Therefore, it is also not clear whether the extent of the non-targeted response will actually surpass the targeted effects over time under the given exposure conditions, as is hinted at in figure 15.1.

15.3. Is the HTR Method a Suitable Tool for Prediction of Microbiologic Radiation Effects?

In the current ICRP recommendations, the LET is promoted as the physical quantity that may be translated into radiation quality, which describes the relative effectiveness of a given radiation field to induce a specific biologic response. The HTR, a measured quantity derived from LiF:Mg,Ti glow curves, shows a dependence on LET similar to Q(LET), the quality factor introduced to calculate dose equivalent, which originates from a manifold of radiobiologic and epidemiological data on radiation-induced effects.

Recent insights on non-targeted radiation effects strongly argue for the necessity of a refined, microscopic approach in the assessment of effects induced by low radiation doses, especially when they are delivered by high-energy charged particles. Efforts in this field make use of recently developed methods that allow for the evaluation of biologic events triggered by single particles. While the macroscopic concept of dose is of little significance from a cellular point of view due to the highly localized deposition of energy along a small number of particle tracks, the inherent characteristics of TL-materials, which result in a complex shape of TL glow curves, appear to be able to mimic specific properties of tissue, thus allowing for conclusions on radiation quality based on physical measurements.

In this thesis, differences in radiation quality have been shown to result in a cellular response that varies in extent, localization and time course. Comparison with measured TL results has shown that the cellular response to DNA DSBs at the earliest time point investigated (20') exhibits a dependence on LET similar to the HTR (see section 14.2). At this time, non-targeted radiation-induced effects may be safely neglected, and therefore, the biologic results are easily understood: With rising lineal energy, the probability for the incidence of one or more DSBs along a particle track increases. It has been demonstrated that at high ionization densities, corresponding to a radiation LET somewhere between 60 and 200 keV/µm H_2O, every particle causes at least one DSB upon its traversal through the cell nucleus. At even higher lineal energies, an equal dose is delivered by lowering the particle fluence. Therefore, the detected number of foci, as well as the total focal area due to a relatively smaller increase in the mean focus size, have to decrease due to the lower particle count, since the "excess" energy deposited is not likely to directly induce lesions in DNA molecules further off the track. It is thus tempting to speculate that qualitatively similar processes of energy deposition in LiF:Mg,Ti TL materials may account for the LET-dependent behavior of high-temperature TL emissions, which would be able to explain the similar LET-dependence of HTR and focus formation.

However, the processing and repair of the initial DNA damage is where or, better, when the good correspondence between the HTR(LET) and DSB-induced signalling ends. Evidence has been presented that foci due to lower LET radiation are dissolved much faster than those induced by higher-LET particles, which is also backed up by a recently published study (172). Due to the rather "flat" arrangement of gathered HTR data around the value of 6 for the whole LET range from 50 to 200 keV/µm H_2O (see figure 12.2), this appears to be a rather serious issue. This is illustratively shown by the time-dependent persistence of foci due to ^{28}Si (56 keV/µm H_2O) irradiation, which has been found to differ massively from samples exposed to ^{56}Fe (197.8 keV/µm H_2O), while similar HTR values of 5.73±0.32 and 5.82±0.33 were obtained under equivalent conditions. Therefore, the attempt to derive conclusions on the time course of DSB repair from HTR values between 5.5 and 6.5 seems to be bound to fail miserably.

From the viewpoint of radiation protection, on the other hand, it can be argued that the course and duration of events in DSB-induced signalling may not be as important for radiation risk as the initial damage extent, which results in the introduction of permanent

DNA alterations via the error-prone NHEJ mechanism. Furthermore, as is a major issue for many quantitative indicators of radiation risk, the assessment of an effect of interest is limited to a selected moment or period in the long-term response of tissue to a radiation hazard, which can hardly include all aspects with relevance for risk estimation. Thus, in case of this experimental work, the investigation of the early cellular response to DSBs is suited to elucidate the immediate detrimental effects, which constitute the starting point of the biologic reaction to radiation, but cannot provide conclusions on the outcome.

Another matter is the microscopic structure of tissue and its implications on the interpretation of damage patterns. What is a sensible quantity for dosimetric correlation that reflects the initial damage and the cellular repair efforts induced by low doses of particle radiation? For the initial cellular response to radiation, the evaluation of either the number of foci or the fraction of affected cells appear to be equivalent, which is suggested by the pATM results, where the number of foci equals the number of nuclear particle hits and the determined fraction of cells exhibiting foci is identical to those with nuclear traversals. However, with the prospect of non-targeted effects that seem to contribute as early as two hours after irradiation, it can no longer be safely assumed that both views must lead to the same conclusions, since bystander cells may well exhibit damage patterns different from those due to direct exposure.

Generally speaking, non-targeted effects are bound to complicate any attempt at predicting the biologic damage potential from measured dosimetric quantities, which is due to several reasons: Firstly, they introduce a significant deviation from the linearity between dose and effects for specific exposure situations. Furthermore, the delayed nature of damage occurrence in bystander cells, which may reach its maximum when a large amount of the direct radiation damage is already repaired, leads to severe difficulties in the assessment of the overall damage extent. Apart from that, it is unclear whether non-targeted damage is equally hazardous to genomic integrity as targeted lesions, since the underlying mechanisms are not fully understood. Finally, the bystander response has been demonstrated to exhibit rather surprising dependencies on a manifold of parameters, so that a general prediction of its consequences in a given exposure situation is not easily achieved.

Despite these yet unsolved issues, due to the similarity between the HTR and the initial cellular response, the HTR method may still be considered a promising future option for estimation of radiation effects in many situations. The generated data on pATM and pDNA-PKcs focal area as a function of LET suggests that for a recovery time somewhere between 20' and 1 hour, these parameters will reach a maximum at the same LET value as HTR(LET). There, the focal area may be mapped onto the HTR in a well-defined manner over the whole investigated LET range up to 200 keV/μm H_2O, thus compensating for the problematic shape of HTR(LET) with minimal error. In this manner, TL-measurements of dose and HTR may be, in principle, directly translated into a specific cellular response.

Very briefly, these insights may be summarized by the following points:

- **Macroscopic concepts such as dose are not well-suited to describe cellular events induced by high-energy charged particles. Instead, LET-dependent characteristics of single particle tracks and their (sub-)cellular localization must be accounted for.**
- **For equal doses, the initial DNA DSB-induced cellular response exhibits a similar LET-dependence to the HTR, which is for two reasons: The probability for a single particle to cause one or more DSBs increases with LET, whereas at higher LET-values, the number of damaged sites decreases due to decreasing particle fluence.**
- **The extent of the biochemical cellular response deviates from HTR(LET) with increasing time due to LET-dependent damage processing and a contribution from a non-targeted bystander or cytoplasmic response, which may severely limit the prediction of cellular effects from HTR measurements.**
- **Yet, the initial biochemical response to radiation may be mapped onto the HTR in a well-defined manner. This represents a promising starting point for the direct determination of biologic radiation effects by means of LiF:Mg,Ti TL detectors.**

Obviously, in order to turn these results into a practical tool for the assessment of radiation risk, further efforts are needed in the future, which shall focus on the following problems:

- **The influence of dose on the LET-dependence of the investigated biologic indicators is to be assessed.** While it seems plausible that the shape of the function of the focal area should not be affected for relevant doses lower than 60 mGy – overlap of particle tracks has already been negligible for the higher LET particles and will further decrease with dose, and non-targeted effects do not contribute significantly at this early time point – this is yet to be shown.

- **Much more work is to be dedicated to the consequences of both targeted and non-targeted effects, so that finally, by determination of the initial damage, conclusions on overall health risks can be drawn.** As a first step towards this goal, it seems warranted to investigate various aspects of damage incidence and processing in both targeted and bystander cells by application of particle microbeams, which are designed to precisely distinguish between and selectively initialize targeted, bystander and cytoplasmic effects. Based on current scientific opinion, a few attempts at modeling the bystander response by mathematical means have already been made (e.g. 174, 175), which, however, are in need of continual refinement in order to account for the developing knowledge about the underlying biochemical mechanisms.

- **Studies intended to determine radiation-induced damage must include the time-dependent aspects of the cellular response to fully grasp the significance of common damage indicators.** For γH2AX or pATM, this necessity has been outlined by experiments within this thesis and by others (172). For this purpose, the scope needs to be extended beyond pure quantification of DNA damage and also has to include the assessment of repair and repair fidelity, which strongly mediates long-term effects of radiation exposure.

Eventually, the cellular effects of natural radiation hazards with a particle component, such as the aviation and space environment, may be modeled based on these future investigations. For extended exposure to such mixed radiation fields, where single cells are subjected to radiation of varying quality, it is exceptionally difficult to correctly predict biologic consequences, since different and counteracting mechanisms such as targeted and non-targeted damage induction as well as adaptive response can be expected to contribute. In these environments, LiF:Mg,Ti detectors have already been successfully applied for characterization of specific exposure conditions. Within this thesis, further prospects of TL-dosimetry as a direct way of determining biologic effects have been pointed out based on the observed behavior of early radiation-induced cellular signalling. Promising correspondence between exemplary biochemical events and the HTR promote the necessity of further investigations aimed at establishing TL-dosimetry as a quasi-biologic method for assessment of radiation risks.

References

1. International Commission on Radiological Protection. 1990 Recommendations of the International Commission on Radiological Protection. ICRP Publication 60, Ann. ICRP 21;1-3, Pergamon Press, Oxford, United Kingdom. 1991.
2. International Commission on Radiological Protection (ICRP). SE-171 16 Stockholm, Sweden. http://www.icrp.org.
3. International Commission on Radiological Protection. ICRP approves new fundamental recommendations on radiological protection. 2007 Mar 21. http://www.icrp.org/docs/ICRP_approves_new_fundamental_Recommendations.pdf
4. McKeever SW. Thermoluminescence of solids. Cambridge University Press, Cambridge, United Kingdom. July 1985.
5. Randall TJ, Wilkins MH. Phosphorescence and electron traps I. Proc Roy Soc London. 1945;A184:366.
6. Chen R, McKeever SW. Theory of thermoluminescence and related phenomena. World Scientific, Singapore. 1997.
7. McKeever SW, Chen R. Luminescence Models. Radiat Meas. 1997;27(5/6):625-661.
8. Alberts G, Bray D, Lewis J. Molecular Biology of the Cell. Garland Science. 2002 Mar 30.
9. Fuchs G, Schlegel HG. Allgemeine Mikrobiologie. Thieme Verlag, Stuttgart. 2006 Sep; 8th ed. (in german).
10. Sullivan J. Cells Alive! http://www.cellsalive.com/. 2006 Nov.
11. Wilson GD. Radiation and the cell cycle, revisited. Cancer Metastasis Rev. 2004 Aug-Dec;23(3-4):209-25.
12. Pawlik TM, Keyomarsi K. Role of cell cycle in mediating sensitivity to radiotherapy. Int J Radiat Oncol Biol Phys. 2004 Jul 15;59(4):928-42.
13. Schafer KA. The cell cycle: a review. Vet. Pathol. 1998 Nov;35(6):461-78.
14. Forshier S. Essentials of Radiation Biology and Protection. Delmar Thomson Learning. 2002 Jan.
15. Kiefer J. Biological Radiation Effects. Springer. 1990 Apr.
16. Hoffmann ME, Mello-Filho AC, Meneghini R. Correlation between cytotxic effect of hydrogen peroxide and the yield of DNA strand breaks in cells of different species. Biochim Biophys Acta. 1984 Apr 5;781(3):234-8.

17. Mello Filho AC, Hoffmann ME, Meneghini R. Cell killing and DNA damage by hydrogen peroxide are mediated by intracellular iron. Biochem J. 1984 Feb 15;218(1):273-5.
18. Isaacs RJ, Spielmann HP. A model for initial DNA lesion recognition by NER and MMR based on local conformational flexibility. DNA Repair (Amst). 2004 May 4;3(5):455-64.
19. Rydberg B. Radiation-induced DNA damage and chromatin structure. Acta Oncol. 2001;40(6):682-5.
20. Iliakis G, Wang H, Perrault AR, Boecker W, Rosidi B, Windhofer F, Wu W, Guan J, Terzoudi G, Pantelias G. Mechanisms of DNA double strand break repair and chromosome aberration formation. Cytogenet Genome Res. 2004;104(1-4):14-20.
21. Savitsky K, Bar-Shira A, Gilad S, Rotman G, Ziv Y, Vanagaite L, Tagle DA, Smith S, Uziel T, Sfez S, et al. A single ataxia telangiectasia gene with a product similar to PI-3 kinase. Science. 1995 Jun 23;268(5218):1749-53.
22. Shiloh Y. ATM and related protein kinases: safeguarding genome integrity. Nat Rev Cancer. 2003 Mar;3(3):155-68.
23. Kitagawa R, Kastan MB. The ATM-dependent DNA damage signaling pathway. Cold Spring Harb Symp Quant Biol. 2005;70:99-109.
24. Shiloh Y. ATM: ready, set, go. Cell Cycle. 2003 Mar-Apr;2(2):116-7.
25. Khanna KK, Lavin MF, Jackson SP, Mulhem TD. ATM, a central controller of cellular responses to DNA damage. Cell Death Differ. 2001 Nov;8(11):1052-65.
26. Kurz EU, Lees-Miller SP. DNA damage-induced activation of ATM and ATM-dependent signaling pathways. DNA Repair (Amst). 2004 Aug-Sep;3(8-9):889-900.
27. Savitsky K, Sfez S, Tagle DA, Ziv Y, Sartiel A, Collins FS, Shiloh Y, Rotman G. The complete sequence of the coding region of the ATM gene reveals similarity to cell cycle regulators in different species. Hum Mol Genet. 1995 Nov;4(11):2025-2032.
28. Smith GC, Jackson SP. The DNA-dependent protein kinase. Genes Dev. 1999 Apr 15;13(8):916-934.
29. Featherstone C, Jackson SP. Ku, A DNA repair protein with multiple cellular functions? Mutat Res. 1999 May 14;434(1):3-15.
30. Lee SH, Kim CH. DNA-dependent protein kinase complex: a multifunctional protein in DNA repair and damage checkpoint. Mol Cells. 2002 Apr 30;13(2):159-66.
31. Burma S, Chen DJ. Role of DNA-PK in the cellular response to DNA double-strand breaks. DNA Repair (Amst). 2004 Aug-Sep;3(8-9):909-18.
32. Dip R, Naegeli H. More than just strand breaks: the recognition of structural DNA discontinuities by DNA-dependent protein kinase catalytic subunit. FASEB J. 2005 May;19(7):704-15.
33. Jackson SP. Sensing and repairing DNA double-strand breaks. Carcinogenesis. 2002 May;23(5):687-96.
34. Zhu C, Roth DB. Mechanism of V(D)J recombination. Cancer Surv. 1996;28:295-309.
35. Olive PL. The role of DNA single- and double-strand breaks in cell killing by ionizing radiation. Radiat Res. 1998 Nov;150(5 Suppl):S42-51.

36. Hoeijmakers JH. Genome maintenance mechanisms for preventing cancer. Nature. 2001 May 17;411(6835):366-74.
37. Rothkamm K, Krüger I, Thompson LH, Löbrich M. Pathways of DNA double-strand break repair during the mammalian cell cycle. Mol Cell Biol. 2003 Aug;23(16):5706-15.
38. Chan DW, Chen BP, Prithivirajsingh S, Kurimasa A, Story MD, Qin J, Chen DJ. Autophosphorylation of the DNA-dependent protein kinase catalytic subunit is required for rejoining of DNA double-strand breaks. Genes Dev. 2002 Sep 15;16(18):2333-8.
39. Pastwa E, Blasiak J. Non-homologous DNA end joining. Acta Biochim Pol. 2003;50(4):891-908.
40. Ting NSY, Lee WH. The DNA double-strand break response pathway: becoming more BRCAish than ever. DNA Repair (Amst.) 2004 Aug-Sep;3(8-9):935-44.
41. Bassing CH, Alt FW. The cellular response to general and programmed DNA double strand breaks. DNA Repair (Amst.) 2004 Aug-Sep;3(8-9):781-96.
42. Stiff T, O'Driscoll M, Rief N, Iwabuchi K, Löbrich M, Jeggo PA. ATM and DNA-PK Function Redundantly to Phosphorylate H2AX after Exposure to Ionizing Radiation. Cancer Res. 2004 Apr 1;64(7):2390-6.
43. Lavin MF. The Mre11 complex and ATM: a two-way functional interaction in recognising and signaling DNA double strand breaks. DNA Repair (Amst.) 2004 Nov 2;3(11):1515-20.
44. Stracker TH, Theunissen JWF, Morales M, Petrini JHJ. The Mre11 complex and the metabolism of chromosome breaks: the importance of communicating and holding things together. DNA Repair (Amst.) 2004 Aug-Sep;3(8-9):845-54.
45. Bekker-Jensen S, Lukas C, Kitagawa R, Melander F, Kastan MB, Bartek J, Lukas J. Spatial organization of the mammalian genome surveillance machinery in response to DNA strand breaks. J Cell Biol. 2006 Apr 24;173(2):195-206.
46. Kobayashi J, Antoccia A, Tauchi H, Matsuura S, Komatsu K. NBS1 and its functional role in the DNA damage response. DNA Repair (Amst.) 2004 Aug-Sep;3(8-9):855-61.
47. Smith J, Baldeyron C, de Oliveira I, Sala-Trepat M, Papadopoulo D. (2001) The influence of DNA double-strand break structure on end-joining in human cells. Nucleic Acids Res. 2001 Dec 1;29(23):4783–92.
48. Lisby M, Rothstein R. DNA damage checkpoint and repair centers. Curr Opin Cell Biol. 2004 Jun;16(3):328-34.
49. Lees-Miller SP, Meek K. Repair of DNA double strand breaks by non-homologous end joining. Biochimie. 2003 Nov;85(11):1161-73.
50. Lengauer C, Kinzler KW, Vogelstein B. Genetic instabilities in human cancers. Nature. 1998 Dec 17;396(6712):643–9.
51. Ding Q, Reddy YV, Wang W, Woods T, Douglas P, Ramsden DA, Lees-Miller SP, Meek K. Autophosphorylation of the catalytic subunit of the DNA-dependent protein kinase is required for efficient end processing during DNA double-strand break repair. Mol Cell Biol. 2003 Aug;23(16):5836–48.

52. Soubeyrand S, Pope L, Pakuts B, Hache RJ. Threonines 2638/2647 in DNA-PK are essential for cellular resistance to ionizing radiation. Cancer Res. 2003 Mar 15;63(6):1198-201.
53. Chan DW, Ye R, Veillette CJ, Lees-Miller SP. DNA-dependent protein kinase phosphorylation sites in Ku 70/80 heterodimer.
54. Woo RA, Jack MT, Xu Y, Burma S, Chen DJ, Lee PW. DNA damage-induced apoptosis requires the DNA-dependent protein kinase, and is mediated by the latent population of p53. EMBO J. 2002 Jun 17;21(12):3000–8.
55. Dai Y, Kysela B, Hanakahi LA, Manolis K, Riballo E, Stumm M, Harville TO, West SC, Oettinger MA, Jeggo PA. Nonhomologous end joining and V(D)J recombination require an additional factor. Proc Natl Acad Sci U S A. 2003 Mar 4;100(5): 2462–7.
56. Leber R, Wise TW, Mizuta R, Meek K. The XRCC4 gene product is a target for and interacts with the DNA-dependent protein kinase. J Biol Chem. 1998 Jan 16;273(3):1794–801.
57. Ma Y, Pannicke U, Schwarz K, Lieber MR. Hairpin opening and overhang processing by an Artemis/DNA-dependent protein kinase complex in nonhomologous end joining and V(D)J recombination. Cell. 2002 Mar 22;108(6):781–94.
58. Merkle D, Douglas P, Moorhead GB, Leonenko Z, Yu Y, Cramb D, Bazett-Jones DP, Lees-Miller SP. The DNA-dependent protein kinase interacts with DNA to form a protein-DNA complex that is disrupted by phosphorylation. Biochemistry. 2002 Oct 22;41(42):12706–14.
59. Cox MM. Recombinational DNA repair of damaged replication forks in Escherichia coli: questions. Annu Rev Genet. 2001;35:53–82.
60. Jackson SP. Sensing and repairing DNA double-strand breaks. Carcinogenesis 2002 May;23(5):687-96.
61. Wyman C, Ristic D, Kanaar R. Homologous recombination-mediated double-strand break repair. DNA Repair (Amst.) 2004 Aug-Sep;3(8-9):827-33.
62. Cromie GA, Connelly JC, Leach DR. Recombination at double-strand breaks and DNA ends: conserved mechanisms from phage to humans. Mol Cell. 2001 Dec;8(6):1163-74.
63. Shiloh Y. The ATM-mediated damage response: taking shape. Trends Biochem Sci. 2006 Jul;31(7):402-10.
64. Van Dyck E, Stasiak AZ, Stasiak A, West SC. Binding of double-strand breaks in DNA by human Rad52 protein. Nature 1999 Sep 23;401(6751):403.
65. Andegeko Y, Moyal M, Mittelman L, Tsarfaty I, Shiloh Y, Rotman G. Nuclear Retention of ATM at Sites of DNA Double Strand Breaks. J Biol Chem. 2001 Oct 12;276(41):38224-30.
66. Mirzoeva OK, Petrini JH. DNA damage-dependent nuclear dynamics of the mre11 complex. Mol. Cell. Biol. 21 (2001) 281–288.
67. Uziel T, Lerenthal Y, Moyal L, Andegeko Y, Mittelman L, Shiloh Y. Requirement of the MRN complex for ATM activation by DNA damage. EMBO J. 2003 Oct 15;22(20):5612–21.

68. Bakkenist CJ, Kastan MB. DNA damage activates ATM through intermolecular autophosphorylation and dimer dissociation. Nature. 2003 Jan 30;421(6922):499-506.
69. Wu X, Ranganathan V, Weisman DS, Heine WF, Ciccone DN, O'Neill TB, Crick TB, Pierce KA, Lane WS, Rathbun G, Livingston DM, Weaver DT. ATM phosphorylation of Nijmegen breakage syndrome protein is required in a DNA damage response. Nature. 2000 May 25;405(6785):477-82.
70. Mochan TA, Venere M, DiTullio Jr. RA, Halazonetis TD. 53BP1 and NFBD1/MDC1-Nbs1 function in parallel interacting pathways activating ataxia-telangiectasia mutated (ATM) in response to DNA damage. Cancer Res. 2003 Dec 15;63(24):8586-91.
71. Sigurdsson S, Trujillo K, Song B, Stratton S, Sung P. 2001. Basis for avid homologous DNA strand exchange by human Rad51 and RPA. J Biol Chem. 2001 Mar 23;276(12):8798-806.
72. Takata M, Sasaki MS, Tachiiri S, Fukushima T, Sonoda E, Schild D, Thompson LH, Takeda S. Chromosome instability and defective recombinational repair in knockout mutants of the five Rad51 paralogs. Mol Cell Biol. 2001 Apr;21(8):2858-66.
73. Van den Bosch M, Lohman PH, Pastink A. DNA double-strand break repair by homologous recombination. Biol Chem. 2002 Jun;383(6): 873-92.
74. Symington LS. Role of RAD52 epistasis group genes in homologous recombination and double-strand break repair. Microbiol Mol Biol Rev. 2002 Dec;66(4):630-70
75. Sonoda E, Sasaki MS, Buerstedde JM, Bezzubova O, Shinohara A, Ogawa H, Takata M, Yamaguchi-Iwai Y, Takeda S. 1998. Rad51-deficient vertebrate cells accumulate chromosomal breaks prior to cell death. EMBO J. 1998 Jan 15;17(2):598-608.
76. Lukas J, Lukas C, Bartek J. Mammalian cell cycle checkpoints: signalling pathways and their organization in space and time. DNA Repair (Amst). 2004 Aug-Sep;3(8-9):997-1007.
77. Ahn J, Urist M, Prives C. The Chk2 protein kinase. DNA Repair (Amst). 2004 Aug-Sep;3(8-9):1039-47.
78. Chen Y, Sanches Y. Chk1 in the DNA damage response: conserved roles from yeasts to mammals. DNA Repair (Amst.) 2004 Aug-Sep;3(8-9):1025-32.
79. Buscemi G, Perego P, Carenini N, Nakanishi M, Chessa L, Chen L, Khanna KK, Delia D. Activation of ATM and Chk2 kinases in relation to the amount of DNA strand breaks. Oncogene. 2004 Oct 7;23(46):7691-700.
80. Denekamp J. Cell kinetics and radiation biology. Int J Radiat Biol Relat Stud Phys Chem Med. 1986 Feb;49(2):357-80.
81. Sionov RV, Haupt Y. The cellular response to p53: the decision between life and death. Oncogene. 1999 Nov 1;18(45):6145-57.
82. Sherr CJ, Roberts JM. CDK inhibitors: positive and negative regulators of G1-phase progression. Genes Dev. 1999 Jun 15;13(2):1501-12.
83. Shakkelford RE, Kaufmann WK Paules RS. Cell cycle control, checkpoint mechanisms, and genotoxic stress. Environ Health Perspect. 1999 Feb;107 Suppl 1:5-24.

84. Miller ME, Cross FR. Cyclin specificity: how many wheels do you need on a unicycle? J Cell Sci. 2001 May;114(Pt 10):1811-20.
85. Shechter D, Costanzo V, Gautier J. Regulation of DNA replication by ATR: signaling in response to DNA intermediates. DNA Repair (Amst). 2004 Aug-Sep;3(8-9):901-8.
86. Donzelli M, Draetta GF. Regulating mammalian checkpoints through Cdc25 inactivation. EMBO Rep. 2003 Jul;4(7):671-7.
87. Jiang K, Pereira E, Maxfield M, Russell B, Goudelock DM, Sanchez Y. Regulation of Chk1 includes chromatin association and 14-3-3 binding following phosphorylation on Ser-345. J Biol Chem. 2003 Jul 4;278(27):25207–25217.
88. Meek DW. The p53 response to DNA damage. DNA Repair (Amst). 2004 Aug-Sep;3(8-9):1049-56.
89. Appella E, Anderson CW. Post-translational modifications and activation of p53 by genotoxic stresses. Eur J Biochem. 2001 May;268(10):2764-72.
90. Thompson T, Tovar C, Yang H, Carvajal D, Vu BT, Xu Q, Wahl GM, Heimbrook DC, Vassilev LT. Phosphorylation of p53 on key serines is dispensable for transcriptional activation and apoptosis. J Biol Chem. 2004 Dec 17;279(51):53015-22.
91. Taylor WR, Stark GR. Regulation of the G2/M transition by p53. Oncogene. 2001 Apr 5;20(15):1803-15.
92. Nyberg KA, Michelson RJ, Putnam CW, Weinert TA. Toward maintaining the genome: DNA damage and replication checkpoints. Annu Rev Genet. 2002;36:617-56.
93. Oda K, Arakawa H, Tanaka T, Matsuda K, Tanikawa C, Mori T, Nishimori H, Tamai K, Tokino T, Nakamura Y, Taya Y. p53AIP1, a potential mediator of p53-dependent apoptosis, and its regulation by Ser-46-phosphorylated p53. Cell. 2000 Sep 15;102(6):849-62.
94. Wu X, Bayle JH, Olson D, Levine AJ. The p53-mdm-2 autoregulatory feedback loop. Genes Dev. 1993 Jul;7(7A):1126-32.
95. Fernandez-Capetillo O, Lee A, Nussenzweig M, Nussenzweig A. H2AX: the histone guardian of the genome. DNA Repair (Amst). 2004 Aug-Sep;3(8-9):959-67.
96. Mannironi C, Bonner WM, Hatch CL. H2A.X. a histone isoprotein with a conserved C-terminal sequence, is encoded by a novel mRNA with both DNA replication type and polyA 3' processing signals. Nucleic Acids Res. 1989 Nov 25;17(22):9113-26.
97. Rogakou EP, Pilch DR, Orr AH, Ivanova VS, Bonner WM. DNA double-stranded breaks induce histone H2AX phosphorylation on serine 139. J Biol Chem. 1998 Mar 6;273(10):5858-68.
98. Celeste A, Fernandez-Capetillo O, Kruhlak MJ, Pilch DR, Staudt DW, Lee A, Bonner RF, Bonner WM, Nussenzweig A. Histone H2AX phosphorylation is dispensable for the initial recognition of DNA breaks. Nat Cell Biol. 2003 Jul;5(7):675-9.
99. Yoshida K, Yoshida S, Shimoda C, Morita T. Expression and radiation-induced phosphorylation of histone H2AX in mammalian cells. J Radiat Res (Tokyo). 2003 Mar;44(1):47-51.

100. Rogakou EP, Boon C, Redon C, Bonner WM. Megabase chromatin domains involved in DNA double-strand breaks in vivo. J Cell Biol. 1999 Sep 6;146(5):905-16.
101. Lisby M, Mortensen UH, Rothstein R. Colocalization of multiple DNA double-strand breaks at a single Rad52 repair centre. Nat Cell Biol. 2003 Jun;5(6):572-7.
102. Ward IM, Chen J. Histone H2AX is phosphorylated in an ATR-dependent manner in response to replicational stress. J Biol Chem. 2001 Dec 21;276(51):47759-62.
103. Mukherjee B, Kessinger C, Kobayashi J, Chen BP, Chen DJ, Chatterjee A, Burma S. DNA-PK phosphorylates histone H2AX during apoptotic DNA fragmentation in mammalian cells. DNA Repair (Amst). 2006 May 10;5(5):575-90.
104. Burma S, Chen BP, Murphy M, Kurimasa A, Chen DJ. ATM phosphorylates histone H2AX in response to DNA double-strand breaks. J Biol Chem. 2001 Nov 9;276(45):42462-7.
105. Fernandez-Capetillo O, Chen HT, Celeste A, Ward I, Romanienko PJ, Morales JC, Naka K, Xia Z, Camerini-Otero RD, Motoyama N, Carpenter PB, Bonner MW, Chen J, Nussenzweig A. DNA damage-induced G2-M checkpoint activation by histone H2AX and 53BP1. Nat Cell Biol. 2002 Dec;4(12):993-7.
106. Huang X, Halicka HD, Traganos F, Tanaka T, Kurose A, Darzynkiewicz Z. Cytometric assessment of DNA damage in relation to cell cycle phase and apoptosis. Cell Prolif. 2005 Aug;38(4):223-43.
107. Mothersill C, Seymour C. Radiation-induced bystander effects, carcinogenesis and models. Oncogene. 2003 Oct 13;22(45):7028-33.
108. Balajee AS, Ponnaiya B, Baskar R, Geard CR. Induction of replication protein A in bystander cells. Radiat Res. 2004 Dec;162(6):677-86.
109. Mothersill C, Seymour C. Medium from irradiated human epithelial cells but not human fibroblasts reduces the clonogenic survival of unirradiated cells. Int J Radiat Biol. 1997 Apr;71(4):421–7.
110. Mothersill C, Seymour CB. Cell-cell contact during gamma irradiation is not required to induce a bystander effect in normal human keratinocytes: evidence for release during irradiation of a signal controlling survival into the medium. Radiat Res. 1998 Mar;149(3):256-62.
111. Yang H, Asaad N, Held KD. Medium-mediated intercellular communication is involved in bystander responses in X-ray-irradiated normal human fibroblasts. Oncogene. 2005 Mar 17;24(12):2096-2103.
112. Nagasawa H, Little JB. Induction of sister chromatid exchanges by extremely low doses of alpha-particles. Cancer Res. 1992 Nov 15;52(22):6394-6.
113. Suzuki M, Zhou H, Hei TK, Tsuruoka C, Fujitaka K. Effects of irradiated medium on chromatid aberrations in mammalian cells using double mylar dishes. Biol Sci Space. 2004 Nov;18(3):110-1.
114. Suzuki M, Zhou H, Hei TK, Tsuruoka C, Fujitaka K. Induction of a bystander chromosomal damage of He-ion microbeams in mammalian cells. Biol Sci Space. 2003 Oct;17(3):251-2.
115. Seymour CB, Mothersill C. Relative contribution of bystander and targeted cell killing to the low-dose region of the radiation dose-response curve. Radiat Res. 2000 May;153(5 Pt 1):508-11.

116. Sawant SG, Randers-Pehrson G, Geard CR, Brenner DJ, Hall EJ. The bystander effect in radiation oncogenesis: I. Transformation in C3H 10T1/2 cells in vitro can be initiated in the unirradiated neighbors of irradiated cells. Radiat Res. 2001 Mar;155(3):397-401.
117. Sokolov MV, Smilenov LB, Hall EJ, Panyutin IG, Bonner WM, Sedelnikova OA. Ionizing radiation induces DNA double-strand breaks in bystander primary human fibroblasts. Oncogene. 2005 Nov 10;24(49):7257-65.
118. Azzam EI, De Toledo SM, Spitz DR, Little JB. Oxidative metabolism modulates signal transduction and micronucleus formation in bystander cells from alpha-particle-irradiated normal human fibroblast cultures. Cancer Res. 2002 Oct 1;62(19):5436-42.
119. Belyakov OV, Malcolmson AM, Folkard M, Prise KM, Michael BD. Direct evidence for a bystander effect of ionizing radiation in primary human fibroblasts. Br J Cancer. 2001 Mar 2;84(5):674-9.
120. Shao C, Folkard M, Michael BD, Prise KM. Targeted cytoplasmic irradiation induces bystander responses. Proc Natl Acad Sci U S A. 2004 Sep 14;101(37):13495-500.
121. Frankenberg D, Greif KD, Giesen U. Radiation response of primary human skin fibroblasts and their bystander cells after exposure to counted particles at low and high LET. Int J Radiat Biol. 2006 Jan;82(1):59-67.
122. Burdak-Rothkamm S, Short SC, Folkard M, Rothkamm K, Prise KM. ATR-dependent radiation-induced gammaH2AX foci in bystander primary human astrocytes and glioma cells. Oncogene. 2006 Aug 7; [Epub ahead of print]
123. Howell RW, Bishayee A. Bystander effects caused by nonuniform distributions of DNA-incorporated (125)I. Micron. 2002;33(2):127-32.
124. Xue LY, Butler NJ, Makrigiorgos GM, Adelstein SJ, Kassis AI. Bystander effect produced by radiolabeled tumor cells in vivo. Proc Natl Acad Sci U S A. 2002 Oct 15;99(21):13765-70.
125. Frank DK, Szymkowiak B, Josifovska-Chopra O, Nakashima T, Kinnally KW. Single-cell microinjection of cytochrome c can result in gap junction-mediated apoptotic cell death of bystander cells in head and neck cancer. Head Neck. 2005 Sep;27(9):794-800.
126. Azzam EI, de Toledo SM, Gooding T, Little JB. Intercellular communication is involved in the bystander regulation of gene expression in human cells exposed to very low fluences of alpha particles. Radiat Res. 1998 Nov;150(5):497-504.
127. Zhou N, Suzuki M, Randers-Pehrson G, Vannais D, Chen G, Trosko J, Waldren CA, Hei TK. Radiation risk to low fluences of alpha particles may be greater than we thought. Proc Natl Acad Sci U S A. 2001 Dec 4;98(25):14410-5.
128. Azzam EI, De Toledo SM, Little JB. Direct evidence for the participation of gap junction-mediated intercellular communication in the transmission of damage signals from alpha-particle irradiated to nonirradiated cells. Proc Natl Acad Sci U S A. 2001 Jan 16;98(2):473-8.
129. Hei TK, Persaud R, Zhou H, Suzuki M. Genotoxicity in the eyes of bystander cells. Mutat Res. 2004 Dec 2;568(1):111-20.

130. Goldberg Z, Lehnert BE. Radiation-induced effects in unirradiated cells: a review and implications in cancer. Int J Oncol. 2002 Aug;21(2):337-49.
131. Narayanan PK, Goodwin EH, Lehnert BE. Alpha particles initiate biological production of superoxide anions and hydrogen peroxide in human cells. Cancer Res. 1997 Sep 15(18):3963-71.
132. Persaud R, Zhou H, Baker SE, Hei TK, Hall EJ. Assessment of low linear energy transfer radiation-induced bystander mutagenesis in a three-dimensional culture model. Cancer Res. 2005 Nov 1;65(21):9876-82.
133. Mothersill C, Seymour C. Radiation-induced bystander effects and adaptive responses--the Yin and Yang of low dose radiobiology? Mutat Res. 2004 Dec 2;568(1):121-8.
134. Watson GE, Lorimore SA, MacDonald DA, Wright EG: Chromosomal instability in unirradiated cells induced in vivo by a bystander effect of ionizing radiation. Cancer Res. 2000 Oct 15;60(20):5608-11.
135. Matsumoto H, Takahashi A, Ohnishi T. Radiation-induced adaptive response and bystander effects. Biol Sci Space. 2004 Dec;18(4):247-54.
136. Coen N, Mothersill C, Kadhim M, Wright EG. Heavy metals of relevance to human health induce genomic instability. J Pathol. 2001 Oct;195(3):293-9.
137. Brooks AL. Paradigm shifts in radiation biology: their impact on intervention for radiation-induced disease. Radiat Res. 2005 Oct;164(4 Pt 2):454-61.
138. Iyer R, Lehnert BE. Alpha-particle-indued increases in the radioresistance of normal human bystander cells. Radiat Res. 2002 Jan;157(1):3-7.
139. Vana N, Erlach R, Fugger M, Gratzl W, Reichhalter I. A computerised TL read out system for dating and phototransfer measurements. Nucl Tracks Radiat Meas. 1988;14(1/2):181.
140. Schöner W. Die HTR Methode zur Messung des mittleren LET der Strahlung im Weltraum mit Thermolumineszenz-Dosimetern und ihre mikrodosimetrische Interpretation. Ph.D. thesis, 1987. Atomic Institute of the Austrian Universities, Vienna, Austria.
141. Hajek M. Applied neutron spectrometry – applications atop high-altitude mountains and onboard aircraft. Ph.D. thesis, 2002 Feb. Atomic Institute of the Austrian Universities, Vienna, Austria.
142. Vana N, Schöner W, Fugger M, Akatov Y A (1992) DOSIMIR – Radiation measurements inside the Soviet space station MIR – First results. Proc Intern Space Year Conference. 1992;ESA ISY-4:193.
143. Driscoll CM. Studies of the effect of LET on the thermoluminescent properties of thin lithium fluoride layers. Phys Med Biol. 1978 Jul;23(4):777-81.
144. Hoffmann W, Prediger B. Heavy particle dosimetry with high temperature peaks of CaF_2:Tm and ^{7}LiF phosphors. Radiat Prot Dosim. 1983;6:149-52.
145. Schöner W, Vana N, Fugger M. The LET-dependence of LiF:Mg,Ti-dosemeters and its application for LET-measurements in mixed fields. Radiat Prot Dosim. 1999;85(1-4):263-6.
146. National Institute of Radiological Sciences. Heavy Ion Medical Accelerator in Chiba: HIMAC. http://www.nirs.go.jp/ENG/pub/himac/himac.pdf. 2006 Dec.

147. National Institute of Radiological Sciences. Brochure. http://www.nirs.go.jp/ENG/publications/pdf/bro-e.pdf. 2007 Jan.
148. Berger T. Dose assessment in mixed radiation fields, special emphasis on space dosimetry. Ph.D. thesis, 2003 May. Atomic Institute of the Austrian Universities, Vienna, Austria.
149. Ziegler JF, Ziegler MD, Biersack JP. SRIM ver. 2006.02. http://www.srim.org. 2006 Dec.
150. TLD (TL OSL) version V03.28. Wegs data, 2006.
151. Berger T, Hajek M, Schoener W, Fugger M, Vana N, Noll M, Ebner R, Akatov Y, Shurshakov V, Arkhangelsky V. Measurement of the depth distribution of average LET and absorbed dose inside a water-filled phantom on board space station MIR. Phys Med. 2001;17 Suppl 1:128-30.
152. Cucinotta FA, Katz R, Wilson JW, Dubey RR. Heavy ion track-structure for radial dose in arbitrary materials. NASA technical paper 3497. 1995 Feb 1.
153. Hajek M, Berger T, Hofmann P, Fugger M, Vana N. Results for ATI passive detectors exposed during ICCHIBAN-4. HIMAC 2007 (in press).
154. Hajek M, Berger T, Fugger M, Fuerstner M, Vana N, Akatov Y, Shurshakov V, Arkhangelsky V. BRADOS – Dose determination in the Russian segment of the International Space Station. Adv Space Res. 2006;37:1664–7.
155. Berger T, Hajek M, Summerer L, Fugger M, Vana N. The efficiency of various thermoluminescence dosemeter types to heavy ions. Radiat Prot Dosimetry. 2006;120(1-4):365-8.
156. Protocol Online: Your lab's reference book. http://www.protocol-online.org, 1999-2006.
157. Rothkamm K, Lobrich M. Evidence for a lack of DNA double-strand break repair in human cells exposed to very low x-ray doses. Proc Natl Acad Sci U S A. 2003 Apr 29;100(9):5057-62.
158. Rasband WS. ImageJ v1.35p. U.S. National Institutes of Health, Bethesda, Maryland, USA. http://rsb.info.nih.gov/ij/, 1997-2006.
159. Bennet J and the AutoIt Team. AutoIT v.3.1.1. http://www.autoitscript.com/autoit3/. 1999-2006.
160. Van der Laak JA, Pahlplatz MM, Hanselaar AG, de Wilde PC. Hue-saturation-density (HSD) model for stain recognition in digital images from transmitted light microscopy. Cytometry. 2000;39:275-84.
161. Jakob B, Scholz M, Taucher-Scholz G. Biological imaging of heavy charged-particle tracks. Radiat Res. 2003 May;159(5):676-84.
162. Wicht H, Maronde E, Olcese J, Korf H. A semiquantitative image-analytical method for the recording of dose–response curves in immunocytochemical preparations. J Histochem Cytochem. 1999 Mar;47(3):411-20.
163. Fürweger C, Hajek M, Vana N, Kodym R, Okayasu R. Cellular signal transduction events as a function of linear energy transfer (LET). Radiat Prot Dosim. 2007 Jun 18; [Epub ahead of print].
164. Buscemi G, Carlessi L, Zannini L, Lisanti S, Fontanella E, Canevari S, Delia D. DNA damage-induced cell cycle regulation and function of novel chk2 phosphoresidues. Mol Cell Biol. 2006 Nov;26(21):7832-45.

165. Lukas C, Falck J, Bartkova J, Bartek J, Lukas J. Distinct spatiotemporal dynamics of mammalian checkpoint regulators induced by DNA damage. Nat Cell Biol. 2003 Mar;5(3):255–260.
166. Ward IM, Wu X, Chen J. Threonine 68 of chk2 is phosphorylated at sites of DNA strand breaks. J Biol Chem. 2001 Dec 21;276(51):47755-8.
167. Okayasu R, Okada M, Okabe A, Noguchi M, Takahura K, Takahashi S. Repair of DNA damage induced by accelerated heavy ions in mammalian cells proficient and deficient in the non-homologous end-joining pathway. Radiat Res. 2006 Jan;165(1):59-67.
168. Suzuki K, Okada H, Yamauchi M, Oka Y, Kodama S, Watanabe M. Qualitative and quantitative analysis of phosphorylated ATM foci induced by low-dose ionizing radiation. Radiat Res. 2006 May;165(5):499-504.
169. Wu L, Randers-Pehrson G, Xu A, Waldren CA, Geard CR, Yu Z, Hei TK. Targeted cytoplasmic irradiation with alpha particles induces mutations in mammalian cells. Proc Natl Acad Sci U S A. 1999 Apr 27;96(9):4959-64.
170. Wang H, Wang M, Wang H, Böcker W, Iliakis G. Complex H2AX phosphorylation patterns by multiple kinases including ATM and DNA-PK in human cells exposed to ionizing radiation and treated with kinase inhibitors. J Cell Physiol. 2005 Feb;202(2):492-502.
171. Costes SV, Boissiere A, Ravani S, Romano R, Parvin B, Barcellos-Hoff MH. Imaging features that discriminate between foci induced by high- and low-LET radiation in human fibroblasts. Radiat Res. 2006 May;165(5):505-15.
172. Leatherbarrow EL, Harper JV, Cucinotta FA, O'Neill P. Induction and quantification of gamma-H2AX foci following low and high LET-irradiation. Int J Radiat Biol. 2006 Feb;82(2):111-8.
173. Yamada S. Commissioning and performance of the HIMAC medical accelerator. Proc 1995 IEEE Particle Accelerator Conf. Dallas, USA. 1995; 9-13.
174. Brenner DJ, Little JB, Sachs RK. The bystander effect in radiation oncogenesis: II. A quantitative model. Radiat Res. 2001 Mar;155(3):402-8.
175. Nikjoo H, Khvostunov IK. A theoretical approach to the role and critical issues associated with bystander effect in risk estimation. Hum Exp Toxicol. 2004 Feb;23(2):81-6.
176. Iyer R, Lehnert BE. Low dose, low-LET ionizing radiation-induced radioadaptation and associated early responses in unirradiated cells. Mutat Res. 2002 Jun 19;503(1-2):1-9.

Appendix A: SRIM Simulations

In the following, SRIM2006-based graphs for determination of particle LET at the sample position are given as a complement to section 10.2. For all graphs, particle species, energy, the number of calculated particles and the thickness of binary filters are given if applied. A 1 mm thick layer of polyethylene is used for simulation of the Permanox slide, with the cell layer being located immediately after (i.e. on the right-hand side of) the slide. "Energy Loss (eV/Angstrom)" is to be multiplied by 10 to get the LET in keV/µm H_2O.

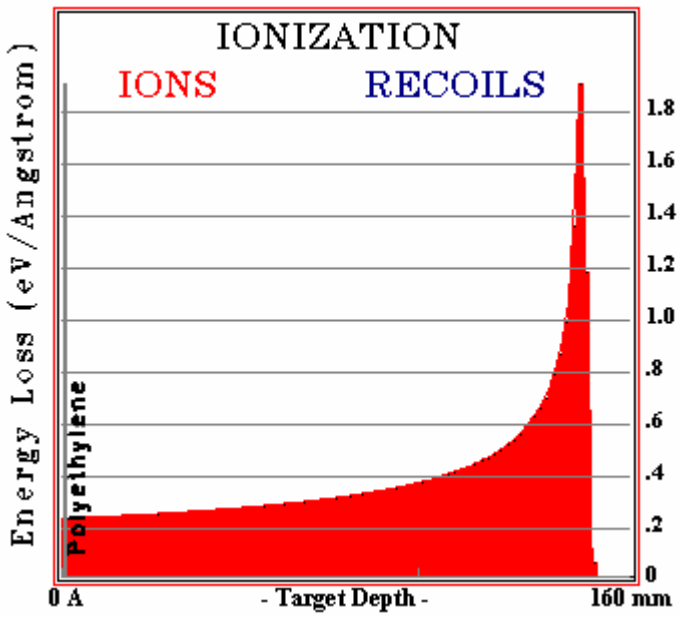

^{4}He, 144.2 MeV/n, 10^4 particles, no binary filter

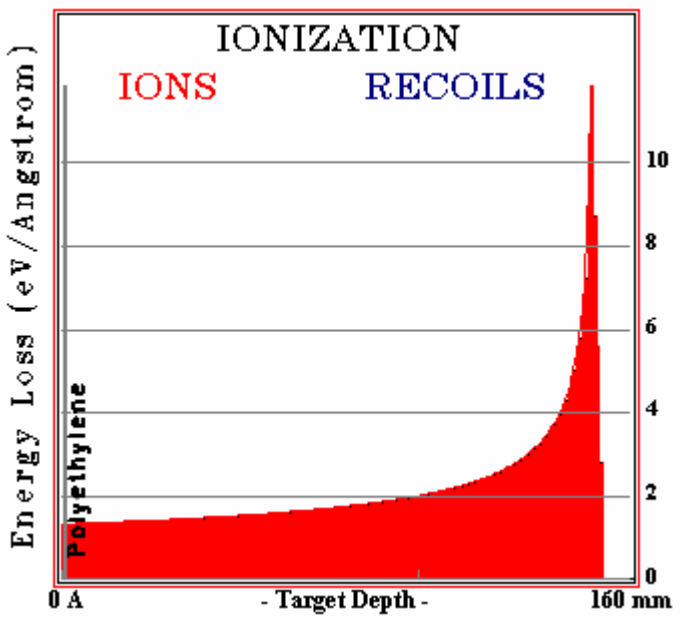

^{12}C, 273.3 MeV/n, 5000 particles, no binary filter

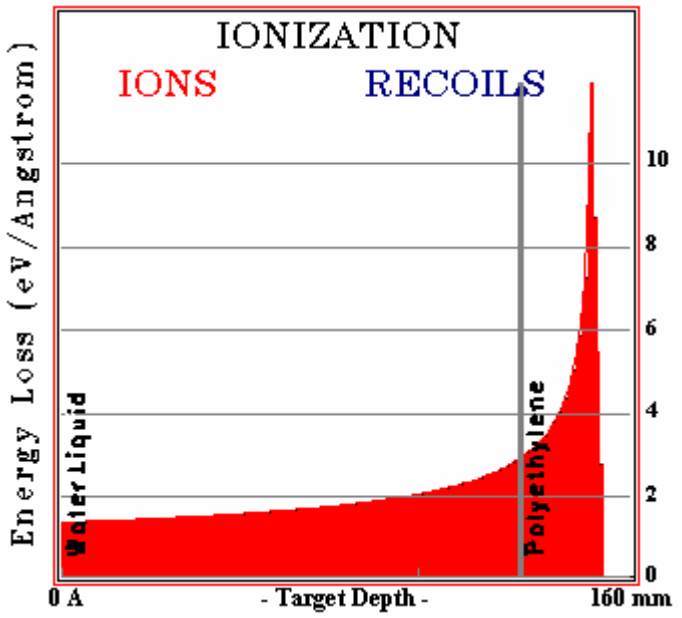

^{12}C, 273.3 MeV/n, 5000 particles, 128.74 mm PMMA

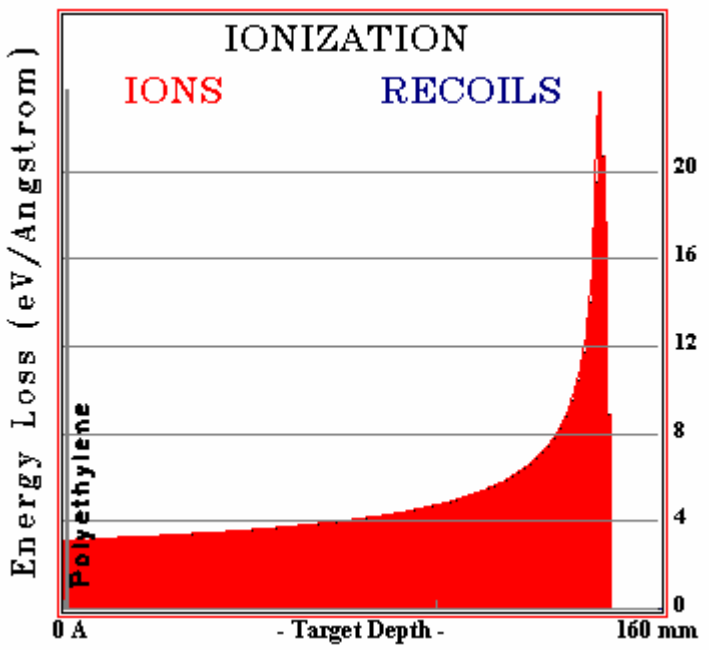

^{20}Ne, 367.9 MeV/n, 5000 particles, no binary filter

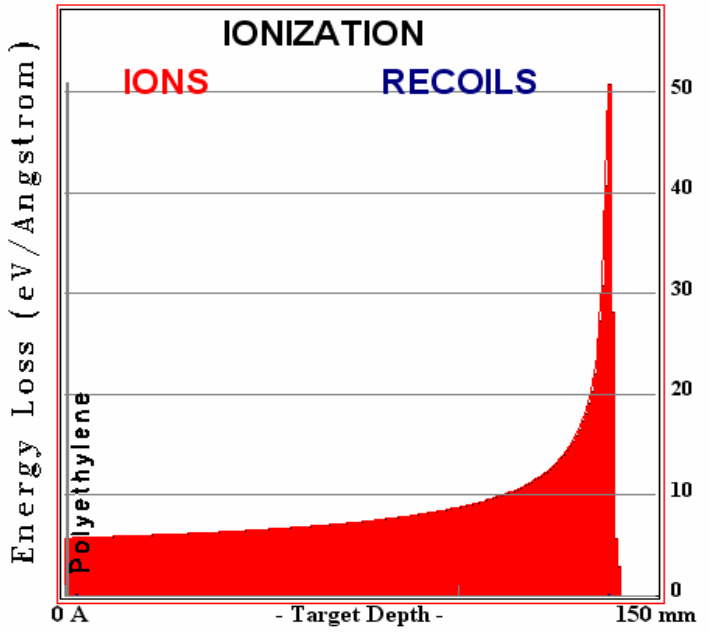

^{28}Si, 443.8 MeV/n, 5000 particles, no binary filter

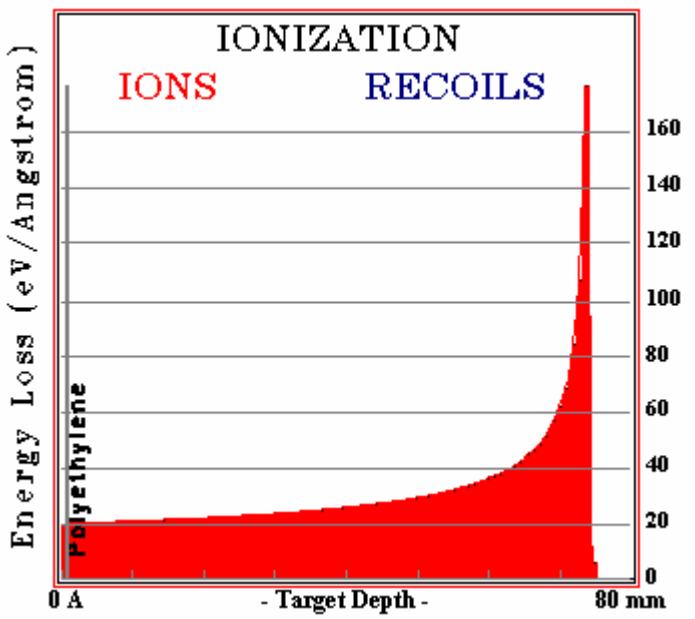

^{56}Fe, 414.7 MeV/n, 3000 particles, no binary filter

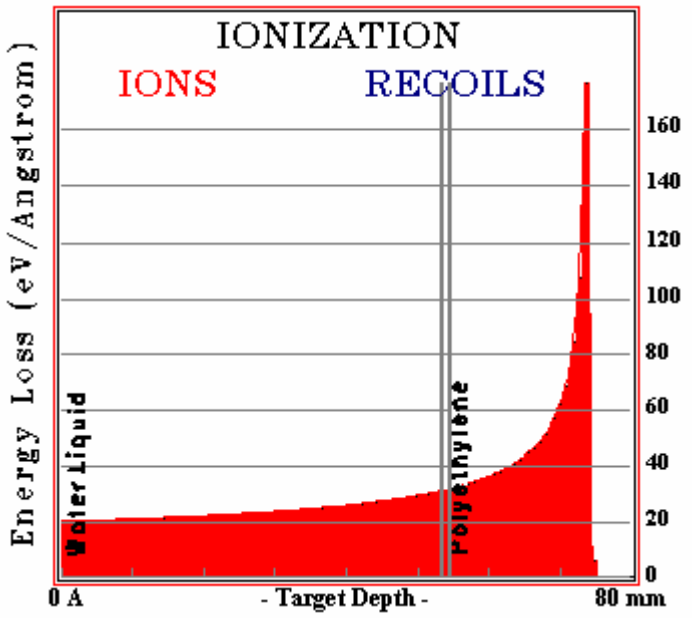

^{56}Fe, 414.7 MeV/n, 3000 particles, 53.62 mm PMMA

Appendix B: Suppliers of Materials, Chemicals and Devices

1. Thermo Fisher Scientific. Inc. 81 Wyman Street, Waltham, MA 02454, USA. http://www.thermo.com.
2. Sigma-Aldrich. 3050 Spruce St., St. Louis, MO 63103, USA. http://www.sigmaaldrich.com.
3. Invitrogen Corporation. 1600 Faraday Ave., Carlsbad, CA 92008, USA. http://www.invitrogen.com.
4. Nunc GmbH & Co. Rheingaustraße 32, D 65201 Wiesbaden, Germany. http://www.nunc.de.
5. Calbiochem, A Brand of EMD Biosciences, Inc. 10394 Pacific Center Court, San Diego, CA 92121, USA. http://www.calbiochem.com.
6. Lab Vision Corporation. 47790 Westinghouse Dr. Fremont, CA 94538, USA. http://www.labvision.com.
7. Rockland Immunochemicals, Inc. Gilbertsville, PA 19525, USA. http://www.rockland-inc.com.
8. Cell Signaling Technology, Inc. 3 Trask Lane, Danvers, MA 01923, USA. http://www.cellsignal.com.
9. Upstate Cell Signalling Solutions. 48 Barn Road, Lake Placid, NY 12946, USA. http://www.upstate.com.
10. Jackson ImmunoResearch Laboratories, Inc. 872 West Baltimore Pike, West Grove, PA 19390, USA. http://www.jacksonimmuno.com.
11. Olympus Austria GmbH. Shuttleworthstrasse 25, 1210 Wien, Austria. http://www.olympus.at.
12. Vilber Lourmat Deutschland GmbH. Wielandstrasse 2, D-88436 Eberhardzell, Germany. http://vilber.de.
13. Pinnacle Systems GmbH. Frankfurter Str. 3 c, Braunschweig, D-38122, Germany. http://www.pinnaclesys.com.
14. Merck KGaA. Frankfurter Str. 250, 64293 Darmstadt, Germany. http://www.merck.de.

Curriculum Vitae

DI Christoph Fürweger September 2007

Siedlungsring 11
3350 Haag
Austria

mobile: +43 (0)680 3027366
e-mail: fuerweger@ati.ac.at

Date of Birth: 18. 3. 1977, Austrian Citizenship

Education:

1983-1987	Primary School
1987-1995	High School

Military Service: Okt. 1995 – Sept. 1996 Training as non-commissioned officer for ABC-Defence

Academic Curriculum:

Oct. 1996 – Jul. 2003: Study of Technical Physics at the Vienna University of Technology. Master Thesis: *Cold Oxidation of Soot Particles by a unipolar Plasma* at the Atomic Institute of the Austrian Universities (Prof. Carl M. Fleck). Additional courses in Microbiology and Genetics at the University of Vienna.

Nov. 2003 – Sep. 2007: PhD Thesis at the Atomic Institute of the Austrian Universities and the Clinic for Radiotherapy and Radiobiology, Vienna. Title: *Thermoluminescence Dosemeters as Biologically relevant Detectors* (Prof. Norbert Vana and Prof. Reinhard Kodym).

May 2004 – Sep. 2006: Research Assistant at the Clinic for Radiotherapy and Radiobiology, Medical University of Vienna. Main research areas: Thermoluminescence dosimetry, radiation protection, cellular signal transduction mechanisms, bystander effects.

Jan. 2005 – Mar. 2006: Several stays at the National Institute of Radiological Sciences (NIRS), Chiba, Japan.

Language Skills:

English (fluent) French (basic notions) Latin (basic notions)

Further Information:

Research scholarships of the Vienna University of Technology. Member of the Austrian Society for Radiation Protection and the Alumni Association of the Vienna University of Technology.